

AD-A202 391

DTIC FILE COPY

ARO 21690.16-M

(2)

ENVIRONMENTAL EFFECTS ON THE TIME DEPENDENT  
FAILURE OF NON-OXIDE CERAMICS

FINAL REPORT

RICHARD E. TRESSLER

AUGUST 15, 1984 - JULY 14, 1988

U. S. ARMY RESEARCH OFFICE

DAAG29-84-K-0170

DEPARTMENT OF MATERIALS SCIENCE AND  
ENGINEERING, THE PENNSYLVANIA STATE UNIVERSITY

APPROVED FOR PUBLIC RELEASE;  
DISTRIBUTION UNLIMITED

3 DTIC  
ELECTED  
DEC 01 1988  
9E D

88 1122 090

**ENVIRONMENTAL EFFECTS ON THE TIME DEPENDENT  
FAILURE OF NON-OXIDE CERAMICS**

**FINAL REPORT**

**RICHARD E. TRESSLER**

**AUGUST 15, 1984 - JULY 14, 1988**

**U. S. ARMY RESEARCH OFFICE**

**DAAG29-84-K-0170**

Accession For	
NTIS GRA&I	<input checked="" type="checkbox"/>
DTIC TAB	<input type="checkbox"/>
Unannounced	<input type="checkbox"/>
Justification	
By _____	
Distribution/	
Availability Codes	
Dist	Avail and/or Special
A-1	

**DEPARTMENT OF MATERIALS SCIENCE AND  
ENGINEERING, THE PENNSYLVANIA STATE UNIVERSITY**

**APPROVED FOR PUBLIC RELEASE;  
DISTRIBUTION UNLIMITED**

UNCLASSIFIED  
SECURITY CLASSIFICATION OF THIS PAGE

MASTER COPY

FOR REPRODUCTION PURPOSES

REPORT DOCUMENTATION PAGE

1a. REPORT SECURITY CLASSIFICATION <u>Unclassified</u>		1b. RESTRICTIVE MARKINGS										
2a. SECURITY CLASSIFICATION AUTHORITY		3. DISTRIBUTION/AVAILABILITY OF REPORT  Approved for public release; distribution unlimited.										
2b. DECLASSIFICATION/DOWNGRADING SCHEDULE												
4. PERFORMING ORGANIZATION REPORT NUMBER(S)		5. MONITORING ORGANIZATION REPORT NUMBER(S)  ARO 21690.16-MS										
6a. NAME OF PERFORMING ORGANIZATION The Pennsylvania State Univ.	6b. OFFICE SYMBOL (If applicable)	7a. NAME OF MONITORING ORGANIZATION  U. S. Army Research Office										
6c. ADDRESS (City, State, and ZIP Code) 410 Walker Building University Park, PA 16802		7b. ADDRESS (City, State, and ZIP Code) P. O. Box 12211 Research Triangle Park, NC 27709-2211										
8a. NAME OF FUNDING/SPONSORING ORGANIZATION U. S. Army Research Office	8b. OFFICE SYMBOL (If applicable)	9. PROCUREMENT INSTRUMENT IDENTIFICATION NUMBER  DAAG629-84-K-0170										
8c. ADDRESS (City, State, and ZIP Code) P. O. Box 12211 Research Triangle Park, NC 27709-2211		10. SOURCE OF FUNDING NUMBERS  PROGRAM ELEMENT NO.      PROJECT NO.      TASK NO.      WORK UNIT ACCESSION NO.										
11. TITLE (Include Security Classification) Environmental Effects on the Time Dependent Failure of Non-Oxide Ceramics												
12. PERSONAL AUTHOR(S) Richard E. Tressler												
13a. TYPE OF REPORT Final Report	13b. TIME COVERED FROM 8/84 TO 6/88	14. DATE OF REPORT (Year, Month, Day) 1988, November, 3	15. PAGE COUNT 206									
16. SUPPLEMENTARY NOTATION The view, opinions and/or findings contained in this report are those of the author(s) and should not be construed as an official Department of the Army position, policy, or decision, unless so designated by other documentation.												
17. COSATI CODES <table border="1"><tr><th>FIELD</th><th>GROUP</th><th>SUB-GROUP</th></tr><tr><td>/</td><td></td><td></td></tr><tr><td>/</td><td></td><td></td></tr></table>	FIELD	GROUP	SUB-GROUP	/			/			18. SUBJECT TERMS (Continue on reverse if necessary and identify by block number) Silicon nitride, silicon carbide, oxidation, high temperature strength, threshold stress intensity, slow crack growth, tensile creep behavior, cavitation, creep damage. (TEC !)		
FIELD	GROUP	SUB-GROUP										
/												
/												
19. ABSTRACT (Continue on reverse if necessary and identify by block number) The mechanical and chemical factors that contribute to time dependent strength changes have been investigated for a variety of non-oxide materials including silicon nitride, silicon carbide and siliconized silicon carbide.												
The flaw behavior in an as-machined and oxidized HIP'ed silicon nitride under static load was investigated at various stress intensities, times, and temperatures. Flaw origins were of the pore/cavity and iron-based inclusion type. There was no strength increase or degradation in as-machined and oxidized samples static loaded for ten hours at 1100°C in air below the threshold stress intensity. The threshold stress intensity for crack growth at 1100°C were determined to be 1.75 and 2.00 MPa·m <sup>0.5</sup> for the as-machined and oxidized HIPSN, respectively. A strength decrease with increased applied stress was observed in as-machined specimens static loaded at 1200°C and 1300°C in air. This effect is due to the creation of a new flaw population with more severe flaws. -cont.-												
20. DISTRIBUTION/AVAILABILITY OF ABSTRACT <input checked="" type="checkbox"/> UNCLASSIFIED/UNLIMITED <input type="checkbox"/> SAME AS RPT. <input type="checkbox"/> DTIC USERS		21. ABSTRACT SECURITY CLASSIFICATION Unclassified										
22a. NAME OF RESPONSIBLE INDIVIDUAL		22b. TELEPHONE (Include Area Code)	22c. OFFICE SYMBOL									

Block 19 (Cont.)

Oxidized HPSN does not experience any strength degradation when static loaded at 1200°C below a threshold stress intensity of  $1.50 \text{ MPa} \cdot \text{m}^{\frac{1}{2}}$ . The oxidation treatment causes microstructural changes in the ceramic, resulting in a material with improved creep and crack growth resistance.

The interrupted static fatigue test was applied to three commercially available silicon nitride-based materials in the as-machined condition at 1200°C in air for ten hours. The effect of initial applied stress on the fracture stress indicated threshold stresses of 162 MPa, 375 MPa and 388 MPa for the AY6, PY6 and SN250M materials, respectively. The threshold stress was found to depend on the nature of the grain boundary phase in beta-silicon nitride ceramics with similar grain size and morphology. Differences in grain boundary structure from amorphous to crystalline accounted for an increase in the threshold stress by more than a factor of two.

Tensile creep tests were performed on the more stable oxidized silicon nitride using an optical extensometer and a flat dogbone-shaped specimen. Typical primary and secondary creep behavior was observed at 1100°C in air at applied stresses below the predicted threshold stress. Creep tests at 1150°C at 200 MPa show both creep behavior and slow crack growth rupture behavior. All creep tests at 1200°C led to very short term failure at applied stresses of 100-200 MPa.

The threshold stress intensity for crack growth in three types of dense polycrystalline silicon carbide ceramics was investigated at 1200, 1300 and 1400°C. Tests done on the CVD beta silicon carbide showed very low reliability at these temperatures and considerable strength degradation was observed due to the presence of unreacted silicon in this material. Delayed failure was observed, but reliable threshold stress intensity values at these temperatures could not be determined due to the low Weibull modulus.

The threshold stress intensity values of oxidized specimens of sintered silicon carbide were 3.75, 2.47 and  $2.42 \text{ MPa} \cdot \text{m}^{\frac{1}{2}}$  at 1200, 1300 and 1400°C, respectively. Indentation-induced tensile residual stresses were completely relieved under ten-hour static loading at 1300 and 1400°C but not at 1200°C. Subcritical crack growth in the indented material relaxes the residual stress during the static load test. Stress independent constant crack velocity values of  $6.0 \times 10^{-9}$  and  $2.3 \times 10^{-8} \text{ m/sec}$  were calculated by using dynamic fatigue tests at 1200 and 1300°C, respectively. Constant crack growth velocity values of  $2.0 \times 10^{-8}$  and  $1.0 \times 10^{-8} \text{ m/sec}$  were measured at 1300°C and 1400°C, respectively.

The threshold stress intensity values of HIP'ed silicon carbide were 3.52, 2.93 and 2.51  $\text{MPa} \cdot \text{m}^{\frac{1}{2}}$  at 1200, 1300, 1400°C, respectively. Indentation-induced residual stresses were relieved upon oxidation at elevated temperatures accompanied by flaw healing in the HIP'ed silicon carbide.

Activation energies of 46 and 34 KJ/mole were calculated for the threshold stress intensity for crack growth for the sintered and HIP'ed SiC, respectively. Stress relaxation via viscous deformation and microscopic flaw healing and blunting becomes more probable with decreasing grain size and increasing internal oxygen content in oxidized silicon carbide ceramics.

The tensile creep behavior of a siliconized silicon was investigated as a function of temperature and stress, using a modified flat dogbone-shaped specimen and an electro-optical extensometer to measure creep strain. The results of the creep study revealed the existence of a threshold stress for cavity formation. At applied stresses below the threshold stress, the creep behavior was controlled by the deformation of the silicon phase, while at applied stresses greater than the threshold, cavity formation contributed to this deformation

**UNCLASSIFIED**  
**SECURITY CLASSIFICATION OF THIS PAGE**

Block 19 (cont.)

process.

Quantitative microscopy determined the threshold stress for cavity formation to be 125.4 MPa at 1373 K. Both the areal density and area fraction of cavities increased linearly with creep strain. TEM analysis was used to determine that dislocation processes were active in the silicon phase during deformation of the siliconized silicon carbide.

The steady-state stress exponent for creep at 1373 K was approximately four at applied stress levels less than the threshold for cavity formation and the activation energy for steady-state creep in the absence of cavity formation was approximately 175 KJ/mole for the temperature range of 1373 K to 1473 K, under an applied stress of 103.4 MPa. The rate controlling mechanism was determined to be dislocation glide in the silicon phase. At stresses above the threshold, the steady-state stress exponent increased to ten at 1373 K and the activation energy increased to 315 and 380 KJ/mole for the temperature ranges of 1373 - 1423 K and 1423 - 1473 K, respectively. The cavity formation process was responsible for the increases.

Analysis of the experimental data established that the cavity formation was nucleation controlled and the proposed mechanism was heterogeneous nucleation of cavities at the silicon-silicon carbide interface. Cavity growth occurred very rapidly under the stresses and temperatures used in this study. The proposed mechanism for cavity growth was the diffusional transport of matter away from the crack tip and down the boundary between the silicon and silicon carbide.

The oxidation behavior of black and green single crystal silicon carbide materials under different oxygen partial pressures was studied over the temperature range 1200 - 1500°C. Parabolic behavior was observed for both materials. The calculated activation energies for the fast growth face (000I) for black single crystal SiC in the lower temperature range were 112, 94, and 95.4 KJ/mole under oxygen partial pressures of 0.1, 0.01 and 0.001 atmospheres, respectively. At higher temperatures the values were 257, 285, and 288 KJ/mole, respectively at the same partial pressures. For the fast growth face (000I) of green single crystal SiC the values of the activation energy at the lower temperatures were 115, 100, and 127 KJ/mole at 0.1, 0.01 and 0.001 atmospheres, respectively. At higher temperatures the values are 234, 265, and 232 KJ/mole for the same three partial pressures.

The transition temperatures at which the oxidation rate controlling mechanism changed increased with an increase in oxygen partial pressure. The values of the transition temperature for the black single crystal silicon carbide were lower than those of the green single crystal silicon carbide.

In the lower temperature range, the oxidation was believed to be controlled by oxygen permeation through the amorphous silica film. In the higher temperature range, two possible rate controlling mechanisms were the ionic or atomic diffusion via a lattice exchange mechanism and the out-diffusion of an oxidation by-product such as carbon monoxide, away from the  $\text{SiO}_2$ -SiC interface.

**UNCLASSIFIED**  
**SECURITY CLASSIFICATION OF THIS PAGE**

## Final Report on Funding Document DAAG29-84-K-0170

The research on this project has proceeded in four general areas.

- a) Flaw behavior and tensile creep behavior in silicon nitride ceramics at elevated temperatures.
- b) Microstructural and environmental effects on the static fatigue limit in silicon carbide ceramics at elevated temperatures.
- c) Tensile creep of silicon carbide ceramics.
- d) Oxidation of silicon carbide materials.

### Summary of Results

- a) M. Foley has defended his M.S. thesis entitled "Flaw Behavior Near the Threshold Stress Intensity in a Hot Isostatically Pressed Silicon Nitride at Elevated Temperatures." The abstract is included in the appendix. Preliminary tensile creep rupture tests on silicon nitride were performed and are summarized in a paper entitled "Time Dependent Mechanical Behavior of Silicon Nitride Ceramics above 1100°C," also included in the appendix.
- b) B. Yavuz has defended his Ph.D. Thesis entitled "Subcritical Crack Growth Behavior and Threshold Stress Intensity for Crack Growth in Silicon Carbide Ceramics at Elevated Temperatures," and the abstract is included in the appendix.
- c) D. Carroll has defended his Ph.D. Thesis entitled "Tensile Creep Behavior and Cavity Damage in a Siliconized Silicon Carbide," and the abstract is included in the appendix.
- d) Z. Zheng has defended his M.S. Thesis entitled "Oxidation of Single Crystal Silicon Carbide," and the abstract is included in the appendix.

Also included in the appendix are copies of all manuscripts published or submitted under ARO sponsorship during the project period of August 15, 1984 through July 14, 1988, including journal references.

### List of Manuscripts

1. "Kinetics of Oxidation of SiC Crystals and Ceramics, Part I: In Dry Oxygen," J. A. Costello and R. E. Tressler, *J. Amer. Ceram. Soc.*, 69 (9), 674-681 (1986).
2. "Isotope Labeling Studies of the Oxidation of Silicon at 1000° and 1300°C," J. A. Costello and R. E. Tressler, *J. Electrochem. Soc.* 131 (8) 1944-47 (1984).

3. "Oxygen Penetration into Silicon Carbide Ceramics During Oxidation," J. A. Costello and R. E. Tressler, *Ceramics International*, 11 (2), 39-44 (1985).
4. "Static Fatigue Limit for Silicon Carbide Based Ceramics - Flaw Blunting Flaw Growth," R. E. Tressler, E. J. Minford, and D. F. Carroll, *Proceedings of the Second International Conference on Creep and Fracture of Engineering Materials and Structures*, April 1-6, 1984, University of Wales.
5. "Time Dependent Strength of Siliconized Silicon Carbide Under Stress at 1000°C and 1100°C," D. F. Carroll and R. E. Tressler, *J. Amer. Ceram. Soc.*, 68 (3) 143-146 (1985).
- \* 6. "Oxidation of Silicon Carbide Ceramics," R. E. Tressler, J. A. Costello, and Z. Zheng, in *Industrial Heat Exchangers*, Ed. A. J. Hayes, W. W. Liang, S. L. Kishler and E. S. Tabb, American Society for Metals, 1985, pp. 307-314.
7. "High Temperature Mechanical Properties of Siliconized Silicon Carbide Composites," D. F. Carroll, R. E. Tressler, Y. Tsai, and C. Near, in *Tailoring of Multiphase and Composite Ceramics* Ed. R. E. Tressler, G. L. Messing, C. G. Pantano and R. E. Newnham, Plenum Publishing, November 1986, pp. 775-788.
- \* 8. "On the Static Fatigue Limit at Elevated Temperature," T. Chuang, R. E. Tressler, and E. J. Minford, *Materials Science and Engineering* 82 187-195 (1986).
- \* 9. "Time Dependent Mechanical Behavior of Silicon Carbide Ceramics at Elevated Temperatures," D. F. Carroll and R. E. Tressler, *High Tech Ceramics*, Ed. P. Vincenzini, Elsevier, Amsterdam, 1987, 1335-1344.
10. "Oxidation Kinetics of Silicon Carbide Crystals and Ceramics: I, In Dry Oxygen," John A. Costello, and R. E. Tressler, *Journal of the American Ceramic Society*, Vol. 69, No. 9, pp. 674-681, September 1986.
11. "Accumulation of Creep Damage in a Siliconized Silicon Carbide," by D. F. Carroll and R. E. Tressler, *J. Amer. Ceram. Soc.*, Vol. 71 (6), pp. 472-477, 1988.
12. "Threshold Stress Intensity for Crack Growth at Elevated Temperature in a Silicon Nitride Ceramic," by M. R. Foley and R. E. Tressler, *Advanced Ceramic Materials*, Vol. 3 (4), pp. 382-386.
13. "Effect of Creep Damage on the Tensile Creep Behavior of a Siliconized Silicon Carbide," by D. F. Carroll and R. E. Tressler accepted by the *J. Amer. Cer. Soc.*

\* Manuscripts previously submitted in ARO progress reports

Delete the restricted article entitled:  
 "Oxidation of Silicon Carbide Ceramics."  
 Per Ms. Sylvia Hall, ARO/Library



Accession For	
NTIS GRAIL	
DTIC TAB	
Unannounced	
Justification	
By _____	
Distribution/	
Availability Codes	
Distr	Avail and/or Special
A-1	

14. "Time Dependent Mechanical Behavior of Silicon Nitride Ceramics Above 1100°C," M. R. Foley and R. E. Tressler, to be published in Proceedings of the Third International Symposium on ceramic Materials and Components for Engines, Las Vegas, NE, November 1988.
15. "Comparisons of the Time Dependent Strength of Three Commercially available Silicon Nitride Materials," M. R. Foley, C. A. Randall and R. E. Tressler, to be submitted.

The Pennsylvania State University  
The Graduate School  
Department of Materials Science and Engineering

Flaw Behavior Near the Threshold Stress Intensity in a Hot  
Isostatically Pressed Silicon Nitride at Elevated Temperatures

A Thesis in  
Ceramic Science  
by  
Michael R. Foley

Submitted in Partial Fulfillment  
of the Requirements  
for the Degree of

Master of Science

November 1986

I grant The Pennsylvania State University the nonexclusive right  
to use this work for the University's own purposes and to make single  
copies of the work available to the public on a not-for-profit basis  
if copies are not otherwise available.

---

Michael R. Foley

## ABSTRACT

The flaw behavior in as-machined and oxidized AY6 hot isostatically pressed silicon nitride (HIPSN) under static load was investigated at various stress intensities, times and temperatures. The short term fracture stress and fracture toughness at room temperature and elevated temperatures were not affected by oxidation. Flaw origins were of the pore/cavity type and iron-based inclusion type. There was no strength increase or degradation in as-machined and oxidized specimens static loaded at 1100°C in air below the threshold stress intensity. The threshold stress intensities for crack growth at 1100°C were determined to be 1.75 and 2.00 MPa . m<sup>1/2</sup> for the as-machined and oxidized HIPSN, respectively. A strength decrease with increased applied stress was observed in as-machined specimens static loaded at 1200°C and 1300°C in air. This effect is due to the creation of a new flaw population with more severe flaws and/or increasing the severity of the original flaws. Threshold stresses of 160 MPa and 90 MPa were observed at 1200°C and 1300°C, respectively. Oxidized HIPSN does not experience any strength degradation when static loaded at 1200°C below a threshold stress intensity of 1.50 MPa.m<sup>1/2</sup>. The oxidation treatment is thought to produce microstructural changes resulting in a material with improved creep resistance. Due to the extensive plastic deformation occurring in samples static loaded at 1300°C no further testing of oxidized samples was done at 1300°C.

The Pennsylvania State University  
The Graduate School  
Department of Materials Science and Engineering

Subcritical Crack Growth Behavior and Threshold Stress  
Intensity for Crack Growth in Silicon Carbide Ceramics at  
Elevated Temperatures

A Thesis in  
Ceramic Science  
by  
Bülent Osman Yavuz

Submitted in Partial Fulfillment  
of the Requirements  
for the Degree of

Doctor of Philosophy  
December 1987

Copyright 1987 Bülent Osman Yavuz

## ABSTRACT

The threshold stress intensity for crack growth in three types of dense polycrystalline silicon carbide ceramics was investigated at 1200, 1300 and 1400°C. In order to study the effect of variable grain boundary composition, a chemically vapor deposited silicon carbide with no cationic additive, an aluminum-doped pressureless sintered silicon carbide and a HIPed silicon carbide densified with no sintering additives were tested. The modified static loading technique which was developed by Minford and Tressler<sup>3</sup> was used to determine the threshold stress intensities.

It was shown that when a knowledge of the strength distribution is explicitly incorporated with the modified static loading data, the threshold stress intensity values can be obtained with a 95% confidence.

An interpretation of the dynamic fatigue test results was developed for ceramics which have threshold stress intensities equal to a significant fraction of its fracture toughness.

Tests done on the chemically vapor deposited beta silicon carbide revealed that this material contains unreacted silicon. Significant tensile residual stresses were nonuniformly distributed within this material. Strength distribution tests done on this material showed

very low reliability (i.e., low Weibull modulus at every temperature). At temperatures above 1300°C, considerable strength degradation was observed due to the presence of free silicon in this material. Delayed failure was observed at 1300 and 1400°C, but reliable threshold stress intensity values at these temperatures could not be determined using 10-hour modified static loading due to the very low Weibull modulus of the material.

Modified static loading tests of ten hours duration were performed on the oxidized as-machined specimens of sintered silicon carbide to determine the threshold stress intensity at 1200, 1300 and 1400°C. When the same tests were applied to the indented specimens,  $K_{th}$  values of 3.75, 2.47 and 2.42 MPa.m<sup>1/2</sup> were determined at 1200, 1300 and 1400°C, respectively. These values correspond to 79, 67 and 58% of the fracture toughness values at 1200, 1300 and 1400°C, respectively, and are in excellent agreement with those obtained from as-machined specimens.

Indentation-induced tensile residual stresses were found to have significant effects on crack propagation in sintered silicon carbide at every testing temperature. These stresses were relieved completely under 10-hour static loading at 1300 and 1400°C. A major portion of the indentation-induced residual stress was not relieved at 1200°C. Subcritical crack growth in the indented material relaxes the residual stress which is acting along the

crack front during the modified static loading test.

Dynamic fatigue tests were performed at 1200, 1300 and 1400°C. Stress independent constant crack velocity values were calculated by using the dynamic fatigue test data at 1200 and 1300°C. These values were  $6.0 \times 10^{-9}$  and  $2.3 \times 10^{-9}$  m/sec at 1200 and 1300°C, respectively. Slow crack growth velocity measurements were done on the indented samples at 1300 and 1400°C. Constant crack growth velocity values of  $2.0 \times 10^{-9}$  and  $1.0 \times 10^{-9}$  m/sec were measured at 1300 and 1400°C, respectively.

Modified static loading tests of 10 hours duration of oxidized as-machined specimens were performed to determine the threshold stress intensities of the HIPed silicon carbide at 1200, 1300 and 1400°C. The expected, upper and lower bound values of the  $K_{th}$  values, when expressed as a fraction of the fracture toughness, were determined, with 95% confidence, as (0.74, 0.71, 0.80), (0.71, 0.62, 0.92) and (0.58, 0.51, 0.75) at 1200, 1300 and 1400°C, respectively. The corresponding expected stress intensity values are 3.52, 2.93 and 2.51 MPa.m<sup>1/2</sup> at these temperatures.

Indentation-induced residual stresses were relieved upon oxidation at elevated temperatures accompanied by flaw healing in the HIPed silicon carbide. A microscopic flaw blunting mechanism becomes active at stress

intensities below the threshold causing strengthening of this material.

The experimentally obtained results of the threshold stress intensity for crack growth for the silicon carbide materials were best described by the slow crack growth model developed by Chuang.<sup>32</sup> Activation energies of 46000 and 34000 Joules/mole were calculated for the threshold stress intensity for crack growth for the sintered and the HIPed silicon carbide, respectively.

Comparison of the results of this work to those obtained in previous works<sup>2-4</sup> shows that aluminum added sintered silicon carbide has a higher threshold stress intensity than the boron doped sintered silicon carbide, (3.75 vs. 1.75 MPa.m<sup>1/2</sup> at 1200°C and 2.42 vs. 1.25 MPa.m<sup>1/2</sup> at 1400°C). Stress relaxation via viscous deformation and microscopic flaw healing and blunting becomes more probable with decreasing grain size and increasing internal oxygen content in oxidized silicon carbide ceramics.

The Pennsylvania State University  
The Graduate School  
Department of Materials Science and Engineering

Tensile Creep Behavior and Cavity Damage in  
a Siliconized Silicon Carbide

A Thesis in  
Ceramic Science  
by

Daniel Franke Carroll

Submitted in Partial Fulfillment  
of the Requirements  
for the Degree of

Doctor of Philosophy

May 1987

©1987 Daniel Franke Carroll

I grant The Pennsylvania State University the nonexclusive right  
to use this work for the University's own purposes and to make single  
copies of the work available to the public on a not-for-profit basis  
if copies are not otherwise available.

---

Daniel Franke Carroll

## ABSTRACT

The tensile creep behavior of a siliconized silicon carbide was investigated as a function of temperature and stress, using a modified flat dogbone-shaped specimen and an electro-optical extensometer to measure creep strain. Creep tests were conducted in air, at temperatures of 1373 to 1473 K under stresses ranging from 103.4 to 172.3 MPa (15,000 to 25,000 psi). An extensive study using scanning electron microscopy (SEM) and transmission electron microscopy (TEM) was conducted on deformed specimens, to aid in the identification of the mechanism(s) responsible for creep.

The results of this creep study revealed the existence of a threshold stress for cavity formation. At applied stresses less than the threshold for cavity formation, the creep behavior of the siliconized silicon carbide was controlled by the deformation of the silicon phase. At applied stresses greater than the threshold, cavity formation contributed to this deformation process.

Quantitative microscopy was used to determine the threshold stress for cavity formation to be approximately 125.4 MPa (18,200 psi) at 1373 K. Both the areal density and area fraction of cavities increased linearly with creep strain. This result indicated that once a cavity nucleated, it grew very rapidly to an equilibrium size. The maximum size of the cavities was limited to the size of the surrounding silicon carbide grains.

TEM analysis was used to determine that dislocation processes were active in the silicon phase during deformation of the siliconized silicon carbide. The dislocation densities were relatively low and

confined to groups randomly distributed throughout the silicon phase. There was no evidence of dislocation motion in the silicon carbide grains.

The steady-state stress exponent for creep at 1373 K was determined to be approximately four at applied stress levels less than the threshold for cavity formation (103.4 to 120.6 MPa). The corresponding activation energy for steady-state creep in the absence of cavity formation, was determined to approximately 175 kJ/mole for the temperature range of 1373 to 1473 K, under an applied stress of 103.4 MPa. Based upon these results, at 1373 K, the rate controlling mechanism for steady-state creep below the threshold stress for cavity formation, was dislocation glide in the silicon phase. Dislocation glide was limited by the formation of double kinks which assisted dislocations in overcoming the Peierl's barrier.

At stresses above the threshold for cavity formation, the steady stress exponent increased to approximately ten at 1373 K. The activation energy for creep in the presence of cavities increased to approximately 315 and 380 kJ/mole for the temperature range of 1373 to 1423 K and 1423 to 1473 K, respectively, at a stress level of 172.3 MPa. The cavity formation process was responsible for the increase in the stress exponent and activation energy for creep.

Analyses of the experimental data using the various nucleation and growth models established that the cavity formation process was nucleation controlled. The proposed mechanism was heterogeneous nucleation of cavities at the silicon-silicon carbide interface. The continuous nucleation of cavities with strain was the result of inhomogeneous deformation and an increasing effective stress in the

matrix from cavity formation. Cavity growth occurred very rapidly under the stresses and temperatures used in this study. The proposed mechanism for cavity growth was the diffusional transport of matter away from the crack tip and down the boundary between the silicon and silicon carbide as described by the diffusional models of Raj<sup>47</sup> and Chuang et al.<sup>52</sup> The maximum size of the cavities was not limited by growth but by the rigidity of the silicon carbide grains.

The Pennsylvania State University

The Graduate School

Department of Materials Science and Engineering

Oxidation of Single Crystal Silicon Carbide

A Thesis in

Ceramic Science

by

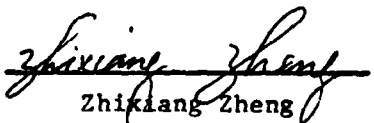
Zhixiang Zheng

Submitted in Partial Fulfillment  
of the Requirements  
for the Degree of

Master of Science

May, 1985

I grant The Pennsylvania State University the nonexclusive  
right to use this work for the University's own purposes and to  
make single copies of the work available to the public on a not-  
for-profit basis if copies are not otherwise available.

  
Zhixiang Zheng

0.1, 0.01, and 0.001 atmospheres, respectively. For green single crystal SiC, the transition temperatures were 1411° C, 1345° C, and 1314° C for oxidation under the oxygen partial pressures of 0.1, 0.01, and 0.001 atmospheres, respectively. The values of the transition temperature for the black single crystal silicon carbide were lower than those of the green single crystal silicon carbide.

In the lower temperature range, the oxidation was believed to be controlled by oxygen permeation through the amorphous silica film. In the higher temperature range, two possible oxidation rate controlling mechanisms were the ionic or atomic oxygen diffusion via a lattice (network) exchange mechanism and the out-diffusion of an oxidation by-product, such as carbon monoxide, away from the  $\text{SiO}_2 - \text{SiC}$  interface.

The oxygen diffusivities during oxidation of the green material at two different oxygen partial pressures and two different temperatures were derived from double oxidation experiments. These isotope diffusion constants could not supply a high enough flux of oxygen to produce the observed oxidation rate for the material under the experimental environments studied.

## ABSTRACT

The oxidation behavior of black and green single crystal silicon carbide materials under different oxygen partial pressures ( $10^{-3}$  -  $10^{-1}$  atmosphere) was studied over the temperature range  $1200^{\circ}\text{C}$  -  $1500^{\circ}\text{C}$ .

Parabolic behavior was observed for both materials in this investigation. For the fast growth face (0001) of black single crystal SiC, at the lower temperatures studied, the calculated activation energies were 112 KJ/mole, 94 KJ/mole, and 95.4 KJ/mole for oxidation under oxygen partial pressures of 0.1, 0.01, and 0.001 atmospheres, respectively. At the higher temperatures studied, the calculated activation energies were 257 KJ/mole, 285 KJ/mole, and 288 KJ/mole for oxidation under oxygen partial pressures of 0.1, 0.01, 0.001 atmospheres, respectively. For the fast growth face (0001) of green single crystal SiC, at the lower temperatures, the calculated activation energies were 115 KJ/mole, 100 KJ/mole, and 127 KJ/mole for oxidation under oxygen partial pressures of 0.1, 0.01, and 0.001 atmospheres, respectively. At the higher temperatures studied, the calculated activation energies were 234 KJ/mole, 265 KJ/mole, and 232 KJ/mole for oxidation under oxygen partial pressures of 0.1, 0.01, and 0.001 atmospheres, respectively.

The transition temperatures at which the oxidation rate controlling mechanism changed increased with an increase in oxygen partial pressure. For black single crystal SiC, the transition temperatures were  $1382^{\circ}\text{C}$ ,  $1301^{\circ}\text{C}$ , and  $1287^{\circ}\text{C}$  for oxidation under the oxygen partial pressures of

KINETICS OF OXIDATION OF SiC CRYSTALS AND  
CERAMICS, PART I: IN DRY OXYGEN

J. A. Costello\* and R. E. Tressler  
Department of Materials Science and Engineering  
The Pennsylvania State University  
University Park, PA 16802

ABSTRACT

The oxidation kinetics in dry oxygen of several single crystal and polycrystalline silicon carbide materials and single crystal silicon over the temperature range 1200°C-1500°C were fitted to the linear-parabolic model of Deal and Grove. The lower oxidation rates for silicon carbide compared to silicon can be rationalized by additional consumption of oxidant in oxidizing carbon to carbon monoxide. The (0001) Si face of the silicon carbide platelets exhibited lower parabolic oxidation rates than the (0001̄) C face, by a factor of ten at 1200°C. Apparent activation energies increased from a value of approximately 120 kJ/mole below 1400°C to a value of approximately 300 kJ/mole above this temperature with the (0001) Si face exhibiting this high activation energy over the entire temperature range.

The CNTD material exhibited the highest oxidation rates of the polycrystalline materials followed by the hot pressed and sintered alpha silicon carbides. In general, the oxidation rates of the polycrystalline materials were bracketed by the oxidation rates of the basal planes of the single crystal materials. Higher impurity concentrations and higher density of nucleation sites led to a higher susceptibility to crystallization of the scale. The crystallization of the oxide films retarded the oxidation rates when coherent but accelerated the oxidation rate when the coherent cristobalite spherulitic scale reacted to form mullite.

\* Now at U. S. Army Electronics Technology and Devices Lab., Fort Monmouth, NJ 07703

## I. Introduction

The oxidation of silicon carbide materials has been the subject of many investigations over a few decades because of their use for many years in high temperature applications. The excellent oxidation resistance which silicon carbide exhibits is due to the formation of a coherent layer of silicon dioxide on the surface which suppresses further oxidation. Oxidation kinetics can generally be described using the linear-parabolic model of Deal and Grove<sup>1</sup>. This model was formulated to characterize the oxidation behavior of single crystal silicon accounting for both linear and parabolic dependences of oxide thickness with time. The linear dependence arises from interface reaction control of the oxidation in the early stages. Reported activation energies in the linear growth regime correspond to the Si-Si bond energy ( $\sim 84$  kJ/mole). With increasing oxide thickness, the oxidation is controlled by diffusion of oxidant through the oxide to the growth interface. Under these conditions, classic parabolic oxidation kinetics are observed where the oxide thickness is proportional to the square root of time. The reported activation energy in this regime (117 kJ/mole) agrees very well with the energy required for molecular oxygen diffusion in fused silica as reported by Norton<sup>2</sup>. Other experimental evidence has been reported in support of this rate controlling mechanism<sup>1-5</sup>. Both regimes exhibit a linear dependence on oxygen partial pressure as predicted by the model.

The oxidation behavior of silicon carbide oxidation is not as well understood<sup>6-16</sup>. In most studies, only parabolic oxidation kinetics have been reported. Activation energies range from 84 to 498 kJ/mole. The large variation in reported kinetics has been attributed to the differences in the materials used in each investigation. Powders, single crystal and polycrystalline materials with varying amounts and types of impurities have been

investigated. In contrast, the better characterized silicon oxidation has been obtained with single crystal material having precisely controlled impurity concentrations.

Very few studies of the oxidation behavior of single crystal silicon carbide have been reported in the literature presumably due to the difficulty in acquiring the single crystal material. Harris<sup>8</sup> reported the oxidation of {0001} faces of the 6H polytype silicon carbide platelets in dry oxygen at 970-1245°C. Parabolic behavior was exhibited on the (0001) face at each temperature for thicknesses greater than 250 nm. The activation energy of 197 kJ/mole was slightly larger than the corresponding value for silicon. On the opposing face, a greater oxidation resistance was observed. The difference in oxidation behavior is attributed to the polar form of the tetrahedral bonding in the 6H structure. Linear kinetics were reported for all temperatures and times. An activation energy of 356 kJ/mole was calculated and suggested to correspond to the chemical reaction at the SiC surface. The effect of orientation, polytype, and dopant level on the oxidation of SiC platelets was discussed by von Münch and Pfaffender<sup>9</sup>. Oxide thickness values for the two {0001} faces differed by a factor of 7-10 and intermediate values were observed for (1120) and (1100) orientations. The 15R polytype oxidized faster than the 6H variety. High dopant concentrations ( $>10^{18}$  cm<sup>-3</sup>) enhanced the oxidation rates. Single crystal oxidation carried out in wet oxygen exhibited increases of approximately twenty compared to dry oxygen results.

The oxidation of polycrystalline SiC materials has shown a considerable range of behavior<sup>7,11-16</sup>. Several investigations report extremely large activation energies (>400 kJ/mole) for the oxidation process and conclude that a mechanism other than oxygen permeation controls the oxidation<sup>11-13</sup>. In contrast, several other investigations report lower activation energies for

results below 1400°C and suggest that oxygen permeation is rate-controlling<sup>11,13-16</sup>. Increased activation energies above 1400°C were similar in magnitude to the values previously reported and indicate a change in the oxidation mechanism. A complicated oxygen partial pressure dependence for oxidation of hot pressed silicon carbide was reported by Tripp et al.<sup>12</sup> varying from 0.55 at 1300°C to nearly independent (0.03) at 1500°C. Higher oxidation rates have been measured for materials with greater concentrations of dopant additives<sup>15-17</sup>. These additives which are necessary for successful fabrication of the ceramic redistribute into the oxide during oxidation and lower the viscosity of the film thereby increasing the transport of oxidant<sup>17-20</sup>.

These factors significantly alter the oxidation kinetics resulting in considerable differences in reported behavior. The purpose of this paper is to report the oxidation behavior of several single crystal and polycrystalline SiC materials in dry oxygen at 1200-1500°C. Oxidation kinetics of the single crystal faces are described and extended to the polycrystalline materials to explain the observed kinetics.

## II. Experimental Procedure

### 1. Materials

The silicon carbide materials used in this study are listed in Table 1. The single crystal materials consist of black and transparent green varieties of the alpha or hexagonal structure type. The coloring arises from the presence of aluminum and nitrogen impurities respectively, both in the ppm range. The crystals are predominantly thin platelets with the major surfaces being (0001) basal surfaces of the hexagonal structure. Boron doped single crystal silicon having (111) orientation was also used for comparison. Polycrystalline materials included sintered alpha SiC (SASC)<sup>\*</sup>, hot pressed SiC (HPSC)<sup>+</sup>, and controlled nucleation, thermally deposited SiC (CNTD)<sup>x</sup>.

\*Carborundum Company, Niagara Falls, NY

+NC-203, Norton Company, Worcester, MA

<sup>x</sup>San Fernando Laboratories, Pacoima, CA

Sample preparation included cutting, polishing and cleaning. Sample size was typically 1 cm x 1 cm x .2 cm. The single crystal platelets were extracted from growth clusters in material from the Acheson furnace process. Polycrystalline materials were supplied in billet form and were cut to size using a diamond saw. The carbon substrate of the CNTD material was removed by pyrolysis at 600°C. Samples were polished to a 1/4 $\mu$ m diamond finish using an automatic polishing apparatus. An oxidation screening of the single crystal samples was used to distinguish the (0001) face from the (000 $\bar{1}$ ) face using the earlier result that the (000 $\bar{1}$ ) face oxidizes faster than the (0001) face. Prior to oxidation, successive treatments of acetone, trichloroethylene, dilute hydrochloric acid, dilute hydrofluoric acid and deionized water were used to thoroughly clean all the samples.

## 2. Oxidation Experiments and Characterization

Oxidations were performed in a horizontal mullite tube furnace equipped with MoSi<sub>2</sub> heating elements. A three inch hot zone ( $\pm 1^\circ\text{C}$ ) was present over the temperature range 1200-1500°C. A controlled atmosphere of dry oxygen flowing at 200 ccpm was used. Temperature equilibration following insertion of the holder typically occurred in less than two minutes.

Oxide thickness measurements were obtained using ellipsometry and profilometry. The precision of each technique was determined in this investigation to be  $\pm 3$  nm and  $\pm 50$  nm respectively. The morphologies of the oxide films were characterized using x-ray diffraction analysis, optical, and scanning electron microscopy. Long term oxidation of the hot pressed and sintered alpha materials was investigated by thermogravimetric analysis (TGA).<sup>\*</sup> These oxidations were performed at 1300 and 1400°C in reduced oxygen pressure (0.2 atm) for 24 hrs. The samples were rectangular coupons with one of the major surfaces polished to 1/4 $\mu$ m finish for a final oxide thickness determination.

---

\*H. Graham, Wright Patterson AFB, Dayton, OH

### III. Results and Discussion

#### 1. Single Crystals

The data have been analyzed using the model of Deal and Grove<sup>1</sup>.

The oxide thickness,  $x$ , is expressed as a function of time,  $t$ , by the equation

$$x^2 + Ax = B(t + \tau) \quad (1)$$

where  $A$ ,  $B$  and  $\tau$  are experimental constants for a given oxidation condition.

$B$  is the parabolic rate constant and the linear rate constant is equal to  $B/A$ . The time constant,  $\tau$ , is a constant that accounts for an initially rapid oxidation period which is not expressed by linear or parabolic kinetics. It is usually significant at lower temperatures and in this study was found to be zero for all oxidation conditions of all materials.

The oxide thickness data for the {0001} faces of the black single crystal material is shown in Figure 1(a+b). The data exhibits parabolic behavior as indicated by the one-half slope dependence. Linear oxidation kinetics were not observed in any dry oxidation case.

As expected, the two {0001} faces exhibit markedly different oxidation rates. The {0001} face having the faster growth kinetics will be referred to as the fast growth face. Correspondingly, the {0001} face will be referred to as the slow growth face. In all the single crystal materials, crystallization of the oxide films was not observed. The onset of crystallization was readily observed on polycrystalline material using the optical microscope, by the appearance of isolated spherulitic crystallites. Extensive crystallization of the oxide films on several polycrystalline materials was observed and caused appreciable changes in their oxidation behavior.

Rearrangement of equation (1) into the form

$$x = B(t/x) - A \quad (2)$$

allows for the extraction of the constants by simple linear regression analysis. The parabolic rate constants for the single crystal materials are compiled in Table 2. Each value is accompanied by an experimental error value assuming a 95% confidence limit. Little significance could be attached to the observed linear rate constants which varied erratically, at times assuming negative values. Silicon exhibited the fastest oxidation rate at each temperature. The observed value at 1200°C compares favorably to literature values ( $750 \text{ nm}^2/\text{min}$ )<sup>1</sup>. The fast growth face exhibits similar rates to those reported by Harris ( $317 \text{ nm}^2/\text{min}$  at 1200°C)<sup>5</sup>. The slow growth face exhibited parabolic behavior in contrast to the reported behavior by Harris. However, careful examination of the Harris data indicates that the upper temperature data is actually in the linear-parabolic transition region. In calculating the rate constants, Harris regarded this as linear behavior. In contrast, the 1200°C data presented here has a clearly delineated slope of one-half.

Activation energies calculated using the Arrhenius relation are listed in Table 2. The temperature dependencies are also plotted in Figure 2. In this case, activation energies are determined from the slope of the line. The energy value for silicon oxidation (120 kJ/mole) agrees quite well with the literature (117 kJ/mole). Similar values were calculated for the fast growth faces over the temperature range 1200-1400°C. Above 1400°C, an increase in the activation energy occurs for the fast growth face. The slow growth faces exhibit a large energy value over the entire range studied.

Differences in the parabolic oxidation behavior of silicon and the fast growth faces of silicon carbide at 1200-1400°C can be explained by the additional oxidant needed to oxidize the carbon in silicon carbide<sup>3,4</sup>. As illustrated in Table 3, observed parabolic rate ratios for the single crystal data agree with the predicted ratio when carbon monoxide is formed during

silicon carbide oxidation. A smaller percentage of oxidant reaching the growth interface is available to form silicon dioxide from silicon carbide, resulting in the lower parabolic rates that are observed.

This evidence and the similar temperature dependence strongly suggests that the fast growth face of silicon carbide exhibits the same rate controlling oxidation mechanism as silicon over the temperature range 1200-1400°C. It is relatively well established that this oxidation mechanism for silicon involves molecular oxygen permeation through the growing oxide film<sup>1-6</sup>.

The increase in activation energy above 1400°C implies that a change in the oxidation mechanism takes place. Isotope labelling studies have shown that appreciable lattice diffusion of oxygen occurs during oxidation of silicon and silicon carbide at 1300°C<sup>5</sup>. The activation energy for this process in the thermal oxides is currently being investigated using the isotope labelling technique. The activation energy reported for fused silica by Sucov is equal to 298 kJ/mole<sup>21</sup>. Recent studies indicate the value could be as high as 450 kJ/mole<sup>22,23</sup>. These results suggest that lattice oxygen diffusion can explain the oxidation kinetics at temperatures above 1400°C. The similar magnitude of the calculated energy for the slow growth faces suggests that the same mechanism applies over the entire temperature range. It is not clear at this time why the oxidation of the slow growth face should be controlled by lattice diffusion instead of oxygen permeation at the lower temperatures. Several investigations have also suggested that the desorption of carbon monoxide could control the oxidation rate and exhibit a large activation energy<sup>7,11-13</sup>.

## 2. Polycrystalline Materials

The oxidation behavior of the polycrystalline materials is complicated by the higher levels of dopant impurities which causes higher oxidation rates. In addition, the polycrystalline materials exhibited a greater propensity for

crystallization of the oxide film. Roughening of the oxide surface and the oxide SiC interface made thickness determinations difficult. At longer times and higher temperatures, a thickness range is presented because of the uncertainties caused by this difficulty.

The oxide thickness data for the three polycrystalline materials are shown in Figures 3-5. The CNTD material exhibited similar behavior to that of the fast face single crystal SiC with parabolic behavior for up to ten hours. The sintered alpha also exhibited this behavior at lower temperatures. However, at longer times and/or higher temperatures, a decrease in rate from the early parabolic behavior was observed. This effect results from the increased crystallization of the oxide film. Transport through the crystalline oxide is much slower than through the amorphous oxide. X-ray diffraction analyses of the more heavily crystallized films indicated the presence of cristobalite.

A much more complicated oxidation behavior is found for the hot pressed silicon carbide. Whereas at 1200°C parabolic behavior is exhibited out to ten hours, at higher temperatures both increasing and decreasing trends in behavior are observed. Cristobalite and mullite have been identified in the oxide films<sup>10-12</sup>. Morphological details of the crystallization of the oxide films provide insight into the complicated growth behavior observed. Shown in Figures 6 and 7 are SEM micrographs of the different crystal morphologies for the sintered and hot pressed materials respectively. A coherent layer of cristobalite in the form of spherulites is found on the surface of the sintered alpha SiC. This formation significantly reduces the transport of oxidant leading to decreasing kinetics. The morphology of the crystallites on the hot pressed material is quite different with small crystallite particles presumed to be mullite imbedded in a glassy matrix. During the early stages of crystallization, spherulitic growth features were observed and identified

as cristobalite. These features apparently break up into the finer crystallites during continued oxidation and segregation of  $\text{Al}^{3+}$  into the oxide. In terms of the oxidation behavior exhibited, the decreasing trend is presumably caused by the spherulitic crystals forming in much the same manner as described for the sintered material. The break-up of these features into the finer crystallites apparently allows for increased transport through the oxide film. The reasons for and the details of this microstructural change are a topic for further research. However, similar microstructural features were reported by MacDowell and Beall<sup>24</sup> in an investigation of the liquid-liquid immiscibility in the  $\text{Al}_2\text{O}_3-\text{SiO}_2$  system and subsequent crystallization of the phases present (which were mullite and cristobalite).

Parabolic rate constants for the oxidation of the polycrystalline materials are given in Table 4. In several instances a rate constant is not reported because the oxidation deviated from parabolic behavior. The CNTD material exhibited the highest oxidation rates even though it contained significantly lower levels of cation impurities. However, free silicon was identified in the starting material by X-ray diffraction. The higher oxidation rates for the hot pressed material compared to the sintered SiC agree with previously reported observations<sup>11</sup>. Higher levels of cations in the hot pressed material effectively lower the viscosity of the oxide film increasing the transport of the oxidant.

The temperature dependence of the parabolic rate constants for the materials is shown in Figure 6 and calculated activation energies are listed in Table 4. Strong similarities of the CNTD oxidation behavior to that of the fast face single crystals suggest that similar oxidation mechanisms are operative. Slightly larger activation energies were calculated for the hot pressed and sintered materials. These values are complicated by the differing temperature dependencies exhibited on each crystallite face exposed to the oxidant.

The individual grains oxidize at different rates depending on their orientation, a fact that is easily observed with the optical microscope using thickness interference colors. Comparing the oxidation behavior of the single crystal faces and the sintered alpha material as in Figure 9, one can see that the polycrystalline data falls between the data corresponding to the fast and slow growth faces of the single crystal materials. The observed temperature dependence of the polycrystalline materials should reflect the trends of the individual growth faces.

The long term oxidation behavior of the sintered alpha and hot pressed materials at 1300 and 1400°C was obtained by thermogravimetric analysis. In both cases, parabolic oxidation kinetics were exhibited after roughly four hours. The hot pressed material exhibited a higher oxidation susceptibility as found in the short term case. Direct comparison of the rate constants at short and long times was made by converting the weight gain data to thickness data assuming a density of 2.20 gms/cc. For the sintered alpha material, a lower oxidation rate was observed for the long term runs. The hot pressed material exhibited a significantly greater rate for long term oxidation than was observed at short times. As described earlier the different oxidation rates observed are related to the morphology of the crystallized oxide films. Oxide thickness determinations on the TGA samples gave results which fell, within experimental error, into the thickness range predicted by extrapolation of the short term data out to 24 hours.

#### IV. Summary and Conclusions

It has been shown that the basal plane of SiC which exhibits a fast oxidation rate behaves similarly to single crystal silicon in the temperature range 1200-1400°C. The lower oxidation rate of silicon carbide can be explained by the

consumption of oxidant to oxidize the carbon in the silicon carbide. In light of the low activation energies (~120 kJ/mole), it is suggested that the oxidation mechanism is controlled by permeation of molecular oxygen through the growing oxide film. At temperatures greater than 1400°C, the significantly increased activation energy indicates a change in oxidation mechanism. Lattice diffusion of oxygen is suggested as the rate controlling mechanism in light of the relative agreement of activation energies and the isotope labelling experiments which have verified the appreciable transport of oxidant by this mechanism at temperatures above 1300°C. The slow growth face exhibited lower oxidation rates and a high activation energy over the entire temperature range which may indicate that lattice oxygen diffusion is the rate controlling process over the entire temperature range for this crystal face. Additional isotope labelling studies are necessary to elucidate the rate controlling processes.

The oxidation behaviors of the polycrystalline materials are similar to the single crystal behavior but are significantly altered by several factors. The oxidation rates of sintered alpha SiC are bracketed by the two extremes of single crystal oxidation behavior corresponding to the fast and slow growth faces, presumably because of the random orientation of the individual grains. The observed activation energies for the polycrystalline materials are generally intermediate to those observed for the various single crystal faces. The presence of higher concentrations of impurities altered the oxidation behavior by forming low viscosity oxides which increase the oxidant flux to the growth interface. A much higher susceptibility to crystallization was exhibited by the polycrystalline materials due to this reduced viscosity and the numerous nucleation sites such as multi-grain junctions. The

decreasing trend in the oxidation rate with time of sintered silicon carbide at higher temperatures results from the formation of a coherent layer of cristobalite, which presumably reduces the transport of oxidant through the growing oxide. For the hot pressed material, the subsequent disruption of the coherent cristobalite layer and the formation of fine scale crystals, presumably mullite, produced an increase in the oxidation rate. These trends in oxidation behavior for the polycrystalline material are accentuated in the long term experiments as determined by thermogravimetric analyses. The sintered material exhibited a reduced parabolic growth rate after 24 hours while the hot pressed material showed an increased parabolic growth rate.

#### Acknowledgment

This work was supported by the U.S. Army Research Office Division of Metallurgy and Materials Science.

### References

1. B. E. Deal and A. S. Grove, "General Relationship for the Thermal Oxidation of Silicon," *J. App. Phys.* 36 (12), 3770-3778 (1965).
2. F. J. Norton, "Permeation of Gaseous Oxygen Through Vitreous Silica," *Nature* 191, 701 (1961).
3. P. J. Jorgensen, "Effect of an Electric Field on Silicon Oxidation," *J. Chem. Phys.* 37, 874-877 (1962).
4. E. Rosenthaler, A. Straboni, S. Rigo and G. Ansel, "An <sup>18</sup>O Study of the Thermal Oxidation of Silicon in Oxygen," *Appl. Phys. Lett.* 34, 254-256 (1979).
5. J. A. Costello and R. E. Tressler, "Isotope Labelling Studies of the Oxidation of Silicon at 1000 and 1300°C," submitted to *J. Electrochem. Soc.*
6. K. Motzfeldt, "On the Rates of Oxidation of Silicon and of Silicon Carbide in Oxygen, and Correlation with Permeability of Silica Glass," *Acta Chem. Scand.* 18 (7), 1596-1606 (1964).
7. R. F. Adamsky, "Oxidation of Silicon Carbide in the Temperature Range 1200 to 1500°C," *J. Phys. Chem.* 63, 305-307 (1959).
8. R.C.A. Harris, "Oxidation of 6-H SiC Platelets," *J. Amer. Ceram. Soc.* 58 (1-2), 7-9 (1975).
9. W. Von Münch and I. Pfaffender, "Thermal Oxidation and Electrolytic Etching of SiC," *J. Electrochem. Soc.* 122 (5), 642-643 (1975).
10. A. Suzuki, H. Ashida, N. Furui, K. Mameno and H. Matsunami, "Thermal Oxidation of SiC and Electrical Properties of Al-SiO<sub>2</sub>-SiC MOS Structure," *Japanese Journal of Applied Physics* 21 (4), 579-585 (1982).
11. J. A. Costello and R. E. Tressler, "Oxidation Kinetics of Hot-Pressed and Sintered Alpha SiC," *J. Amer. Ceram. Soc.* 64 (5-6), 327-331 (1981).
12. W. C. Tripp, J. W. Hinze, M. G. Mendiratta, R. M. Huff, A. F. Hampton, J. E. Stroud and E. T. Rodine, "Internal Structure and Physical Properties of Ceramics at High Temperatures," ARC Final Technical Report, Report Number ARL-75-0130, June (1975).
13. S. C. Singhal, "Oxidation Kinetics of Hot Pressed SiC," *J. Mat. Sci.* 11, 1246-1253 (1976).
14. E. Fitzer and R. Ebi, "Kinetic Studies on the Oxidation of Silicon Carbide," *Silicon Carbide 1973*, R. C. Marshall, J. W. Faust, C. E. Ryan, Eds., University of South Carolina Press (1973) 320-328.

15. J. Schlichting, "SiC as an Oxidation Reactant Refractory Material, Parts I and II," *Ber. Dt. Keram. Ges.* 56 (8-9), 196-206 (1979).
16. J. Schlichting and K. Kriegsmann, "Oxidation Behaviour of Hot Pressed SiC," *Ber. Dt. Keram. Ges.* 56 (3-4), 72-75 (1979).
17. S. C. Singhal and F. F. Lange, "Effect of Alumina Content in the Oxidation of Hot Pressed-SiC," *J. Amer. Ceram. Soc.* 58 (9-10), 433-435 (1975).
18. J. A. Costello, I.S.T. Tsong and R. E. Tressler, "Boron Redistribution in Sintered Alpha SiC During Thermal Oxidation," *J. Amer. Ceram. Soc.* 64 (5-6), 332-335 (1981).
19. A. S. Grove, O. Leistiko, Jr., and C. T. Sah, "Redistribution of Acceptor and Donor Impurities During Thermal Oxidation of Silicon," *J. App. Phys.* 35 (9), 2695-2704 (1964).
20. E. A. Irene and R. Ghez, "Silicon Oxidation Studies: The Role of H<sub>2</sub>O," *Semiconductor Silicon 1977*, H. R. Huff and E. Sirth, Eds., The Electron. Chem. Soc., Inc. (1977) 313-323.
21. E. W. Sucov, "Diffusion of Oxygen in Vitreous Silica," *J. Amer. Ceram. Soc.* 46 (1), 14-20 (1963).
22. R. H. Doremus, "Oxidation of Silicon by Water and Oxygen and Diffusion in Fused Silica," *J. Phy. Chem.* 80 (16), 1773-1775 (1976).
23. J. Mikkelsen, private communication, 1983.
24. J. F. MacDowell and G. H. Beall, "Immiscibility and Crystallization in Al<sub>2</sub>O<sub>3</sub>-SiO<sub>2</sub> Glasses," *J. Amer. Ceram. Soc.* 52 (1), 17-25 (1969).

**Table 1**  
**Description of SiC Materials**

Material	Nomenclature	Density g/cm <sup>3</sup>	Grain Size μm	Major Impurity
Single Crystal SiC Black	SCSC BL	3.21	-	Al (ppm)
Single Crystal SiC Green	SCSC GR	3.21	-	N (ppm)
Single Crystal Si	SCS1	2.32	-	B (ppm)
Sintered α-SiC	SASC	3.18	5-7	B (.5 wt %)
Hot Pressed SiC	HPSC	3.23	1,10 (bimodal)	Al (2-3 wt %)
Controlled Nucleation Thermal Deposition SiC	CNTD	-	.01-.1	Si -

Table 2

Parabolic rate constants and activation energies for the oxidation of the single crystal materials in dry oxygen.

Temp. °C	scsc	$k_{par}$ ( $\text{cm}^2/\text{min}$ )			scsc cr st.
		scsc nl. p	scsc cr. p	scsc nl. st.	
1200	$7.12 \times 10^2 \pm 2.34 \times 10^1$	$2.84 \times 10^2 \pm 5.76 \times 10^1$	$3.46 \times 10^2 \pm 4.70 \times 10^1$	$1.89 \times 10^1 \pm 4.89 \times 10^0$	$4.86 \times 10^1 \pm 1.92 \times 10^0$
1300	$1.13 \times 10^3 \pm 2.38 \times 10^2$	$6.20 \times 10^2 \pm 1.60 \times 10^1$	$6.58 \times 10^2 \pm 2.78 \times 10^1$	$1.73 \times 10^2 \pm 9.09 \times 10^1$	$3.31 \times 10^2 \pm 7.22 \times 10^1$
1400	$2.32 \times 10^3 \pm 2.29 \times 10^2$	$1.04 \times 10^3 \pm 7.37 \times 10^1$	$1.13 \times 10^3 \pm 1.60 \times 10^2$	$0.46 \times 10^2 \pm 2.28 \times 10^2$	$9.43 \times 10^2 \pm 1.79 \times 10^2$
1450	---	$1.92 \times 10^3 \pm 6.09 \times 10^1$	$2.31 \times 10^3 \pm 1.06 \times 10^3$	$1.64 \times 10^3 \pm 4.12 \times 10^2$	$2.86 \times 10^3 \pm 7.86 \times 10^2$
1500	---	$2.31 \times 10^3 \pm 3.95 \times 10^2$	$3.84 \times 10^3 \pm 1.04 \times 10^3$	$1.77 \times 10^3 \pm 2.78 \times 10^2$	$4.97 \times 10^3 \pm 7.93 \times 10^2$
$E_a$ (kJ/mole)	120	124-197	121-297	372	319

**Table 3**  
**Comparison of Oxidation Rates of Single Crystal Materials**

Temp °C	$K_{par}$ SiC BL F		$1/2$	$K_{par}$ SiC GR F		$1/2$
	$K_{par}$	Si		$K_{par}$	Si	
1200	.63			.70		
1300	.68			.70		
1400	.67			.70		

Predicted  
Rate Ratio

Equation

- (1)  $Si(s) + O_2(g) = SiO_2(s)$  ---
- (2)  $SiC(s) + O_2(g) = SiO_2(s) + CO(s)$  1.0
- (3)  $SiC(s) + 3/2O_2(g) = SiO_2(s) + CO_2(g)$  .66
- (4)  $SiC(s) + 2O_2(g) = SiO_2(s) + CO_2(g)$  0.5

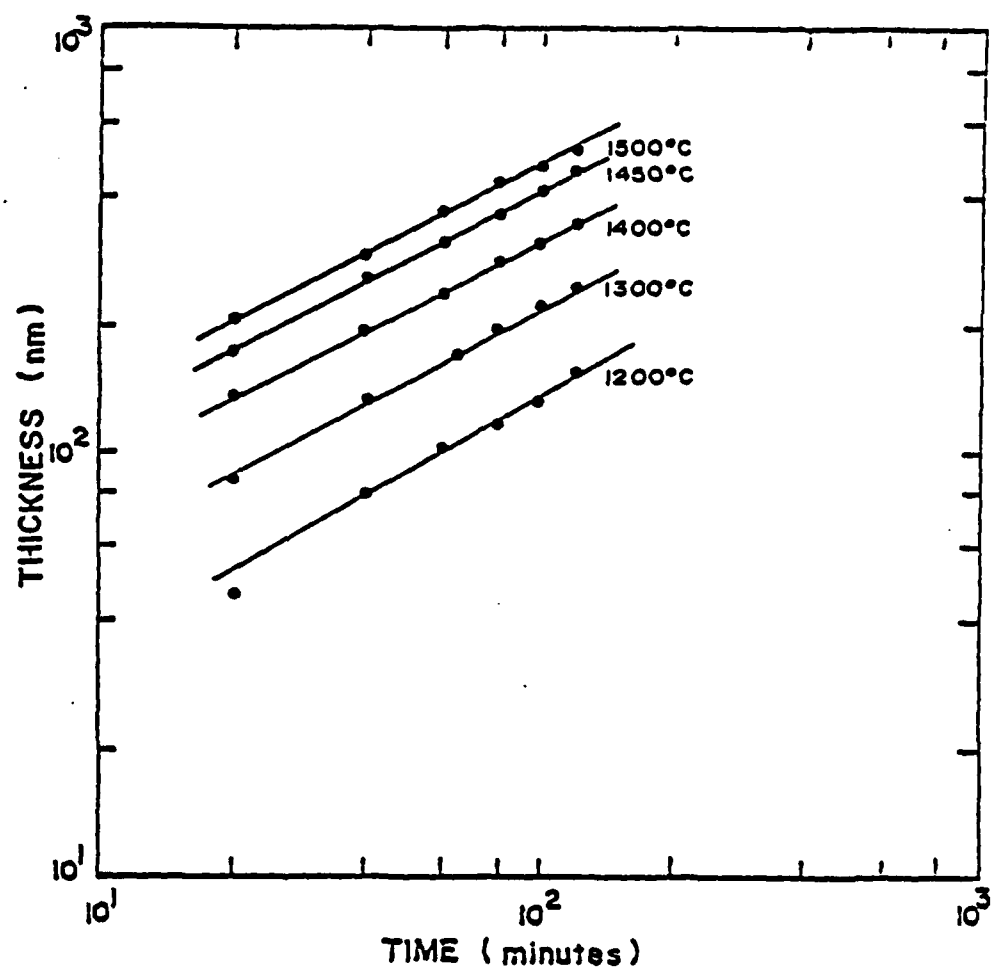
Table 4

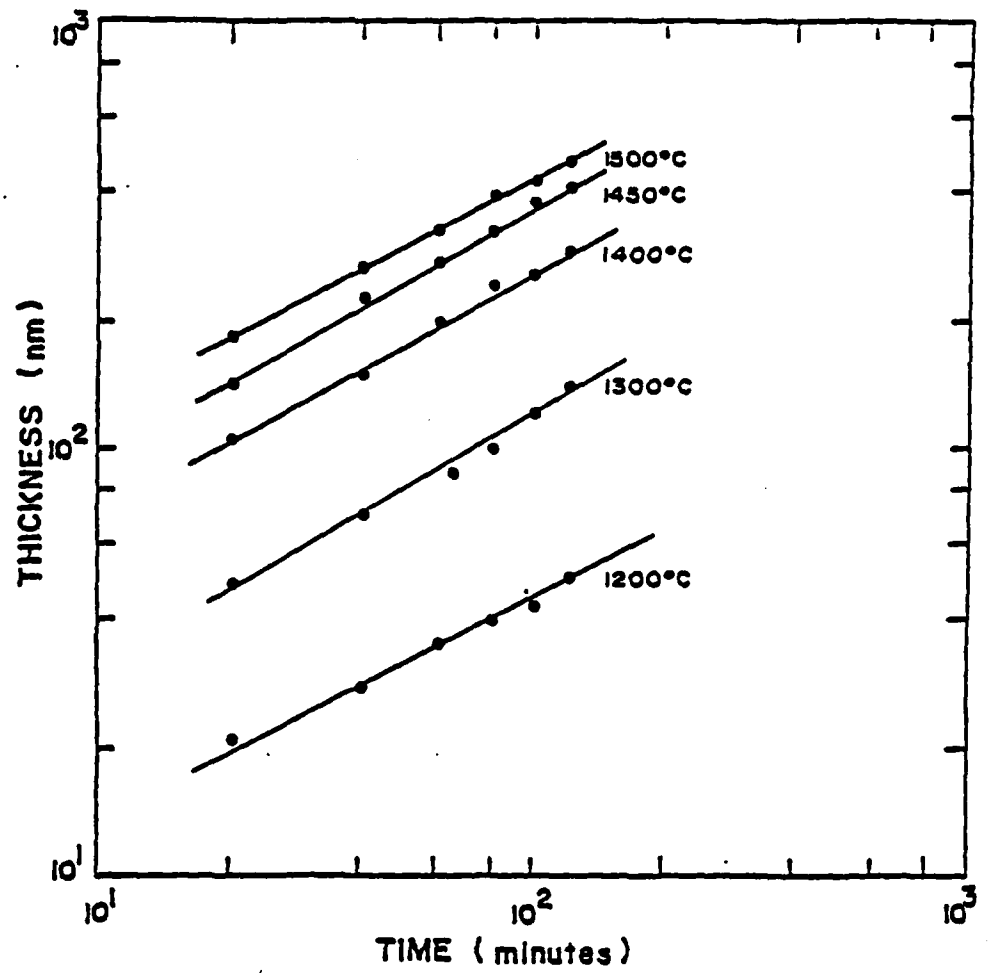
Parabolic rate constants and activation energies for the oxidation of the polycrystalline materials in dry oxygen.

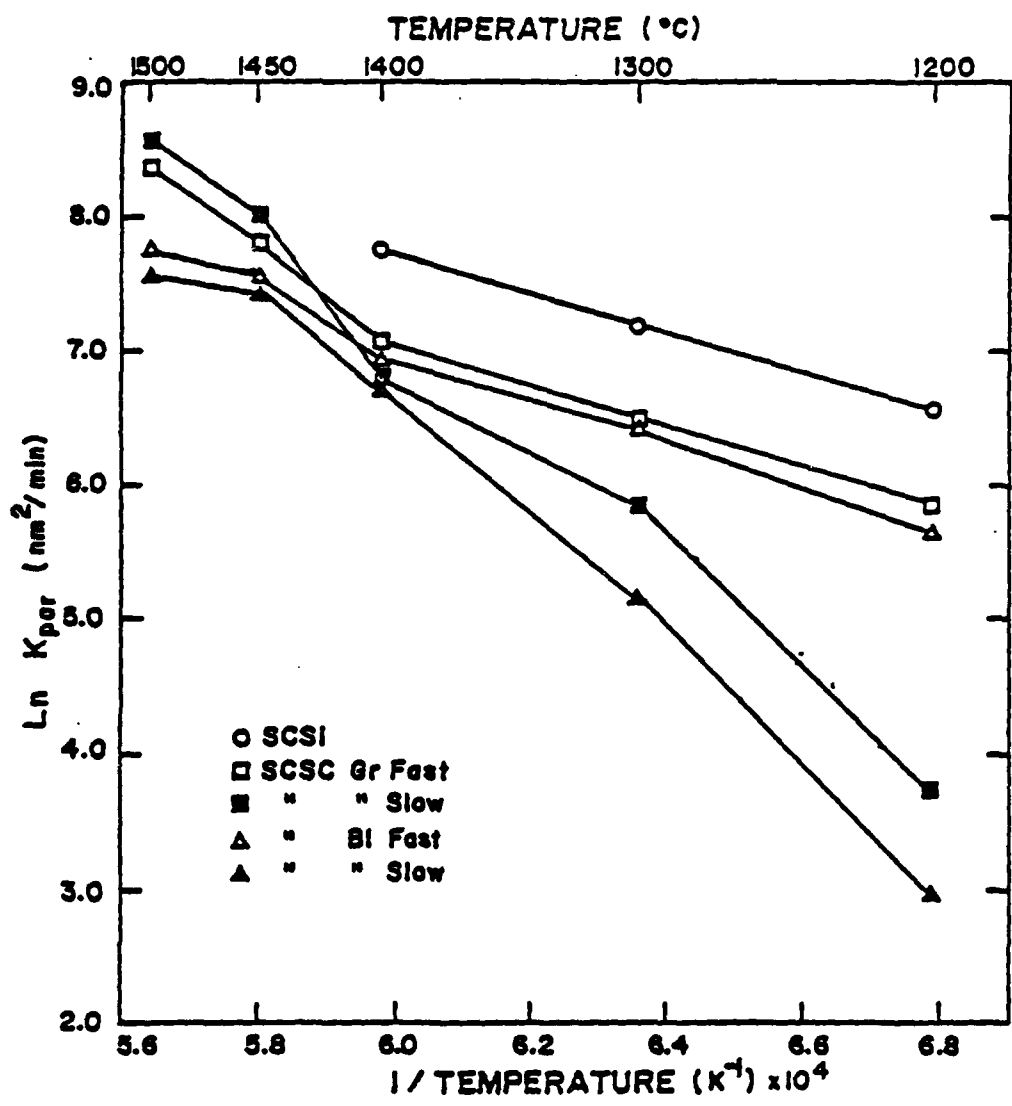
Temp. °C	CNTD	$K_{par}$ ( $\text{nm}^2/\text{min}$ )		$E_a$ (kJ/mole)
		SASC	HPSC	
1200		$3.44 \times 10^2 \pm 5.34 \times 10^1$	$1.75 \times 10^2 \pm 6.7 \times 10^1$	$2.20 \times 10^2 \pm 8.20 \times 10^1$
1300		$7.45 \times 10^2 \pm 2.03 \times 10^2$	$5.40 \times 10^2 \pm 7.11 \times 10^1$	$6.95 \times 10^2 \pm 2.11 \times 10^2$
1400		$1.37 \times 10^3 \pm 2.55 \times 10^2$	$9.49 \times 10^2 \pm 2.72 \times 10^2$	$1.86 \times 10^3$
1450		$2.69 \times 10^3 \pm 5.37 \times 10^2$	$1.77 \times 10^3$	---
1500		$4.51 \times 10^3 \pm 7.58 \times 10^2$	---	---
	$142-293$	217-289	221	

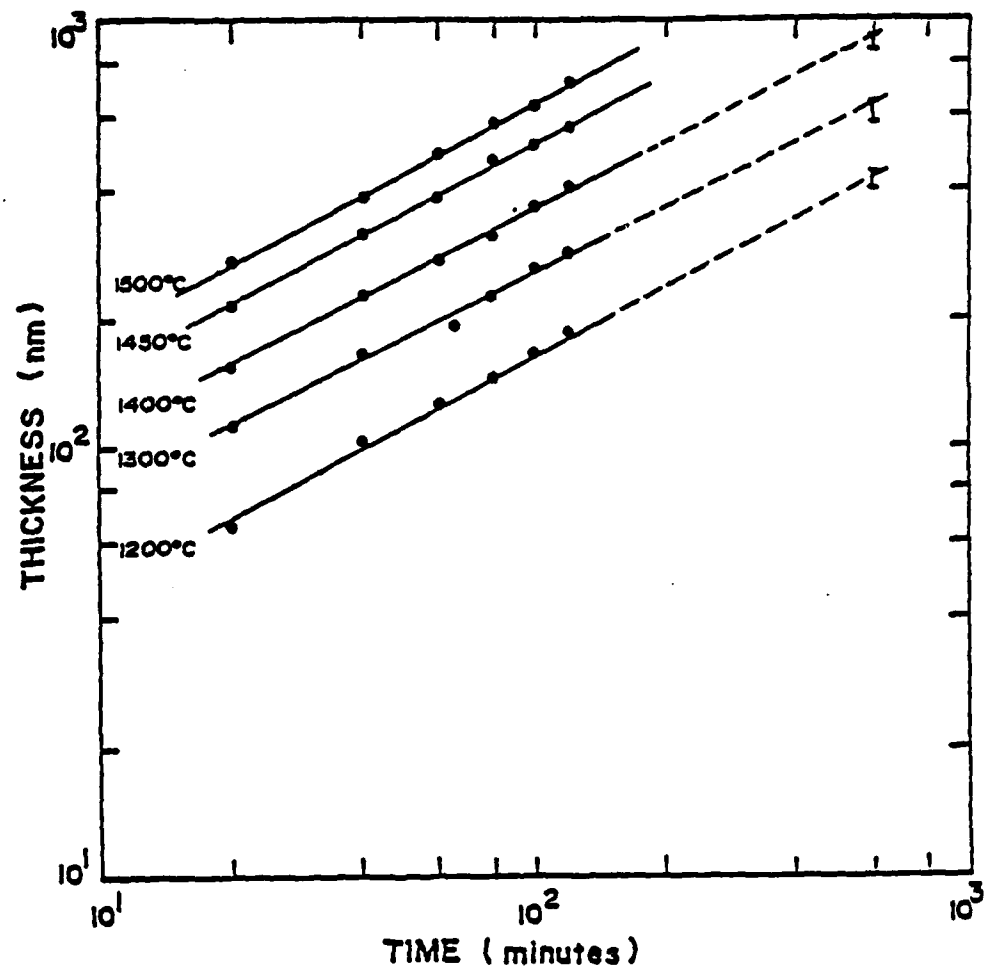
#### LIST OF FIGURES

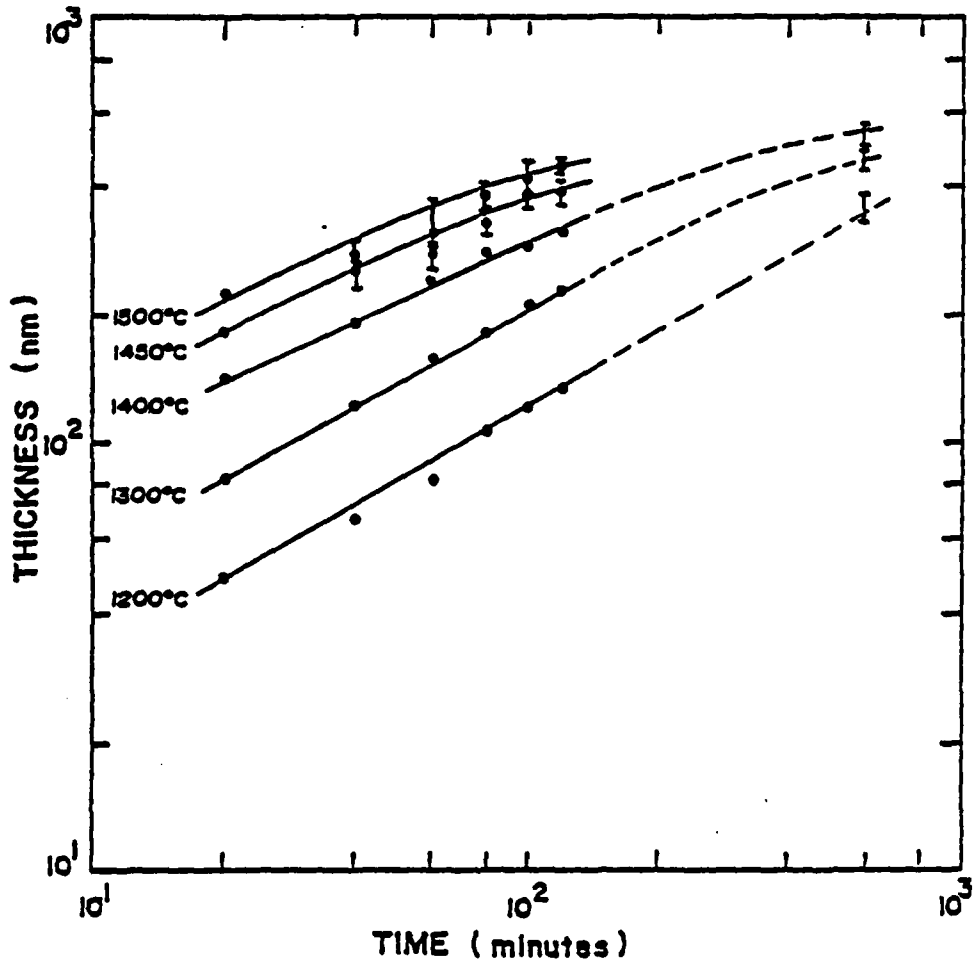
- Figure 1. Oxidation kinetics data for (a) the (000 $\bar{1}$ ), and (b) the (0001) black single crystal silicon carbide.
- Figure 2. Temperature dependence of parabolic rate constants for the single crystal materials.
- Figure 3. Oxidation kinetics data for CNTD silicon carbide.
- Figure 4. Oxidation kinetics data for sintered alpha silicon carbide.
- Figure 5. Oxidation kinetics data for hot pressed silicon carbide.
- Figure 6. Scanning electron micrograph of spherulitic features in the oxide film on sintered alpha silicon carbide.
- Figure 7. Scanning electron micrograph of crystalline features in oxide film on hot pressed silicon carbide.
- Figure 8. Temperature dependence of parabolic rate constants for the polycrystalline materials.
- Figure 9. Comparison of the oxidation kinetics of single crystal and sintered alpha silicon carbide materials.

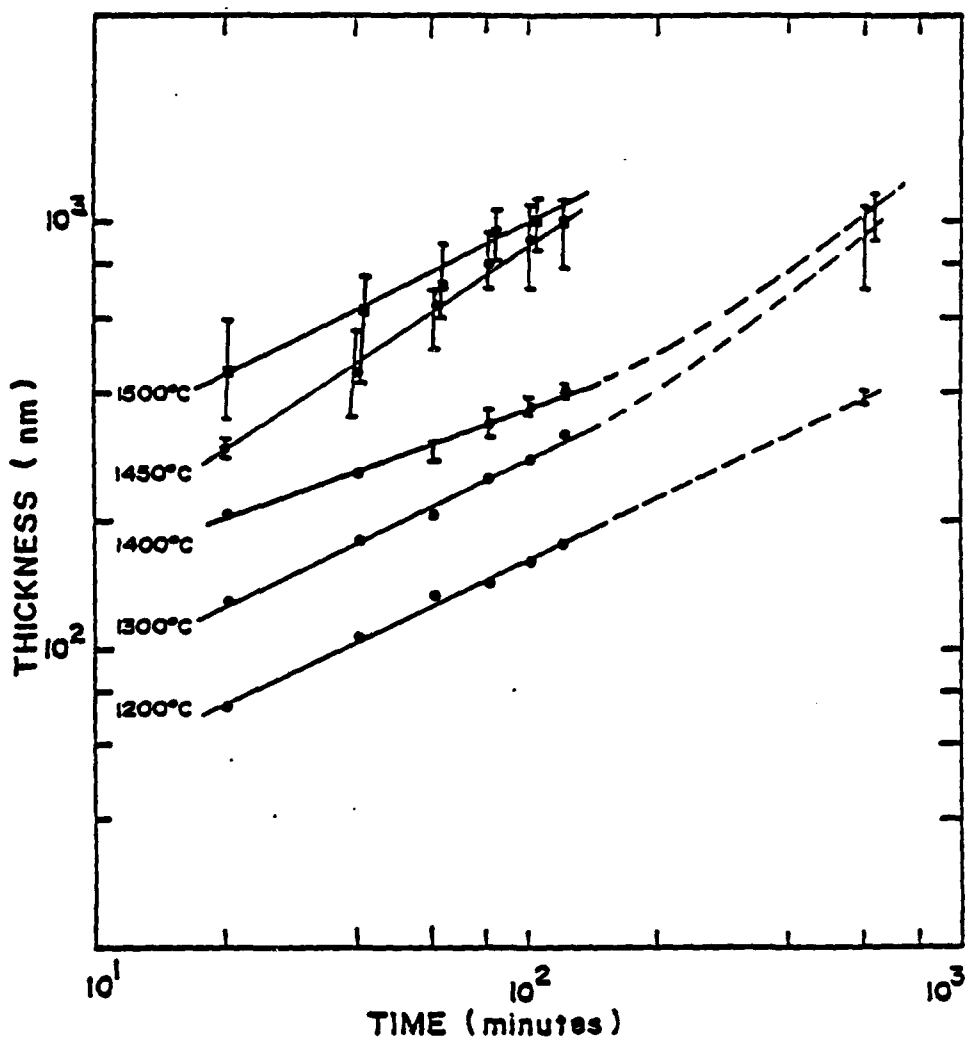


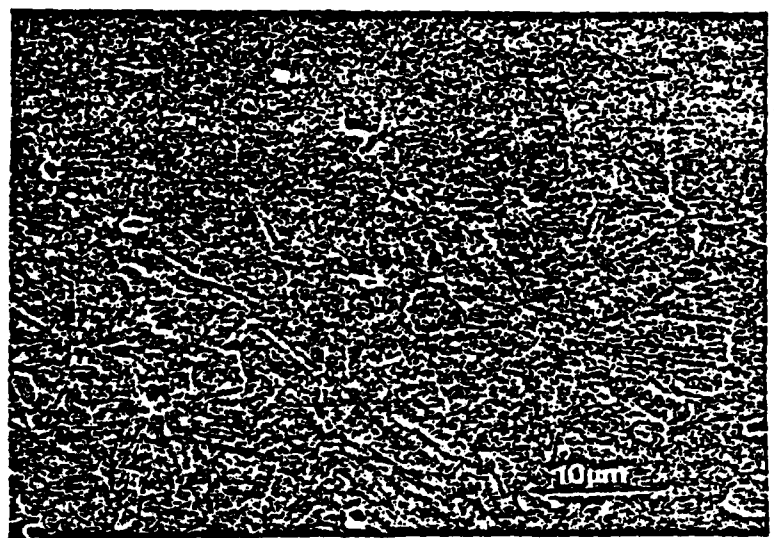


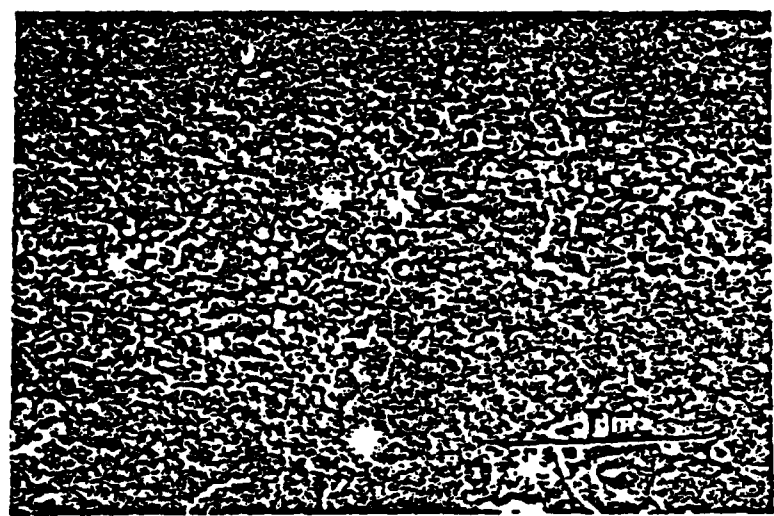
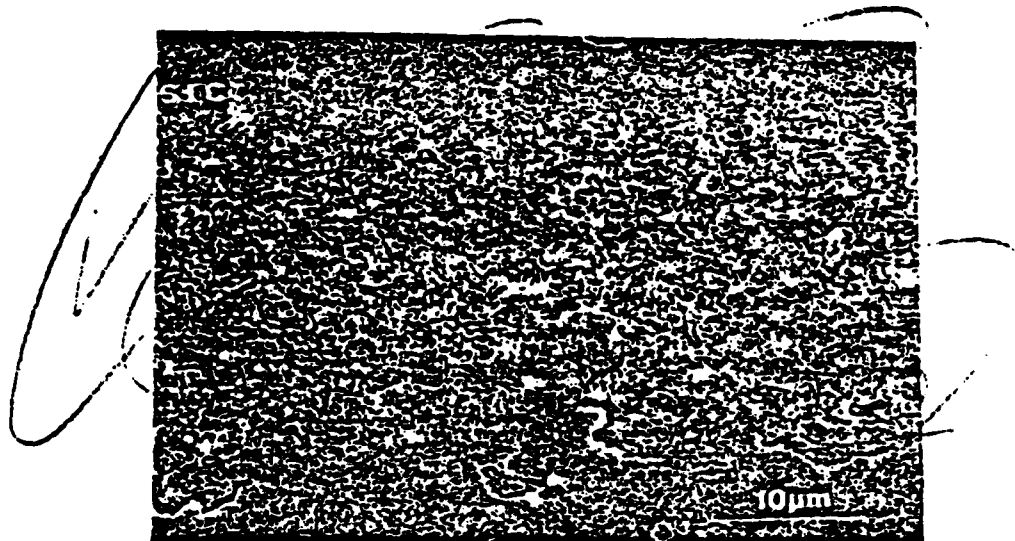


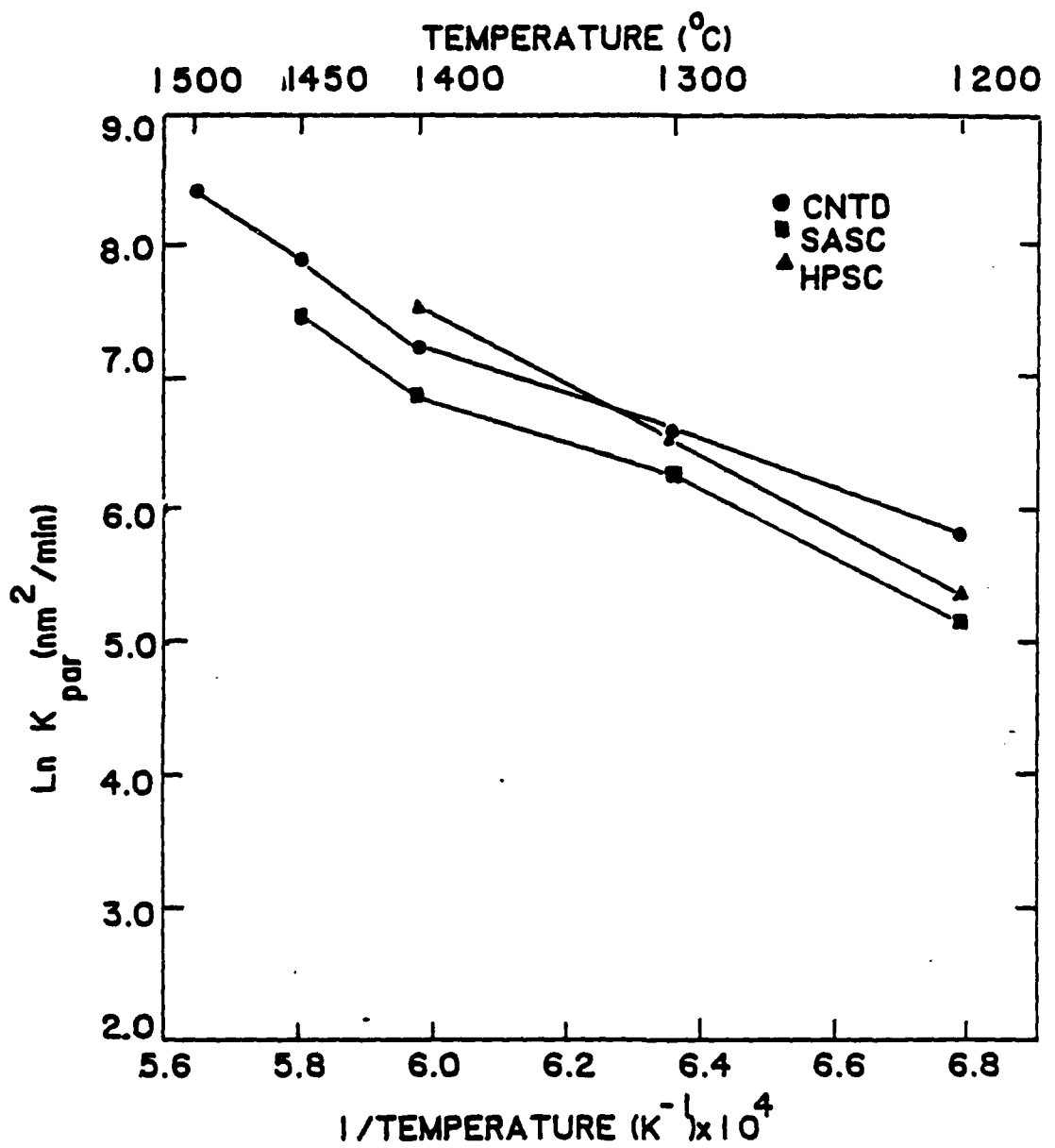


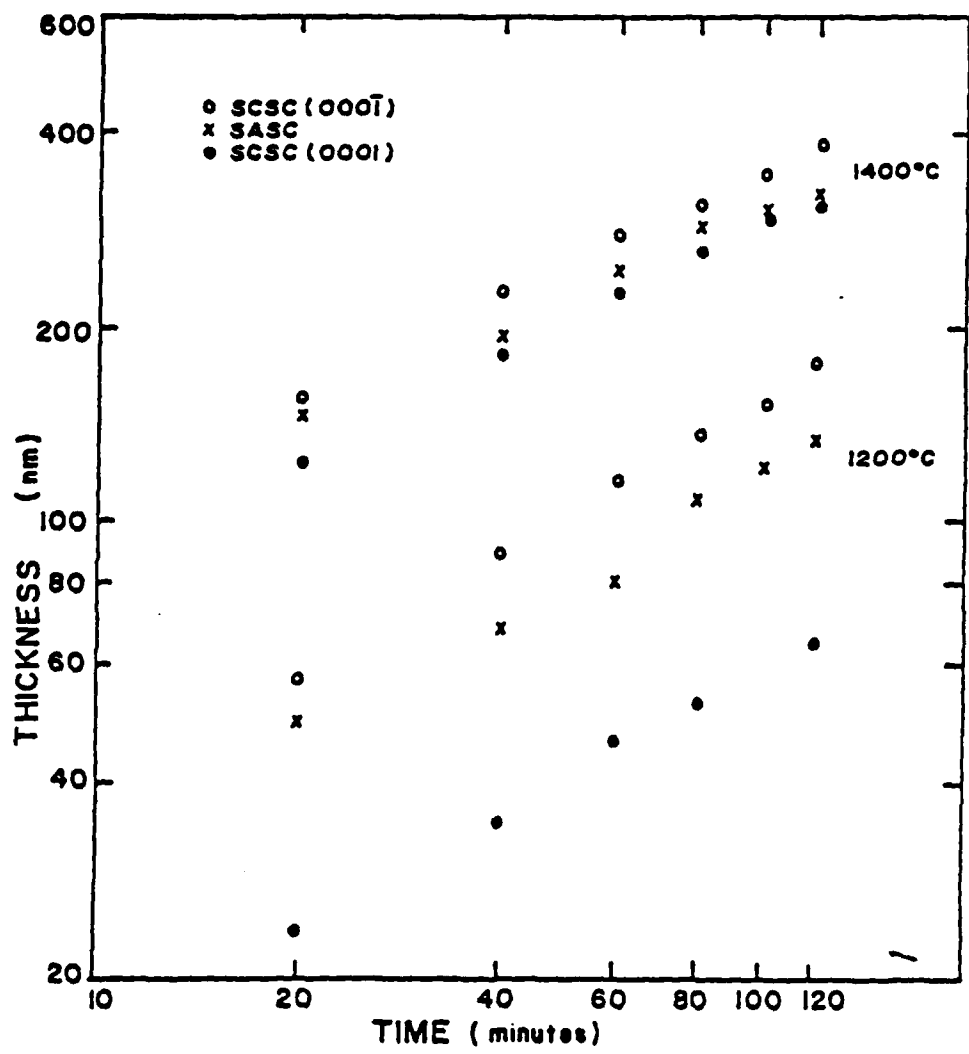












# Isotope Labeling Studies of the Oxidation of Silicon at 1000° and 1300°C

J. A. Costello<sup>\*†</sup> and R. E. Tressler

Department of Materials Science and Engineering, The Pennsylvania State University, University Park, Pennsylvania 16802

## ABSTRACT

Oxygen-18 profiles in thermal oxides grown on silicon at 1000° and 1300°C in sequential oxidation steps in the parabolic oxidation regime indicate a change in the dominant oxygen transport process. At 1000°C, oxygen-18 pile-up at the surface and at the oxide/silicon interface is consistent with a large flux of oxygen via molecular oxygen permeation and very slow diffusion of lattice oxygen ions ( $D_o = \sim 4 \times 10^{-18} \text{ cm}^2/\text{s}$ ). At 1300°C, the oxygen-18 concentration is uniformly high across the oxide, which suggests a much larger lattice oxygen diffusivity and a total flux due to lattice oxygen diffusion which contributes significantly to the supply of oxygen to the growth interface.

Owing to its importance in the semiconductor industry, the oxidation of silicon has been extensively studied. It is generally accepted that the oxidation process in the parabolic growth regime is controlled by the permeation of oxygen molecules through the oxide film (1-3). Indirect evidence supporting this conclusion includes platinum marker experiments (4), the linear oxygen partial pressure dependence of the parabolic oxidation rate (1), and the correspondence with oxygen permeation studies of fused silica (5). The most direct evidence comes from isotope labeling studies. The technique involves the sequential oxidation of the silicon in oxygen-18- and oxygen-18-rich environments. Following the oxidation treatments, an appropriate measurement technique which can discriminate between the two oxygen isotopes is used to profile each across the oxide film. The most common include nuclear reaction resonance and secondary ion mass spectrometry (SIMS). The location of each isotope in the oxide profiles provides information about the migrating species which control the oxidation reaction.

The nuclear reaction resonance technique was used by Rosencher et al. (6) to investigate silicon oxidation in dry oxygen at 930°C. The oxygen isotope profiles resulting from the double oxidation sequence revealed that the majority of oxygen-18 isotope accumulates near the oxide-silicon interface. This result and the correspondingly low oxygen-18 concentration in the bulk oxide indicated that the permeation of the oxidant to the interface is responsible for the parabolic oxidation of silicon, as proposed by Deal and Grove (1). A thin oxygen-18-rich layer (7-12 Å) was observed near the oxide surface, which was explained as isotope exchange between the oxidant and the lattice bound oxygen at the oxide surface. It has been reported that the exchange mechanism is enhanced by trace amounts of water in the oxidation environment (7). Rosencher et al. assumed that the water content in their system was in the ppm range in light of the shallowness of the exchanged layer.

A superior detection sensitivity is obtained using the SIMS technique. The analysis provides a direct measure of the isotope concentration profile and eliminates the laborious deconvolution procedures required by the nuclear reaction resonance technique. However, profile broadening due to ion beam mixing must be accounted for when considering the measured profile. Cristi and Condon (8) reported ion microprobe mass analyzer results for silicon doubly oxidized at 700°C. Similar to Rosencher et al., an interstitial diffusion (permeation) of oxygen molecules was suggested as the mechanism controlling oxidation. Isotope exchange with the lattice oxygen was observed at the oxide surface, and a diffusion coefficient corresponding to oxygen diffusion via the oxygen sublattice was calculated to be  $\sim 10^{-18} \text{ cm}^2/\text{s}$  at 700°C. It was

calculated that a diffusion coefficient of this low magnitude was insufficient to support the observed oxidation rate. Recent work by Rouse et al. (9) demonstrates the sensitivity of the SIMS technique when applied to the double oxidation experiment. Using a purified oxygen gas having a reduced oxygen-18 background, a slightly decreasing isotope profile was measured through the bulk oxide in addition to the isotope build up in the new oxide and at the oxide surface as previously described. The profile indicated that permeation mechanisms control the oxidation and that exchange of the diffusing oxidant occurs throughout the oxide. The exchange rate is much higher at the oxide surface. Special treatment of the gases minimized the water content in the system, suggesting that these artifacts were not water related.

In the present study, double oxidation of silicon was investigated at 1000° and 1300°C. Differences in the isotope profiles obtained by SIMS are discussed in terms of the competing transport processes.

## Experimental Procedure

Boron-doped silicon (100) having a 3.5 Ω-cm resistivity was used in this investigation. Samples were prepared from a full wafer by dicing into 1/4 × 1/4 in. squares, the sample size required by the SIMS holder. The first oxidation was performed in dry oxygen at 1000°C for 2 h. The oxide thickness as measured by ellipsometry was 103 nm. The background oxygen-18 concentration in the gas was 0.2%. The second oxidation was performed in an isotope exchange furnace where following the evacuation of the oxidation chamber, an oxygen-18 enriched gas is introduced (10).<sup>1</sup> The percentage of oxygen-18 in the gas was adjusted to approximately 40% each time. In the enriched gas, samples were oxidized at 1000° and 1300°C for 10 and 35 min, respectively.

Isotope profiling of the samples was accomplished using the SIMS mode of the Gatan scanning ion microscope.<sup>2</sup> The ion beam consisted of positive argon ions accelerated to 7 keV and focused to a diameter of approximately 100 μm. Adjustable beam rastering and signal gating were set for optimum depth resolution. A focused electron gun provided charge neutralization of the sputtering surface during profiling. Three mass settings were continuously monitored during profiling, including oxygen-16, oxygen-18, and silicon-30.

## Results and Discussion

The SIMS profile shown in Fig. 1 corresponds to the silicon sample oxidized in the oxygen-18 enriched gas at 1000°C for 10 min. The silicon-30 mass is monitored to indicate that proper charge neutralization is provided with the electron gun. This process is characterized by a uniform silicon signal across the oxide, as shown in Fig. 1.

<sup>\*</sup>Electrochemical Society Active Member.

<sup>†</sup>Present address: U.S. Army Electronics Technology and Devices Laboratory, Fort Monmouth, New Jersey 07703.

<sup>1</sup>J. Cauley, Case Western Reserve University, 1982.

<sup>2</sup>Gatan, Incorporated, Pittsburgh, Pennsylvania.

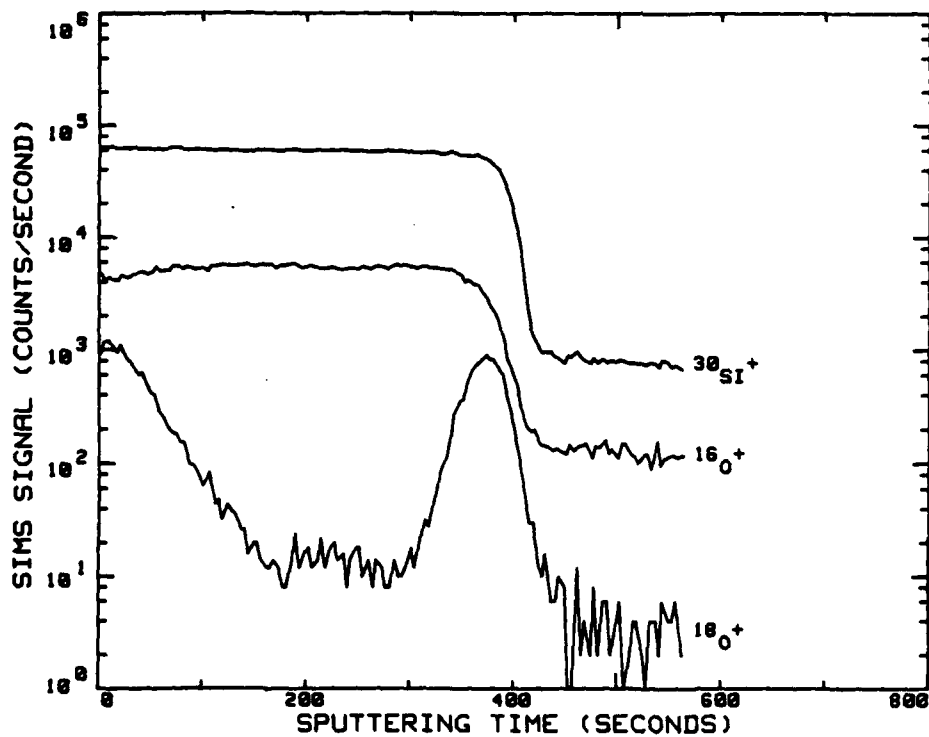


Fig. 1. SIMS data for silicon sample oxidized at 1000°C for 2h in dry oxygen-16 followed by 10 min in oxygen-18-enriched gas.

Signal instability at the oxide surface was typically less than 30s in duration. The changing oxygen signals, however, correspond to actual concentration variations of each isotope across the oxide film. Upon reaching the oxide-silicon interface, a sharp drop in signal of up to 3 orders of magnitude occurs in each case. In the silicon, the oxygen counts approach system background levels. The relatively high background signal for oxygen-16 in the silicon is caused by electron stimulated desorption (ESD) from the electron beam interacting with the sample surface. This signal does not significantly contribute to the overall oxygen-16 signal when profiling through the oxide.

The isotope profiles can be better analyzed by converting the data into the oxygen-18 fraction as a function of depth. The oxygen-18 fraction is obtained by dividing the oxygen-18 signal by the sum of the two oxygen signals. An experimentally measured sputtering rate of 17 nm/min in the oxide was used to convert to units of depth. Figures 2 and 3 are profiles for samples oxidized 10 and 35 min, respectively, at 1000°C in the oxygen-18-rich environment. As found by other investigations, the isotope is concentrated at the oxide-silicon interface as well as at the surface. The maximum isotope concentration corresponds to the amount of oxygen-18 enrichment of the oxidizing gas (~40%). The minimum concentration

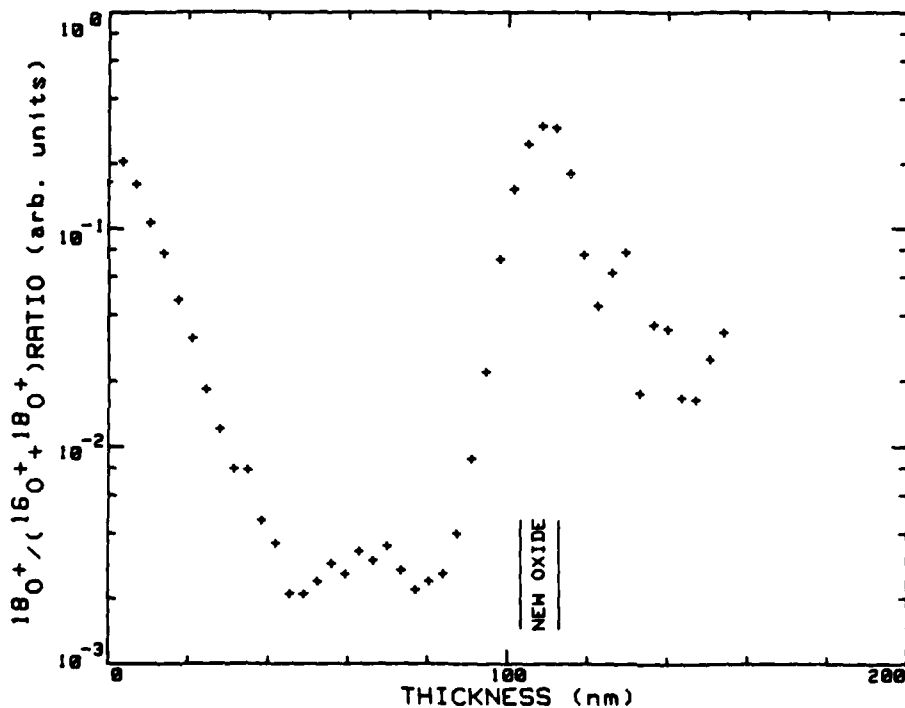


Fig. 2. Oxygen-18 profile for 10 min reoxidation sample at 1000°C.

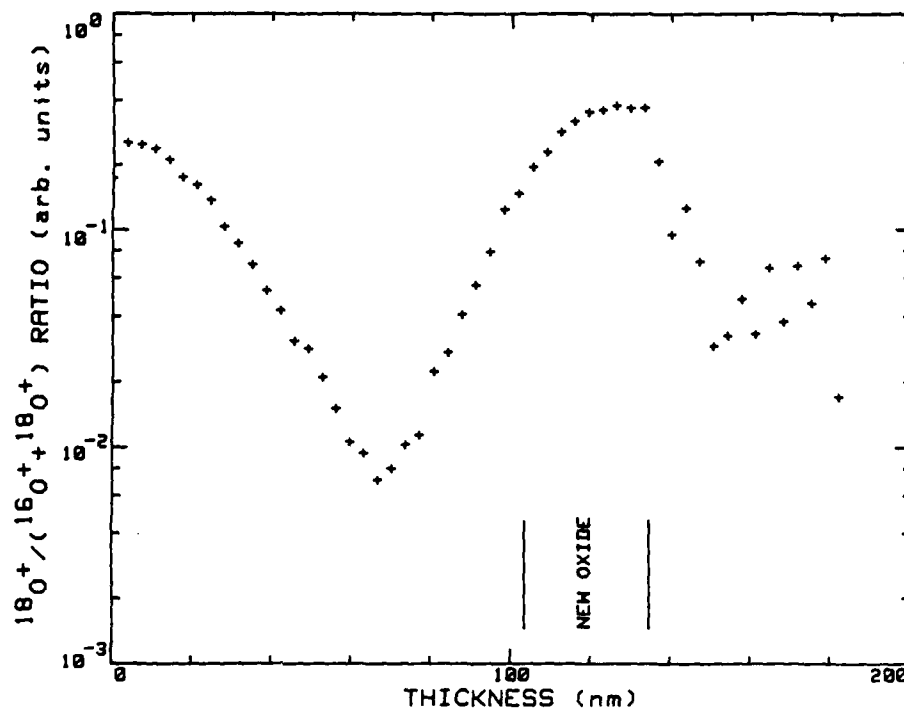


Fig. 3. Oxygen-18 profile for 35 min reoxidation sample at 1000°C.

which is found in the bulk oxide (Fig. 2) is equal to the background concentration of oxygen-18 in the original oxidizing gas (0.2%).

The observed profiles are explained in terms of the transport mechanisms present, as well as by the exchange of the oxidant with the lattice oxygen. The accumulation of oxygen-18 isotope near the oxide-silicon interface results from the permeation of oxygen molecules through the oxide and formation of new oxide at the oxide/silicon interface. The decreasing profile near the oxide surface into the bulk oxide is explained by the diffusion of the oxygen isotope through the oxygen sublattice following exchange at the oxide surface. A diffusion coefficient for the isotope of  $4 \times 10^{-15} \text{ cm}^2/\text{s}$  was calculated from the initial profile using the complementary error function. This

value is in good agreement with literature values for oxygen diffusion in fused silica (11, 12). As indicated in previous investigations, a diffusion coefficient of this magnitude could not by itself provide sufficient flux of oxygen to cause the observed oxidation rate. In addition to the isotope diffusion into the bulk from the oxide surface, the isotope can diffuse into the bulk from the newly formed oxide. This is apparent from the sloped isotope profiles near the original oxide-silicon interface.

The isotope profiles for samples oxidized at 1300°C were quite different. As shown in Fig. 4 for the 10 min oxidation, the oxygen-18 isotope profiles were uniform across the oxide. This result implies that lattice diffusion of oxygen is significant at this temperature and contributes to the supply of oxidant to the growth interface; a

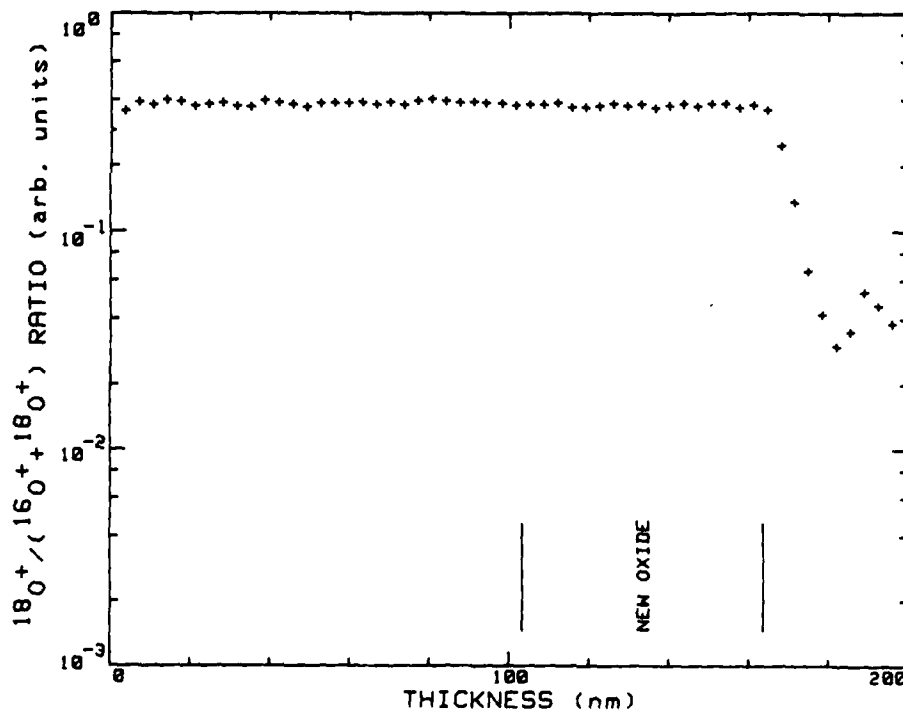


Fig. 4. Oxygen-18 profile for 10 min reoxidation sample at 1300°C.

calculated profile using oxygen diffusivity values in fused silica from the literature approximates the observed flat profile. The single activation energy reported for the parabolic oxidation of silicon (27 kcal/mol) holds up to near the melting point, however, and is much lower than the value reported for lattice diffusion (70 kcal/mol) by Sucov (11). This would imply that the oxidant supply at 1300°C is dominated by the permeation mechanism. The activation energy value reported by Sucov has been questioned by other investigators (12, 13), who suggest that the lattice diffusion of oxygen is characterized by a much lower activation energy. The temperature dependence of the lattice diffusion mechanism is currently being investigated by the authors using the present technique. It is interesting to note that other silicon-base materials such as SiC, TiSi<sub>x</sub>, and MoSi<sub>x</sub> exhibit an increase in the activation energy for the parabolic oxidation at temperatures above 1400°C (14, 15). This change in activation energy may correspond to control of oxidation by the lattice diffusion mechanism.

This discussion has not addressed the possibility that the oxygen-18 profiles are the result of an exchange reaction between the permeating isotope species and point defects (presumably oxygen vacancies) in the oxide. The isotope profile would then be flatter at 1300° than at 1000°C if the vacancies were created at the gas/SiO<sub>2</sub> interface and diffused much more rapidly at 1300° than at 1000°C. Future experiments will discriminate between these two possibilities.

#### Summary

Silicon oxidation in the parabolic growth regime at 1000° and 1300°C was investigated using isotope labeling experiments with SIMS for profiling. At the lower temperature, the measured profiles indicate that the oxidation process is controlled by the permeation of oxygen molecules through the oxide film to the oxide-silicon growth interface. Isotope exchange and subsequent diffusion via the oxygen sublattice apparently occurs near the oxide surface. A calculated value for the lattice diffusivity of oxygen is significantly below the value necessary to sustain the observed oxidation rate; this corroborates the domination of the oxidation process by permeation. At the higher temperature, the lattice diffusion of oxygen is significantly increased, which may lead to domination of

the oxidation rate by lattice diffusion at higher temperatures. An alternative interpretation of the observed oxygen-18 profiles may be that the exchange reaction between permeating O<sub>2</sub> and vacant lattice sites causes the observed profiles if the vacancies are created at the gas/SiO<sub>2</sub> interface and diffuse much faster at 1300° than at 1000°C.

#### Acknowledgments

This work was supported by the U. S. Army Research Office, Division of Materials Science. The authors are grateful to Dr. J. Cauley and Dr. J. Halloran, Case Western Reserve University, Cleveland, Ohio who performed the oxygen-18 treatments.

Manuscript submitted Dec. 16, 1983; revised manuscript received March 30, 1984.

The Pennsylvania State University assisted in meeting the publication costs of this article.

#### REFERENCES

1. B. E. Deal and A. S. Grove, *J. Appl. Phys.*, **36**, 3770 (1965).
2. J. R. Ligenza and W. G. Spitzer, *J. Phys. Chem. Solids*, **14**, 131 (1960).
3. R. H. Doremus, *J. Phys. Chem.*, **80**, 1773 (1976).
4. P. J. Jorgensen, *J. Chem. Phys.*, **37**, 874 (1962).
5. R. J. Norton, *Nature*, **171**, 701 (1961).
6. E. Rosenthaler, A. Straboni, S. Rigo, and G. Amsel, *Appl. Phys. Lett.*, **34**, 255 (1979).
7. R. Pfeiffer and M. Ohring, *J. Appl. Phys.*, **52**, 777 (1981).
8. S. S. Cristi and J. B. Condon, *This Journal*, **128**, 2170 (1981).
9. J. W. Rouse, C. R. Helms, and C. J. Han, in "Computer-Aided Design of Integrated Circuit Fabrication Processes for VLSI Devices," Final Report, p. 261, Stanford University, Stanford, CA (1982).
10. A. R. Cooper, A. H. Heuer, and L. D. Majors, Jr., "Use of Nuclear-microanalysis, Part 1 — Proton Activation Studies of the Thermal Oxidation of Silicon," Tech. Report AFML-TR-78-119; Part 1, Air Force Materials Laboratory (1978).
11. E. W. Sucov, *J. Am. Ceram. Soc.*, **46**, 14 (1963).
12. E. L. Williams, *ibid.*, **48**, 190 (1965).
13. A. G. Revesz and H. A. Schaeffer, *This Journal*, **129**, 357 (1982).
14. J. Costello, Ph.D. Thesis, The Pennsylvania State University, University Park, PA (1983).
15. J. Schlichting, *Ceram. Int.*, **4**, 162 (1978).



---

**REPRINTED FROM**

**CERAMICS  
international**

**Vol. 11 No. 2 1985**



# Oxygen Penetration Into Silicon Carbide Ceramics During Oxidation

J.A. COSTELLO\* and R.E. TRESSLER

Department of Materials Science and Engineering, The Pennsylvania State University,  
University Park, PA USA 16802

The penetration of oxygen into polycrystalline silicon carbide ceramics, in advance of the oxide/substrate interface, during oxidation for 1-100 hrs at 1200-1400°C was studied using SIMS and TEM techniques. Fully dense hot pressed ceramics containing aluminum additives, with and without an oxide grain boundary phase and CVD silicon carbide exhibited sharp interfaces. Sintered silicon carbides with boron and carbon additives (~97% dense) and aluminum carbide additive (~90% dense) exhibited a region of oxygen penetration ~10-15 µm in depth beneath the oxides scale, the depth of which was insensitive to the time and temperature of oxidation. The amorphous oxide phase in this zone was located at three and four grain junctions but the two grain junctions were unaffected in this zone by oxidation. This oxygen affected region, which is responsible for the slow crack growth susceptibility of these ceramics after oxidation, results from gaseous oxygen penetration along interconnected or nearly interconnected pores and oxidation of impurity laden channels and SiC surfaces. The depth of penetration is presumably limited by closure of the channels by the oxidation products.

## 1 - INTRODUCTION

During the thermal oxidation of sintered and hot-pressed silicon carbide which contain sintering aids and other impurities, complex microchemical changes occur in the growing film and in the substrate ceramic. For example, boron segregates into the oxide scale and is depleted in the substrate ceramic<sup>1</sup>. Aluminum has been found to concentrate in the oxide to form mullite during high temperature oxidation<sup>2, 3</sup>. In a separate paper we have reported the effects of various impurities on the kinetics of the early stages of oxidation of single crystals of silicon carbide and polycrystalline materials<sup>4</sup>.

The presence of an oxide phase at the grain boundaries in hot-pressed silicon carbide has been shown to result in slow crack growth by viscous separation of the grain boundaries<sup>5</sup>. Although sintered silicon carbides with nonoxide sintering additives are quite resistant to slow crack growth before oxidation and/or during tests in a nonoxidizing environment<sup>6-9</sup>, they become susceptible to crack growth analogous to the hot pressed materials upon oxidation<sup>9, 10</sup>. This effect has been attributed in a preliminary way to preferentially oxidized grain boundaries as determined by neutron activation analysis of unoxidized, oxidized, and oxidized and etched samples<sup>11</sup> and by secondary ion mass spectrometry (SIMS)<sup>12</sup>.

In this paper more extensive studies of oxygen penetration into silicon carbide ceramics with various additives and with and without some porosity are reported. A process by which the oxygen penetrates into the substrate during oxidation is described.

## 2 - EXPERIMENTAL DETAILS

### 2.1 - Materials

Single crystal silicon carbide (SCSC) extracted from Acheson furnace crystal clusters was used as a standard for oxide/silicon carbide interface sharpness because the basal planes of these thin platelet shaped, hexagonal crystals oxidize uniformly with a very sharp interface between the growing oxide and the silicon carbide crystal.

The polycrystalline materials investigated include sintered alpha silicon carbide\* (SASC), hot pressed silicon carbide\*\* (HPSC), controlled nucleation thermally deposited silicon carbide (CNTD)\*\*\*. Experimental sintered alpha silicon carbides (ESASC) with aluminum carbide as the sintering aid were also studied. In Table I the materials are listed with some of their characteristics.

TABLE I - Description of the polycrystalline materials.

Material	Density <sup>a</sup> g/cm <sup>3</sup>	Grain size µm	Major impurity	Oxygen content
SASC	3.16 O <sup>(1)</sup>	5-7	.5% B	.014 wt%
HPSC	3.23	~1-10 (bimodal)	2-3 wt% Al	.85 wt% O <sup>(1)</sup>
CNTD	—	0.01-0.1	H, Cl, Si	—
ESASC	—	—	1 wt% Al	—
(1)	3.23	—	1 wt% Al	—
ESASC	2.89	—	1 wt% Al	—
(2)	—	—	—	—

\* Theoretical density of SiC = 3.21 g/cm<sup>3</sup>.

These materials were selected to represent a fully dense polycrystalline ceramic with an oxide grain boundary phase containing aluminum (HPSC), a fully dense material with a non-oxide additive containing aluminum (ESASC-1), ~90% dense material with nonoxide aluminum containing additive (ESASC-2), a nearly dense material with nonoxide, boron-containing additive (SASC), and a fully dense polycrystalline material with no deliberately added cation impurities (CNTD).

### 2.2 - Oxidation

All oxidation runs were performed in a horizontal mullite tube furnace using MoSi<sub>2</sub> heating elements. A 7.5 cm hot zone with  $\pm 1^\circ\text{C}$  was maintained over the temperature range of 1200°C to 1400°C. A dry O<sub>2</sub> atmosphere flowing at 200 cc/min was used for the dry oxidation experiments.

The samples were prepared for oxidation by diamond sawing to approximately 0.5 cm by 0.5 cm  $\times$  0.13 cm dimensions. The CNTD material was removed from the carbon mandrel by oxidation in air at 600°C. The materials were polished to a mirror finish with 1/4 µm diamond in the final stage. The samples were carefully cleaned in acetone, DI water, dilute hydrochloric acid and trichloroethylene.

\* Now at U.S. Army Electronics Technology and Devices Lab., Fort Monmouth, NJ 07703.

\*\* Carborundum Co., Niagara Falls, New York.

\*\*\* NC203, Norton Company, Worcester, Massachusetts.

\*\*\*\* San Fernando Labs, Pacoima, California.

### 2.3 - SIMS analysis

The Gatan Scanning Ion Microprobe<sup>+</sup> was used to perform elemental depth profiles through the oxide and into the silicon carbide substrate. Argon ions accelerated to 7KeV were used as the primary ion source. A quadrupole mass analyzer was used in conjunction with a microcomputer to simultaneously record up to nine separate mass settings. The focussed ion beam was typically of the order of 100  $\mu\text{m}$  in diameter. A Faraday cup was used to measure the primary beam current which was typically  $\sim 0.26 \mu\text{A}$ . Both the static beam and rastered beam with electronic gating modes of analysis were used. For the depth profiling necessary for this study oxidized samples were angle lapped at a shallow angle from the original surface and the static beam was stepped along the surface in controlled increments as shown schematically in Figure 1. Optical microscopy was used following the SIMS analysis to accurately determine the depth corresponding to each sputtered crater. With this technique, depths of up to 50  $\mu\text{m}$  into the specimen could be analyzed. In some instances, a 3° angle lap was used to increase the depth of analysis. Charge neutralization of the surface was accomplished with an electron gun which could be focussed over the sputtered area. The true signal was obtained from the total signal by subtracting out the electron stimulated desorption contribution caused by the electron beam.

### 2.4 - Transmission electron microscopy

Transmission electron microscopy (TEM) analyses of unoxidized and oxidized materials were performed to determine the microstructural changes in the substrate caused by the oxidation. Oxidized specimens, following SIMS analysis, were prepared for TEM analysis as illustrated in Figure 1. The samples were ground from the backside to  $\sim 200 \mu\text{m}$ . They were sectioned into 16 pieces using a precision diamond saw, and then ground to  $\sim 30 \mu\text{m}$  thickness. They were then ion milled to electron transparency.

Selected samples were analyzed at Oak Ridge National Laboratory<sup>++</sup> using TEM's equipped with electron energy loss spectrometry (EELS) energy and X-ray energy dispersive spectroscopy (XEDS) instruments for comprehensive microchemical analyses. A conventional Philips EM 300 was used for extensive microstructural evaluation.

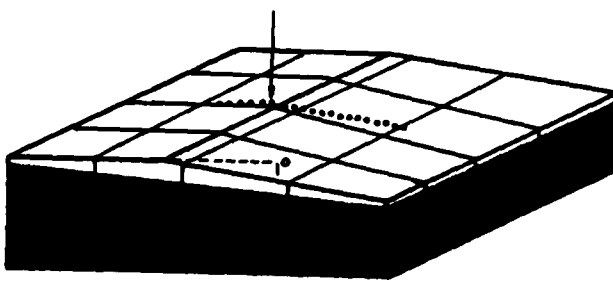


FIGURE 1 - Schematic of an angle lapped specimen for SIMS analysis, and, subsequently, for TEM specimens as ruled.

## 3 - RESULTS

### 3.1 - Oxygen profiles (SIMS analyses)

The polycrystalline materials were analyzed following oxidation treatments of 1, 10, and 100 hours at 1200°C, 1300°C and 1400°C. The details of scale formation for these conditions are described in a separate paper<sup>4</sup>. In Figure 2, the SIMS profiles are presented for the CNTD silicon carbide for the conditions listed above. The oxygen profiles are normalized by plotting the  $^{16}\text{O} / ^{28}\text{Si}^+$  ratio. The use of the static beam with  $\sim 100 \mu\text{m}$  diameter results in a 1.75  $\mu\text{m}$  depth increment contributing to the signal at each beam position on the 1° angle lapped specimen. As a result, the very sharp interface of the oxidized CNTD appears to be a few microns in width. Note that the time and temperature of oxidation do not affect the observed oxygen profiles.

The corresponding oxygen profiles for SASC are presented in Figure 3. The profiles indicate oxygen penetration to  $\sim 15 \mu\text{m}$  before reaching the background signal. The profiles are not significantly affected by the time and temperature of oxidation in this range of conditions.

In Figure 4, the SIMS profiles for hot pressed silicon carbide are presented for the same conditions as reported for the other materials. The significantly higher oxygen content of the hot pressed material is reflected in the much higher

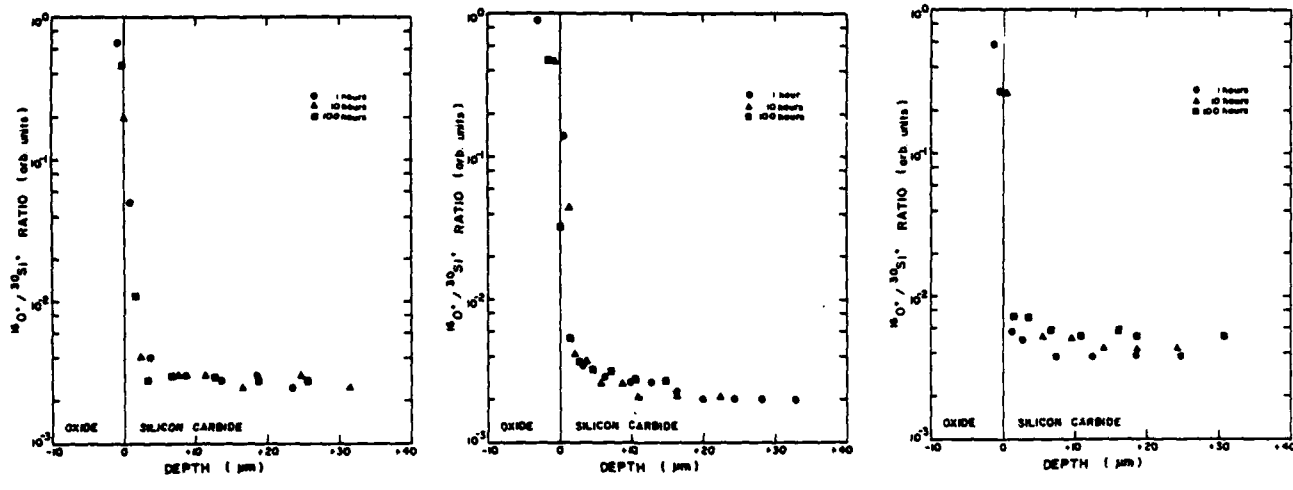


FIGURE 2 - Oxygen profiles into CNTD silicon carbide oxidized at (a) 1200°C, (b) 1300°C, and (c) 1400°C for 1, 10, and 100 hours.

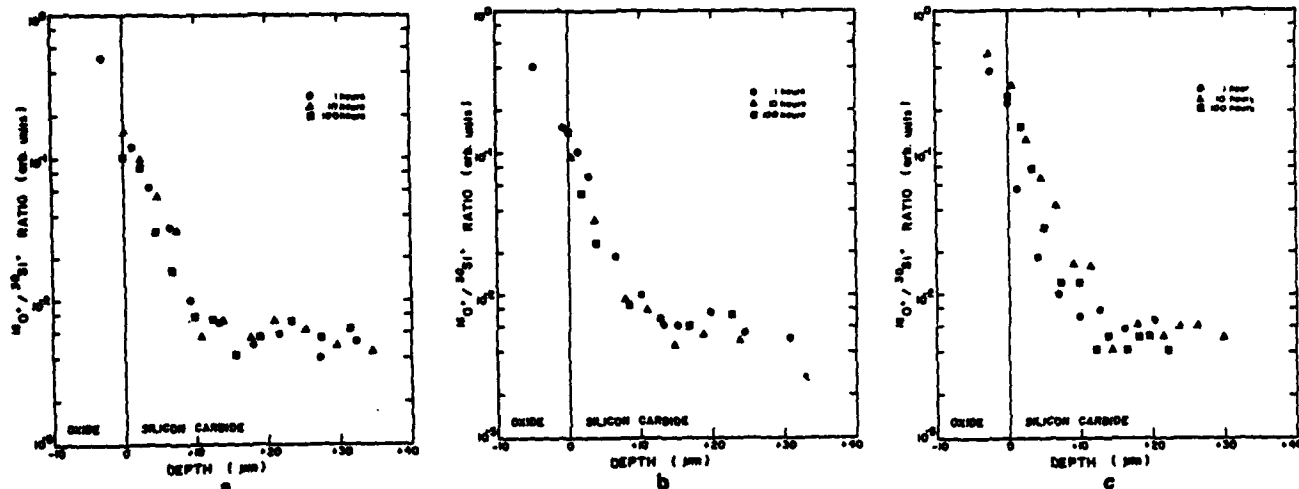


FIGURE 3 - Oxygen profiles into sintered alpha silicon carbide oxidized at (a) 1200°C, (b) 1300°C, and (c) 1400°C for 1, 10, and 100 hours.

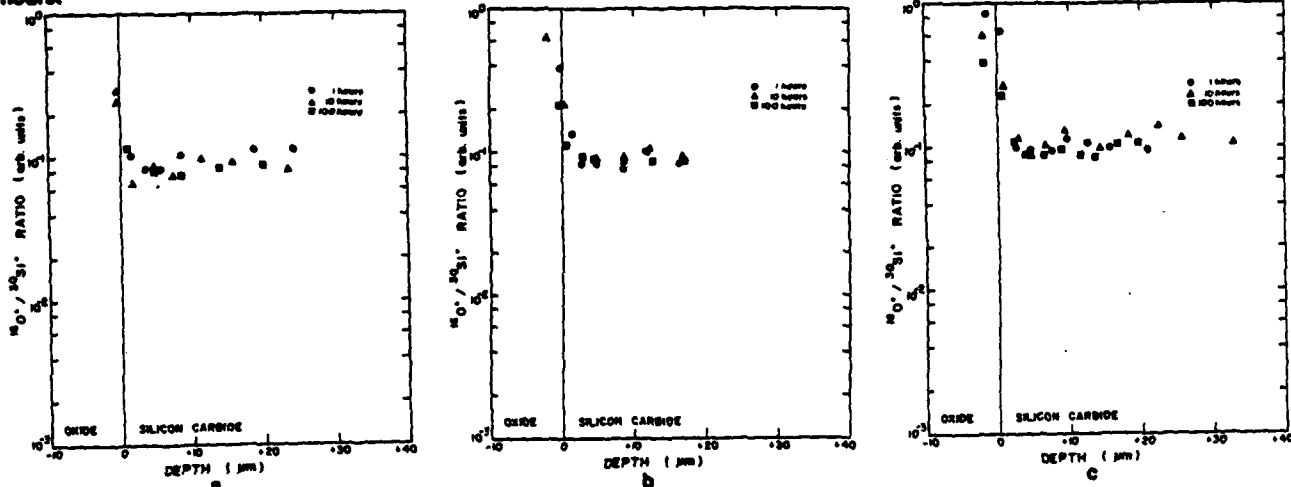


FIGURE 4 - Oxygen profiles into hot pressed silicon carbide oxidized at (a) 1200°C, (b) 1300°C, and (c) 1400°C for 1, 10, and 100 hours.

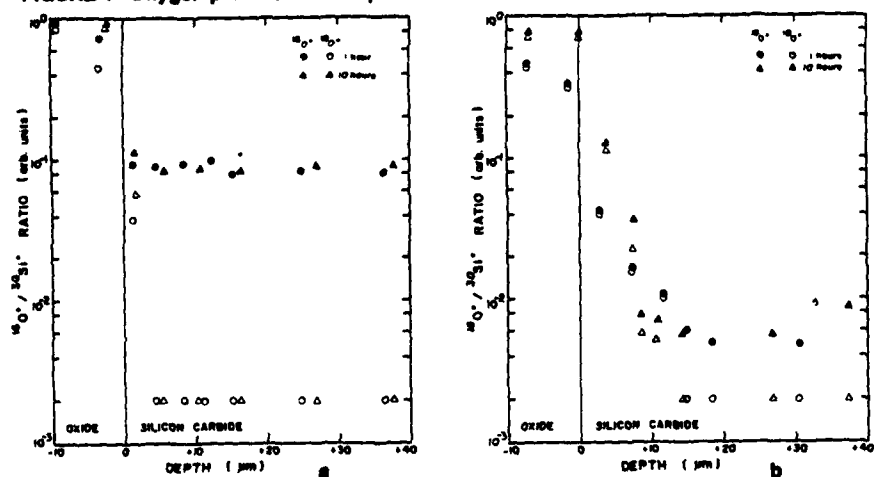


FIGURE 5 - Oxygen isotope profiles into (a) hot pressed silicon carbide, and (b) sintered alpha silicon carbide oxidized at 1300°C for 1 and 10 hours.

background counts compared to the other materials. Again, the time and temperature of oxidation has no significant effect on the observed profiles. Because of the high background oxygen concentration, one cannot determine whether there is broad region of penetration as there is in the sintered material. To clarify the breadth of the oxygen affected zones in the hot-pressed and sintered materials, oxidations were performed at 1300°C for one and ten hours in an environment enriched in  $^{18}\text{O}$  (Ref. 13).

In Figure 5, the resulting  $^{18}\text{O}$  and  $^{16}\text{O}$  profiles are compared for the two materials. From these profiles one can clearly separate the oxygen incorporated during processing from the oxygen introduced by the oxidation treatment. For the sintered material we see a similar profile for both  $^{18}\text{O}$  and  $^{16}\text{O}$  except for a much lower background  $^{18}\text{O}$  signal in the unaffected region of the substrate. In the hot-pressed material the interface as indicated by the  $^{18}\text{O}$  is very sharp indicating that there is no oxidation affected region of the substrate material as there is for the SASC.

To attempt to assess the role of porosity in controlling the penetration of oxygen into the substrate, the two types of silicon carbide with aluminum

carbide sintering aid, being 100% dense and ~90% dense, were oxidized and analyzed with the SIMS. In Figure 6, the results are presented for oxidations for 1 and 10 hours at 1300°C. There is a rather sharp interface for the fully dense material, and a somewhat broader oxygen affected region for the less dense material. However, the high oxygen content of the material tends to obscure the full penetration profile. As in the other cases, the time of oxidation has little or no effect on the profile.

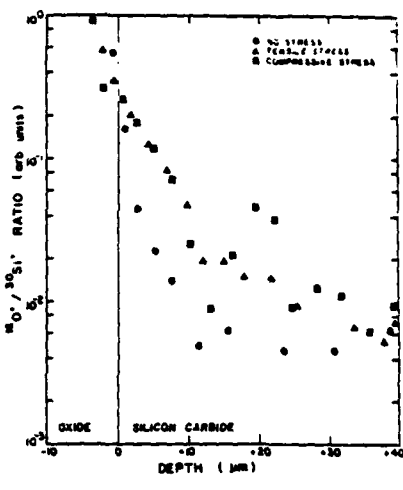
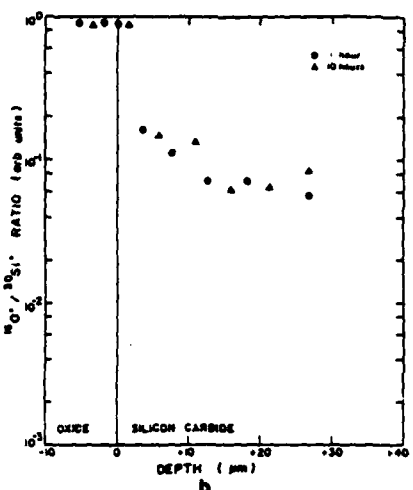
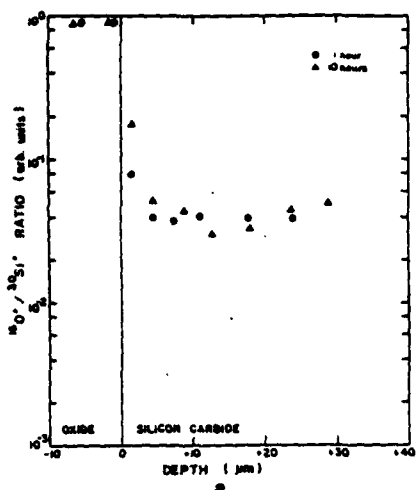


FIGURE 6 - Oxygen profiles into Al-doped silicon carbide, (a) 100% dense, and (b) 90% dense, oxidized at 1300°C for 1 and 10 hours.

FIGURE 7 - The effect of stress on the oxygen profiles into sintered alpha silicon carbide oxidized at 1200°C for 10 hours in air (maximum tensile stress = 264 MPa).

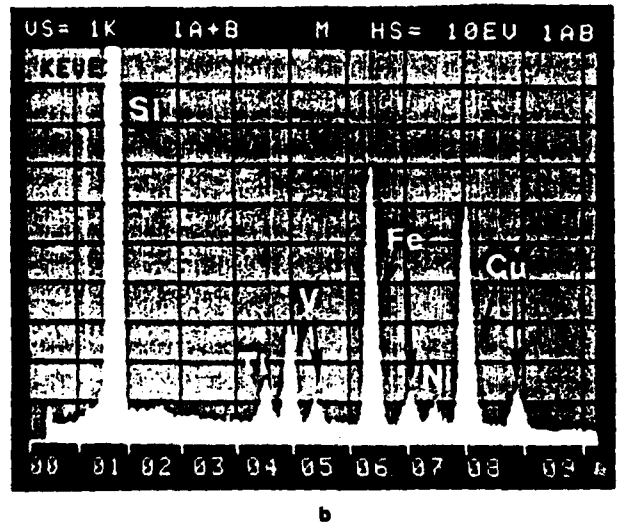
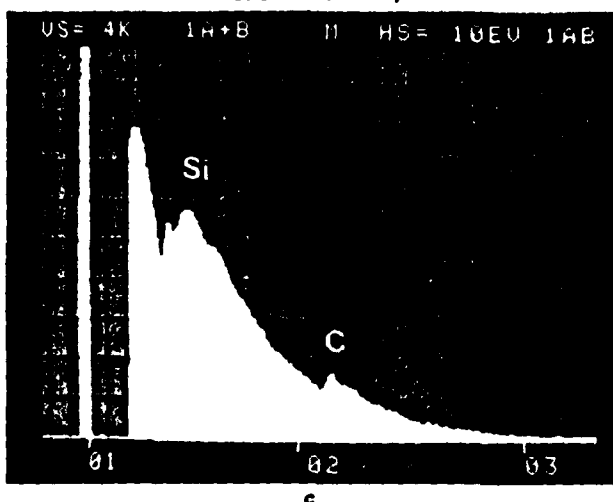
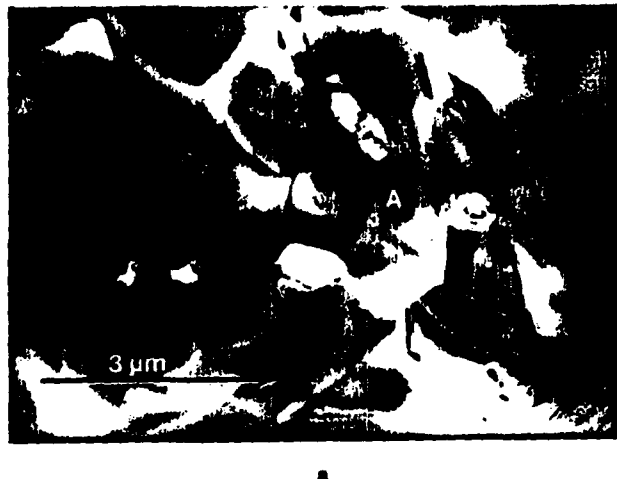


FIGURE 8 - (a) Transmission electron micrograph of sintered alpha silicon carbide (unoxidized), (b) XEDS analysis of area indicated by the arrow, and (c) EELS spectra of silicon carbide grain (A).

an experiment in which the material was statically loaded in a four-point bend test to 80% of the average short term fracture stress at 1200°C for 10 hrs are presented. Angle lapped specimens from both surfaces in the constant stress region were analyzed in addition to a specimen from the unstressed region. In both stressed specimens increased penetration was observed with occasional spikes in the count rate as the beam was stepped along the surface compared to the profile from the unstressed region. These features are attributed to microcracks or fissures which opened up normal to the tensile component of the stress on both surfaces (see Discussion below).

Samples similarly stressed for 100 hrs showed penetration profiles similar to those observed for the 10 hr specimens.

### 3.3 - TEM analyses

The TEM analyses of the hot-pressed materials before and after oxidation showed the presence of cemented carbide particles in the SiC matrix. No differences in the microstructures in the oxidized (near the oxide/SiC-interface) and unoxidized material were observed.

In Figure 8, a TEM micrograph of unoxidized sintered silicon carbide illustrates typical features of this material.

### 3.2 - Effect of stress on oxygen penetration

Since the ultimate concern with the oxidation behavior of silicon carbide is the long term reliability under stress, the effect of stress on the penetration of oxygen into the sintered silicon carbide was briefly studied. In Figure 7 the results of

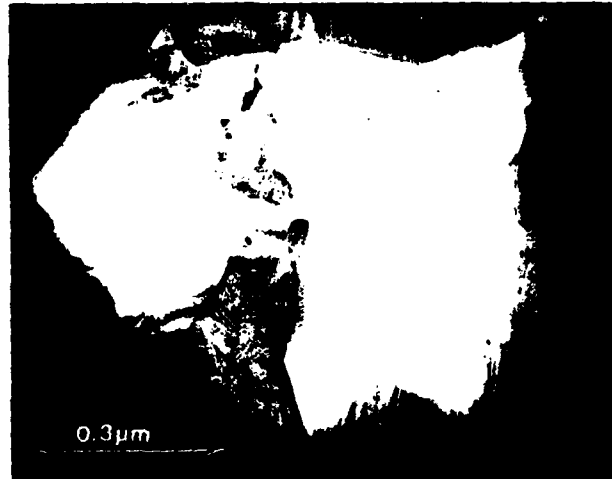


FIGURE 9 - Transmission electron micrographs of (a) sintered alpha silicon carbide oxidized at 1200°C for 10 hours showing oxidized pores and unaffected two-grain junctions, and (b) magnified view of pore region.

Several pores are apparent, and measurable concentrations of impurities are segregated around these pores. An XEDS spectrum of the area marked by the arrow indicates the presence of Ti, Fe, V, Cr and Ni. The EELS spectrum from a neighboring grain (A) indicates that these impurities are not dissolved into the individual grains. The two grain junctions were very sharp indicating the absence of a second phase there.

The oxidized material exhibited some differences from the unoxidized material. The two grain junctions in the oxygen penetrated region were not altered by oxidation but the three grain pipes and multigrain junctions contain a second phase. In Figure 9, an example of these features is presented showing the presence of amorphous material extending into the pore. The EELS spectrum from this material shows basically Si and O (Figure 10) and the microdiffraction pattern from the same region indicates that the material is amorphous. Features similar to these were plentiful in the TEM foils from the angle lapped specimen in the oxygen affected region confirming that the oxygen profiles result from preferential oxidation of three grain pipes and multigrain junctions which contain the impurities in the starting material. The two grain boundaries are largely unaffected in this region.

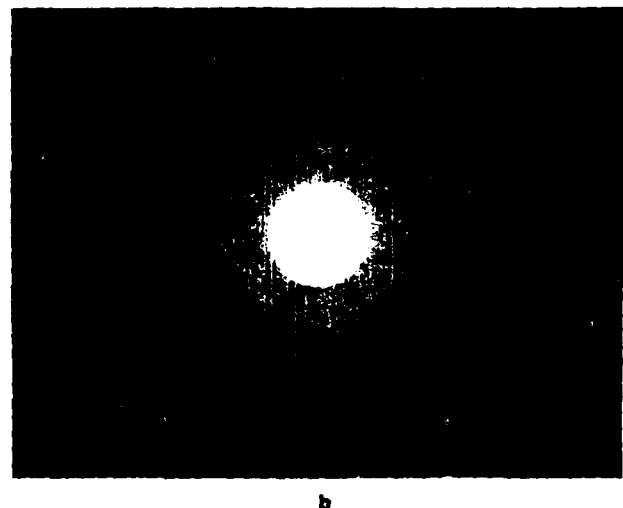
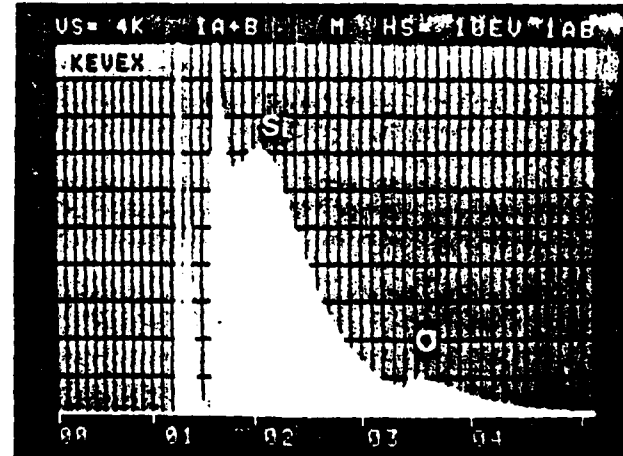


FIGURE 11 - (a) EELS spectra of center region of pore in Figure 9, and (b) Microdiffraction pattern of this region analyzed indicating the amorphous character.

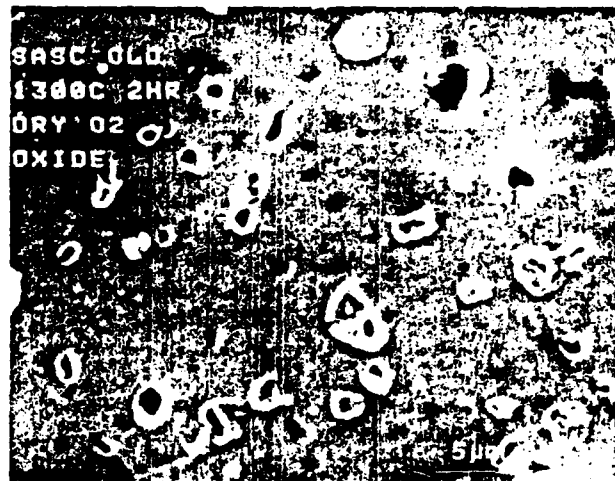


FIGURE 11 - Scanning electron micrograph of oxide surface on sintered alpha silicon carbide (SASC) oxidized at 1300°C for two hours in dry oxygen.

#### 4 - DISCUSSION

Several contributing processes to the oxidation of the substrate silicon carbide ceramic in advance of the general oxidation interface must be considered. The localized presence of viscosity-reducing impurities when incorporated into the amorphous silica scale may be responsible for the preferential penetration of oxygen along impurity laden boundaries in the sintered silicon carbide. In Figure 11, the regions of thicker oxide around pores in SASC demonstrate that the scale formation is indeed faster in these regions. In this material, the gaseous reaction products which form during oxidation tend to cause bubbles to form at these multigrain junctions presumably because the silica viscosity is lowest at these impure locations<sup>4</sup>. However, the presence of these impurities alone cannot cause the very large penetration (relative to the oxide thicknesses) because the hot-pressed materials would behave similarly since the sintering aids are segregated in the grain boundary phase.

Internal oxidation in a manner similar to the preferential oxidation internally of alloying elements in metals with much greater affinities for oxygen than the matrix metal has been suggested as a possible mechanism. However, in the present study the fully dense aluminum-containing (nonoxide) additive did not show the penetration behavior while the less dense material did show a region of oxygen penetration.

The materials which exhibited the oxygen penetration zone all contain porosity, some of which is interconnected. Therefore, we propose that the oxygen penetration process involves rapid transport along interconnected three grain pipes which are laden with impurities. Rapid oxygen transport along pore channels via the gas phase would permit oxidation of internal SiC surfaces until the pores become filled with the oxidation product. Gaseous reaction product generation could actually cause sufficient internal pressure to clear low viscosity liquid silicate reaction products from channels near the surface, thus creating the "craters" observed around pores which are open to the surface.

The absence of a time and temperature dependence to the process is compatible with a rapid gas phase diffusion process which becomes limited in depth by closure of channels with reaction products. Also, the enhanced penetration under stress may be due to the opening of channels (cracks and fissures) allowing deeper penetration and perhaps more channels for penetration. Those materials exhibiting essentially zero porosity were not susceptible to penetration as we would expect if the pore channels are responsible. The role of free carbon and the chemical nature of the carbon reaction product(s) are unclear at this point and are the topic of current research.

This internal oxidation process is similar to that observed by many investigators for reaction sintered silicon nitride but at much higher densities than typically encountered with reaction sintered silicon nitride. Thus, as explained by Grathwohl and Thümmler<sup>14</sup>, as the pore channels become smaller in dimension and volume fraction the penetration is less extensive, and as a result, the creep resistance of the small grain size, high density reaction sintered silicon nitride is much better than the more porous material or material with larger pore channels.

#### 5 - CONCLUSIONS

1. Fully dense chemical vapor deposited (CNTD) and hot pressed silicon carbide materials exhibited sharp oxide/silicon carbide interfaces after oxidation for 1-100 hrs at 1200-1400°C.
2. Less dense sintered alpha silicon carbide with boron and carbon sintering aids (~97% of theoretical density) and with aluminum carbide sintering aid (~90% of theoretical density) contained an oxygen penetrated zone of ~10-15 μm under the oxide scale. The depth of the oxygen penetrated zone was not significantly affected by the time and temperature of oxidation.
3. It is proposed that the oxygen penetration process involves gas phase transport of oxygen along impurity laden three and four grain channels and oxidation of the impurities and internal SiC surfaces. The internal oxidation causes closure of the pore channels thus limiting further penetration to a process of solid state diffusion, the same process which limits the rate of oxide scale growth.

#### ACKNOWLEDGMENT

*This work was supported by the U.S. Army Research Office, Division of Materials Science.*

#### REFERENCES

1. J.A. COSTELLO and R.E. TRESSLER, *J. Am. Ceram. Soc.* 64 (6) (1981) 332.
2. S.C. SINGHAL and F.F. LANGE, *J. Am. Ceram. Soc.* 58 (9-10) (1975) 433.
3. J. SCHLICHTING and K. KRIEGSMANN, *Ber. Dt. Keram. Ges.* 56 (3-4) (1979) 72.
4. J.A. COSTELLO and R.E. TRESSLER, accepted by *J. Am. Ceram. Soc.*
5. A.G. EVANS and F.F. LANGE, *J. Mater. Sci.* 10 (1975) 1659.
6. J.L. HENSHALL, D.J. ROWCLIFFE and J.W. EDINGTON, *J. Am. Ceram. Soc.* 62 (1-2) (1979) 36.
7. K.D. McHENRY and R.E. TRESSLER, *J. Am. Ceram. Soc.* 63 (3-4) (1980) 152.
8. G.G. TRANTINA and C.A. JOHNSON, *J. Am. Ceram. Soc.* 58 (7-8) (1975) 344.
9. K.D. McHENRY and R.E. TRESSLER, *J. Am. Ceram. Soc.* 59 (4) (1980) 459.
10. E.J. MINFORD, D.M. KUPP and R.E. TRESSLER, *J. Am. Ceram. Soc.* 66 (11) (1983) 769.
11. K.D. McHENRY, Ph. D. Thesis, The Pennsylvania State University (1978).
12. E. MINFORD, J.A. COSTELLO, I.S.T. TSONG and R.E. TRESSLER, in "Fracture Mechanics of Ceramics Vol. 6", ed. by R.C. Bradt, A.G. Evans, D.P.H. Hasselman and F.F. Lange, Plenum Publishing (1983) 511.
13. J.A. COSTELLO and R.E. TRESSLER, *J. Electrochem. Soc.* 131 (8) (1984) 1944.
14. G. GRATHWOHL and F. THÜMMLER, *J. Mater. Sci.* 13 (1978) 1177.

Received February 6, 1984; accepted March 9, 1984.

STATIC FATIGUE LIMIT FOR SILICON CARBIDE BASED CERAMICS -  
FLAW BLUNTING VS FLAW GROWTH

R. E. Tressler, E. J. Minford\* and D. F. Carroll

Department of Materials Science and Engineering  
The Pennsylvania State University  
University Park, PA U.S.A., 16802

SUMMARY

The determination of the threshold stress intensity factor for crack growth in silicon carbide ceramics using an interrupted static fatigue test is described. Oxidation of the sintered silicon carbide reduces  $K_{Ic}^{th}$  by the creation of oxidized grain boundaries which changes the mechanism of crack growth. At  $K$ -values below the threshold, cracks are blunted by local plastic relaxation in the ceramic. In siliconized silicon carbide the plastic blunting is accentuated resulting in very significant strengthening during static loading at 1000 and 1100°C. The blunting is accompanied by cavity nucleation, which after 1100°C static loading, causes significant reductions in the room temperature strength due to a high density of cavities locally.

INTRODUCTION

The possibility of using silicon carbide ceramics and siliconized silicon carbide ceramics at elevated temperatures for structural applications has prompted many studies of the oxidation behavior of these materials and the strength retention after oxidation at elevated temperatures (see for example Ref 1). Static fatigue studies have generally indicated that survivors of long term static fatigue tests are stronger than the starting material, particularly for sintered SiC and siliconized SiC [2,3]. Although there have been several studies of the growth of macroscopic and microscopic flaws in sintered and hot-pressed silicon carbide, only recently have there been attempts to determine the threshold stress intensity for crack growth in these

\*now at United Tech. Res. Center, East Hartford, CT

materials [4,5]. The influence of corrosive environments on the threshold stress intensity or static fatigue limit is obviously also a central issue for the use of these materials and for tailoring new materials to resist crack growth in severe environments. In this paper, our recent studies of the fatigue limit in hot-pressed and sintered SiC are reviewed with emphasis on the effect of oxidizing conditions. The possibility of accentuating the flaw blunting regime is explored with recent studies of the behavior of flaws in siliconized silicon carbide.

#### EXPERIMENTAL DETAILS

Since our interest is in the behavior of microscopic flaws, the behavior of which may be altered by an oxidized region at the surface, strength measurements were selected as the means by which to examine the competitive processes of blunting and growth. Dynamic fatigue tests (stressing rate dependence of strength) are not definitive when a threshold stress intensity and/or flaw blunting process are observed [6]. The most definitive approach to examining the behavior of flaws near the threshold stress intensity is to examine the strength distributions after exposure to a static load near the threshold stress intensity value. An interrupted static fatigue test has been employed to study the behavior of flaws at elevated temperature. By measuring strengths at temperature by rapidly loading from the static load level, the threshold stress intensity factor can be estimated from a knowledge of the starting strength distribution and the strength distribution after static loading [7].

The materials used in this study were a hot-pressed SiC (Norton's NC-203), a sintered SiC (Carborundum's sintered  $\alpha$ -SiC) and a siliconized SiC (experimental Carborundum material KX-01 with 29 volume % Si and 4-6 $\mu$ m grain size SiC). The strength samples were cut from billets to nominal 2.5 by 0.25 by 0.25 cm dimensions, and the major faces were ground flat and parallel with a 600-grit diamond wheel. They were tested in four point bending with 4.75 mm and 19.05 mm inner and outer spans. The tests were run in a controlled atmosphere furnace in which argon, air, or a controlled CO/CO<sub>2</sub> ratio could be maintained so that the P<sub>O<sub>2</sub></sub> was below the active to passive oxidation transition at the various temperatures.

In all cases the samples were proof tested to narrow the strength distribution. The initial strength distribution after proof testing was measured at room temperature and at elevated temperature to establish the starting strength/flaw size distribution.

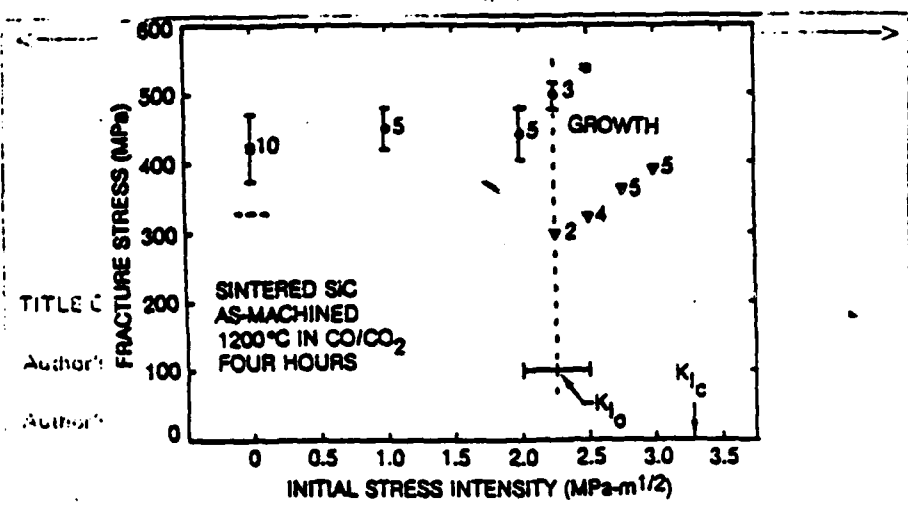


**Figure 1.** Effect of initial applied stress intensity on fracture stress of as-machined sintered  $\alpha$ -silicon carbide at 1200°C.

Start at page

- Proof stress level.
- Tested at room temperature in air after proof testing.
- o - Tested at temperature in CO/CO<sub>2</sub>, after four hours static loading.
- v - Tested at temperature in CO/CO<sub>2</sub>, failed during static loading.
- 5 - Number indicates number tested.

To examine the effect of oxidation on the flaw behavior the sintered silicon carbide was oxidized at 1200°C for 10 hrs and tested either in the low P environment or in air. This oxidation treatment results in an oxide thickness of ~0.23  $\mu\text{m}$  and oxygen penetration into the SiC to a depth on the average of 15-20  $\mu\text{m}$ .

The initial stress intensity factors reported below represent the  $K_I$  values calculated from the applied static load level assuming half-penny shaped surface flaws, and using the measured  $K_{Ic}^{If}$  values and initial strengths to calculate the maximum flaw size in the distribution. The observed failure origins were associated with surface or near surface features. For the siliconized silicon carbide the apparent  $K_{Ic}^{If}$  values measured with SENB specimens were stressing rate dependent. Therefore, the static load levels are reported as a fraction of the short term fracture strength at elevated temperature which should represent an initial  $K$ -value which is the same fraction of  $K_{Ic}^{If}$ . If final failure results from the same flaw distribution before and after static loading these assumptions concerning initial  $K$ -values are justified. In some cases, described below, this assumption is not accurate.

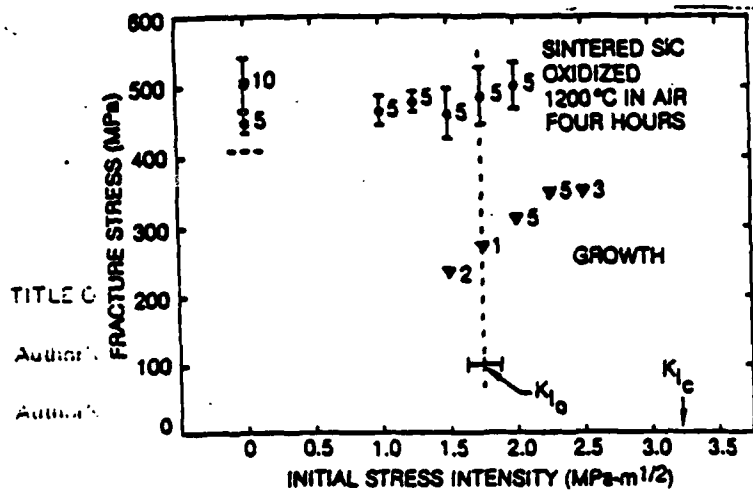


**Figure 2.** Effect of initial applied stress intensity on fracture stress of oxidized sintered  $\alpha$ -silicon carbide at  $1200^{\circ}\text{C}$ .

- — Proof stress level.
- Tested in liquid nitrogen after proof testing.
- o - Testing at temperature in  $\text{CO}/\text{CO}_2$ , after four hours static loading.
- V - Testing at temperature in  $\text{CO}/\text{CO}_2$ , failed during static loading.
- 5 - Number indicates number of samples tested.

#### RESULTS AND DISCUSSIONS

Despite observations from dynamic fatigue tests on sintered silicon carbide in which there were no indication of slow crack growth, the present study reveals a threshold initial applied stress intensity above which cracks grow in unoxidized material tested in an inert environment. In Figure 1 the threshold value is estimated from four hour tests to be approximately  $2.25 \text{ MPa}\cdot\text{m}^{1/2}$  or  $\approx 0.7 K_{Ic}$ . Samples static loaded below this value show indications of strengthening. In a separate study we have shown that materials with a threshold which is a significant fraction of  $K_{Ic}$  and/or in which cracks can blunt show very little dependence of strength on stressing rate or a minimum in the strength vs stressing rate plot [6].

The corresponding data at  $1400^{\circ}\text{C}$  show similar behavior with the threshold  $K$ -value  $\approx 1.75 \text{ MPa}\cdot\text{m}^{1/2}$ , and with a more pronounced strengthening below the threshold than observed at  $1200^{\circ}\text{C}$ .

The effect of oxidation on the threshold for crack growth is apparent in Figure 2 which indicates a reduction

in  $K_{th}$  to ~1.75 at 1200°C for material which was oxidized at 1200°C for 10 hrs and tested in an inert environment. At 1400°C the  $K_{th}$  was reduced to ~1.25 by oxidation. Similar results were obtained when the tests were performed in air.

To more accurately define the threshold value, a larger group of samples was selected for more extensive tests at 1200°C in air after oxidation at 1200°C for 10 hrs. The samples were proof tested in liquid nitrogen (oxidized specimens exhibited slow crack growth when proof tested at room temperature in air) in order to truncate the strength distribution. The survivors were divided into three lots for static loading at 0.5 MPa·m<sup>0.5</sup>, 1.75 MPa·m<sup>0.5</sup>, and for determination of the starting strength distribution at 1200°C. These initial K-values represent the maximum values because they are based on the maximum flaw size which could be present after prooftesting.

The results of these tests conducted in air at 1200°C are shown in Figure 3. The short term strength distribution without static loading falls below the proof stress level because of the decrease in strength from the liquid N<sub>2</sub> temperature to 1200°C. There is little

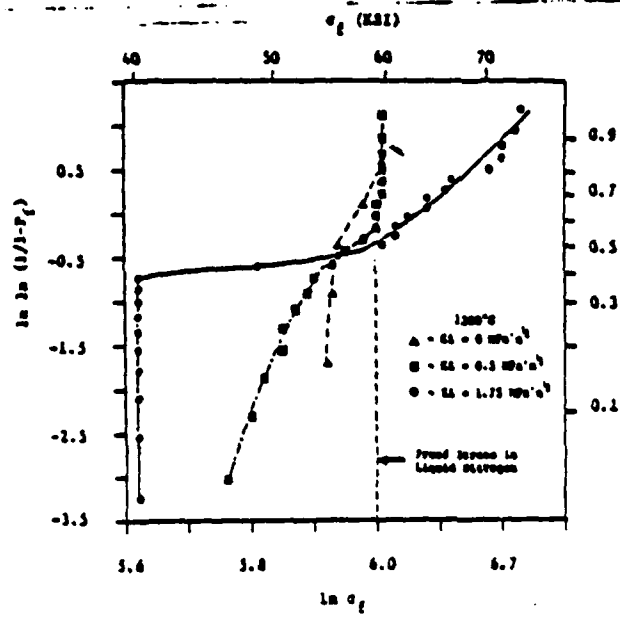


Figure 3. Strength distributions at 1200°C in air for oxidized sintered silicon carbide before and after static loading at various initial stress intensities for 4 hours.

evidence of change in the strength distribution after static loading at  $K_{Ii} = 0.5 \text{ MPa}\cdot\text{m}^{\frac{1}{2}}$ . The distribution after static loading at  $K_{Ii} = 1.75 \text{ MPa}\cdot\text{m}^{\frac{1}{2}}$  is drastically changed. The failed specimens are all plotted to the far left of the diagram to indicate no retained strength but are included to indicate the position of the survivors relative to their original positions in the strength distribution. Large flaws which were loaded above the threshold grew during static loading and most of the samples failed. Small flaws which experienced K-values just below the threshold were substantially blunted resulting in strengthening of those samples relative to the starting strength. Flaws loaded at the threshold value experienced no change, or perhaps those loaded at a K-value at which the extent of crack growth was exactly offset by a plastic blunting resulted in strengths identical to the starting distribution. Using the original strength at the crossover of the initial flaw distribution with the final strength distribution, one can estimate the threshold K-value from the relationship.

$$\frac{K_{th}}{K_{Ic}} = \frac{\sigma_{\text{static load}}}{\sigma_{f,t=0}} \quad (1)$$

From the data in Figure 3, this estimate of  $K_{th}$  is  $1.61 \text{ MPa}\cdot\text{m}^{\frac{1}{2}}$ . ( $\sigma_{f,t=0} = 378 \text{ MPa}$ ,  $\sigma_{\text{static load}} = 178 \text{ MPa}$ ). This value is slightly lower than the estimate of  $1.75 \text{ MPa}\cdot\text{m}^{\frac{1}{2}}$  by Minford et al. [5] illustrated in Figure 2. At  $1400^\circ\text{C}$  a similar experimental analysis of  $K_{th}$  was frustrated by nucleation of a new flaw population, presumably by selective oxidation of microstructural inhomogeneities.

The blunting process is clearly shown to be a stress dependent one by the large strengthening increment caused by the increase in the static load level from  $K_{Ii} = 0.5 \text{ MPa}\cdot\text{m}^{\frac{1}{2}}$  to  $K_{Ii} = 1.75 \text{ MPa}\cdot\text{m}^{\frac{1}{2}}$ .

#### RATIONALIZATION OF $K_{th}$

The thermodynamic analyses of crack stability and instability in brittle solids is the appropriate starting point from which to rationalize the observed values for  $K_{th}$  and the observed changes with temperature, and oxidation. These analyses define the lower limit of  $K_{th}$  since at stress intensities above this value the kinetics of crack growth may be offset by the kinetics of blunting which would lead to a measured limit above the equilibrium  $K_{th}$ . The detailed analyses of competing kinetic processes in the crack tip region are not sufficiently refined, nor

Table 1. Predictions of the Threshold Stress Intensity Based on Crack Growth Models at 1200°C

Author	Model for $K_{th}$	Prediction for $K_{th}$ (MPa·m $^{1/2}$ )		
		Hot-Pressed <sup>a</sup> , [4]	Oxidized <sup>b</sup>	As-Machined Sintered <sup>b</sup> Sintered <sup>c</sup>
Griffith [14]	$\frac{\theta M^2 E \gamma_s}{\pi^2}$	0.356	0.334	0.518
Charles and Willig [15]	$\frac{3M^2}{2\pi} E \gamma_s^{-1/4}$	0.273	0.257	0.398
Lawn and Wilshaw [16]	$\frac{2}{(1-\nu^2)} E \gamma_s^{-1/4}$	0.546	0.515	0.798
Dutton [12]	$\frac{2M^2}{\pi(1-\nu^2)} E \gamma_{gb}^{-1/4}$	0.634	0.599	0.928
Lange [9]	$\frac{8M}{d_V} \frac{c}{\pi} \gamma_s^{-1/4}$	2.066	1.116	5.127

<sup>a</sup>  $\gamma_{gb} = \gamma_s = 0.35 \frac{\text{N}}{\text{mm}}$ ,  
for silicate glass [9]  
(in boundary)  
 $E = 420 \text{ GPa}$  [19]  
 $\nu = 0.11$  [19]  
 $c = 103.2 \frac{\text{mm}}{\text{m}}$   
 $d_V = 80 \times 10^{-10} \text{ m}$  [18]

<sup>b</sup>  $\gamma_{gb} = \gamma_s = 0.35 \frac{\text{N}}{\text{mm}}$ ,  
for silicate glass [9]  
(in boundary)  
 $E = 372 \text{ GPa}$  [19]  
 $\nu = 0.14$  [4]  
 $c = 30.1 \frac{\text{mm}}{\text{m}}$   
 $d_V = 50 \times 10^{-10} \text{ m}$  [18]

<sup>c</sup>  $\gamma_{gb} = \gamma_s = 0.84 \frac{\text{N}}{\text{mm}}$ ,  
for silicon carbide [17]  
(no boundary phase)

are the confirming experimental data sufficiently compelling to allow direct comparison with the present study [8].

We have examined the applicability of the various models which have attempted to define a lower limit stress or stress intensity for crack growth [5]. The results are summarized in Table I. We've included results from parallel studies of hot-pressed SiC which contains amorphous aluminosilicate at grain boundaries [4]. Without reviewing the details of the analysis, one is led to the conclusion that Lange's model [9] of the growth of preexisting voids in a viscous grain boundary phase best fits the results for the oxidized sintered SiC and hot-pressed SiC, both of which have amorphous oxide material in grain boundaries. Previous investigators have described slow crack growth in these materials as viscous separation of the amorphous grain boundary phase [10,11].

The as machined sintered SiC does not contain an amorphous grain boundary phase when tested in a nonoxidizing environment. Dutton's [12] threshold value is closest to matching the observed one although significantly too low. To further test his model diffusivities for the various diffusion paths determined by Hong et al. [13] and other material properties from the literature were used to estimate times to failure ( $t_f$ ) [5]. The experimental values fall between the calculated  $t_f$ 's for grain boundary diffusion and vapor phase transport.

Our attempts to identify voids in the crack tip region in either the oxidized or the nonoxidized material have not resulted in clear identification of void growth and coalescence as the overall process leading to crack growth. The materials with an oxide grain boundary phase show evidence, in the form of fractured ligaments, of void growth and coalescence on the fracture surfaces. The as machined material may well fail by a process more like the Dutton model of crack propagation by material transport away from the crack tip which need not involve void nucleation, growth, and coalescence.

#### FLAW BLUNTING AND SILICONIZED SILICON CARBIDE

The stress dependent increases in strength below the threshold stress intensity indicate a crack blunting or crack tip stress field relaxation process. This phenomenon is well known in alumina ceramics which contain a glass phase and has been assumed to result from viscous deformation in the crack tip region [20]. More recent studies have concluded that the stress relaxation is accompanied by a damage zone with full facet-sized cavities [8]. We have not been able to document

these microstructural changes in sintered or hot pressed silicon carbide, but our recent investigations of a fine grained siliconized silicon carbide have been illuminating in this respect [21].

The siliconized silicon carbide deformed excessively at 1200°C and above (3% in 2 hrs at 0.75  $\delta_f$  at 1200°C); thus, the interrupted static loading tests were conducted at 1000 and 1100°C. Four sets of data for static loading times of 2 hr and 10 hr at 1000°C and 1100°C in air and argon are presented in Figures 4 and 5 in the form of probability plots. All samples survived a proof test of 72,000 psi at room temperature and the static loading level was held constant at 0.80  $\delta_f$  at the two temperatures. The fracture toughnesses of this material measured by the SENB technique were 5.00 and 5.17 MPa·m<sup>0.5</sup> at 1000°C and 1100°C, respectively.

At these temperatures there is relatively little effect of oxidation (1200°C for 15 hr) on the initial strength distributions. Similarly, there is relatively little effect of the air environment during static loading on the strength distributions after static loading. The major effect is a dramatic strengthening of the material after the static

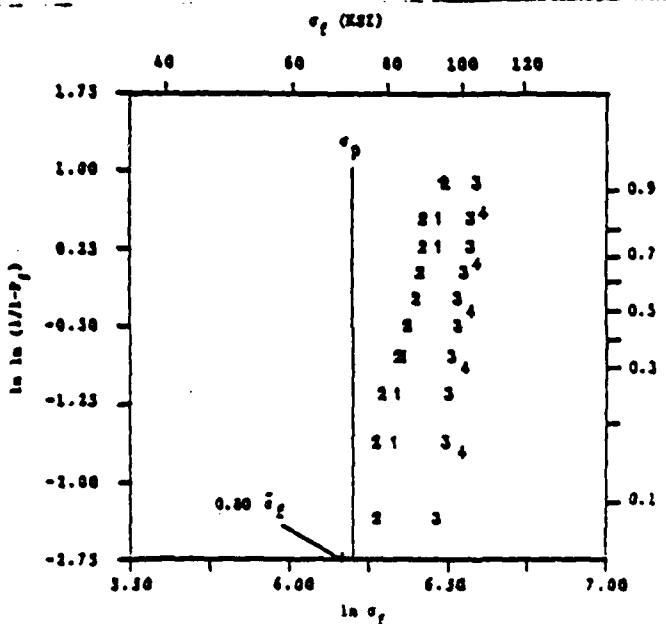


Figure 4. Strength distributions at 1000°C before<sup>(1)</sup> and after oxidation<sup>(2)</sup> and after 2 hours<sup>(3)</sup> and 10 hour<sup>(4)</sup> static loading in air.

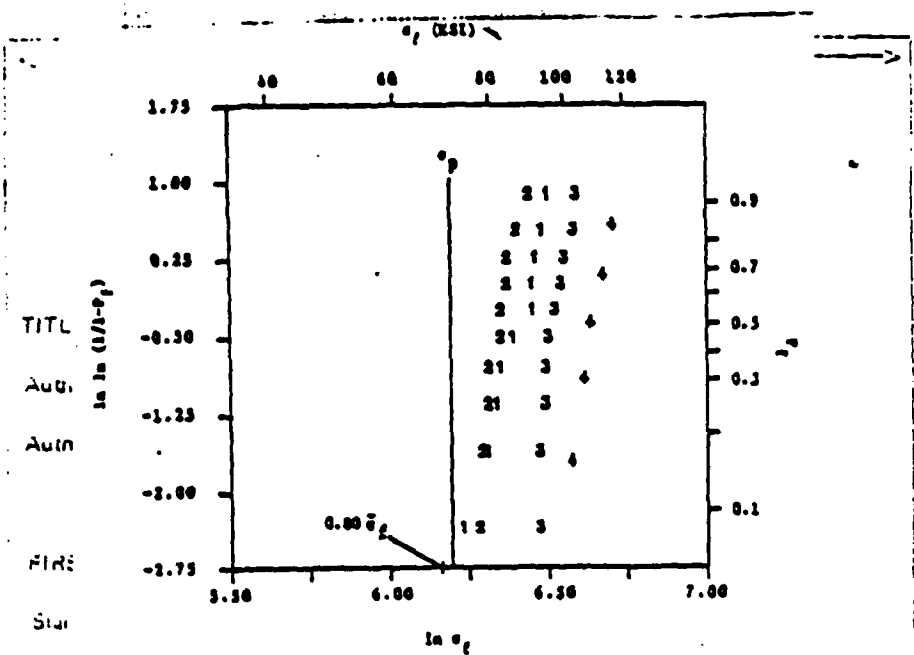


Figure 5. Strength distributions at 1100°C before<sup>(1)</sup> and after oxidation<sup>(2)</sup> and after 2 hour<sup>(3)</sup> and 10 hour<sup>(4)</sup> static loading in air.

Figure 6. Scanning electron micrograph of the KX-01 material static loaded at 1100°C for 10 hours in air (cavity region).

loading treatment (Figures 4 and 5) and a clear time dependence of strengthening which is most evident in the data at 1100°C. After ten hours of static loading at 1100°C the average fracture stress at temperature is 27% higher than the starting fracture stress with a plastic strain of 2.7% measured on specimens which were static loaded but not broken.

Since oxidation did not significantly affect the strengthening, the flaw blunting is due to deformation processes in the substrate ceramic. SEM examination of polished surfaces of specimens which were static loaded but not broken revealed isolated cavities which form primarily at SiC-SiC grain boundaries (Figure 6). The cavities are limited by the surrounding silicon; there is little evidence of linkup or coalescence under the conditions used in these experiments. Careful measurements are underway to determine how much of the plastic strain can be accounted for by cavitation as compared to plastic deformation of the matrix. Attempts to study the process of cavity nucleation and growth at the tips of large artificial flaws have been frustrated by rapid healing of these flaws during heat up to the test temperature. Thus, the relative importance of plastic relaxation in the silicon and blunting by nucleation of cavities to relax stress concentrations is not known at this point.

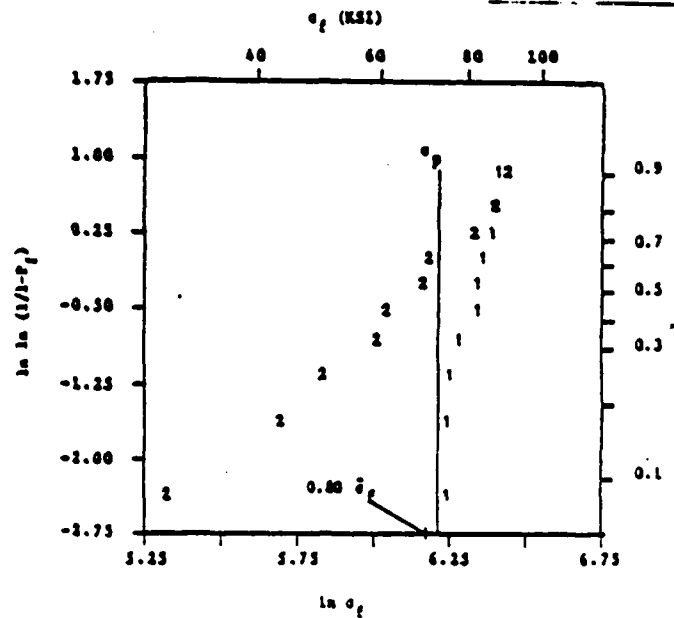


Figure 7. Room temperature strength distributions after proof testing (1) and after 2 hour static loading at 1100°C in argon.

The room temperature strength distributions after static loading at these temperatures suggest that at 1000°C the cavities are small and isolated since the strengths are marginally higher than the original strengths. However, after the 1100°C treatment (Figure 7), the room temperature strengths are significantly reduced for most of the population, and careful SEM fractography reveals a high density of cavities at the failure origin. Therefore, we must expect, at these very high stresses and stress intensities, cavity linkup and coalescence to dominate the time dependent failure of this material. The stress dependence and temperature dependence of the plastic deformation processes and failure are the subject of current research.

#### ACKNOWLEDGMENT

This work was supported by the U.S. Army Research Office and Exxon Research and Engineering Company.

S. G. T.

#### REFERENCES

1. Becher, P. F., Comm. Am. Ceram. Soc., 1983, C-120.
2. Quinn, G. D., Ceram. Eng. Sci. Proc., 1982, 3(1-2), 77.
3. Easler, T. E., Bradt, R. C., and Tressler, R. E., J. Am. Ceram. Soc., 1981, 64(12), 731.
4. Minford, E. J., and Tressler, R. E., J. Am. Ceram. Soc., 1983, 66(5), 338.
5. Minford, E. J., Kupp, D. M., and Tressler, R. E., J. Am. Ceram. Soc., to be published.
6. Minford, E. J., and Tressler, R. E., to be published.
7. Wilkins, B. J. S., and Dutton, R., J. Am. Ceram. Soc., 1976, 59(3-4), 108.
8. Evans, A. G., and Blumenthal, to be published in 'Deformation of Crystals and Ceramics', (Ed. R. E. Tressler and R. C. Bradt) Plenum Press, New York, 1984.
9. Lange, F. F., 'Deformation of Ceramics', (Ed. by R. C. Bradt and R. E. Tressler), Plenum Press, New York, 1975, p. 361.
10. Evans, A. G., and Lange, F. F., J. Mater. Sci., 1975, 10 (10), 1659.
11. McHenry, K. D., and Tressler, R. E., Am. Ceram. Soc. Bull., 1980, 55(4), 459.
12. Dutton, R., 'Fracture Mechanics of Ceramics, V2', (Ed. by R. C. Bradt, D. P. H. Hasselman and F. F. Lange), Plenum Press, New York, 1974, 647.
13. Hong, J. D., Hon, M. H., and Davis, R. F., Ceramurgia Int'l., 1979, 5(4), 155.
14. Griffith, A. A., Phil. Trans. Roy. Soc. Lond., 1920, 7221, 163.

16. Lawn, B. R., and Wilshaw, T. R., 'Fracture of Brittle Solids', Cambridge University Press, Cambridge, 1975, p. 168.
17. Allen, B. C., and Kingery, W. D., Trans. AIME, 1959, 215 (2), 30.
18. McHenry, K. D., Ph.D. Thesis, The Pennsylvania State University, University Park, PA, 1978.
19. Walton, M. A., and Bradt, R. C., 'Engineering with Ceramics', Brit. Ceram. Soc., London, 1981.
20. Davidge, R., 'Mechanical Behavior of Ceramics', Cambridge University Press, Cambridge, 1979, p. 100.
21. Carroll, D. F., and Tressler, R. E., to be published.

FIRST READING

SIXTY SEVEN

# Time-Dependent Strength of Siliconized Silicon Carbide under Stress at 1000° and 1100°C

D. F. CARROLL\* and R. E. TRESSLER\*

Department of Materials Science and Engineering, The Pennsylvania State University, University Park, Pennsylvania 16802

The time-dependent strength of a fine-grained siliconized silicon carbide under stress at 1000° and 1100°C was investigated. Both macroscopic stress redistribution and localized flaw blunting were found to contribute to the strengthening of siliconized silicon carbide in bending tests. Strengthening through macroscopic stress redistribution involved nonlinear creep behavior which decreased the maximum outer fiber stress in the bending beam. Localized flaw blunting processes were determined to be operative in this material through artificial flaw tests using a prestress to prevent flaw healing. The sharp artificial cracks were blunted during static load tests by localized deformation processes at the crack tip.

## I. Introduction

SILICONIZED silicon carbide materials are prime candidates for ceramic components in gas turbine engines, heat exchangers, fusion reactors, and wear resistant seals.<sup>1-3</sup> The properties which make these materials unique for these types of applications are good oxidation resistance, high thermal conductivity, low thermal expansion, and adequate mechanical strength.<sup>1,4</sup> Along with these properties, siliconized silicon carbides can be fabricated into fully dense complex shapes without shrinkage. From these characteristics, siliconized silicon carbide has an advantage over other structural ceramics and has great potential as a high-performance ceramic.

Past investigations have revealed a strengthening phenomena in some types of siliconized silicon carbide under stress at elevated temperatures. This strengthening process has been attributed to flaw blunting and stress relaxation processes around the crack tip.<sup>5-7</sup> More recently, an approach has been developed which describes the strengthening process as a macroscopic stress redistribution in the bending beam due to the nonlinear creep behavior of siliconized silicon carbide.<sup>8</sup> This stress redistribution process reduces the maximum outer fiber stress in the bending beam. After static loading, the superposition of the reduced outer fiber stress with the stress due to fast fracture results in a strength increase. The objectives of this paper are to demonstrate how the applied stress, temperature, and time of static load affect the degree of strengthening in a specific siliconized silicon carbide and to determine what processes are responsible for the strength increase.

## II. Experimental Procedure

The material used in this investigation was a siliconized silicon carbide containing 29 vol % of free silicon metal and 4 to 6  $\mu\text{m}$  SiC grains.\* The density of this material was 2.95 g/cm<sup>3</sup>. Four-point bend specimens were cut from billets using a diamond saw and the major faces were ground parallel with a 600-grit diamond wheel. The final dimensions were nominally 25 by 2.5 by 2.5 mm. The corresponding edges which formed the tensile plane were beveled by hand with 600-grit SiC grinding paper to remove any edge checking flaws. In all cases, the bend bars were proof tested using a stress of 495 MPa to narrow the strength distribution. To establish the initial strength distribution of the material after proof testing, the strengths were measured at room temperature and at

Presented at the 86th Annual Meeting and Exposition, The American Ceramic Society, Pittsburgh, PA, May 3, 1984 (Basic Science Division, Paper No. 259-B-84). Received September 4, 1984; revised copy received December 7, 1984; approved December 10, 1984.

\*Supported by the Exxon Engineering and Research Company.

<sup>†</sup>Member, The American Ceramic Society.

<sup>‡</sup>KX-01, Carbonium Co., Niagara Falls, NY.

elevated temperatures. The crosshead speed used during proof and fracture testing was 0.254 cm/min.

Static load tests were conducted at 1000° and 1100°C in both argon and air environments for 2 and 10 h at applied stress levels of  $0.50\sigma_f$  (300 MPa) and  $0.80\sigma_f$  (480 MPa), where  $\sigma_f$  is the average fracture stress at test temperature. After static loading, the specimens were fractured at temperature by rapidly loading from the static load level. The specimens which were statically loaded in air were preoxidized in air for 15 h at 1200°C.

Some of the specimens statically loaded at  $0.80\sigma_f$  for 2 h at 1000° and 1100°C were not fractured at the end of the static load time but were unloaded and cooled to room temperature. These specimens were then fractured to determine if any residual stresses were developed by the stress redistribution process described by Cohr *et al.* During static loading, the nonlinear creep behavior causes stress redistribution to occur on both the tensile and compressive side of the bending beam. If the specimens were unloaded after static loading and cooled to room temperature, a residual compressive stress would develop on the tensile side of the specimen while a residual tensile stress would develop on the compressive side. By fracturing these specimens with the appropriate surface in tension during four-point bend fracture, the existence of residual compressive or tensile stresses could be determined by comparing the initial distribution with the strength distribution of these specimens.

In an attempt to separate the strengthening contributions of localized flaw blunting and macroscopic stress redistribution, a series of artificial flaw experiments were conducted. Large artificial flaws were introduced into proof-tested specimens using the controlled flaw technique.<sup>9</sup> A 19.6-N Knoop indentation was used to produce the artificial surface crack. After indenting, the crater was removed by grinding the surface to eliminate residual stresses. The resulting strength distributions were measured at room temperature, at 1100°C in argon and at 1100°C in air after 10 h of annealing. During furnace heatup to 1100°C, a prestress of  $0.75\sigma_{f1}$ , where  $\sigma_{f1}$  is the average room temperature strength of the indented specimens, was applied to prevent flaw healing.<sup>10</sup> This 195-MPa prestress corresponds to an initial applied stress intensity of  $0.75K_{Ic}$ . Indented specimens were also static loaded for 10 h in argon at an applied stress level of  $0.80\sigma_{f1}$  (320 MPa), where  $\sigma_{f1}$  is the average fracture stress of the indented specimens at 1100°C. Again, the same prestress level was applied during furnace heatup. This applied stress was equivalent to a stress intensity of  $0.80K_{Ic}$ .

## III. Results

### (1) Time and Temperature Dependence

The time and temperature dependence of the strengthening process of siliconized silicon carbide under stress was investigated by static loading oxidized specimens for 2 and 10 h at 1000° and 1100°C. The static load level was held constant at  $0.80\sigma_f$  (480 MPa) for both temperatures. All specimens survived during the time of the static load. Figure 1 summarizes the results at 1000° and 1100°C. At these temperatures, there was relatively little effect of oxidation on the initial strength distributions. Similar static load tests of unoxidized specimens in argon have shown that the resulting strength distributions were generally unaffected by oxidation or the test environment under these conditions. A dramatic strength increase was observed in this material after static loading at the applied stress of  $0.80\sigma_f$ . The time dependence of the strengthening process can be seen at both temperatures but its more

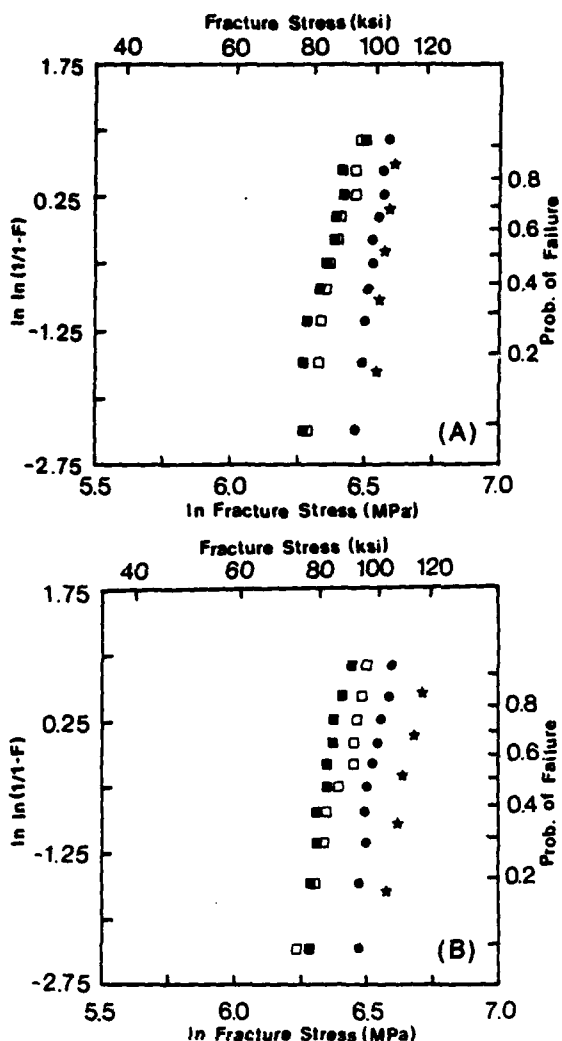


Fig. 1. Strength distributions at (A) 1000°C and (B) 1100°C (□) before and (■) after oxidation and (●) after 2 h and (★) 10 h of static loading in air at  $0.80\sigma_f$ .

evident at 1100°C. The average fracture stress after static loading at 1100°C for 10 h was 27% higher than the initial distribution, whereas at 1000°C, the average fracture stress was 20% higher. The difference in the amount of strengthening at these two temperatures indicates a temperature-dependent strengthening process. The permanent strains in the specimens were determined by measuring the outer fiber strain. The permanent strains at 1000° and 1100°C after 10 h of static loading were 1.8 and 2.7%, respectively.

#### (2) Stress Dependence

Specimens were statically loaded for 2 and 10 h in an argon environment at a lower applied stress of  $0.50\sigma_f$  (300 MPa). Again, there were no specimen failures during static loading. At an applied stress of  $0.50\sigma_f$ , there was no strengthening observed after static loading for either of the two times at 1000° or 1100°C. The strength distributions after 2 and 10 h of static loading were almost identical with the initial distribution. These results indicate a threshold stress for time-dependent strengthening. The permanent strains measured after 10 h of static loading were 0.6 and 1.3% at 1000° and 1100°C, respectively.

#### (3) Cavity Formation

The polished tensile surfaces of specimens static loaded but not broken at various test conditions were examined for micro-



Fig. 2. Scanning electron micrographs of (A) polished tensile surface and (B) cavity region of specimen statically loaded for 10 h at 1100°C in air at  $0.80\sigma_f$ .

structural rearrangement by scanning electron microscopy (SEM). This examination revealed formation of cavities only in the specimens that were static loaded at  $0.80\sigma_f$  (Fig. 2(A)). These cavities formed primarily between SiC grains in regions of locally high SiC content and were limited or blunted by the surrounding silicon matrix (Fig. 2(B)). The size and density of the cavities were proportional to the time and temperature of static loading. There is little evidence of cavity coalescence or linkage under the conditions used in these experiments. The absence of cavities in the specimens statically loaded at  $0.50\sigma_f$  suggests a threshold stress for cavity formation.

#### (4) Residual Stresses

In order to examine the possibility of macroscopic stress redistribution as a cause of strengthening during static loading, specimens were statically loaded at  $0.80\sigma_f$  (480 MPa) for 2 h in argon at 1000°C, unloaded, and fractured at room temperature. The data collected by fracturing the specimens with the original tensile surface in tension and the original compressive surface in tension are shown in Fig. 3(A). The results indicate a residual compressive stress in the specimens fractured with the original tensile surface in tension. This residual compressive stress produces an increase in strength from the initial room-temperature distribution. In the specimens which were fractured with the original compressive surface in tension, the strength decreased compared to the initial distribution. This strength decrease is attributed to a residual tensile stress. The existence of these residual stresses in the specimens after static loading suggests that the type of macroscopic strengthening discussed by Cohrt *et al.*<sup>4</sup> may be operative. The effect of beam curvature on these results was determined to be negligible for

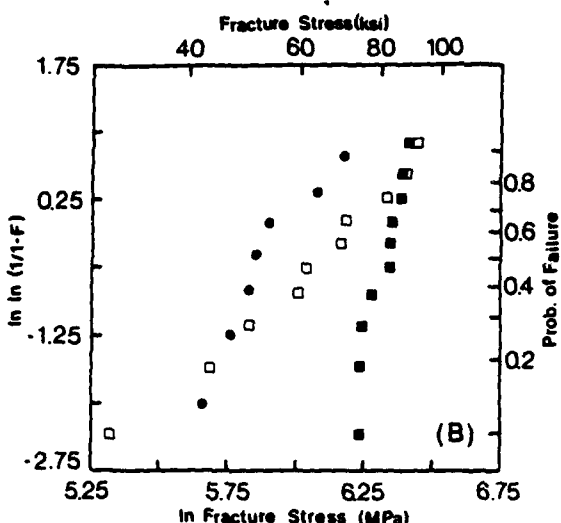
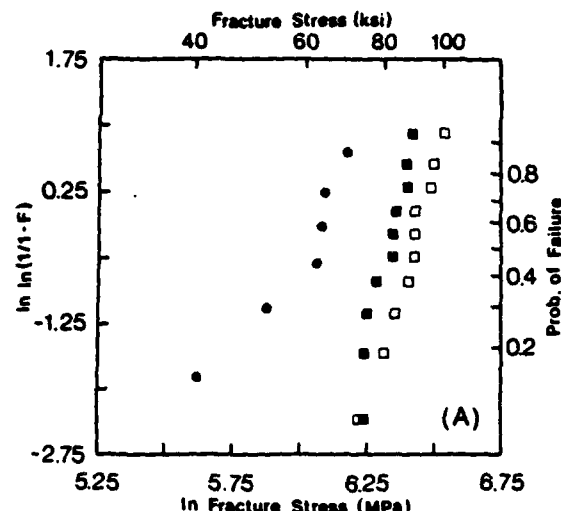


Fig. 3. Strength distributions of specimens statically loaded at  $0.80\sigma_c$  for 2 h at (A) 1000°C and (B) 1100°C in argon (unloaded and fractured at room temperature): (■) initial room-temperature strength distribution; (□) strength distribution for specimens fractured with original tensile surface in tension (residual compressive stress); (●) strength distribution for specimens fractured with original compressive surface in tension (residual tensile stress).

the degree of curvature obtained in the specimens.<sup>11</sup>

The results for the specimens statically loaded at 1100°C, unloaded, and fractured at room temperature are shown in Fig. 3(B). A similar residual tension stress is observed in the compressive side of these specimens. However, a different type of behavior was found when the specimens were fractured with the original tensile surface in tension. The resulting strengths are lower than the initial strengths. This result is quite different from what was obtained for specimens statically loaded at the 1000°C. Careful SEM examination of the fracture surfaces has revealed a high density of cavities around the fracture origins (Fig. 4). The interaction between the critical flaws and the cavities reduces the strength below the initial distribution, even with a residual compressive stress present. This interaction was not observed at 1000°C because the cavities formed at this temperature are small and isolated. SEM examination of the compressive surfaces has revealed no evidence of cavities; thus, the strength decrease is probably related to the residual tensile stress alone.



Fig. 4. Scanning electron micrograph of fracture surface of specimen statically loaded for 2 h at 1100°C in argon at  $0.80\sigma_c$ , and fractured at room temperature.

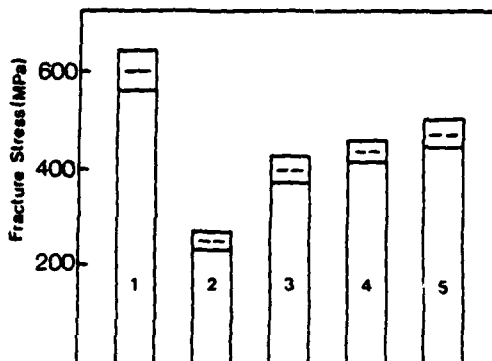


Fig. 5. Effect of annealing and static loading on average fracture stress of indented specimens: (1) 1100°C, no indentation; (2) room temperature, 19.6-N indentation; (3) 1100°C, 19.6-N indentation, no anneal; (4) 1100°C, 19.6-N indentation, 10-h anneal at 1100°C; (5) 1100°C, 19.6-N indentation, 10-h static loading at  $0.80K_c$ . In (4) and (5), a prestress of 75% of average room-temperature indented fracture stress was applied during furnace heatup to prevent flaw healing.

##### (5) Artificial Flaws

The artificial flaws introduced into the specimens by using a 19.6-N Knoop indentation (followed by surface grinding to remove the crater) decreased the average room-temperature fracture stress to 260 MPa (Fig. 5). At 1100°C, the strength of the indented specimens with an applied prestress of 195 MPa increased 55% to 400 MPa. This large strength increase may be attributed to flaw healing and flaw blunting, although the applied load during heatup tends to hold open the flaw and retard healing. After 10 h of annealing under the same conditions, the strength increased slightly to 430 MPa. The indented specimens which were statically loaded at 320 MPa ( $0.80K_c$ ) for 10 h were approximately 10% stronger than the annealed specimens. The average fracture stress was 480 MPa. All specimens fractured at the indentation cracks. This small 10% strength increase over the annealed specimens suggests that a stress-induced, microscopic strengthening process has blunted the sharp artificial flaw. Since the applied stress of 320 MPa during the static load tests is well below the stress needed for strengthening by macroscopic stress redistribution, the strength increase is related to localized blunting processes around the crack tip.

#### IV. Discussion

The strengthening process in siliconized silicon carbide containing 29 vol% of free silicon metal and 4 to 6  $\mu\text{m}$  SiC grains has been shown to be a time-, temperature-, and stress-dependent strengthening process. The strengthening process is caused by both a macroscopic and a microscopic process. On the macroscopic level, the strengthening process is due to stress redistribution in the bend bar through the nonlinear creep behavior of the material in four-point bending.<sup>9</sup> During stress redistribution, the maximum outer fiber stress decreased resulting in a strength increase when the bending beams were loaded to failure from the static load level. Residual stresses found in specimens which were statically loaded at elevated temperatures, unloaded, and fractured at room temperature also confirmed the macroscopic stress redistribution process to be operative at elevated temperatures. Both the residual tensile and compressive stresses were clearly shown in the specimens statically loaded at 1000°C. However, for the specimens statically loaded at 1100°C, the flaw population was modified by the formation of a high density of cavities. Therefore, the effects of the residual compressive stress could not be detected. The cavities formed at 1000°C had no apparent influence on residual compressive stress since they were small and isolated. Quantitative assessment of the magnitude of the residual stresses in these specimens is the subject of current research.

Cavity formation occurred only in the specimens statically loaded at the higher applied stress of  $0.80\sigma_y$ . This result indicates that the threshold stress for cavity formation is greater than  $0.50\sigma_y$ . The amount of permanent strain in the specimens statically loaded at the higher applied stress is greater than in the specimens statically loaded at lower applied stress level. The larger amount of permanent strain at the higher applied stress level is accommodated through cavity formation and may be responsible for the nonlinear creep behavior that produced the stress redistribution. Neither strengthening nor cavity formation occurred at the lower applied stress level which suggests a linear creep behavior. The permanent strain in these specimens is strictly due to accommodated plastic deformation. These results imply that the nonlinear creep behavior may be due to cavity nucleation and growth or, in other words, unaccommodated plastic deformation. If static load tests were conducted at applied stresses below the threshold for cavity formation, no strengthening through macroscopic stress redistribution would be expected. Experiments in pure tension are now being conducted to separate the effects of accommodated and unaccommodated (cavity-induced) plastic deformation.

Strengthening at the microscopic level was determined through artificial flaw tests. The results show that the indented specimens statically loaded for 10 h at 320 MPa ( $0.80K_L$ ) are approximately 10% stronger than the indented specimens annealed for 10 h. This strength increase suggests a localized blunting phenomena at the sharp crack tip when the material is under stress. The static load of 320 MPa is approximately equal to the applied stress which yielded no macroscopic strengthening during static load tests with natural flawed specimens. SEM examination has also confirmed the absence of cavity formation in these specimens after static loading. Since this applied stress is too low for macroscopic stress redistribution, the strength increase must be due to a localized blunting phenomena at the crack tip. This type of localized blunting can also have an effect on the  $K_L$  values determined by the SENB method.<sup>12</sup> The  $K_L$  of siliconized silicon carbide containing 29 vol% of free silicon metal and 4 to 6  $\mu\text{m}$  SiC grains has been shown to increase from a room temperature value of 2.95 to 5.00 and  $5.17 \text{ MPa} \cdot \text{m}^{1/2}$  at 1000° and 1100°C, respectively.<sup>13</sup> A similar increase was also observed by Fuller.<sup>14</sup> This increase in fracture toughness can be related to the localized blunting of the microscopic crack ahead of the saw notch.

Trantina<sup>7</sup> has tried to investigate this type of behavior with artificial flaws in another siliconized silicon carbide.<sup>7</sup> After annealing these specimens for 1 h at 1200°C, the strength of the indented specimens approached that of the original material. This strength increase occurred presumably because the flaws were not held open and probably healed during annealing. Indentation tests with siliconized silicon carbide containing 29 vol% of free silicon metal and 4 to 6  $\mu\text{m}$  SiC grains at 1300°C have shown a similar flaw healing behavior.<sup>15</sup> The strength of the indented specimens increased to approximately 90% of the initial strength with some of the specimens not fracturing at the indentation crack. In order to impede this flaw blunting behavior, a prestress of 195 MPa was applied to the indented specimens during furnace heatup. This stress produced an initial stress intensity of  $0.75K_L$  at the crack tip. With this prestress, strengthening still occurred probably by a combination of flaw blunting and flaw healing. Annealing of residual stresses probably did not contribute to this strength increase since the specimens were fractured almost immediately upon reaching test temperatures. The small strength increase after the 10 h of annealing at 1100°C may be due to annealing of residual stresses or localized flaw blunting caused by the prestress.

#### V. Summary

Both macroscopic stress redistribution and localized flaw blunting were found to contribute to the strengthening of siliconized silicon carbide under stress. Strengthening through macroscopic stress redistribution involved unaccommodated deformation processes which may have been responsible for the nonlinear creep behavior. No macroscopic strengthening is expected in this material below the threshold stress for cavity formation. Localized flaw blunting processes were also determined to be active through the artificial flaw tests that employed a prestress to prevent flaw healing. The sharp artificial cracks were blunted during static load tests at an applied stress significantly lower than the stress needed for macroscopic stress redistribution. This flaw blunting behavior was the result of localized deformation processes at the crack tip.

#### References

- <sup>1</sup>B. North and K. E. Kilchrist, "Effect of Impurity Doping on a Reaction-Bonded Silicon Carbide," *Am. Ceram. Soc. Bull.*, **60** [5] 549-52 (1981).
- <sup>2</sup>G. G. Trantina, "Design Techniques for Ceramics in Fusion Reactors," *Nucl. Eng. Des.*, **54** [1] 67-77 (1979).
- <sup>3</sup>G. C. Wei and V. J. Tennery, "Evaluation of Tubular Ceramic Heat Exchanger Materials in Residual Oil Combustion Environment," ORNL/TM-7578, March 1981.
- <sup>4</sup>C. W. Forrest, P. Kennedy, and J. V. Shennan; pp. 99-123 in *Special Ceramics*, Vol. 5. Edited by P. Popper. British Ceramic Research Association, Stoke-on-Trent, England, 1972.
- <sup>5</sup>M. K. Ferber and V. J. Tennery, "Evaluation of Tubular Ceramic Heat Exchanger Materials in Acidic Coal Ash from Coal-Oil-Mixture Combustion," ORNL/TM-7958, Dec. 1981.
- <sup>6</sup>R. E. Tressler, E. J. Minford, and D. F. Carroll; pp. 551-63 in *Creep and Fracture in Engineering Materials and Structures*, Part I. Edited by B. Wilshire and D. R. J. Owen. Pineridge Press, Swansea, U.K., 1984.
- <sup>7</sup>G. G. Trantina, "Strengthening and Proof Testing of Siliconized SiC," *J. Mater. Sci.*, **17**, 1487-92 (1982).
- <sup>8</sup>H. Cohn, G. Grathwohl, and F. Thummel; pp. 515-26 in *Creep and Fracture of Engineering Materials and Structures*, Part I. Edited by B. Wilshire and D. R. J. Owen. Pineridge Press, Swansea, U.K., 1984.
- <sup>9</sup>J. J. Petrovic, L. A. Jacobson, P. K. Tally, and A. K. Vasudevan, "Controlled Surface Flaws in Hot-Pressed Silicon Nitride," *J. Am. Ceram. Soc.*, **58** [3-4] 113-16 (1975).
- <sup>10</sup>W. Blumenthal and A. G. Evans, "Characterization of Cracks Subject to Creep"; presented at the International Symposium of Plastic Deformation of Ceramic Materials. The Pennsylvania State University, University Park, PA, July 30-22, 1983.
- <sup>11</sup>J. M. Lissell and G. S. Cherniak; pp. 525-26 in *Handbook of Engineering Fundamentals*, Third Ed. Edited by O. W. Eshbach and M. Souders. John Wiley & Sons, Inc., New York, 1975.
- <sup>12</sup>M. Srinivasan and R. H. Smoak, "Elevated Temperature Strength and Fracture Toughness Determination of Sintered Alpha Silicon Carbide"; presented at the International Conference on Fracture Mechanics in Engineering Applications. Bangalore, India, March 26-30, 1979.
- <sup>13</sup>D. F. Carroll, "Flaw Behavior in Siliconized Silicon Carbide at Elevated Temperatures Under Static Load"; M. S. Thesis. The Pennsylvania State University, May 1984.
- <sup>14</sup>E. R. Fuller; private communication.
- <sup>15</sup>D. F. Carroll; unpublished data.

## HIGH TEMPERATURE MECHANICAL PROPERTIES OF SILICONIZED SILICON CARBIDE COMPOSITES

D. F. Carroll, R. E. Tressler, Y. Tsai and C. Near

The Pennsylvania State University  
Department of Materials Science and Engineering  
University Park, PA 16802

### INTRODUCTION

Siliconized silicon carbide composites are candidate materials for ceramic components in gas turbines and heat exchangers (1,2). Properties which make these materials suited for these applications are good oxidation resistance, high thermal conductivity, low thermal expansion and adequate mechanical strength (1,3). Siliconized silicon carbide is a two-phase material whose microstructure consists of interpenetrating phases of silicon and silicon carbide. The silicon phase is dispersed throughout the continuous silicon carbide phase in either a continuous or non-continuous matrix, depending upon the amount of free silicon in the material.

Past investigations have revealed a strengthening phenomena in some types of siliconized silicon carbides during interrupted static load tests in bending at elevated temperatures (4-6). This strengthening phenomena has been attributed to either localized flaw blunting processes or macroscopic stress redistribution in the bending beam. Recently, Carroll and Tressler have shown both of these processes to be operative in a specific siliconized silicon carbide (7). Flaw blunting may result in strengthening through localized deformation processes around the crack tips of severe flaws in the material.

Strengthening through macroscopic stress redistribution during static load tests may also occur in a material that exhibits non-linear creep behavior or a different creep rate in tension than in compression. An analysis developed by Cohrt et al. enables the calculation of the stress redistribution process in a bend beam as a function of time (8). Figure 1 summarizes the stress redistribution process in a bending beam for a material that exhibits non-linear creep behavior only (i.e., the creep exponent ( $n$ ) is greater than one, while the ratio ( $S$ ) of the creep rate in tension to compression is equal to one). At time  $t=0$ , the initial applied stress is linear throughout the beam. As time progresses, the non-linear creep behavior of the material causes a redistribution of the stress in the beam. At  $t=t_1$ , the stress at the outer tensile and compressive fiber has decreased while the stress around the neutral axis has increased compared to the initial values. If the beam is loaded to failure at  $t=t_1$ , a strength increase would be observed due to the reduction of the outer fiber tensile stress. If the specimen is unloaded at  $t=t_1$ , a residual compressive stress would develop on the tensile surface while a residual

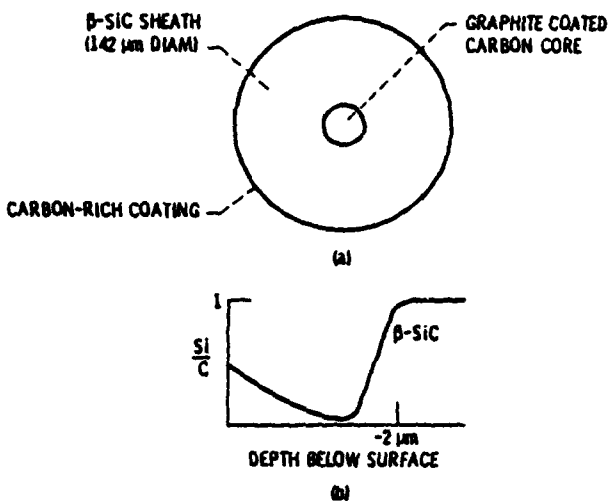
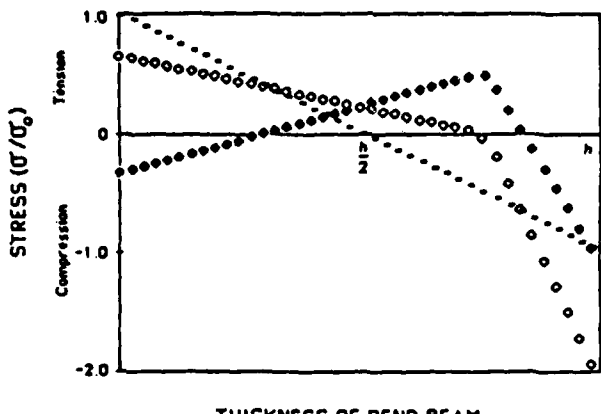


Figure 1. Stress redistribution in a four-point bend beam with time for a material which exhibits non-linear creep behavior only ( $n=2$ ,  $S=1$ ,  $\sigma =$  initial outer fiber tensile stress).  
 - initial stress distribution at  $t=0$ ,  
 ◦ stress distribution at  $t=t_1$ ,  
 ♦ residual stress distribution after unloading specimen  
 at  $t=t_1$

tensile stress would develop on the compressive side.

The stress redistribution process in a bend beam, when the material exhibits linear creep behavior ( $n=1$ ) and a creep rate in tension that is ten times greater than in compression ( $S=10$ ), is summarized in figure 2. Again, at time  $t=0$ , the initial stress distribution is linear throughout the bend beam. At time  $t=t_1$ , the stress redistribution process has again caused the outer fiber tensile stress to decrease. In contrast to the previous example, the outer fiber compressive stress has not decreased. The outer fiber compressive stress has increased compared to its initial value. The neutral axis has shifted from  $h/2$  toward the compressive side of the specimen. If at  $t=t_1$ , the specimen is loaded to failure, a strength increase would be observed due to the reduction of the outer fiber tensile stress. If the specimen is unloaded at  $t=t_1$ , a residual compressive stress would develop on both the tensile and compressive surfaces while a residual tensile stress would develop in the interior of the bend beam.

The purpose of this paper is to summarize the strengthening phenomena observed in two commercially available siliconized silicon carbides with significantly different volume fractions of silicon, during static load tests at elevated temperatures. The relative amount of strengthening in each material due to localized flaw blunting processes and macroscopic stress redistribution will also be discussed.



**Figure 2.** Stress redistribution in a four-point bend beam with time for a material which exhibits linear creep behavior and a creep ratio in tension ten times greater than in compression ( $n=1$ ,  $S=10$ ,  $\sigma =$  initial outer fiber tensile stress).  
 —○— initial stress distribution at  $t=0$   
 -○- stress distribution at  $t=t_1$   
 ● residual stress distribution after unloading specimen  
 at  $t=t_1$

#### EXPERIMENTAL PROCEDURE

The two commercially available siliconized silicon carbide materials investigated in this study were designated A and B.\* The material specifications are summarized in table I. Material A is composed of 4-6 micron SiC grains and approximately 29 volume percent free silicon in a continuous matrix. Material B contains a bimodal distribution of 10 and 100 micron SiC grains with 15 volume percent free silicon dispersed throughout the continuous SiC network. The densities of material A and B were 2.95 and 3.08 g/cc, respectively.

Bend beams of material A were cut from billets using a diamond saw. The major faces were ground parallel with a 600 grit diamond wheel. The approximate specimen dimensions were 25 by 2.5 by 2.5 mm. The edges forming the tensile plane were bevelled by hand with 600 grit SiC grinding paper to remove any edge checking flaws. In all cases, the bend beams were proof tested at 495 MPa to narrow the strength distribution. This proof stress yielded a survival rate of 70%.

The as-received material B was precut into specimens with approximate dimensions of 76.2 by 7.6 by 6.3 mm. The tensile and compressive surfaces were finished to 320 grit while the other two faces were finished to 150 grit. The edges which formed the tensile plane in these specimens were bevelled using a 15 micron diamond wheel. Since these specimens exhibited a narrow starting strength distribution, proof testing was not necessary to

\* Material A - KX01, Sohio Engineered Materials Co., Niagara Falls, NY  
 Material B - NC630, Norton Co., Worcester, MA

Table 1. Description of material characteristics

Material	SiC Grain Size	Volume % Silicon	Density (g/cc)
A	4-6 $\mu\text{m}$	29	2.95
B	Bimodal 10 $\mu\text{m}$ 100 $\mu\text{m}$	15	3.08

apply the technique described by Tressler et al. (4). Smaller specimens were also cut and machined from these specimens to dimensions similar to that of material A.

The fracture toughnesses of these specimens were determined as a function of temperature using the single edge notch beam technique (9). An argon environment was used during the fracture toughness tests at elevated temperatures. The notched specimens were fractured in four-point bending using a crosshead speed of 0.25 cm/min.

The strength distributions of the siliconized silicon carbides were determined as a function of temperature in four-point bending. The inner and outer span dimensions of the knife edges used for the A specimens were 4.76 and 19.05 mm, respectively. The knife edge dimensions used for the B specimens were 12.7 and 50.8 mm, respectively. A crosshead speed of 0.25 cm/min was used for all fracture tests.

In order to observe the strengthening phenomena in these two siliconized silicon carbides under stress, interrupted static load tests were conducted at temperatures between 1000 and 1300°C for times up to 50 hours. The applied stress levels during static loading varied from 0.50 to 0.80  $\sigma_f$ , where  $\sigma_f$  is the average fracture stress of the material at test temperature. A summary of the static loading conditions is shown in table 2. At the end of the static load time, the specimens were fractured at test temperature by rapidly loading from the static load level.

Some of the specimens, after static loading, were not fractured at the end of the static load time, but were unloaded and cooled to room temperature. By fracturing these specimens with either the original tensile or compressive surface in tension, the existence of residual stresses was determined by comparing the resulting strengths to those in the initial distribution. If a residual compressive stress exists on the tensile surface of the specimen and either a residual tensile or compressive stress exists on the compressive surface, strengthening through macroscopic stress redistribution as described by Cohrt et al. has occurred (8). The smaller B specimens were used in this phase of the investigation.

In order to attempt to separate the strengthening contributions of localized flaw blunting and macroscopic stress redistribution, a series of artificial flaw experiments were conducted. Large artificial flaws were introduced into specimens using the controlled flaw technique (10). A 19.6 and 88.2 N Knoop indentation was used to produce artificial surface cracks in the A specimens and the smaller B specimens. The larger indentation load was necessary for the B material so that the artificial flaws would be larger than the inherent flaws in the material. After indenting, the crater was removed by grinding the surface to eliminate residual stresses.

Table 2. Summary of static load conditions used in this investigation

Material	Temperature (°C)	Static Load Stress	Time of Static Load (hrs)
A	1000	0.50 $\sigma_f$	2
	1100	0.80 $\sigma_f$	10
B	1300	0.50 $\sigma_f$	4
		0.75 $\sigma_f$	16
			50

The resulting strength distributions of the indented A specimens were determined at room temperature, 1100°C in argon and 1100°C in argon after a 10 hour anneal. During furnace heat-up to 1100°C, a prestress of 0.75  $\sigma_{fI}$ , where  $\sigma_{fI}$  is the average room temperature strength of the indented specimens, was applied to prevent flaw healing (11). Indented A specimens were then static loaded for 10 hours in argon at an applied stress of 0.80  $\sigma_{fI}'$ , where  $\sigma_{fI}'$  is the average fracture stress of the indented specimens at 1100°C. The strength distributions of the indented B specimens were determined at room temperature and 1300°C in argon. A prestress of 0.50  $\sigma_{fI}$  was used during furnace heat-up to help prevent flaw healing. Four hour static load tests of the indented B specimens were also conducted at 1300°C using applied stresses of 0.50 and 0.75  $\sigma_{fI}'$ .

## RESULTS AND DISCUSSION

### Fracture Toughness

The fracture toughnesses of materials A and B as a function of temperature are summarized in figure 3. At room temperature, where the silicon is not as tough as silicon carbide, material A has the lower toughness due to its higher silicon content. The fracture toughnesses at room temperature for materials A and B are on the average 2.95 and 3.73 MPa.m<sup>0.5</sup>, respectively. As temperature is increased, the fracture toughness of material A increases sharply while the toughness for material B decreases slightly. The increase in fracture toughness of material A is due to the free silicon phase which is ductile at these temperatures. The silicon phase (29 volume percent) in material A forms a continuous matrix. The plastic strain capabilities of the ductile matrix are responsible for the increase in fracture toughness. A similar increase in toughness with temperature of material A was reported by Chuck et al. (12). There was no increase observed in the fracture toughness of material B at elevated temperatures even though this material contains 15 volume percent free silicon. The fracture toughness of this material is controlled by the rigid SiC network. During processing, the rigid SiC network is formed during the refire step which partially sinters the SiC structure (13). The molten silicon is then infiltrated into this porous structure reacting with the free carbon to form SiC. The remaining pores are then filled with silicon. The resulting silicon phase is located in pockets throughout the SiC network forming a semi-continuous matrix. The deformation capabilities of the silicon are restricted by the SiC network. Therefore, the fracture toughness does not change dramatically with temperature. The fracture toughness of material B as a function of temperature, reported by Fuller, is shown to remain relatively constant for a displacement rate of 0.05

cm/min (14). However, his results did show a slight increase in toughness with temperature when a much slower displacement rate,  $5 \times 10^{-4}$  cm/min, was used. This result suggests that the higher displacement rate, 0.25 cm/min, used in the present work does not allow sufficient time for silicon deformation to have an effect on the fracture toughness.

#### Strengthening Behavior During Static Load Tests

The results of the static load tests as a function of time for materials A and B are summarized in figure 4. Material A was static loaded at  $0.80 \sigma_f$  (480 MPa) at  $1000^\circ\text{C}$  and  $1100^\circ\text{C}$  for 2 and 10 hours while material B was static loaded at  $0.75 \sigma_f$  (170 MPa) at  $1300^\circ\text{C}$  for 4, 16 and 50 hours. Both materials exhibit an increase in strength with time of static loading. The increase in strength in material A is larger than that observed in material B. For example, after two hours of static loading at

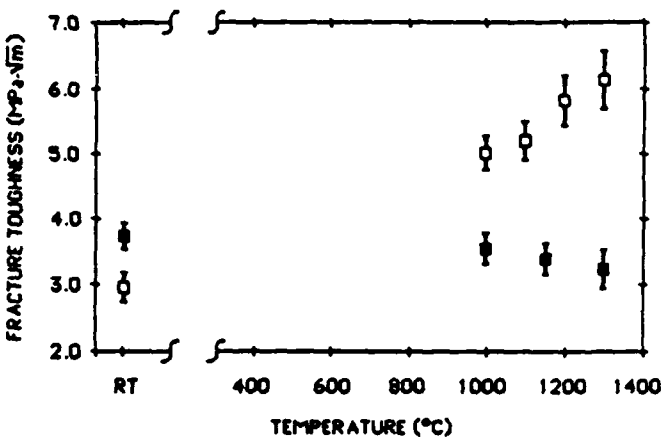


Figure 3. Fracture toughnesses versus temperature for materials A (□) and B (■) determined using the notched-beam method.

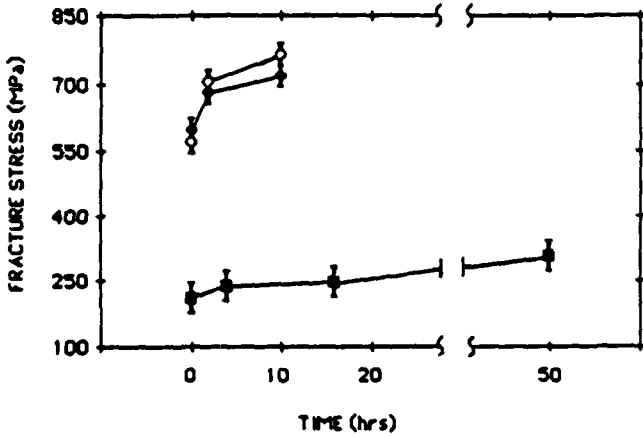


Figure 4. Fracture stress of material A after static loading at  $0.80 \sigma_f$  for 2 and 10 hours at  $1000^\circ\text{C}$  (◆) and  $1100^\circ\text{C}$  (◇) and material B after static loading at  $0.75 \sigma_f$  for 4, 16 and 50 hours at  $1300^\circ\text{C}$  (■).

an applied stress of  $0.80 \sigma_f$  at  $1100^\circ\text{C}$ , the average fracture stress of material A increased 19% from 570 to 680 MPa. The average fracture stress of material B after static loading 4 hours at  $0.75 \sigma_f$  increased 14% from 208 to 238 MPa. The amount of strengthening, initially large for both materials at shorter static load times, tends to approach a limiting value at longer times. Strengthening in material B under stress at elevated temperatures has also been reported by Trantina (5). His results have shown a similar time dependent strength increase at  $1200^\circ\text{C}$  under a stress equivalent to 86% of the baseline strength.

A temperature dependence of the strengthening phenomenon is also observed in material A by comparing the results at  $1000$  and  $1100^\circ\text{C}$ . This dependence is more evident after 10 hours of static loading where the average fracture stress at  $1000$  and  $1100^\circ\text{C}$  increased 20 and 27%, respectively, over their initial distributions.

The stress dependence of the strengthening phenomenon during static loading is summarized in figure 5. The results show no observable strength increase after static loading at  $0.50\sigma_f$  for 10 hours at  $1000$  and  $1100^\circ\text{C}$  for material A and for 16 hours at  $1300^\circ\text{C}$  for material B. However, a strength increase was observed after static loading for the same times and temperatures under a higher applied stress of  $0.80 \sigma_f$  and  $0.75 \sigma_f$  for material A and B, respectively. Again, material A exhibits a larger strength increase under the higher applied stress for shorter static load times. These results indicate that a time, temperature and stress dependent strengthening process exists in both materials A and B.

#### Permanent Deformation

The amount of permanent deformation in A and B specimens was determined by measuring the outer fiber strains of specimens which were unloaded after static loading. The permanent strains measured for the various test conditions are summarized in figure 6. The results show that material A experienced more deformation than material B under the higher applied stress levels. The permanent strain in the A specimens after static loading at  $1000$  and  $1100^\circ\text{C}$  for 10 hours at  $0.80 \sigma_f$  was 1.8 and 2.7%, respectively. The permanent strain in the B specimens after static

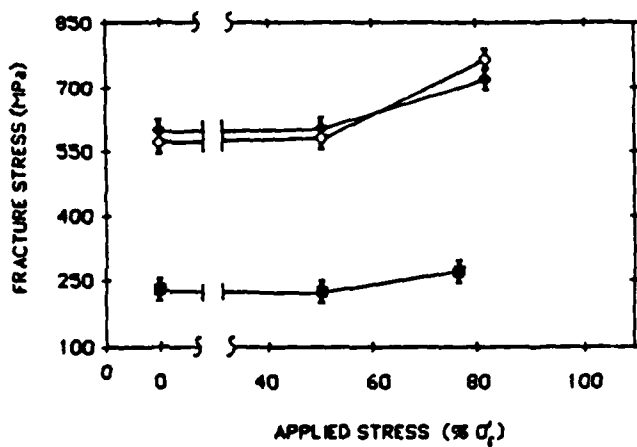


Figure 5. Fracture stress of material A after static loading at  $0.50$  and  $0.80 \sigma_f$  for 10 hours at  $1000$  ( $\blacklozenge$ ) and  $1100^\circ\text{C}$  ( $\lozenge$ ) and material B after static loading at  $0.50$  and  $0.75 \sigma_f$  for 16 hours at  $1300^\circ\text{C}$  ( $\blacksquare$ ).

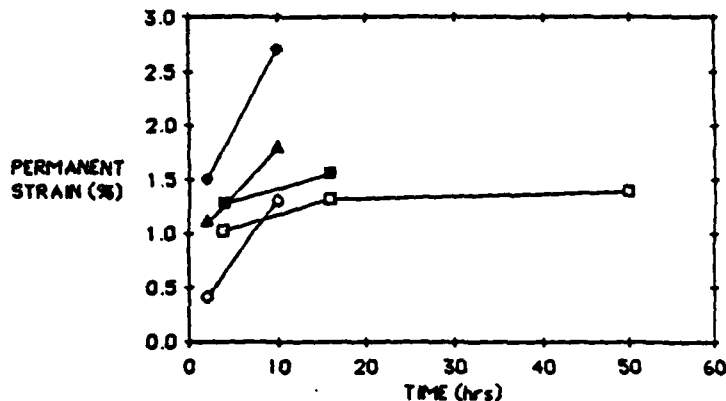


Figure 6. Permanent strains in material A after static loading at  $0.50$  and  $0.80 \sigma_f$  for 2 and 10 hours at  $1000$  and  $1100^\circ\text{C}$  and material B after static loading at  $0.50$  and  $0.75 \sigma_f$  for 4, 16 and 50 hours at  $1300^\circ\text{C}$ .

- material A,  $0.50 \sigma_f$ ,  $1100^\circ\text{C}$
- △ material A,  $0.80 \sigma_f$ ,  $1000^\circ\text{C}$
- ◆ material A,  $0.80 \sigma_f$ ,  $1100^\circ\text{C}$
- material B,  $0.50 \sigma_f$ ,  $1300^\circ\text{C}$
- material B,  $0.75 \sigma_f$ ,  $1300^\circ\text{C}$

loading at  $0.75 \sigma_f$  for 16 hours at  $1300^\circ\text{C}$  was 1.55%. The larger amount of deformation in material A is due to higher silicon content. At the lower applied static load level of  $0.50 \sigma_f$ , the A specimens exhibited approximately the same amount of deformation after static loading for 10 hours at  $1100^\circ\text{C}$ , as the B specimens after static loading for 16 hours at  $1300^\circ\text{C}$ .

#### Cavity Formation

Polished tensile surfaces of unbroken static loaded specimens were examined for microstructural rearrangement by scanning electron microscopy. This examination revealed formation of cavities in the A and B specimens static loaded under the higher applied stress of  $0.80 \sigma_f$  and  $0.75 \sigma_f$ , respectively. The cavities were non-uniformly distributed throughout the tensile plane in regions of locally high SiC content (figures 7a, 7b). The size and density of cavities in both materials were proportional to the time and temperature of static loading. There was little evidence of coalescence or linkage of these cavities for the conditions studied in this investigation. Material A generally contained more cavities than material B at correspondingly larger permanent strains. The permanent strains obtained at these stress levels for both materials is accommodated through cavity formation and matrix deformation. Cavity formation was not observed in either the A or B specimens at the lower static load level of  $0.50 \sigma_f$ . The absence of cavities suggests a threshold stress or strain for cavity formation. The permanent strains at the lower applied stress level is apparently accommodated completely by matrix deformation.

#### Residual Stresses

In order to examine the possibility of macroscopic stress redistributions as a cause of strengthening during static loading, specimens were static loaded at the high applied stress levels, unloaded and fractured at room temperature. The data collected by fracturing the A and B specimens with

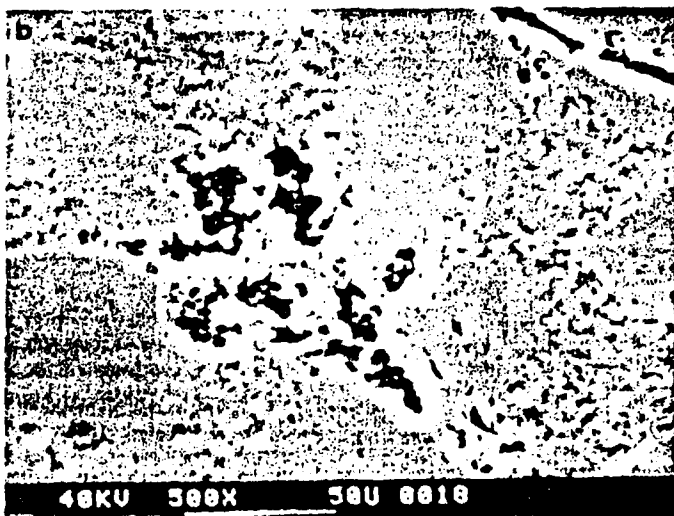


Figure 7. SEM micrographs of polished tensile surfaces of, 7a) material A, static loaded at  $0.80 \sigma_f$  for 10 hours at  $1100^\circ\text{C}$ , and 7b) material B, static loaded at  $0.75 \sigma_f$  for 16 hours at  $1300^\circ\text{C}$ .

the original tensile surface in tension and the original compressive surface in tension are shown in figures 8 and 9. Material A results are for specimens initially static loaded at  $0.80 \sigma_{fI}$  for 2 hours at  $1000^{\circ}\text{C}$ . Material B results are for specimens static loaded at  $0.75 \sigma_{fI}$  for 4 hours at  $1300^{\circ}\text{C}$ . Both materials exhibited a residual compressive stress in the specimens fractured with the original tensile surface in tension. The compressive stress produces an increase in strength from the initial distributions. The residual compressive stress is larger in material A than in material B. For the specimens fractured with the original compressive surfaces in tension, the resulting strengths decreased for both materials as compared to the initial distribution. The strength decrease is attributed to a residual tensile stress. The residual tensile stress is larger in the A specimens than in the B specimens. The existence of these residual stresses after static loading suggests that the type of strengthening described by Cohrt et al. may be operative (8). Since the residual stresses are larger in the A specimens, the stress redistribution process may occur more readily in this material than in material B. This result is expected since the A specimens exhibited more permanent deformation than the B specimens. The larger amount of permanent strain in material A indicates a higher creep rate which would result in a faster stress redistribution process.

#### Artificial Flaw Tests

Strengthening on the microscopic level through localized flaw blunting processes was investigated using artificial flaw tests. The results for material A are summarized in table 3. The 19.6 N Knoop indentation (followed by surface grinding to remove the crater) decreased the average room temperature strength to 260 MPa. At  $1100^{\circ}\text{C}$ , the strength of the indented specimens with an applied prestress of  $0.75 \sigma_{fI}$  (195 MPa) increased to 400 MPa. This large increase may be attributed to flaw blunting or healing, although the applied prestress during furnace heatup tends to hold open the flaw and retard healing. Annealing of residual stresses probably did not contribute much to this increase since the specimens were fractured almost immediately upon reaching test temperature. After 10 hours annealing under the same condition, the strength increased slightly to 430 MPa. This small strength increase may be due to annealing of residual stresses or localized flaw blunting caused by the prestress. The indented specimens static loaded at  $0.80 \sigma_{fI}$  (320 MPa) for 10 hours at  $1100^{\circ}\text{C}$  were approximately 10% stronger than the annealed specimens. The average fracture stress was 480 MPa. All specimens tested under these conditions fractured at the indentation cracks. The average fracture stress after 10 hours of static loading was still less than the as-received  $1100^{\circ}\text{C}$  strengths. The small 10% strength increase over the annealed specimens suggests that a stress induced microscopic strengthening process has blunted the sharp artificial flaws. Since the applied stress of 320 MPa is well below that needed for strengthening by macroscopic stress redistribution, the strength increase is related to localized blunting processes around the crack tip. Since the 10% strength increase is less than the 27% strength increase observed in proof tested A specimens static loaded at  $0.80 \sigma_{fI}$  for 10 hours at  $1100^{\circ}\text{C}$ , the dominant strengthening process in this material is macroscopic stress redistribution.

The results for the artificial flaw tests in material B are summarized in table 4. The 88.2 N Knoop indentation (after surface grinding to remove the crater) reduced the average room temperature fracture stress to 180 MPa. At  $1300^{\circ}\text{C}$ , the strength of the indented specimens under an applied prestress of  $0.50 \sigma_{fI}$  (90 MPa) increased to 240 MPa. All of these specimens fractured at the indentation cracks. The indented specimens static loaded at  $0.50$  and  $0.75 \sigma_{fI}$  exhibited a significant amount of strengthening. Only 2 out of 10 specimens static loaded at  $0.50 \sigma_{fI}$  failed at the indentation cracks, while at  $0.75 \sigma_{fI}$ , none of the specimen

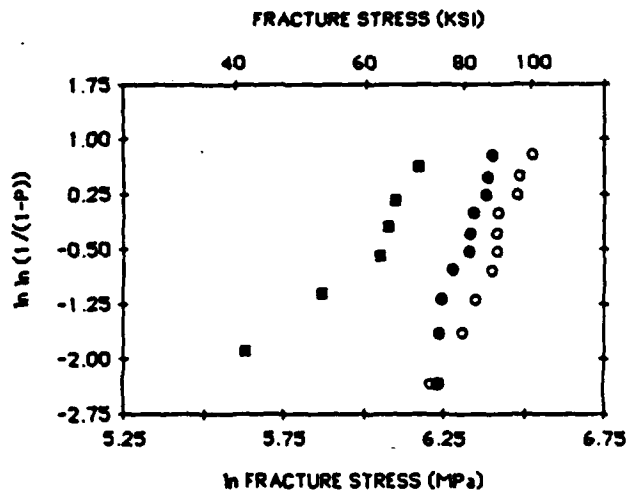


Figure 8. Strength distributions of material A, static loaded at  $0.80 \text{ c}_f$  for 2 hours at  $1000^\circ\text{C}$ , unloaded and fractured at room temperature.

- initial room temperature distribution
- fractured with original tensile surface in tension
- fractured with original compressive surface in tension

~~live program  
mation of  
included  
3 closely  
ume, the  
Science  
results of  
x of in-~~

~~y leading  
key cover  
chapters  
nation of  
, ternary  
38, cover-  
s or point  
sing de-  
sider ox-  
id super-  
al papers  
ep crack  
research  
valuable  
ceramic~~

~~formation  
addition  
fields of  
science,  
hy.~~

1719

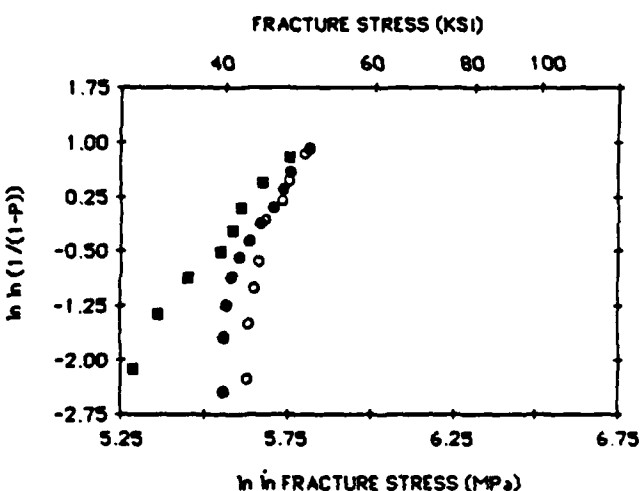


Figure 9. Strength distributions of material B, static loaded at  $0.75 \text{ c}_f$  for 4 hours at  $1300^\circ\text{C}$ , unloaded and fractured at room temperature

- initial room temperature
- fractured with original tensile surface in tension
- fractured with original compressive surface in tension

Table 3. Summary of the average fracture stresses of indented material A specimens at room temperature and at 1100°C after annealing and static loading.

Temperature	Description	Samples Tested	Samples Fractured at Indent	Average Indented Strength (MPa)
Room	No indentation	10	-	570 ± 40
1100°C	No indentation	10	-	600 ± 40
Room	Indentation	10	10	260 ± 15
1100°C	Indentation No static load	5	5	400 ± 30
1100°C	Indentation 10 hour anneal No static load	5	5	430 ± 20
1100°C	Indentation 10 hour static load at 0.80g <sub>fl</sub>	5	5	480 ± 25

Table 4. Summary of the average fracture stresses of indented material B specimens at room temperature and at 1300°C before and after static loading.

Temperature	Description	Samples Tested	Samples Fractured at Indent	Average Indented Strength (MPa)
Room	No indentation	10	-	285 ± 25
Room	Indentation	10	10	180 ± 15
1300°C	Indentation No static load	5	5	240 ± 5
1300°C	Indentation 4 hour static load at 0.50g <sub>fl</sub>	10	2	320 ± 5
1300°C	Indentation 4 hour static load at 0.75g <sub>fl</sub>	10	0	-----

failures occurred at the indentation cracks. It is postulated that even with a prestress of  $0.50 \sigma_{fI}$  to hold open the flaw, strengthening occurred by a combined effect of flaw blunting and healing. This strength increase may also be complicated by annealing of residual stresses that may have been present after crater removal. Since none of the specimens failed at the indentation cracks under the higher applied stress of  $0.75 \sigma_{fI}$ , compared to 2 specimens at  $0.50 \sigma_{fI}$ , a stress induced flaw blunting process must be operative in this material and is apparently the dominant strengthening process under the present experimental conditions.

#### Summary of the Strengthening Phenomenon

Both materials exhibited a time, temperature and stress dependent strengthening process. This strengthening process occurs on both the macroscopic and microscopic levels. Macroscopic strengthening occurs through stress redistribution in the bend beam. This effect was confirmed by the presence of residual stresses found in specimens unloaded after static loading at the high applied stress levels. The larger residual stresses in the A specimens indicates that the stress redistribution process dominates in material A while playing a lesser role in material B. From the results of the artificial flaw tests, both materials exhibited microscopic flaw blunting behavior. Flaw blunting processes in the indented A specimens produced a 10% strength increase after static loading at  $0.80 \sigma_{fI}$  for 10 hours at  $1100^{\circ}\text{C}$ . In comparison, the fracture stress of proof tested A specimens static loaded at  $0.80 \sigma_f$  for 10 hours at  $1100^{\circ}\text{C}$  increased 27%. The 27% strength increase in the proof tested specimens suggests that microscopic stress redistribution is the dominant strengthening process in the A material.

The artificial flaw tests with material B have shown a significant amount of strengthening after static loading for four hours at  $0.50$  and  $0.75 \sigma_{fI}$ . Only 2 of the 10 specimens static loaded at  $0.50 \sigma_{fI}$  failed at the indentation cracks. At the higher static load level of  $0.75 \sigma_{fI}$ , no specimen failures occurred at the indentation cracks due to a dominant flaw blunting process. A 14% strength increase was observed in the as-received B specimens after static loading at  $0.75 \sigma_f$  for four hours. Since the residual stresses were relatively small in similar specimens which were unloaded after static loading and fractured at room temperature, localized flaw blunting processes must be the dominant strengthening process in the material. This conclusion is based upon the large strengthening increment observed in the static load tests with indented B specimens. In future work, strengthening due to localized flaw blunting processes without the contribution of macroscopic stress redistribution will be determined during static load tests in pure tension.

#### ACKNOWLEDGEMENTS

The authors thank the Exxon Engineering and Research Company and the Electric Power Research Institute for their support.

#### REFERENCES

1. B. North and K. E. Kilchrist, "Effect of Impurity Doping on a Reaction-Bonded Silicon Carbide," *Am. Ceram. Soc. Bull.*, 60 (5), 549-52 (1981).
2. G. C. Wei and V. J. Tennery, "Evaluation of Tubular Ceramic Heat Exchanger Materials in Residual Oil Combustion Environments," ORNL/TM-7578, March 1981.

3. C. W. Forrest, P. Kennedy and J. V. Shennan, pp. 99-123 in Special Ceramics Vol. 5, Edited by P. Popper, British Ceramic Research Association, Stoke-on-Trent, England, 1972.
4. R. E. Tressler, and E. J. Minford and D. F. Carroll, pp. 551-563 in Creep and Fracture of Engineering Materials and Structures, Part I, Edited by B. Wilshire and D.R.J. Owen, Pineridge Press, Swansea, U.K., 1984.
5. G. C. Trantina, "Strengthening and Proof Testing of Siliconized Silicon Carbide," J. Mater. Sci., 17 1487-92 (1982).
6. H. Cohrt, G. Grathwohl and F. Thummel, pp. 515-526 in Creep and Fracture of Engineering Materials and Structures, Part I, Edited by B. Wilshire ad D.R.J. Owen, Pineridge Press, Swansea, U.K., 1984.
7. D. F. Carroll and R. E. Tressler, "Time Dependent Strength of Siliconized Silicon Carbide Under Stress at 1000 and 1100°C," J. Am. Ceram. Soc., 68 (3), 143-146 (1985).
8. H. Cohrt, G. Grathwohl and F. Thummel, "Non-Stationary Stress Distribution in a Ceramic Bending Beam During Constant Load Creep," Res. Mechanica, 10 55-71 (1984).
9. M. Srinivasan and R. H. Smak, "Elevated Temperature Strength and Fracture Toughness Determination of sintered Alpha Silicon Carbide," presented at the International Conference on Fracture Mechanics in Engineering Applications, Bangalore, India, March 26-30 (1979).
10. J. J. Petrovic, L. A. Jacobson, P. K. Tally and A. K. Vasudera, "Controlled Surface Flaws in Hot-Pressed Silicon Nitride," J. Am. Ceram. Soc., 58 (3-4), 113-116 (1975).
11. W. Blumenthal and A. G. Evans, "Characterization of Cracks Subjected to Creep," pp. 555-572 in Deformation of Ceramic Materials II, Edited by R. E. Tressler and R. C. Bradt, Plenum Press, New York, NY, 1984.
12. L. Chuck and E. R. Fuller, "Fracture Behavior of a Siliconized Silicon Carbide at Elevated Temperatures," presented at the Fourth International Symposium on the Fracture Mechanics of Ceramics, Blacksburg, VA, June 19-21 (1985).
13. G. Q. Weaver and B. A. Olson, "Process for Fabricating Silicon Carbide Articles," U. S. Patent #4,019,913, April 26, 1977.
14. E. R. Fuller, private communication.

## On the Static Fatigue Limit at Elevated Temperatures

TZE-JER CHUANG

Institute for Materials Science and Engineering, National Bureau of Standards, Gaithersburg, MD 20899 (U.S.A.)

RICHARD E. TRESSLER

Department of Materials Science and Engineering, Pennsylvania State University, University Park, PA 16802 (U.S.A.)

ERIC J. MINFORD

United Technologies Research Center, East Hartford, CT 06108 (U.S.A.)

(Received August 26, 1985; in revised form January 23, 1986)

### ABSTRACT

The static fatigue limit, defined as the stress level below which prolonged service life is expected, is derived first from irreversible thermodynamics and found to be sensitive to kinetics. Existing theories of crack growth based on distinct mechanisms are summarized and discussed to give various values of the predicted static fatigue limit. Data for the static fatigue limit measured from  $\alpha$ -SiC bend bar specimens tested at 1200 °C are compared with those theoretical predictions. The results suggest that, for structural ceramics crept at elevated temperatures, diffusive crack growth along the grain boundary dominates the static fatigue process and provides the fundamental level for the static fatigue limit. Other factors such as plasticity and microstructural inhomogeneities are held responsible for the higher static fatigue limit of any real system.

### 1. INTRODUCTION

This paper is concerned with the static fatigue limit of structural ceramic materials at elevated temperatures. The static fatigue limit is defined as the level of applied stress below which a prolonged service life is expected. Examination of static fatigue data for many materials shows the existence of this behavior. Hence there is a growing interest for material design purposes to measure and predict the static fatigue limit of materials in order to avoid premature failure within the design life.

In the present paper the study is undertaken from theoretical approaches. We shall make a major premise that crack growth is the primary fracture mode. Other modes of fracture such as necking-down or void generation and linkage thus are not considered for the present study. Because of their brittle nature, the grains of ceramic materials deform elastically even at high temperatures, although mass transport may be active at internal surfaces and grain interfaces. Hence, in this paper we shall not consider other types of deformation behavior such as viscoelasticity [1] and time-dependent plasticity which are significant in metal and alloy systems and which may be important for ceramics in some service conditions at very high temperatures. This restriction means that the threshold stress intensity  $K_{th}$  is directly related to the static fatigue limit under these circumstances because applied stress is in direct proportion to the stress intensity for the crack.

We begin by presenting the basic definition of the threshold stress intensity factor in the context of irreversible thermodynamics. It will be shown that  $K$  is in direct proportion to the square of the well-known strain energy release rate and  $K_{th}$  is sensitive to the detailed kinetic mechanisms of crack growth. Hence, in Section 3, we summarized existing theories that are available in the literature which are representative of various kinetic laws of crack growth. Experimental data on  $K_{th}$  of  $\alpha$ -SiC are used to verify the theoretical predictions. The differences are interpreted in terms of complications in the real systems including

size effects, configuration, interface structure, inhomogeneity etc.

## 2. IRREVERSIBLE THERMODYNAMICS

Let us consider an elastic solid containing a crack of length (or area in three dimensions)  $a$ . Let the crack be propagated by an incremental amount  $da$  to  $a + da$ ; then the well-known energy release rate  $G$  is defined by

$$G = - \frac{dP}{da} \quad (1)$$

where  $P$  is the total potential energy of the solid and is given by the following expression:

$$P = F_e - W \quad (2)$$

where  $W$  is the total external work done by the loading device and  $F_e$  is the total strain energy stored in the body.

Dividing both sides of eqn. (1) by a time increment  $dt$  and substituting  $P$  from eqn. (2) we obtain

$$Gu = \dot{W} - \dot{F}_e \quad (3a)$$

where  $v$  is the crack tip velocity and the dot denotes total derivative with respect to time (e.g.  $\dot{W} \equiv dW/dt$ ).

Now, from the first law of thermodynamics, it can be shown [2] that, under isothermal conditions,

$$\dot{F} = \dot{W} - \dot{\Lambda} \quad (3b)$$

where  $F = U - TS$  is the total Helmholtz free energy, and  $U$ ,  $T$  and  $S$  are the total internal energy, the absolute temperature and the entropy respectively;  $\dot{\Lambda}$  is the time rate of dissipative work resulting in total internal entropy production and, according to the second law of thermodynamics,  $\dot{\Lambda} > 0$ .

As  $F = F_e + F_i$ , where  $F_i$  is the total interfacial (internal and external) free energy, combination of eqns. (3a) and (3b) then gives

$$G = f_s + \eta \quad (4)$$

where  $f_s = dF_i/da$  and  $\eta = d\Lambda/da$  are the interfacial and dissipative energies per unit length (area) of crack growth respectively. Depending on the location of the crack, there are two expressions for  $f_s$ : for transgranular cracks,

$$f_s = 2\gamma_s \quad (5a)$$

and, for intergranular cracks,

$$f_s = 2\gamma_s - \gamma_{gb} \quad (5b)$$

where  $\gamma_s$  and  $\gamma_{gb}$  are the surface free energy per unit area and the grain boundary free energy per unit area respectively. Equation (5b) results from the fact that creation of a unit area of an intergranular crack leads to reduction of the grain boundary by the same area.

Now, for an elastic crack under plane strain conditions, the stress intensity  $K$  is related to  $G$  through the well-known Irwin relationship

$$G = \frac{(1 - \nu^2)K^2}{E} \quad (6)$$

or

$$K = \left( \frac{E}{1 - \nu^2} \right)^{1/2} G^{1/2} \quad (6)$$

where  $E$  is Young's modulus and  $\nu$  Poisson's ratio.

The threshold stress intensity  $K_{th}$  is then defined by the minimum value of  $K$ , or

$$K_{th} = \min \left\{ \left( \frac{E}{1 - \nu^2} \right)^{1/2} [f_s + \eta]^{1/2} \right\} \quad (7)$$

This equation clearly indicates that from the standpoint of non-equilibrium thermodynamics, apart from  $\eta$ ,  $K_{th}$  is only a function of the material's intrinsic properties such as the specific surface free energy and the elastic moduli of matrix. Other geometric factors such as crack shape, length or stress concentration are not involved. Further, because eqn. (7) contains  $\eta$  which is sensitive to kinetics of crack growth, the level of  $K_{th}$  is therefore strongly dependent on the operating mechanisms which activate the crack growth processes. In the following section therefore the representative crack growth models based on various kinetic laws are summarized.

## 3. KINETIC LAWS

As discussed in Section 2, the static fatigue limit is strongly influenced by the growing process of the crack responsible for catastrophic failure. Thus there is a need to discuss all possible kinetic laws for crack growth in order to understand quantitatively the predicted  $K_{th}$ .

TABLE 1  
Predictions of  $K_{th}$  at 1200 °C for SiC based on existing crack growth models

Model	Predicted $K_{th}$	Predicted $V_{th}$	Predicted $K_{th}$ (MPa m <sup>1/2</sup> )		
			Hot-pressed α-SiC	Oxidized sintered α-SiC	As-machined sintered α-SiC
Griffith	$\left(\frac{8M^2}{\pi^2} E \gamma_s\right)^{1/2}$	Zero	0.356	0.334	0.518
Lawn and Wilshaw	$\left(\frac{2E\gamma_s}{1-\nu^2}\right)^{1/2}$	Zero	0.546	0.515	0.798
Charles and Hillig	$\left(\frac{3M^2}{2\pi} E \gamma_s\right)^{1/2}$	Finite	0.273	0.257	0.398
Hasselman	$\left(\frac{8M^2}{\pi^2} EN \Delta H\right)^{1/2}$ <sup>a</sup>	Zero	0.838	0.789	0.789
Dutton	$\left\{\frac{8M^2}{\pi(1-\nu^2)} E \gamma_{gb}\right\}^{1/2}$	Zero	0.634	0.599	0.928
Chuang	$1.69 \left\{\frac{E(2\gamma_s - \gamma_{gb})}{1-\nu^2}\right\}^{1/2}$	Finite	1.271	1.201	0.954
Hull and Rimmer	$2M \left(\frac{c}{\pi}\right)^{1/2} \left(p + \frac{2\gamma_{gb}}{\rho}\right)$	Zero	8.266	4.464	12.819
Lange	$\frac{8M}{du} \left(\frac{c}{\pi}\right)^{1/2} \gamma_s$	Zero	2.066	1.116	5.127
Experimental results			$2.25 \pm 0.1$	$1.75 \pm 0.15$	$2.25 \pm 0.25$

<sup>a</sup> $N = 4 \times 10^{19}$  atoms m<sup>-2</sup>;  $\Delta H = 26$  kJ mol<sup>-1</sup>.

Table 1, taken directly from ref. 3, tabulates a collection of eight existing crack growth theories from the literature. To aid discussion, we have classified them in four separate groups based on the distinct built-in kinetic law.

The classical Griffith crack model in its original form envisages an unstable equilibrium state for the cracked body and injects an energy criterion such that the reduction in strain energy resulting from crack extension goes to supply the energy required for creation of new crack surfaces. For a plane strain elastic crack in mode I, linear elasticity theory predicts a singular normal stress

$$\sigma(x) = \frac{K_I}{(2\pi x)^{1/2}}$$

at a distance  $x$  from the crack tip, and a displacement  $u(x)$  normal to the crack plane as

$$u(x) = \frac{4(1-\nu^2)K_I(\Delta a - x)^{1/2}}{E(2\pi)^{1/2}}$$

where  $\Delta a$  is the increment in crack length. The total strain energy reduction due to  $\Delta a$  is

$$-\frac{1}{2} \int_0^{\Delta a} \sigma(2u) dx$$

or

$$\frac{(1-\nu^2)K_I^2 \Delta a}{E}$$

after integration. Accordingly, energy balance requires that

$$\frac{K_I^2 \Delta a (1-\nu^2)}{E} = 2\gamma_s \Delta a$$

or

$$K_{th} = \left( \frac{2E\gamma_s}{1 - \nu^2} \right)^{1/2} \quad (8)$$

This relationship is a special form of eqn. (7) where  $\eta = 0$  means that no irreversible processes have occurred. Here, in eqn. (8),  $K_{th}$  denotes the critical  $K_1$  at the unstable equilibrium point. When the applied  $K$  is in excess of  $K_{th}$ , the crack is predicted to extend indefinitely whereas, if  $K < K_{th}$ , the crack is supposed to heal and disappear. Hence the Griffith model as it originally stands is not capable of predicting any kinetic law of stable crack growth.

Hsieh and Thomson [4] and Lawn and Wilshaw [5] introduced the lattice discreteness into a Griffith crack (*i.e.* the crack is atomically sharp) and found that the single-valued  $K_{th}$  degenerates into a range of  $K$  values over an area known as the lattice trapping region wherein the crack becomes stable against growth or recession.

Rice [6] gave some possible thermodynamically admissible kinetic laws for thermally activated and environmentally assisted Griffith crack growth. However, insofar as  $K_{th}$  is concerned, the expression remains unchanged so long as  $\gamma_s$  is redefined to take into account the surface adsorption isotherm which is generally diminished to some extent from the  $\gamma_s$  value *in vacuo* (and, in some cases,  $\gamma_s$  may even become negative!).

Charles and Hillig [7] developed a classical theory of stress corrosion cracking in which a two-dimensional elliptical crack is considered to grow under the influence of stress and chemical corrosive reaction. On the basis of the assumption that chemical reaction between the surface and environmental species is the rate-limiting process and that the reaction rate follows Eyring's absolute rate equation, they found an applied stress level at which the stress concentration factor at the crack apex remains invariant. Defining this value as the static fatigue limit, they found that this limit is equivalent to  $3^{1/2}\pi/4$  or 0.77 times the Griffith value defined in eqn. (8). They predicted that blunting (sharpening) will occur when the applied stress is below (above) this limit. However, their results are based only on consideration of the crack tip and its immediate neighboring points. A more extensive analysis performed by Chuang *et al.* [8] in-

dicates that the true fatigue limit should be at a level equal to 0.61 times the Griffith value if the reaction of the entire crack surface is considered. Moreover, the results also show that this fatigue limit degenerates from a single-valued level into a range of stresses wherein either enhanced blunting or necking could result depending on a material parameter. It is also interesting to note that, in both the original and the refined version of the Charles and Hillig models, the crack tip velocity at the static fatigue limit has a finite value depending on the chemical corrosion rate of a flat surface in the stress-free state. Evidently, the necessary condition under which this model applies is that the crack must be present in a reactive environment so that corrosive reactions can take place. Glass specimens containing machining flaws at their outer surfaces are an ideal example when mechanically loaded in humid air. Another example is structural ceramics crept at high temperatures in an oxygen-containing environment (such as hot air) where oxidation is expected to play a significant role. Nevertheless, the applicability of this model is somewhat limited because it is not known whether or not the oxidation kinetics follow the absolute rate theory.

Another crack growth mechanism which is likely to be operative at elevated temperatures is thermally activated mass transport processes (*i.e.* atomic self-diffusion) at the crack tip zone. These processes do not involve chemical bond breaking or corrosive reaction. On the basis solely of the principle of energy potential without considering kinetic mobility, Hasselman [9] presented a surface-diffusion-controlled model for the growth of a non-ideal Griffith crack. The static fatigue limit is defined as a stress level at which the energy at the crack tip is just equilibrated with the neighboring atoms at the crack surface so that no atomic flow or vacancy diffusion will occur, resulting in a stationary crack tip. Of course, if the applied stress differs from this limit, either recession or propagation of the crack will result. However, as mentioned before and also remarked by Dutton [10], because the model fails to take the kinetics into consideration, the correctness of the predicted crack growth rate is questionable. Nevertheless, the predicted value of the static fatigue limit is in a reasonable range and falls in the same order

of magnitude as an ideal Griffith value as shown in Table 1, although the value of  $\Delta H$  is difficult to measure in a laboratory.

Stevens and Dutton [11] developed more elaborate diffusional crack growth models of Griffith-type cracks by incorporating the kinetics of atomic transport in the crack tip zone with diffusion paths along the crack surfaces, through the lattice and via evaporation-condensation. Of those proposed models, the surface diffusion model similar to Hasselman's model is probably more applicable to high temperature creep rupture since the contribution of surface diffusion dominates over other transport paths in the practical temperature range. However, regardless of the diffusion path, the static fatigue limit is defined by Dutton and Rogowski [12] as the value of the applied stress when the chemical potential of atoms vanishes at the crack tip. Predictions concerning growth or shrinkage of cracks are similar to Hasselman's model if the applied stresses are different from this limit.

However, it is well known that creep cracks often are located at grain boundary facets normal to the applied tensile axis. Thus the presence of grain boundaries in a polycrystal must play a significant role in the creep rupture processes. Essentially the grain boundary provides a favorable site at triple-point junctions in the form of unsintered pores or, because of grain boundary sliding, for nucleation of cracks and a faster path for matter transport during subsequent growth. Hence, it is most likely that coupled surface and grain boundary self-diffusion play a dominant role in the growth of a grain boundary crack at moderate temperature levels. As a result, residual stresses are generated in the grain boundary, which alter the energy level and chemical potential in the crack tip zone and allow a steady state to develop. Under these circumstances, Chuang and Rice [13] and Chuang [14] developed a grain boundary crack growth model in which the crack tip is advanced in a steady state fashion in an elastic bicrystal (appropriate to a typical brittle ceramic system) by atomic flow from crack surfaces into the grain boundary ahead, by analogy to the classical Hull-Rimmer [15] model. By solving precisely the stress and "wedging shape" ahead of the growing tip concurrently, they were able to find the

kinetic law predicting crack growth rate as a function of applied stress intensity. The threshold intensity factor emerges from this solution automatically. It should be noted that, unlike other crack growth models, the crack is predicted to grow at a finite (slow) rate even when the applied  $K$  is exactly at  $K_{th}$  level.

In view of many similarities between the Stevens-Dutton and the Chuang-Rice models, it is perhaps interesting to make a comparison. The first major departure is the contention concerning the direction of mass flow as demonstrated in Figs. 1(a) and 1(b). In the Stevens-Dutton model (Fig. 1(a)) the grain boundary crack is treated as though it were located in the interior of the matrix. The natural consequence is that the atomic flow must be away from the tip (*i.e.* from right to left in Fig. 1(a)) as accommodation of matter ahead of the tip is not possible. However, by considering the presence of a grain boundary ahead of the tip, the vacancy flows are then reversed in the Chuang-Rice model (and presumably in the Hull-Rimmer model also) (see Fig. 1(b)) because now the grain boundary is capable of releasing vacancies and absorbing matter to form a "wedge". To ascertain which

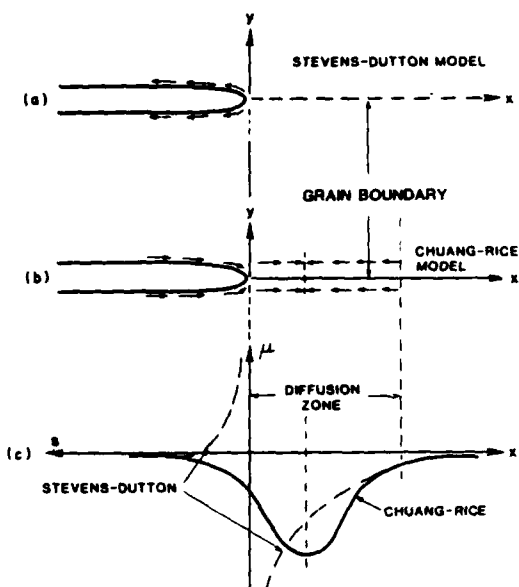


Fig. 1. Schematic diagrams of atomic flows and chemical potential fields in the crack tip zone: (a) the Stevens-Dutton model; (b) the Chuang-Rice model; (c) chemical potential distributions for these models.

direction the atomic flow actually goes in a real system, Varma and Dyson [16] recently performed a novel study on the creep cavity growth of nickel-base alloy IN-597. This material has two-phase microstructures containing soluble carbide particles. The creep tests were performed on 8% prestrained specimens at 154 MPa and 800 °C to avoid complications induced by continuous cavity nucleation. When crept to three-quarters of the lifetime and thereafter (corresponding to 0.65% of creep strain or more), clear zones between adjacent cavities on the boundary were detected from the transmission electron micrographs, indicating that atom plating has already occurred. This experiment confirms the contention of the Chuang-Rice model that vacancies indeed do flow to the tip from the grain boundary ahead of the tip as indicated in Fig. 1(b).

Another major difference lies in the stress and chemical potential fields resulting from the reversed matter flows at the crack tip zone. As illustrated in Fig. 1(c), for the Stevens-Dutton model, the stress distribution along the grain boundary is essentially undisturbed so that it poses an inverse square root singularity at the moving crack tip (see the broken line in Fig. 1(c)). However, in the Chuang-Rice model, because of residual stresses created by the "wedging" effect owing to grain boundary diffusion, the stress field is altered drastically in the diffusion zone such that there no longer exists a stress singularity at the tip (see the full line in Fig. 1(c)). Thus we are led to conclude that the Stevens-Dutton model is appropriate only for transgranular crack growth. However, even in this case, it remains an open question as to whether steady state growth can persist since, as shown in Fig. 1(c) at the crack tip, there exists a discontinuity and singularities in the chemical potential which are inconsistent with a diffusive kinetic law. More detailed discussions on this subject have been given by Rice and Chuang [17] and Puls and Dutton [18].

Finally, Lange [19] developed a void growth model in a liquid phase grain boundary. The static fatigue limit is set at the sintering stress which is a function of the diameter of the spherical void and the liquid-vapor surface free energy. While this model is useful as a first-order estimation and certainly appli-

cable to void growth in high glass content ceramics, its applicability is in doubt for the evaluation of  $K_{th}$  as  $K$  is not defined in the Lange model.

#### 4. DISCUSSION

In Section 3 the threshold stress intensity is discussed in terms of fundamental mechanisms which activate the crack growth processes. These should represent lower bound values for  $K_{th}$ . Other concurrent processes which accompany the crack growth will demand more energy, resulting in an enhanced threshold value. Some notable influencing factors are discussed as follows.

##### 4.1. Plasticity of matrix

So far the evaluations of  $K_{th}$  are based on the elastic grain assumption. At high temperatures the motion of dislocations inside the matrix may result in a certain degree of plasticity. As a result, entropy is produced in the crack tip region and  $\eta > 0$  in eqn. (7), leading to enhanced  $K_{th}$ . This effect could be verified experimentally from observations of the crack size or crack-opening displacement. Examination of data in a variety of materials indicates that, if we plot  $K_{th}$  as a function of the maximum crack thickness normalized by the average grain size, i.e. as a function of  $2W/d$ , as shown in Fig. 2, we find that  $K_{th}$  increases as  $2W/d$  increases. This behavior could be interpreted in terms of the plasticity of the matrix: the more ductile a material, the larger is the crack thickness that can be achieved prior to catastrophic failure. Accordingly, higher values of observed  $2W/d$  imply higher  $K_{th}$  according to eqn. (7) because of higher entropy production rates. For example, when the crack thickness is in the nanometer range, which is typical of brittle ceramics, the measured value of  $K_{th}$  is at the fundamental value ( $0.1-1.0 \text{ MPa m}^{1/2}$ ). Located at the other extreme of the spectrum are superalloys in which engineering-sized cracks are often observed and where the measured values of  $K_{th}$  reported in the literature are in the range  $10-50 \text{ MPa m}^{1/2}$ . In terms of the  $v-K_I$  curves, data collected in the literature, as schematically plotted in Fig. 3, also indicate the trend of crack size dependence on the  $K_{th}$  values and on the subsequent crack growth behavior. It should be noted that these

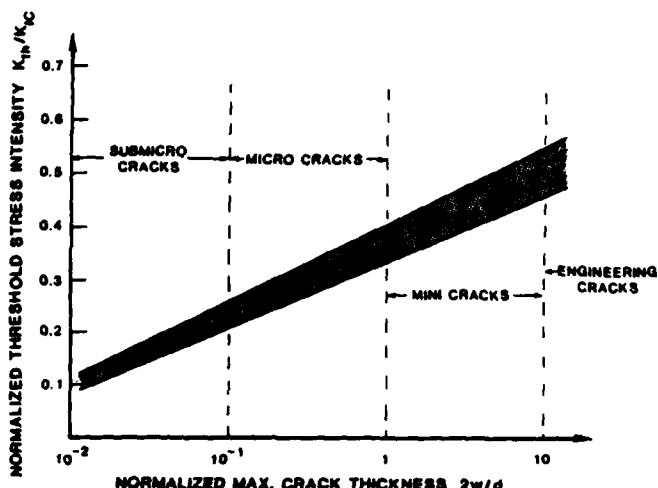


Fig. 2. Schematic diagram illustrating the effect of crack thickness on the threshold stress intensity. The ranges of sizes are labeled for a material having an average grain size of 1  $\mu\text{m}$ .

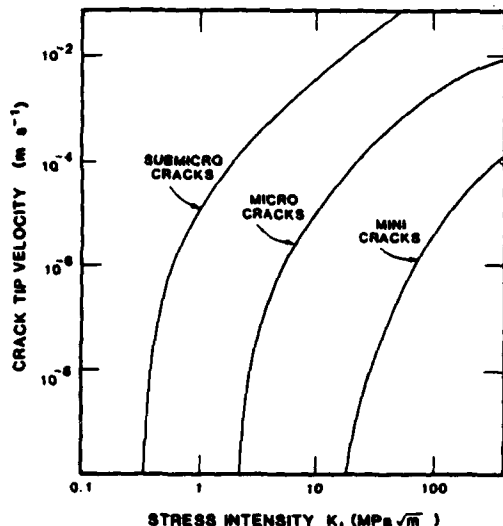


Fig. 3. Schematic plots of the  $v$ - $K_I$  relationship showing the crack size effects.

two figures (Figs. 2 and 3) do not apply to a given material; rather they refer to a broad range of materials including very brittle ceramics and ductile metals, although similar behaviors were occasionally reported for a given material [20].

Incidentally, the term "slow" crack growth often used by experimentalists needs some clarification. Needless to say, "slow" or "fast" is meaningless until a reference speed is de-

fined. In the experimental ceramic community, the reference speed of a crack seems to be set at around  $10^{-7}$ - $10^{-9}$  m  $\text{s}^{-1}$  depending on the test duration. However, in the context of diffusive crack growth during creep fracture processes, it has been established that "rapid" crack growth will proceed above  $K_{th}$ . When  $K < K_{th}$ , the crack ceases to propagate and, instead, the nucleation and growth of small Hull-Rimmer type of cavities dominate the process, leading to long-term cavitation failure by linkage. The reference speed which separates "fast" from "slow" in this case is [14]

$$v_{ref} = 8.13 \frac{D_s^{4/3} \Omega^{7/3}}{KT\gamma_s^2} \left\{ \frac{E}{(1-\nu^2)D_b \delta_b} \right\}^{3/2} \quad (9)$$

where  $D_s \Omega^{1/3}$  and  $D_b \delta_b$  are the surface diffusivity parameter and the grain boundary diffusivity parameter respectively. This quantity is a function of material constants and temperature only. It is possible then that, because of the difference in  $v_{ref}$ , entirely different conclusions may result for a given speed of crack growth. For example, the reference speed in eqn. (9) of a crack ( $2W = 20$  nm) in a  $\text{Y}_2\text{O}_3$ -doped silicon nitride specimen at  $1100^\circ\text{C}$  was calculated to be of the order of  $10^{-13}$  m  $\text{s}^{-1}$  [21]. Then the conventionally termed "slow" crack growth of the order of  $10^{-8}$  m  $\text{s}^{-1}$  based on  $v_{ref} = 10^{-7}$  m  $\text{s}^{-1}$  becomes very "rapid" growth in the context of diffusive crack growth theory since  $v = 10^6 v_{ref}$ .

#### 4.2. Microstructural effects

In addition to the ductility effect as discussed above,  $K_{th}$  can also be affected by a number of microstructural factors.

(1) *Crack deflection.* At high temperatures the crack path generally follows grain interfaces, resulting in intergranular failure. Because of the nature of polycrystal aggregates, the crack tip is first trapped at the triple-point junction of the grain boundary facets. In order to continue the propagation process, the crack must change direction and deflect from its original path. The true  $K$  at the tip is thus reduced, resulting in an enhanced measured value of  $K_{th}$ . In essence, this effect is similar to  $K_{th}$  observed from cleavage of b.c.c. polycrystals enhanced from that of b.c.c. single crystals tested at low temperatures. This enhancement is due to polycrystal effects.

(2) *Inhomogeneity.* In a real ceramic system, impurities in the form of small particles are often introduced as dopants or sintering aids in the grain boundary phase. As a result, the growth behavior of an intergranular crack is altered. The value of  $K_{th}$  will be raised for rigid particles embedded in the grain boundary (e.g. a WC particle in  $\text{Si}_3\text{N}_4$ ). In contrast,  $K_{th}$  may be reduced for polycrystal ceramics produced by liquid phase sintering.

(3) *Shielding effects.* It is known that development of microcracking at the crack tip zone may have a toughening effect. This is because multiple crack interactions give rise to a reduction in the effective  $K$  at the major crack tip. This effect is even more pronounced in bend bar specimens where parallel cracking at the tensile edge is frequently observed.

There are indirect methods of measuring the threshold stress intensity factors. Minford *et al.* [22] used the modified static loading technique to estimate  $K_{th}$  of bend bar specimens for as-machined sintered  $\alpha\text{-SiC}$  and oxidized sintered  $\alpha\text{-SiC}$ . The results of  $K_{th}$  measured for these two materials are included in Table 1. The values range from 1.75 to  $2.25 \text{ MPa m}^{1/2}$ . In contrast, Wiederhorn and Fuller [23] estimate  $K_{th}$  for the same material by virtue of reliability maps which are generated by static load tests of bend bar specimens. By plotting the contours of strength on the axes of stress and time, the curves show either strengthening or degradation behavior. The boundary stress of these two regions is then defined as  $\sigma_{th}$ . In this way, since  $\sigma_{th}$  is directly proportional to  $K_{th}$ , they estimated  $K_{th}$  for  $\alpha\text{-SiC}$  at  $1200^\circ\text{C}$  to be in the neighborhood of  $3 \text{ MPa m}^{1/2}$ . In any event, at  $1200^\circ\text{C}$  the  $K_{th}$  values for  $\alpha\text{-SiC}$  are estimated by both groups to be in the range  $2\text{--}3 \text{ MPa m}^{1/2}$ . The predicted values for  $K_{th}$  based on various theories are computed and tabulated in Table 1. Examination of the table shows that, except for the Hull-Rimmer and Lange models which give extremely high values of  $K_{th}$ , the highest values at around  $1.2 \text{ MPa m}^{1/2}$  predicted by diffusive growth theory are the closest to the experimental data. This comparison led us to conclude that diffusive transport of mass near the crack tip region probably takes place in the bend bar specimens. In addition, because of the complications discussed above,  $K_{th}$  is enhanced by a factor of about 2 from about 1.2 to 2-3  $\text{MPa m}^{1/2}$ .

However, it should be re-emphasized that theoretically a true  $K_{th}$  should not depend on

TABLE 2

Predictions of  $K_{th}$  for an interfacial crack in  $\text{SiC}$  at  $1200^\circ\text{C}$  in terms of distinct crack growth mechanisms

<i>Kinetic model</i>	$K_{th}/K_G$	$K_{th} (\text{MPa m}^{1/2})$		
		<i>Hot-pressed <math>\alpha\text{-SiC}</math></i>	<i>Oxidized sintered <math>\alpha\text{-SiC}</math></i>	<i>As-machined sintered <math>\alpha\text{-SiC}</math></i>
Bond breaking	1.0	0.752	0.711	0.564
Chemical corrosion	0.61	0.459	0.433	0.344
Matter transport	1.69	1.271	1.201	0.954
Experimental results		2.25	1.75	2.25

It should be noted that  $K_G = \{E(2\gamma_s - \gamma_{gb})/(1 - \nu^2)\}^{1/2}$  for a grain boundary crack.

crack tip geometry, crack length or stress concentration factor. Hence there is a need to refine the expressions for  $K_{th}$  in Table 1 based on the ideas discussed in Section 3. So far as we can tell, there are three fundamental crack growth mechanisms which are most likely to be operative in the creep range. Table 2 lists the corresponding (lower bound) values for  $K_{th}$ . These values are indeed quite low. The difference between these values and the observed values, as indicated in Table 2, suggests that submicrocracks propagate along the grain interface via vacancy diffusion mechanisms in the real systems. Other concurrent processes including plasticity and microstructural effects as discussed in the present paper are responsible for the larger value of the observed  $K_{th}$ .

The above conclusions are drawn from the comparisons between the static fatigue data of  $\alpha$ -SiC tested at 1200 °C and various theoretical predictions. It is likely that the same conclusions can also be applied to other structural ceramic systems crept at high temperatures. However, in a general situation, it is recommended that, in addition to static fatigue testing, a complementary microstructural study (similar to that carried out in ref. 21) be performed on the specimen so as to make certain that the actual physical processes do conform with the kinetic model assumptions.

#### ACKNOWLEDGMENT

This work was supported by the U.S. Department of Energy, AR & TD Fossil Energy Materials Program, under Interagency Agreement DE-A105-800R20679 with the National Bureau of Standards.

#### REFERENCES

- 1 M. D. Thouless and A. G. Evans, *Scr. Metall.*, **18** (1984) 1175-80.
- 2 T.-J. Chuang, *Int. J. Fract.*, **23** (1983) 229.
- 3 E. J. Minford, Flaw behavior near the threshold stress intensity for slow crack growth in silicon carbide ceramics at high temperatures, *Ph.D. Thesis*, Pennsylvania State University, University Park, PA, March 1983, p. 131.
- 4 C. Hsieh and R. Thomson, *J. Appl. Phys.*, **44** (1973) 2051.
- 5 B. R. Lawn and T. R. Wilshaw, *Fracture of Brittle Solids*, Cambridge University Press, Cambridge, Cambridgeshire, 1975, pp. 140-167.
- 6 J. R. Rice, *J. Mech. Phys. Solids*, **26** (1978) 61-78.
- 7 R. J. Charles and W. B. Hillig, *Proc. Symp. on the Mechanical Strength of Glass and Ways of Improving It, 1961*, Union Scientifique Continentale du Verre, Charleroi, 1962, pp. 511-527.
- 8 T.-J. Chuang, E. R. Fuller and T. A. Michalske, Stress corrosion induced alteration in crack-tip geometry, to be published.
- 9 D. P. H. Hasselman, in J. J. Burke, N. C. Reed and V. Weiss (eds.), *Ultrafine-grain Ceramics*, Syracuse University Press, Syracuse, NY, 1970, pp. 297-315.
- 10 R. Dutton, in R. C. Bradt, D. P. H. Hasselman and F. F. Lange (eds.), *Fracture Mechanics of Ceramics*, Vol. 2, Plenum, New York, 1974, pp. 647-657.
- 11 R. N. Stevens and R. Dutton, *Mater. Sci. Eng.*, **8** (1971) 220-234.
- 12 R. Dutton and A. J. Rogowski, *J. Can. Ceram. Soc.*, **41** (1972) 53-61.
- 13 T.-J. Chuang and J. R. Rice, *Acta Metall.*, **21** (1973) 1625-1628.
- 14 T.-J. Chuang, *J. Am. Ceram. Soc.*, **65** (1982) 93-103.
- 15 D. Hull and D. E. Rimmer, *Philos. Mag.*, **4** (1959) 673-687.
- 16 R. K. Varma and B. F. Dyson, *Scr. Metall.*, **16** (1982) 1279-1284.
- 17 J. R. Rice and T.-J. Chuang, *J. Am. Ceram. Soc.*, **64** (1981) 46-53.
- 18 M. P. Puls and R. Dutton, in K. Sadananda, B. B. Rath and D. J. Michel (eds.), *Micro and Macro Mechanics of Crack Growth, Proc. AIME Conf., Louisville, KY, October 13-15, 1981*, AIME, New York, 1981, pp. 19-28.
- 19 F. F. Lange, in R. C. Bradt and R. E. Tressler (eds.), *Deformation of Ceramic Materials*, Plenum, New York, 1975, pp. 361-381.
- 20 W. Blumenthal and A. G. Evans, *J. Am. Ceram. Soc.*, **67** (1984) 751.
- 21 T.-J. Chuang, N. J. Tighe and S. M. Wiederhorn, Submicrocrack growth of  $Y_2O_3$ -doped silicon nitride at elevated temperature, *Proc. 6th Int. Conf. on Fracture, New Delhi, December 4-10, 1984*, Pergamon, Oxford, 1984.
- 22 E. J. Minford, D. M. Kupp and R. E. Tressler, *J. Am. Ceram. Soc.*, **66** (1983) 769-773.
- 23 S. M. Wiederhorn and E. R. Fuller, *Mater. Sci. Eng.*, **71** (1985) 169.

#### TIME DEPENDENT MECHANICAL BEHAVIOUR OF SILICON CARBIDE CERAMICS AT ELEVATED TEMPERATURES

D.F. CARROLL and R.E. TRESSLER  
The Pennsylvania State University, Department of Materials Science and Engineering, University Park, PA 16802 (USA)

#### SUMMARY

The tensile creep behavior of a siliconized carbide was measured at 1100°C and stresses of 120 to 172 MPa using an optical extensometer and a modified flat dogbone shaped specimen. Both primary and secondary creep were observed. The primary creep regime was characterized by  $\dot{\epsilon} = \alpha \log(t/t_0 + 1)$ . A steady-state creep stress exponent of 8 was measured for this temperature and stress range. The creep results were then used to calculate the relative amount of apparent strengthening in bending, due to macroscopic stress redistribution. A strength increase of 7% was calculated for specimens static loaded at 1100°C for 2 hours under an applied stress of 480 MPa which accounts for less than half of the observed strengthening in bending.

#### INTRODUCTION

Siliconized silicon carbide is being considered for use in high temperature ( $>1000^\circ\text{C}$ ) structural applications. The mechanical properties of this material are strongly dependent upon the silicon matrix phase which is ductile at these temperatures. Past investigations have shown that siliconized silicon carbide exhibits apparent strengthening after static loading in bending at elevated temperatures (1-4). This strengthening phenomenon has been attributed to both flaw blunting and macroscopic stress redistribution processes. Flaw blunting may result in a strength increase if the effective stress intensity around the crack tips of the severe flaws in the material is reduced through localized stress relaxation processes.

Apparent strengthening through macroscopic stress redistribution can occur if the material exhibits either non-linear creep or a different creep rate in tension than in compression (5-7). Using an analysis developed by Cohrt et al. (5), the stress redistribution process in a bending beam for a material which exhibits non-linear creep behavior only (i.e. the steady-state creep exponents in tension and compression are equal, but greater than 1) is shown in Figure 1. At time  $t=0$ , the initial applied stress is linear throughout the beam. As time progresses, the non-linear creep behavior of the material causes a redistribution of the stress in the beam. At  $t=t_1$ , the stress at the

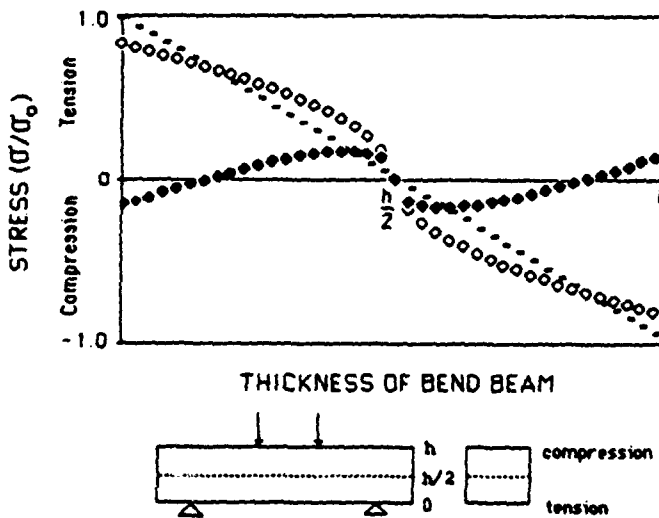


Figure 1. Stress redistribution in a four point bend beam with time for a material which exhibits non-linear creep behavior only ( $n = 2$ ,  $s = 1$ ,  $\sigma_0$  = initial outer tensile fiber stress).

- initial stress distribution at  $t = 0$
- stress distribution at  $t = t_1$
- residual stress distribution after unloading specimen at  $t = t_1$

outer tensile and compressive fiber has decreased while the stress around the neutral axis has increased compared to the initial values. If the beam is loaded to failure at  $t=t_1$ , an apparent strength increase would be observed due to the reduction of the outer tensile fiber stress. If the specimen is loaded at  $t=t_1$ , a residual compressive stress would develop on the tensile surface while a residual tensile stress would develop on the compressive surface.

If the material exhibited a faster creep rate in tension than in compression, the outer tensile fiber stress would again decrease with time, resulting in a strength increase when the specimen was loaded to failure after  $t=t_1$ . However, unlike the previous case, the outer compressive fiber stress increases with time and the neutral axis shifts from  $h/2$  toward the compressive side of the specimen. If the specimen is unloaded at  $t=t_1$ , a residual compressive stress would develop on both the tensile and compressive surfaces while a residual tensile stress would develop in the interior of the bend beam.

Recently, Carroll and Tressler (2) have investigated the strengthening behavior of a specific fine grained siliconized silicon carbide under load in four-point bending. Their results have shown that the average bend strength of specimens static loaded at 1000 and 1100°C for 2 hours under an applied stress of 480 MPa, increased approximately 11 and 18%, respectively over the initial distribution. They also found that this strength increase was accompanied by cavity formation on the tensile sides of the specimens.

Their conclusions from this work are that both macroscopic stress redistribution and localized flaw blunting processes can produce a strength increase in this siliconized silicon carbide under load. Cavity formation, which reduced the room temperature strengths of crept specimens, will eventually lead to the ultimate strength degradation and failure of this material at elevated temperatures (4).

The purpose of this paper is to report on the tensile creep behavior of this siliconized silicon carbide. This information allows one to calculate the relative amount of strengthening due to macroscopic stress redistribution and to make a comparison with the results obtained in bend experiments. Pure tensile tests also allows one to study cavity formation and its contribution to creep under uniform stress conditions without the complications of a non-uniform stress state which changes with time. The cavity formation process is discussed in detail elsewhere (8).

#### EXPERIMENTAL PROCEDURE

##### Material and Specimen Design

The material used in this investigation was a siliconized silicon carbide<sup>1</sup> that contained approximately 33 volume percent of silicon and 4 to 6 micron silicon carbide grains. Tensile creep specimens were cut from blanks approximately 76.2 x 12.7 x 2.54 mm in size, using a wire EDM (electrodischarge machining) technique. The design of the tensile specimens is shown in Figure 2. This design is similar to the modified flat dogbone shaped specimen developed by Wakai et al. (9). The initial gauge length of these specimens was approximately 17.5 mm.

##### Loading System

Tensile loading conditions are obtained by pinning the tensile specimens into two siliconized silicon carbide<sup>2</sup> grips using alpha silicon carbide<sup>3</sup> pins.

<sup>1</sup> KX-01 Sohio Engineered Materials, Niagara Falls, NY

<sup>2</sup> CS101K, Norton Co., Worcester, Mass.

<sup>3</sup> Sintered  $\alpha$ -SiC, Sohio Engineered Materials, Niagara Falls, NY

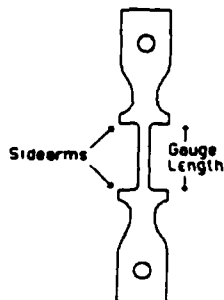


Figure 2. Schematic showing design of tensile specimen.

This pin and grip arrangement is located inside the furnace and is at test temperature. The two grips extend outside the furnace and are connected to two universal joints and the other parts of the load train. The dead load is applied by hanging the desired weights from the bottom fixture. It is critical that the pins sit properly in the holes of the specimen in order to prevent a bending moment. There are two steps that must be taken to obtain proper alignment. First, very close tolerances are needed in machining the specimens. The EDM technique machines to within  $\pm 1$  micron. The holes must be located directly above the centerline of the gauge length and must be machined to a uniform smoothness. Secondly, a preload must be applied to the specimen before furnace heatup so the pin sits firmly in the hole. With these precautions, the differences in creep strain between the side arms on either side of the gauge length are routinely less than 5% after testing.

#### Measurement Technique

The creep deformation of the specimen was measured using an optical extensometer<sup>4</sup> which views the sample through a fused quartz window of the furnace. The optical extensometer focuses on the two side arms of the tensile specimen. The side arms are backlit using a halogen light source that is transmitted through another fused silica window located directly behind the specimen. The optical extensometer detects the shadows of the two side arms using two photocathode screens. As the targets move apart during the creep test, the optical extensometer follows the targets and produces an output proportional to the displacement. The resolution of this device is approximately 1 micron at elevated temperatures in air.

<sup>4</sup> Electroptical extensometer model 200X-2, Zimmer OHG, West Germany

Testing Conditions

Specimens were placed into the loading train under a prestress of approximately 38 MPa. The furnace was then heated to test temperature where the sample was annealed for eight hours. After annealing, the sample was loaded to the desired stress level for the creep test. Creep tests were performed at  $1100 \pm 1^\circ\text{C}$  in air at applied stress levels ranging from 120 to 172 MPa. This stress range was selected because stresses below 120 MPa produce a creep rate too low for measurable displacements during short term creep tests and stresses above 172 MPa approach the tensile fracture stress of this material.

**RESULTS AND DISCUSSION**

Creep Curves

Figure 3 summarizes some of the tensile creep curves at  $1100^\circ\text{C}$  for applied stresses ranging from 120 to 172 MPa. All test were interrupted after a certain period of time to ensure that there was no bending in the gauge length. These results show that the creep behavior exhibits primary and secondary creep regimes. SEM analysis of the polished gauge length sections have shown that creep deformation is also accompanied by cavity formation nucleated first in regions of high SiC content. It has been shown elsewhere, that this material also exhibits tertiary creep at the higher applied stresses if the specimens are allowed to creep to failure (10). Unlike our results,

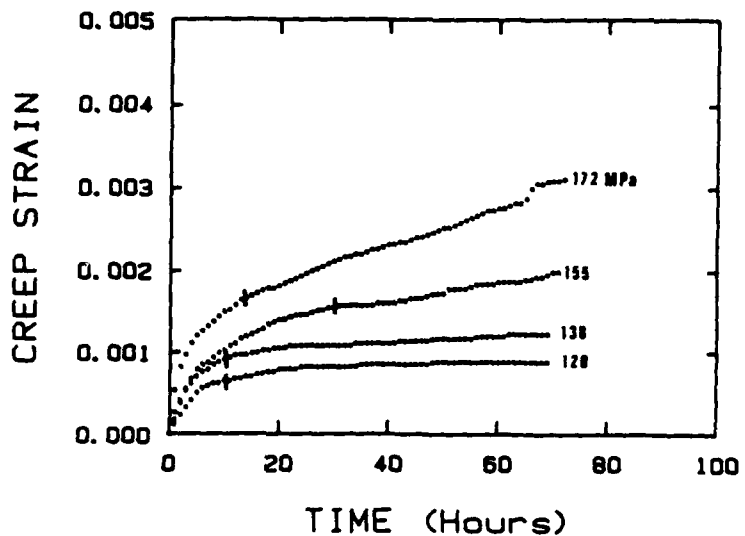


Figure 3. Typical creep curves at  $1100^\circ\text{C}$  showing creep strain versus time under applied stresses of 120 to 172 MPa.

Wiederhorn et al. (4) have observed that in bending this siliconized silicon carbide exhibits only primary creep at 1100°C and primary creep with a transition to tertiary creep at 1300°C. This absence of a secondary or steady-state creep regime in their results may be due to the constantly changing stress state in the bend beam as macroscopic stress redistribution occurred. By plotting the minimum creep rate as a function of stress, they determined that the stress exponent for steady-state creep to be approximately 4 at 1100 and 1200°C and 13 at 1300°C. They concluded that at 1100 and 1200°C, the creep behavior of this material is controlled entirely by the deformation of the silicon phase, since the stress exponent is approximately equal to that for the creep of silicon (10). At 1300°C, the stress exponent of 13 is considerably greater than that for deformation of silicon. This result suggests another creep mechanism is occurring to increase the stress exponent of the creep rate.

A computer program was developed to determine the transition point from primary to secondary creep behavior and to fit the corresponding regimes to empirical equations. The equation found to give the best fit to the primary regime is the logarithmic relationship:

$$\epsilon = \alpha \log(t/t_0 + 1) \quad (1)$$

where  $\epsilon$  is the creep strain,  $t$  is time,  $t_0$  is a time constant assumed to be unity and  $\alpha$  is a constant which varies with applied stress. A plot of the  $\alpha$  coefficient in equation 1 versus applied stress is shown in Figure 4. As the applied stress increases, the  $\alpha$  coefficient also increases linearly. This result indicates that the primary creep strain increases with applied stress at a given time  $t$ . The line crosses the x axis at approximately 80 MPa. Since the  $\alpha$  coefficient can not be negative, this result indicates that there is a threshold stress for creep. The secondary creep regimes were fitted to the equation:

$$\dot{\epsilon}_s = A(\sigma/G)^n \quad (2)$$

where  $\dot{\epsilon}_s$  is the steady-state creep rate,  $A$  is a constant,  $G$  is the shear modulus and  $n$  is the stress exponent for steady-state creep. A log-log plot of the steady-state creep rate versus applied stress is shown in Figure 5. The slope of the curve yields a stress exponent of approximately 8. However, there is a trend of increasing stress exponent with increase stress. This creep exponent is larger than what would be expected if the creep behavior of this material were controlled by the deformation of the silicon matrix. Further evaluation of the creep curves, including the secondary creep regime and the cavity formation process are discussed elsewhere (8).

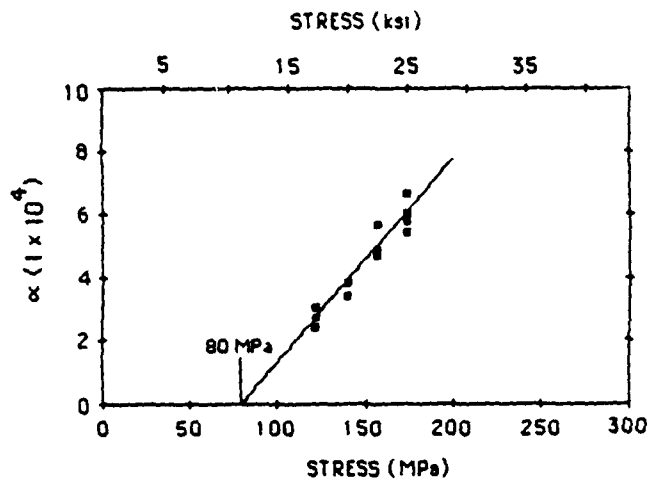


Figure 4. Plot of the coefficient  $\alpha$  in equation (1) versus applied stress at 1100°C.

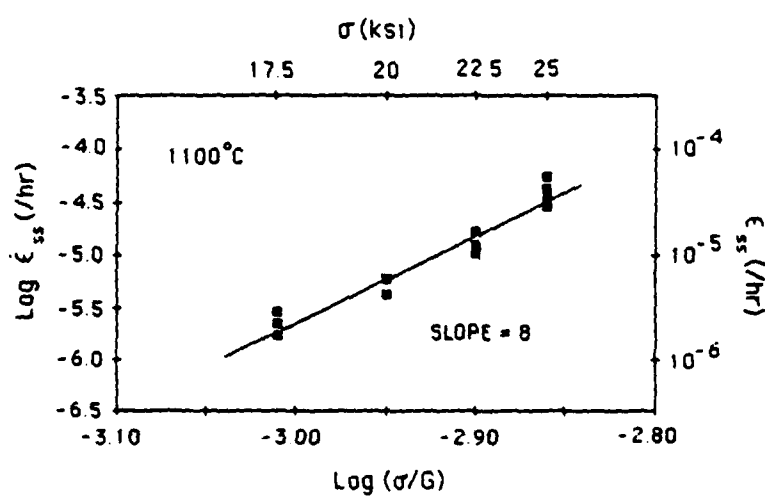


Figure 5. Log steady-state creep rate versus log applied stress normalized to the shear modulus at 1100°C.

Stress Redistribution

The numerical integration used to calculate the stress redistribution process was described earlier (5-7). In order to use this creep data to calculate the amount of stress redistribution that occurred in bending, two assumptions have to be made. First, since there is currently no data available which describes the compressive creep behavior of this material, an assumption about the relative rate of creep in tension to compression must be made. Our bending results for specimens which were static loaded at 480 MPa for 2 hours at 1000°C, unloaded and then fractured at room temperature have indicated that a residual compressive stress exists on the tensile surface and a residual tensile stress exists on the compressive surface. A similar behavior was also found at 1100°C except that the effects of residual compressive stress on the tensile surface could not be determined since the room temperature strengths were reduced by cavity formation. The only way these residual stresses could develop due to stress redistribution is if the rates of creep in tension and compression were equal.

Results obtained by Wiederhorn et al. (4) have shown that this is not the case for this material at higher temperatures and longer static load times. Their results have shown extensive cavity formation which extends past the geometrical center of the bend beam. Using a series of indentations placed on the side of the specimen, they have been able to determine how much the neutral axis has shifted toward the compressive side of the specimen. This type of behavior is due to a faster creep rate in tension than in compression. It has been suggested that this asymmetric creep behavior may be due to cavity formation on the tensile side of the specimen. Cavity formation reduces the effective cross-section of the bend beam which increase the tensile creep rate.

In our bending results the amount of cavities formed after 2 hours of static loading were confined to near the tensile surface. Since these tests were interrupted at a very early stage in the primary creep regime and cavity formation was not extensive, it is reasonable to assume that there is no significant reduction in the cross-section of the bend beam. Therefore, the tensile creep behavior has not been affected by the cavity formation process and the creep in tension and compression should initially be equal, based upon our results. If the tests were carried out for longer times, cavity formation would increase the tensile creep rate producing the results obtained by Wiederhorn et al. (4).

The second assumption involves equation (1) which will be used to numerically integrate the amount of stress redistribution. The first assumption is that the  $\alpha$  coefficient will vary linearly with stresses up to the applied outer tensile fiber stress of 480 MPa. This assumption must be

made because it would be impossible to obtain the tensile creep behavior of this material at stresses which are above the tensile strength of this material. Also, it is assumed that a threshold stress for creep of 80 MPa exists. At any applied stress below this stress, the  $\alpha$  coefficient is zero and there will be no creep strain.

The results of the stress redistribution calculation for a sample initially loaded at an applied stress of 480 MPa for 2 hours is shown in Figure 6. It can be seen that both the outer tensile and compressive fiber stresses have decreased to a magnitude of approximately 440 MPa or 91% of the initial applied outer fiber stress. If the sample is loaded to failure at this time, the average fracture stress of the material will appear to have increased 40 MPa. In our early results, the average apparent fracture stress of the specimens static loaded at 480 MPa at 1100°C for 2 hours increased from 600 to 710 MPa, an 18% strength increase. According to the stress redistribution calculation using our creep data, the average apparent fracture stress should have increased from 600 to 640 MPa, approximately a 7% strength increase. The measured strength increase of 18% is also influenced by flaw blunting processes which have been shown to produce strengthening in this material (2). This strength prediction is only approximate since the creep behavior of this material in pure tension at stresses above the tensile fracture stress must be estimated.

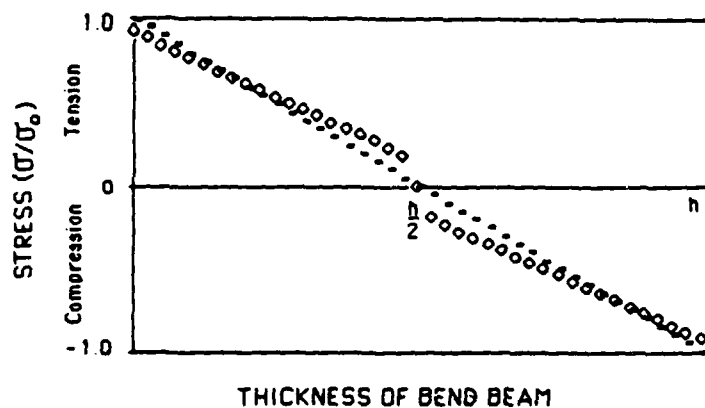


Figure 6. Calculation of the redistribution of stress in a bend beam after 2 hours of static loading at 480 MPa at 1100 C. Calculation is based upon tensile creep data.

- initial stress distribution at  $t = 0$
- $\diamond$  stress distribution at  $t = 2$  hrs

## SUMMARY

The tensile creep behavior of a siliconized silicon carbide was measured using an optical extensometer and a modified flat dogbone shaped specimen. Interrupted creep tests conducted at 1100°C at stresses of 120 to 172 MPa exhibited both primary and secondary creep behavior. The stress exponent for steady-state creep was determined to be approximately 8. The creep results were used to calculate the amount of strengthening due to macroscopic stress redistribution during static loading of a bend beam. A strength increase of 7% was calculated for a static load test at 1100°C for 2 hours under an applied stress of 480 MPa.

## REFERENCES

1. G. G. Trantina, "Strengthening and Proof Testing of Siliconized SiC", *J. Mat. Sci.*, 17, 1487-92 (1982).
2. D. F. Carroll and R. E. Tressler, "Time-Dependent Strength of Siliconized Silicon Carbide under Stress at 1000 and 1100°C", *J. Am. Ceram. Soc.*, 68, 143-146 (1985).
3. D. F. Carroll, R. E. Tressler, Y. Tsai and C. Near, "High Temperature Mechanical Properties of Siliconized Silicon Carbide Composites", in Tailoring Multiphase and Composite Ceramics, held at The Pennsylvania State Univ., University Park, PA, July 17-19, 1985.
4. S. M. Wiederhorn, L. Chuck, E. R. Fuller, J. r, N. J. Tighe, "Creep Rupture of Siliconized Silicon Carbide," in Tailoring Multiphase and Composite Ceramics, held at The Pennsylvania State Univ., University Park, PA, July 17-19, 1985.
5. H. Cohrt, G. Grathwohl and F. Thummel, "Non-Stationary Stress Distribution in Ceramic Bending Beam During Constant Load Creep", *Res Mechanics*, 10, 55-71 (1984).
6. H. Cohrt, G. Grathwohl and F. Thummel, pp. 515-526, in Creep and Fracture of Engineering Materials and Structures, Part I, Edited by B. Wilshire and D. R. J. Owen, Pinridge Press, Swansea, U. K., 1984.
7. T. Chuang, "Estimation of Power-Law Creep Parameters from Bend Test Data" *J. Mat. Sci.*, in press.
8. D. F. Carroll and R. E. Tressler, to be published.
9. F. Wakai, S. Sakaguchi, Y. Matsuno and H. Okunda, "Tensile Creep Test of Hot-Pressed  $\text{Si}_3\text{N}_4$ " presented at International Symposium on Ceramic Components for Engines, held at Hakone, Japan, October 17-21, 1983.
10. H. J. Frost and M. F. Ashby, in Deformation-Mechanism Maps: Plasticity and Creep of Metals and Ceramics, Pergamon Press, New York (1982).

# Oxidation Kinetics of Silicon Carbide Crystals and Ceramics: I, In Dry Oxygen

JOHN A. COSTELLO<sup>\*†</sup> and RICHARD E. TRESSLER<sup>\*</sup>

Department of Materials Science and Engineering, The Pennsylvania State University, University Park, Pennsylvania 16802

The oxidation kinetics of several single-crystal and polycrystalline silicon carbide materials and single-crystal silicon in dry oxygen over the temperature range 1200° to 1500°C were fitted to the linear-parabolic model of Deal and Grove. The lower oxidation rates of silicon carbide compared to silicon can be rationalized by additional consumption of oxidant in oxidizing carbon to carbon dioxide. The (0001) Si face of the silicon carbide platelets exhibited lower parabolic oxidation rates than the (0001) C face, by a factor of 10 at 1200°C. Apparent activation energies increased from a value of ~120 kJ/mol below 1400°C to a value of ~300 kJ/mol above this temperature. The (0001) Si face exhibited this high activation energy over the entire temperature range. The controlled nucleation thermally deposited material exhibited the highest oxidation rates of the polycrystalline materials followed by the hot-pressed and sintered  $\alpha$ -silicon carbides. In general, the oxidation rates of the polycrystalline materials were bracketed by the oxidation rates of the basal planes of the single-crystal materials. Higher impurity concentrations and higher density of nucleation sites led to a greater susceptibility to crystallization of the scale which significantly complicated the oxidation behaviors observed. When crystallization of the oxide scale occurred in the form of a layer of spherulitic cristobalite crystals, a retardation of the oxidation rates was observed. An accelerated oxidation behavior was found when this coherent layer was superseded by the formation of fine mullite crystals.

## I. Introduction

THE oxidation of silicon carbide materials has been the topic of investigation for many years because of their use in high-temperature applications. The excellent oxidation resistance which silicon carbide exhibits is due to the formation of a coherent layer of silicon dioxide on the surface which suppresses further oxidation. Oxidation kinetics can generally be described using the linear-parabolic model of Deal and Grove.<sup>1</sup> This model was formulated to characterize the oxidation behavior of single-crystal silicon accounting for both linear and parabolic dependencies of oxide thickness with time. The linear dependence arises from interface reaction control in the early stages of oxidation. Reported activation energies in the linear growth regime correspond to the Si-Si

bond energy (184 kJ/mol). With increasing oxide thickness, the oxidation is controlled by diffusion of oxidant through the oxide to the growth interface. Under these conditions, classic parabolic oxidation kinetics are observed where the oxide thickness is proportional to the square root of time. The reported activation energy in this regime (117 kJ/mol) agrees very well with the energy required for molecular oxygen permeation in fused silica as reported by Norton.<sup>2</sup> Other experimental evidence has been reported in support of this rate-controlling mechanism.<sup>1-3</sup> Both regimes exhibit a linear dependence on oxygen partial pressure as predicted by the model.

The oxidation behavior of silicon carbide is not as well understood in spite of the attention it has received.<sup>4-16</sup> In most studies, only parabolic oxidation kinetics have been reported. Activation energies range from 84 to 498 kJ/mol. The large variations in reported kinetics have been attributed to the differences in the materials used in each investigation. Powders and single-crystal and polycrystalline materials with varying amounts and types of impurities have been investigated. In contrast, the better-characterized silicon oxidation has been obtained with single-crystal material having precisely controlled impurity concentrations.

Very few studies of the oxidation behavior of single-crystal silicon carbide are present in the literature presumably because of the difficulty in acquiring the single-crystal material. Harris reported the oxidation of (0001) surfaces of transparent green 6H-polytype silicon carbide platelets in dry oxygen at 970° to 1245°C. Parabolic behavior was observed on the (0001) C face at each temperature for thicknesses greater than 250 nm. Below this value, the data approached a linear behavior. The calculated activation energy of 197 kJ/mol was slightly larger than the corresponding value for silicon. Oxide thicknesses were a factor of 7 smaller on the opposing face. This difference in oxidation behavior has been attributed to the polar form of the tetrahedral bonding in the 6H structure. Linear kinetics were reported for all temperatures and times on this face, although at the higher temperatures, a linear-to-parabolic transition is found. The nonlinear behavior introduces a slight error in the calculation of the linear rate constants reported in the paper. An activation energy of 356 kJ/mol was calculated from the linear rate constants and was suggested to correspond to the chemical reaction at the SiC surface. von Munch and Pfaffender<sup>7</sup> reported the effect of orientation, polytype, and dopant level on the oxidation of SiC platelets. Oxide thickness values for the two (0001) faces differed by a factor of 7 to 10 and intermediate values were observed for the (1120) and (1100) orientations. The 15R polytype oxidized faster than the 6H variety. Enhancements in the oxidation rates were reported for dopant concentrations greater than  $10^{16} \text{ cm}^{-3}$ .

Table I. Description of SiC Materials

Material	Nomenclature	Density (g/cm <sup>3</sup> )	Grain size ( $\mu\text{m}$ )	Major impurity
Single-crystal SiC black	SCSC BL	3.21		Al (ppm)
Single-crystal SiC green	SCSC GR	3.21		N (ppm)
Single-crystal Si	SCSi	2.42		B (ppm)
Sintered $\alpha$ -SiC	SASC	3.18	5-7	B (0.5 wt%)
Hot-pressed SiC	HPSC	3.23	1, 10 (bimodal)	Al (2-3 wt%)
Controlled nucleation thermal deposition SiC	CNTD		0.01-0.1	Si

Presented at the 85th Annual Meeting of the American Ceramic Society, Chicago, IL, April 27, 1983 (Basic Science Division, Paper No. 189-B-83). Received February 20, 1984; revised copy received August 26, 1985; approved May 2, 1986.

Supported by the U.S. Army Research Office Division of Metallurgy and Material Science.

<sup>\*</sup>Member, the American Ceramic Society.

<sup>†</sup>Now at the U.S. Army Electronics Technology and Devices Laboratory, Fort Monmouth, NJ 07703

The oxidation of polycrystalline SiC materials has shown a considerable range of behavior.<sup>7,11-16</sup> In the majority of cases, parabolic behavior was reported. Several investigations reported extremely high activation energies (>400 kJ/mol) for the oxidation process and concluded that a mechanism other than oxygen permeation controls the oxidation.<sup>11-13</sup> Singhal<sup>13</sup> suggested CO desorption from the growth interface as the rate-controlling process. This mechanism implies an oxidation rate independent of oxygen partial pressure. Hinze *et al.*<sup>12</sup> reported a complicated oxygen pressure dependence for hot-pressed silicon carbide, varying from 0.35 at 1300°C to nearly independent (0.03) at 1500°C. A linear pressure dependence would be expected for oxidation controlled by oxygen permeation. Several investigations reported lower activation energies below 1400°C and suggested that oxygen permeation is the rate-controlling process in this region.<sup>7,11-16</sup> Above 1400°C, increasing activation energies suggested that a change in the oxidation mechanism takes place.

Several studies have reported the effect of dopant concentrations on the oxidation behavior of polycrystalline SiC materials.<sup>13-17</sup> In general, increased dopant concentrations in the starting material lead to higher oxidation rates. This effect is caused by the redistribution of the impurities into the oxide during oxidation reducing the viscosity and increasing the flux of oxidant to the growth interface.<sup>17-19</sup> These additives, however, are necessary for successful fabrication of the ceramic. The oxidation kinetics are also affected in the same manner by the presence of water.<sup>20,22</sup>

The purpose of this paper is to report the oxidation behavior of several single-crystal and polycrystalline SiC materials in dry oxygen at 1200° to 1500°C. Oxidation kinetics of the single-crystal faces are described and extended to the polycrystalline materials to explain the observed kinetics. The influence of impurities, multiple grain orientations, and oxide crystallization is emphasized.

## II. Experimental Procedure

### (1) Materials

Brief descriptions of the materials used in this study are listed in Table I. Particular attention should be paid to the material nomenclature which is used throughout the text. The single-crystal materials consist of black (SCSC BL) and transparent green (SCSC GR) varieties of the  $\alpha$  or hexagonal structure type. The coloring arises from the presence of aluminum and nitrogen impurities, respectively, both in the ppm range. The crystals are predominantly thin platelets with the major surfaces being {0001} orientations of the hexagonal structure. A preliminary oxidation screening of the single-crystal samples was performed to distinguish between the (0001) and (0001̄) surfaces relying on the previously reported differences in oxidation of the two surfaces. Boron-doped single-crystal silicon (SCSi) having (111) orientation was used in the study to compare to the silicon carbide results. Polycrystalline materials included sintered  $\alpha$ -SiC (SASC),<sup>2</sup> hot-pressed SiC (HPSC),<sup>3</sup> and controlled nucleation thermally deposited SiC (CNTD).<sup>4</sup>

Sample size was generally 1 cm by 1 cm by 0.2 cm. The single-crystal platelets were extracted from growth clusters in material from the Acheson furnace process. Polycrystalline materials were supplied in billet form and were cut to size using a diamond saw. The carbon substrate on which the CNTD material was deposited was removed by pyrolysis at 600°C. Samples were polished to a  $\frac{1}{4}\text{-}\mu\text{m}$  diamond finish using an automatic polishing apparatus. Before oxidation, successive treatments of acetone, trichloroethylene, dilute hydrochloric acid, dilute hydrofluoric acid, and deionized water were used to thoroughly clean all samples. To ensure that the single-crystal samples were not affected by successive oxidation runs due to the redistribution of dopants, prior to reoxidation, they each received a polishing step whereby a thin surface layer of material ( $\approx 1 \mu\text{m}$ ) was removed followed by the normal cleaning procedure.

### (2) Oxidation Experiments and Characterization

Oxidations were performed in a horizontal mullite tube furnace equipped with MoSi<sub>2</sub> heating elements. A 3-in. (7.6-cm) hot zone ( $\pm 1^\circ\text{C}$ ) was present over the temperature range 1200° to 1500°C. Temperature equilibration following insertion of the sample holder typically occurred in <2 min. The oxidation atmosphere consisted of dry oxygen gas (<5 ppm H<sub>2</sub>O) with a flow rate of 200 cm<sup>3</sup>/min and a total pressure of 0.1 MPa (1 atm). Oxide thicknesses were measured using ellipsometry and profilometry. The precision of each technique was determined in this investigation to be  $\pm 3$  and  $\pm 50$  nm, respectively. In several instances, extensive roughening of the oxidized surfaces prevented an accurate measurement from being made. In these cases, an oxide thickness range was determined from profilometer readings and interference color estimates. The morphologies of the oxide films were extensively characterized using X-ray diffraction analysis, optical microscopy, and scanning electron microscopy.

Long-term oxidation behavior of the hot-pressed and sintered  $\alpha$  materials was characterized by thermogravimetric analysis (TGA). The oxidations were performed at 1300° and 1400°C and at a reduced oxygen pressure of 20 kPa (0.2 atm) for 24 h. The samples were rectangular coupons with one of the major faces polished to  $\frac{1}{4}\text{-}\mu\text{m}$  finish for a final thickness determination.

## III. Results and Discussion

### (1) Single Crystal

The oxide thickness data for the {0001} faces of the black single-crystal material are shown in Figs. 1(A) and (B). As previously reported, the two faces exhibited markedly different oxidation rates. The (0001̄) C face having the faster growth kinetics will be referred to as the fast-growth face while the (0001) Si face will be referred to as the slow-growth face. In each figure, the thickness data at each temperature have an approximate slope of one-half, indicating parabolic behavior. Similar results were obtained for the green single-crystal material and single-crystal silicon. No appreciable crystallization of the oxide films on the single-crystal materials was observed at any oxidation condition.

The data have been analyzed using the Deal-Grove model<sup>5</sup> where the oxide thickness,  $X$ , is expressed as a function of the time,  $t$ , by the equation

$$X^2 + AX = B(t + \tau) \quad (1)$$

where  $A$ ,  $B$ , and  $\tau$  are experimental constants for a given oxidation condition. The parameter,  $B$ , is the parabolic rate constant, and the linear rate constant is equal to  $B/A$ . The time constant,  $\tau$ , accounts for an initially rapid oxidation period which is not expressed by linear or parabolic kinetics. It is especially significant at lower temperatures (<1000°C) but approaches zero with increasing temperature. In this study, it was found to be zero for all materials and oxidation conditions. Rearrangement of Eq. (1) into the form

$$X = B(t/X) - A \quad (2)$$

allows for the extraction of the rate constants by simple linear regression analysis. The parabolic rate constants calculated for the single-crystal materials are compiled in Table II. Each value is accompanied by an experimental error value assuming a 95% confidence interval. Little significance could be attached to calculated linear rate constants which varied erratically, at times assuming negative values. The erratic behavior results from the small values of the constant,  $A$ , as the kinetics approach totally parabolic behavior. For parabolic behavior from the outset, the constant is by definition equal to zero. Experimental errors, therefore, significantly influence the calculated value which subsequently affects the calculation of linear rate constants.

Silicon exhibited the highest oxidation rate at each temperature. The calculated value at 1200°C compares favorably to literature values (750 nm/min).<sup>1</sup> The SiC fast-growth faces exhibited growth rates similar to those reported by Harris at 1200°C (317 nm/min).<sup>6</sup> The slow-growth faces also exhibited parabolic behavior in contrast to the linear behavior reported by Harris for

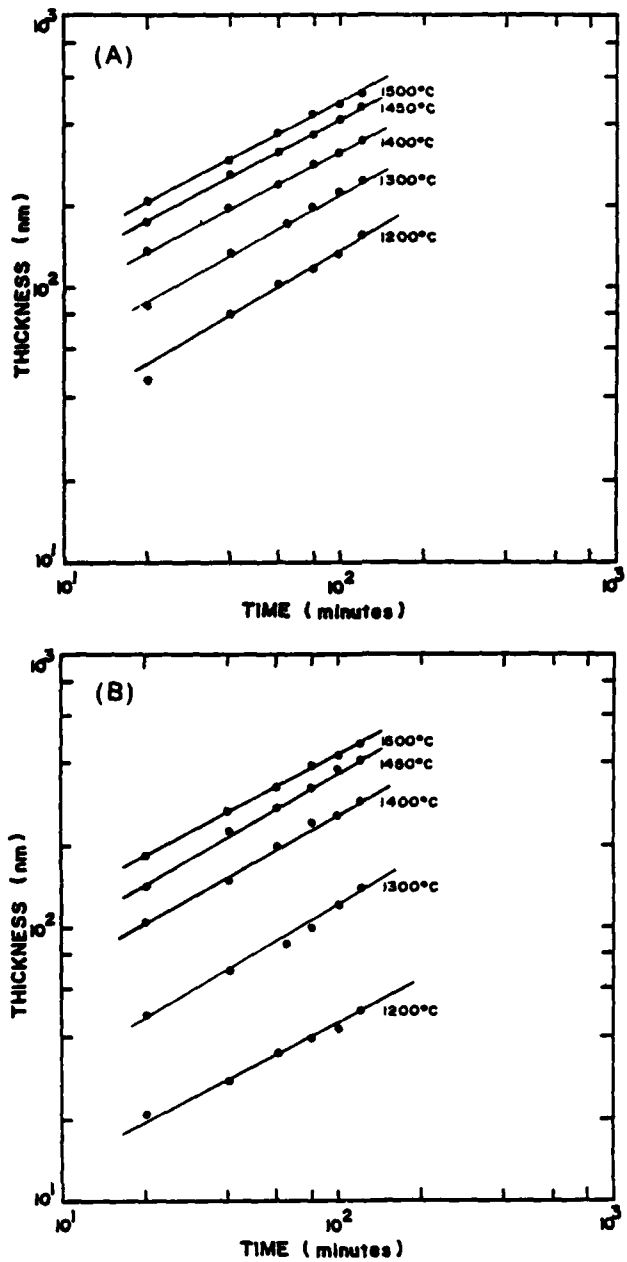


Fig. 1. Oxidation kinetics data for (A) the (0001) face and (B) the (0001) face of black single-crystal silicon carbide in dry  $O_2$ .

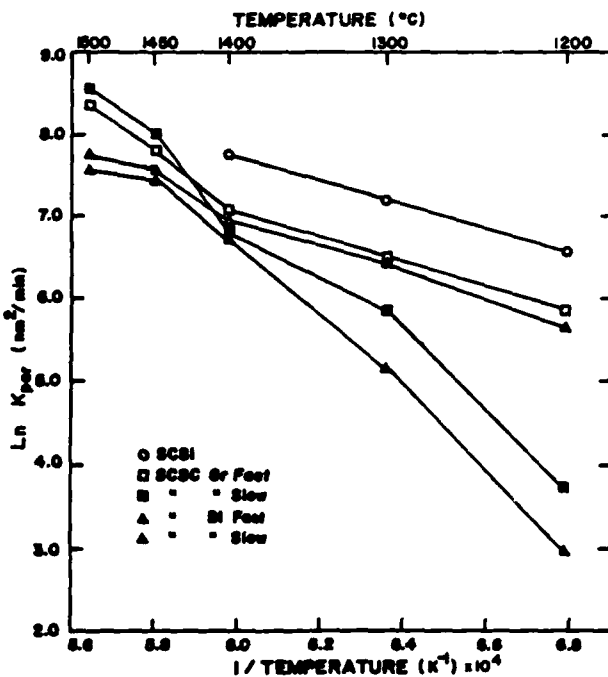


Fig. 2. Temperature dependence of parabolic rate constants for the single-crystal materials oxidized in dry  $O_2$ .

this face. However, as previously mentioned, careful examination of the Harris data indicates that the upper temperature data actually display a linear-parabolic transition.

The temperature dependence of the calculated parabolic rates for the single-crystal materials is plotted in Fig. 2. Activation energies determined from the slope of the line using the Arrhenius relation are listed in Table II. The calculated value for silicon oxidation (120 kJ/mol) agrees quite well with the accepted literature value (117 kJ/mol).<sup>1</sup> Similar values were calculated for the SiC fast-growth faces over the temperature range 1200° to 1400°C. A considerable increase in the activation energy was observed above 1400°C for the green SiC material. A correspondingly large energy value was calculated for the slow-growth face over the entire temperature range studied. The black single-crystal material exhibited similar behavior although a leveling off of the slope above 1450°C indicates a decreasing energy value. It is not clear at this time what causes this behavior.

Differences in the parabolic oxidation behavior of silicon and the fast-growth faces of silicon carbide at 1200° to 1400°C have been explained by the additional oxidant necessary to oxidize the carbon in silicon carbide.<sup>6,11</sup> According to the Deal-Grove model, the

Table II. Parabolic Rate Constants and Activation Energies for the Oxidation of the Single-Crystal Materials in Dry Oxygen\*

Temp (°C)	$K_{par}$ (nm <sup>2</sup> /min)				
	SCSi	SCSC BL F	SCSC GR F	SCSC BL SL	SCSC GR SL
1200	$7.12 \times 10^2 \pm$ $2.54 \times 10^1$	$2.84 \times 10^2 \pm$ $5.76 \times 10^1$	$3.46 \times 10^2 \pm$ $4.70 \times 10^1$	$1.89 \times 10^1 \pm$ $4.83 \times 10^0$	$4.06 \times 10^1 \pm$ $5.93 \times 10^0$
	$1.33 \times 10^3 \pm$ $2.98 \times 10^2$	$6.20 \times 10^2 \pm$ $3.60 \times 10^1$	$6.58 \times 10^2 \pm$ $3.78 \times 10^1$	$1.75 \times 10^2 \pm$ $9.09 \times 10^1$	$3.31 \times 10^2 \pm$ $7.22 \times 10^1$
1300	$2.32 \times 10^3 \pm$ $2.29 \times 10^2$	$1.04 \times 10^3 \pm$ $7.57 \times 10^1$	$1.15 \times 10^3 \pm$ $1.60 \times 10^2$	$8.48 \times 10^2 \pm$ $2.28 \times 10^2$	$9.43 \times 10^2 \pm$ $1.79 \times 10^2$
1400		$1.92 \times 10^3 \pm$ $6.09 \times 10^1$	$1.06 \times 10^3 \pm$ $3.84 \times 10^2$	$1.64 \times 10^3 \pm$ $4.12 \times 10^2$	$2.86 \times 10^3 \pm$ $7.84 \times 10^2$
1450					
1500					
$E_a$ (kJ/mol)	120	134–197	121–297	372	339

\*Note: SCSi = single-crystal Si. SCSC = single-crystal SiC. BL = black. GR = green. F = fast-growth face. SL = slow-growth face.

**Table III. Comparison of Oxidation Rates of Single-Crystal Materials**

Temp (°C)	$K_{\text{par}}(\text{SiC BL F})/K_{\text{par}}(\text{Si})$	$K_{\text{par}}(\text{SiC GR F})/K_{\text{par}}(\text{Si})$
1200	0.396	0.49
1300	0.462	0.49
1400	0.448	0.49
Equation	$N_1$	$K_{\text{par}}(\text{SiC})/K_{\text{par}}(\text{Si})^*$
(1) $\text{Si}(s) + \text{O}_2(g) = \text{SiO}_2(s)$	1.0	
(2) $\text{SiCl}(s) + \text{O}_2(g) = \text{SiO}_2(s) + \text{C}(s)$	1.0	1.0
(3) $\text{SiC}(s) + \frac{1}{2}\text{O}_2(g) = \text{SiO}_2(s) + \text{CO}(g)$	1.5	0.66
(4) $\text{SiC}(s) + 2\text{O}_2(g) = \text{SiO}_2(s) + \text{CO}_2(g)$	2.0	0.5

\*Predicted rate ratio.

parabolic rate constant,  $B$ , is defined as

$$B = 2D_{\text{eff}} C^*/N_1 \quad (3)$$

where  $D_{\text{eff}}$  is the effective diffusion coefficient of the oxidizing species,  $C^*$  is the equilibrium concentration of oxidant in the oxide, and  $N_1$  is the number of oxidant molecules incorporated into a unit volume of the oxide layer. Amorphous silica forms on both materials so it is assumed that the diffusion coefficient of the oxidant is the same for each. Likewise, the equilibrium concentration of oxidant in the oxides is assumed equal since the oxidations were carried out simultaneously. The value of the remaining parameter,  $N_1$ , will be determined by the oxidation products (i.e.,  $\text{SiO}_2$ ,  $\text{C}$ ,  $\text{CO}$ ,  $\text{CO}_2$ ). Hence, the differences in the parabolic rate constants will be inversely proportional to the ratio of the  $N_1$  values for each material. Predicted rate ratios for several possible oxidation products are listed in Table III. The actual rate ratios determined from the present data are also displayed in Table III. The data suggest that the difference in rates results from the formation of  $\text{CO}_2$  gas during silicon carbide oxidation which reduces the amount of oxidant available for formation of silicon dioxide. It is important to note that this analysis cannot differentiate between the formation of carbon dioxide at the  $\text{Si}/\text{SiO}_2$  interface and the formation of the carbon monoxide followed by oxidation to carbon dioxide at some higher oxygen potential within the oxide during outdiffusion of the gaseous byproducts.

This correlation of oxidation rates and the similar magnitude of the activation energies strongly suggest that the oxidation of the fast-growth face of silicon carbide over the temperature range 1200° to 1400°C is controlled by the same mechanism as silicon. It is relatively well established that this mechanism involves the transport of molecular oxygen by permeation across the growing oxide film.<sup>1-6</sup> The increase in activation energy above 1400°C implies that a change in oxidation mechanism takes place.

Several investigators have suggested that outward diffusion of carbonaceous species controls the overall oxidation rate in the high-temperature regime where the high activation energy is observed.<sup>7,10,34</sup> In this case the implication is that the two required sequential processes, delivery of oxidant and removal of reaction products, exchange relative rates as the temperature increases causing a change in activation energy. However, the observed activation energies cannot be explained by this reasoning because the slower of the two sequential processes will be the controlling one. The high-activation-energy process should then be rate controlling at low temperatures and the low-activation-energy process be rate controlling at high temperatures if there is a change in rate-controlling mechanism. Therefore, it is more likely that two parallel processes exchange relative rates with the high-activation-energy one being rate controlling at high temperatures. One cannot rule out change in control of the oxidation rate between two parallel processes of outdiffusion of carbonaceous species with the present data. However, a change in rate control between parallel indiffusion processes of oxidant appears more likely to the authors in view of the correlations between the oxidation rates of silicon and silicon carbide in the low-temperature regime.

Isotope labeling studies have shown that appreciable lattice diffusion of oxygen occurs during oxidation of these materials at 1300°C.<sup>1</sup> The activation energy for lattice diffusion in fused silica

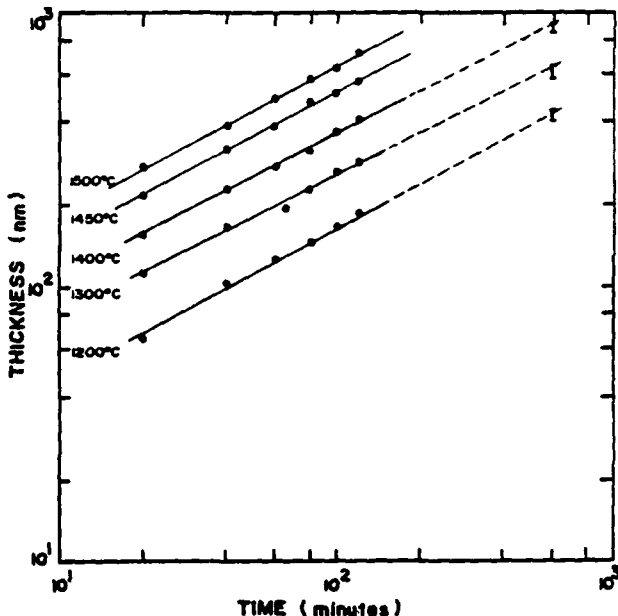


Fig. 3. Oxide thickness vs time plot for the oxidation of CNTD silicon carbide in dry  $\text{O}_2$ .

was reported by Sucov<sup>21</sup> to be 298 kJ/mol whereas recent studies indicate this value could be as high as 450 kJ/mol.<sup>22,23</sup> It is postulated here that the change in mechanism above 1400°C involves the lattice diffusion of oxidant. The similar magnitude of the calculated activation energy for the slow-growth face suggests that this mechanism applies over the entire temperature range studied. It is not clear at this time why the oxidation of the slow-growth face should be controlled by lattice diffusion instead of oxygen permeation at the lower temperatures. Additional information is necessary to further elucidate the oxygen mechanism(s) that are rate controlling in these high-activation-energy regimes. Specifically, experimental determination of the activation energy for lattice diffusion in the thermal oxides using isotope labeling results is currently under way in this laboratory. In addition, the oxygen partial pressure dependence on the oxide growth rate of each face is being studied. Whereas a linear dependence would be expected for the permeation mechanism, the lattice diffusion mechanism should exhibit a pressure dependence of one-half.

Detailed carbon labeling studies in conjunction with oxygen labeling studies are in progress to examine the outdiffusion of carbonaceous species as well.

## (2) Polycrystalline Materials

In general, the oxidation behavior of the polycrystalline materials was complicated compared to the single-crystal materials because of the higher levels of dopant cations present, the greater propensity for crystallization of the oxide films, and the multiple grain orientations on the surface being oxidized. These factors also caused considerable roughening of the oxide surface and the oxide/SiC interface which made thickness determinations difficult.

The oxide thickness data for the three polycrystalline materials are shown in Figs. 3 to 5. Parabolic oxidation behavior was exhibited by all three materials at 1200°C out to 10 h. The CNTD material exhibited parabolic oxidation at 1300° and 1400°C out to 10 h. The sintered material (SASC) exhibited similar behavior at 1300° and 1400°C up to 2 h while the 10-h data suggest that a decrease in the oxidation rate occurs at longer times. At higher temperatures, decreasing trends from parabolic behavior were observed at even shorter times. The most complicated behavior was exhibited by the hot-pressed material (HPSC). At 1200°C, parabolic behavior was found out to 10 h; at higher temperatures, decreasing and increasing oxidation trends were observed.

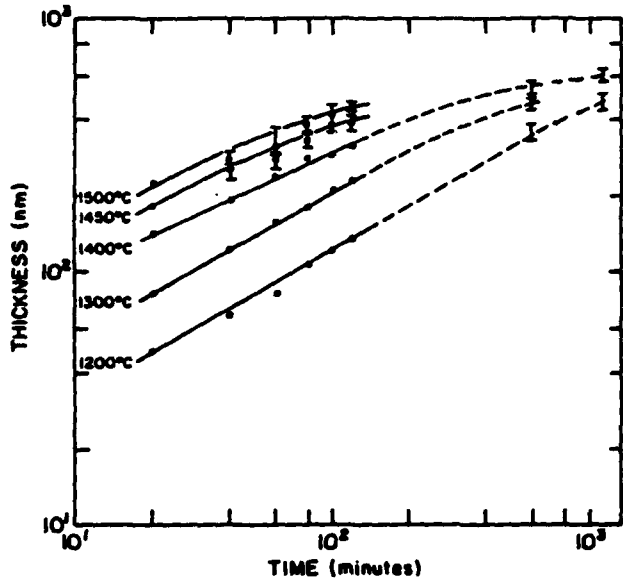


Fig. 4. Oxide thickness vs time plot for the oxidation of sintered  $\alpha$ -silicon carbide (SASC) in dry  $O_2$ .

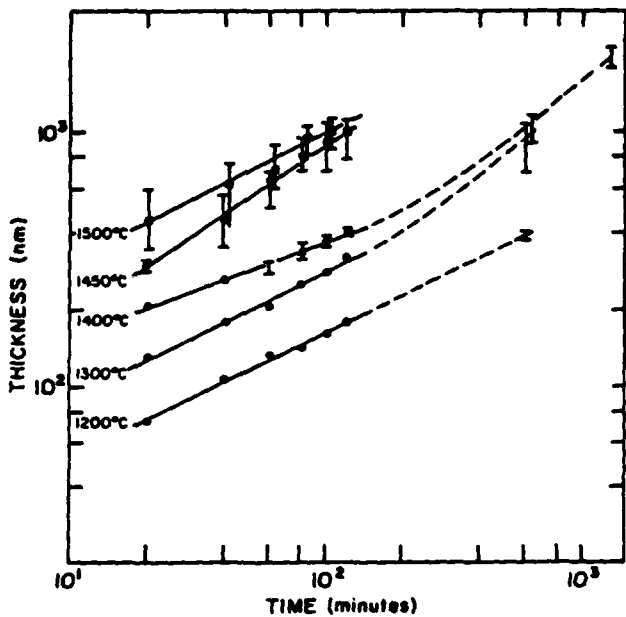


Fig. 5. Oxide thickness vs time plot for the oxidation of hot-pressed silicon carbide (HPSC) in dry  $O_2$ .

It was observed that the range of oxidation behaviors exhibited by these materials was directly related to the extent of crystallization of the oxide film. On the sintered material, crystallization of the oxide film began with the appearance of small spherulitic growth features nucleating at random multigrain junctions across the surface. Using the relationship between oxide thickness and interference colors, these features were readily observed by their color with respect to the amorphous regions. Subsequent X-ray diffraction analyses of heavily crystallized films identified these features to be cristobalite. The oxide thickness over the spherulites was considerably thinner than in the remaining amorphous regions with color estimates differing by as much as a factor of 2. This observation indicated that the transport of oxidant through the crystalline phase was considerably slower than through

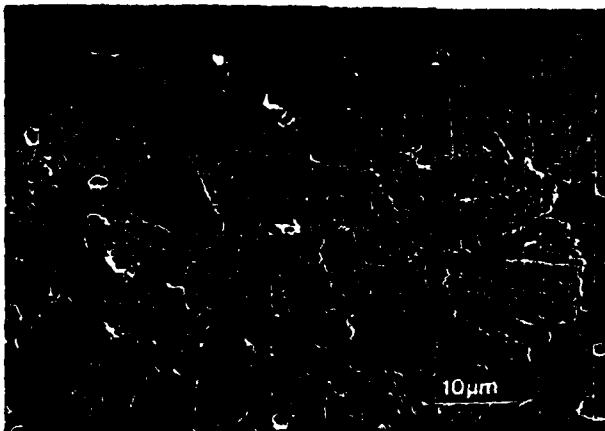


Fig. 6. Scanning electron micrograph of spherulitic features in the oxide film on sintered  $\alpha$ -silicon carbide.

the amorphous phase as previously suggested in an earlier paper.<sup>11</sup>

Decreases in parabolic behavior of the sintered material were correlated with the formation of a continuous layer of these spherulitic crystals over the silicon carbide surface. An example of this coverage is shown in Fig. 6. Delineation of the spherulitic crystals is caused by the preferential removal of the amorphous phase resulting from differences in the etch rate of the oxide phases in the buffered HF etch. Crystallite formation was not observed in the 1200°C oxidized specimens in agreement with the single parabolic behavior exhibited out to 10 h. Likewise, the oxide films on the single-crystal and CNTD materials were free of appreciable crystallization even after the most severe oxidation treatments.

The hot-pressed material exhibits a more complex crystallization behavior. Several investigations have reported the presence of cristobalite and mullite in the oxides formed on this material after long-term oxidation.<sup>11-13</sup> In the present investigation, X-ray diffraction analyses of the more heavily crystallized samples indicated the presence of cristobalite (major phase) and mullite (minor phase). At the higher oxidation temperatures ( $\geq 1400^\circ\text{C}$ ), it was observed that crystallization began in the form of spherulitic growth features similar to the sintered material. At longer times, however, an extremely fine particulate structure surrounded by a glassy matrix phase was present as shown in Fig. 7. The fine particulate structures are presumed to be mullite. Similar microstructural features were reported by MacDowell and Beall<sup>25</sup> in an investigation of the immiscibility and crystallization of  $\text{Al}_2\text{O}_3\text{-SiO}_2$  glasses. It was reported that metastable glass-in-glass separation occurs in these melts followed by the nucleation and growth of both mullite and cristobalite crystals. Depending on the heat treatment, MacDowell and Beall indicated that a variety of structures for mullite were observed including an extremely fine particulate type as reported in this investigation. In these bulk glasses, formation of cristobalite always occurred in the form of three-dimensional spherulitic crystals.

In terms of the oxidation behavior exhibited, the formation of a layer of cristobalite crystals is presumably responsible for the decreasing kinetics in much the same manner as reported for the sintered material. With increased time, and presumably, increased segregation of  $\text{Al}^{1+}$  into the oxide, the finer crystals of mullite form from the  $\text{Al}_2\text{O}_3\text{-SiO}_2$  film presumably at the expense of the cristobalite which leads to an increase in the oxidation rates. The  $\text{Al}^{1+}$  segregation manifested in the formation of mullite particles in the oxide apparently allows more rapid transport of the oxidant. Although the precise reasons for the microstructural instability in these oxidation scales are not known from the present work, the correlations of these changes with the changes in parabolic oxidation rates are quite clear.

Parabolic rate constants for the oxidation of the polycrystalline materials were calculated in the same manner as the single-crystal data and are given in Table IV. In several instances, a rate constant

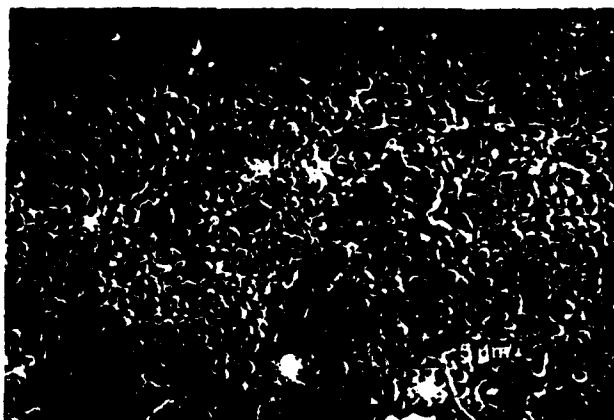


Fig. 7. Scanning electron micrograph of crystalline features in the oxide film on hot-pressed silicon carbide.

is not reported because the oxidation deviated completely from parabolic behavior. The CNTD material exhibited the highest oxidation rates in spite of the low levels of cation impurities present in the material. Free silicon, however, was identified by X-ray diffraction analyses to be present in sufficient quantities to increase its oxidation susceptibility. Of the remaining two materials, the hot-pressed variety exhibited higher oxidation rates compared to the sintered material in agreement with previously reported results.<sup>11</sup> This difference has been explained by the higher levels of additives in the hot-pressed material which effectively lowers the viscosity of the oxide film increasing the diffusivity of species across it.<sup>12-14</sup>

The temperature dependence of the parabolic rate constants for these materials is shown in Fig. 8 and calculated activation energy values are listed in Table IV. The behavior of the CNTD material was quite similar to that of the fast-growth face of the single-crystal SiC materials, suggesting that similar oxidation mechanisms were operative. Slightly larger activation energies were calculated for the hot-pressed and sintered materials. The observed values are complicated by the differing temperature dependencies present for each exposed crystal orientation on the polycrystalline surface. Earlier, it was reported that the temperature dependence of the oxidation rate on the slow- and fast-growth faces of the single-crystal SiC can be different by as much as a factor of 3. That individual grains oxidized at different rates was readily observed using optical microscopy inspection and the interference color-thickness relationship. Oxide thicknesses ranged from the values corresponding to the slow-growth-face value up to the value reported for the fast-growth face. This effect led to an average thickness value for the polycrystalline material as shown in Fig. 9, where the thickness data for the sintered  $\alpha$  polycrystalline material are compared with those of the green single-crystal material at 1200° and 1400°C. In each case, the SASC data are bracketed by the single-crystal data. In turn, the observed temperature dependence of the polycrystalline material should be a composite value of temperature dependencies of individual crystal orientations.

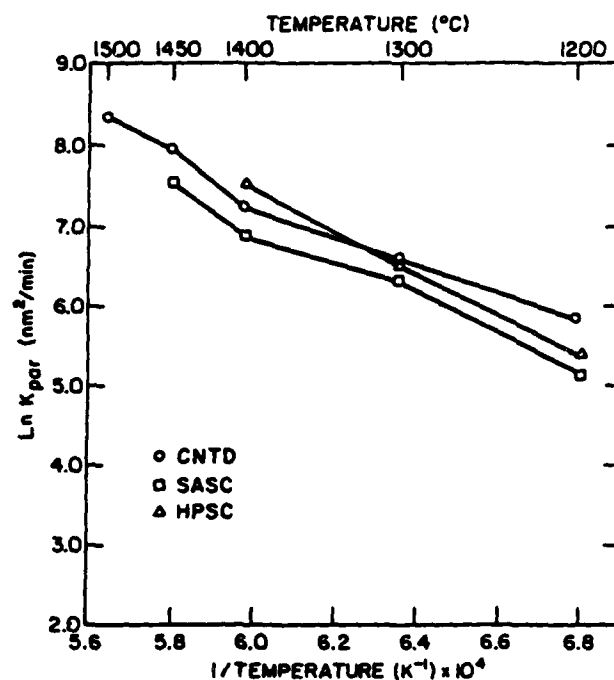


Fig. 8. Temperature dependence of parabolic rate constants for the polycrystalline materials oxidized in dry O<sub>2</sub>.

Thermogravimetric analysis (TGA) was used to characterize the long-term oxidation behavior (up to 24 h) of the hot-pressed and sintered materials. The technique is not as sensitive as the thickness measurement for short-term data but is better suited at longer times where oxide roughening and crystallization preclude the use of the thickness measurement techniques. Data were obtained for both materials at 1400°C but only the sintered material was measured at 1300°C. Similar to the short-term results, the hot-pressed material exhibited a higher oxidation susceptibility than the sintered material. Parabolic oxidation behavior was observed for the sintered material at both temperatures out to 24 h. The hot-pressed material exhibited two separate parabolic oxidation regimes at 1400°C with an increased rate occurring after  $\approx 6$  h, presumably due to the changes in the oxide scale composition and morphology discussed above. Parabolic rate constants calculated from the data using polynomial regression are listed in Table V. For the hot-pressed material, the higher rate is reported.

For direct comparison of the short- and long-term data, it was necessary to convert to similar units. The weight gain units ( $\text{g}^2/\text{cm}^4 \cdot \text{h}$ ) were converted into units of  $\text{nm}^2/\text{min}$  taking into account losses due to volatile oxidation byproducts, the oxide density, and the oxygen partial pressure differences. The actual conversion factors used to change into the thickness units were  $2.15 \times 10^{12}$  and  $1.43 \times 10^{12}$  at 1300° and 1400°C, respectively. The converted TGA data shown in Table V are significantly different from the short-term data, the value for the sintered material being a factor of 4 smaller and the hot-pressed material being a

Table IV. Parabolic Rate Constants and Activation Energies for the Oxidation of the Polycrystalline Materials in Dry Oxygen

Temp (°C)	$k_{par}$ (nm <sup>2</sup> /min)		
	CNTD	SASC	HPSC
1200	$3.44 \times 10^2 \pm 5.34 \times 10^1$	$1.75 \times 10^2 \pm 8.7 \times 10^1$	$2.20 \times 10^2 \pm 8.20 \times 10^1$
1300	$7.45 \times 10^2 \pm 2.03 \times 10^2$	$5.40 \times 10^2 \pm 7.11 \times 10^1$	$6.95 \times 10^2 \pm 2.11 \times 10^2$
1400	$1.37 \times 10^3 \pm 2.55 \times 10^2$	$9.49 \times 10^2 \pm 2.72 \times 10^2$	$1.86 \times 10^3$ *
1450	$2.69 \times 10^3 \pm 5.37 \times 10^2$	$1.77 \times 10^3$ *	
1500	$4.51 \times 10^3 \pm 7.58 \times 10^2$		
$E_a$ (kJ/mol)	142-293	217-289	221

\*Two thickness values used to calculate rate.

**Table V. Comparison of Oxidation Behavior of Polycrystalline Materials Using Thermogravimetric Analysis (TGA) and Thickness Measurements**

Temp (°C)	TGA analysis ( $\text{g}^2/(\text{cm}^4 \cdot \text{h})$ )		$K_{\text{par}}$		Thickness measurements ( $\text{nm}^2/\text{min}$ )	
	SASC	HPSC	SASC	HPSC	SASC	HPSC
1300	$6.21 \times 10^{-11}$			$1.30 \times 10^2$		$5.4 \times 10^2$
1400	$1.68 \times 10^{-10}$	$4.02 \times 10^{-9}$		$2.41 \times 10^2$	$5.74 \times 10^3$	$9.49 \times 10^2$
$E_a$ (kJ/mol)	218				173	213

$$\bullet K_{\text{par}} \left( \frac{\text{nm}^2}{\text{min}} \right) = K_{\text{par}} \left( \frac{\text{cm}^2}{\text{min}^4 \cdot \text{h}} \right) \times \left( \frac{\text{wt of oxide}}{\text{wt gain}} \right)^2 \times \left( \frac{1}{\text{density of oxide}} \right)^2 \times (\text{pressure factor})$$

Specific conversion factors are discussed in the text.

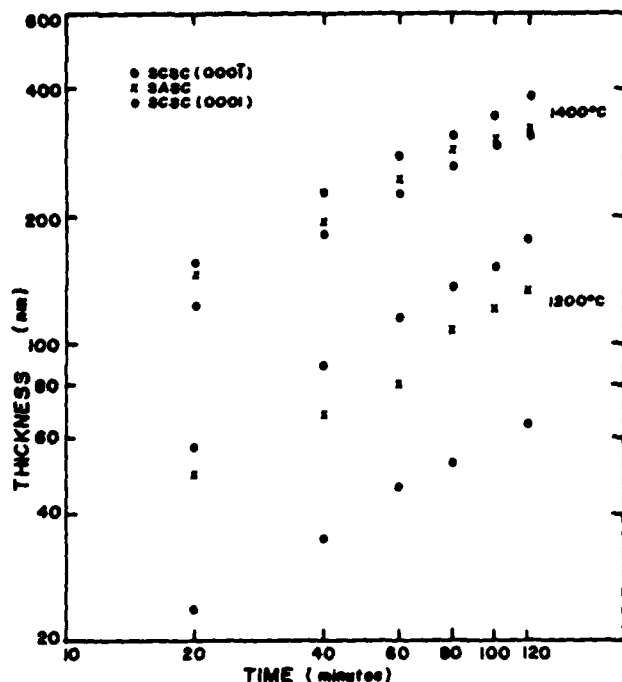


Fig. 9. Comparison of the oxidation kinetics of single-crystal and sintered  $\alpha$ -silicon carbide materials in dry  $O_2$ .

factor of 3 higher. Whereas the magnitudes of these differences are somewhat uncertain because of the assumptions necessary to convert the data, the overall trends are quite relevant. As described earlier, the differing oxidation behaviors of the polycrystalline materials are rather sensitive to structural changes within the oxide. The sintered material exhibited a decreasing oxidation behavior at long times due to the formation of a continuous layer of spherulitic cristobalite crystals through which the transport of oxidant or reaction product species was significantly reduced. As a result, the long-term data indicated a reduced parabolic oxidation rate compared to the short-term results. The hot-pressed material exhibited a much more complex oxide crystallization causing decreasing and increasing oxidation behaviors. At long times, the deterioration of the protective crystallized film causes an enhanced oxidant transport with significantly higher oxidation rates compared to those reported from the short-term results. Measurements of the final oxide thickness on the oxidized TGA specimens were also made and compared to the thickness results. Within experimental error and after compensating for the reduced pressures used in the TGA case, the thicknesses are in good agreement with the values predicted by the dashed curves in Figs. 4 and 5.

#### IV. Summary and Conclusions

It has been shown that the basal plane of SiC which exhibits a fast oxidation rate behaves similarly to a single-crystal silicon in the temperature range 1200° to 1400°C. The lower oxidation rates for silicon carbide can be explained by the additional demands for oxidant to oxidize the carbon in the silicon carbide case. These results and the similar activation energies (120 kJ/mol) strongly suggest that oxidation in this regime is controlled by the permeation of molecular oxygen through the growing oxide film. At temperatures greater than 1400°C, the significantly increased activation energy indicates a change in oxidation mechanism. Lattice diffusion of oxygen is suggested as the rate-controlling mechanism in light of the relative agreement of activation energies and the isotope labeling experiments which have verified the appreciable transport of oxidant by this mechanism at temperatures above 1300°C. The slow-growth face exhibited lower oxidation rates and a higher activation energy over the entire temperature range which is not understood in the context of oxidant or product diffusion through an amorphous scale. Additional studies are necessary to further elucidate the rate-controlling process(es) in these high-activation-energy regimes.

The oxidation behavior of the polycrystalline materials is similar to the single-crystal behavior but is significantly altered by several factors. The oxidation rates of the sintered  $\alpha$ -SiC are bracketed by the fast- and slow-growth faces of the single-crystal material, presumably because of the random orientation of the individual grains. The observed activation energies for the polycrystalline materials are generally intermediate to those observed for the various single-crystal faces. The presence of higher concentrations of impurities altered the oxidation behavior by forming low-viscosity oxides which increase the oxidant flux to the growth interface. A much higher susceptibility to crystallization was exhibited by the polycrystalline materials due to this reduced viscosity and the numerous nucleation sites such as multigrain junctions. The decreasing trend in the oxidation rate with time of the sintered  $\alpha$  material at higher temperatures coincides with the formation of a layer of spherulitic cristobalite crystals at the growth interface which apparently reduces the oxidant transport through the growing oxide. For the hot-pressed material, spherulitic crystallization is followed by the apparent disruption of the cristobalite layer and formation of fine scale crystals, presumably mullite, which allow an increased flux of oxidant to the interface. Thus, a decreasing trend in the oxidation rate was followed by a substantial increase in the oxidation rate. These trends in oxidation behavior for the polycrystalline materials are accentuated in long-term experiments as determined by thermogravimetric analyses. The sintered material exhibited a reduced parabolic growth rate after 24 h while the hot-pressed material exhibited an increased parabolic growth rate compared to the rates derived from film thickness measurements at shorter times.

**Acknowledgment:** We thank H. Graham, Wright-Patterson Air Force Base, Dayton, OH, for his help with the thermogravimetric analysis.

## References

- <sup>1</sup>B. E. Deal and A. S. Grove, "General Relationship for the Thermal Oxidation of Silicon," *J. Appl. Phys.*, **36** [12] 3770-78 (1965).
- <sup>2</sup>F. J. Norton, "Permeation of Gaseous Oxygen Through Vitreous Silica," *Nature (London)*, **191**, 701 (1961).
- <sup>3</sup>P. J. Jorgensen, "Effect of an Electric Field on Silicon Oxidation," *J. Chem. Phys.*, **37**, 874-77 (1962).
- <sup>4</sup>E. Rosenthaler, A. Straboni, S. Rigo, and G. Ansel, "An  $^{18}\text{O}$  Study of the Thermal Oxidation of Silicon in Oxygen," *Appl. Phys. Lett.*, **34**, 254-56 (1979).
- <sup>5</sup>J. A. Costello and R. E. Tressler, "Isotope Labelling Studies of the Oxidation of Silicon at 1000 and 1300°C," *J. Electrochem. Soc.*, **131** [8] 1944-47 (1984).
- <sup>6</sup>K. Mozzfeldt, "On the Rates of Oxidation of Silicon and of Silicon Carbide in Oxygen, and Correlation with Permeability of Silica Glass," *Acta Chem. Scand.*, **18** [7] 1596-606 (1964).
- <sup>7</sup>R. F. Admasyk, "Oxidation of Silicon Carbide in the Temperature Range 1200 to 1500°C," *J. Phys. Chem.*, **63**, 305-307 (1959).
- <sup>8</sup>R. C. A. Harris, "Oxidation of 6-H SiC Platelets," *J. Am. Ceram. Soc.*, **58** [1-2] 7-9 (1975).
- <sup>9</sup>W. Von Milach and I. Pfaffendorf, "Thermal Oxidation and Electrolytic Etching of SiC," *J. Electrochem. Soc.*, **122** [5] 642-43 (1975).
- <sup>10</sup>A. Suzuki, H. Ashida, N. Funai, K. Matsuura, and H. Matsunami, "Thermal Oxidation of SiC and Electrical Properties of Al-SiO<sub>x</sub>-SiC MOS Structure," *Jpn. J. Appl. Phys.*, **21** [4] 579-83 (1982).
- <sup>11</sup>J. A. Costello and R. E. Tressler, "Oxidation Kinetics of Hot-Pressed and Sintered  $\alpha$ -SiC," *J. Am. Ceram. Soc.*, **64** [5-6] 327-31 (1981).
- <sup>12</sup>J. W. Hinze, W. C. Tripp, and H. C. Graham, "The High Temperature Oxidation of Hot-Pressed Silicon Carbide," pp. 409-21 in *Mass Transport Phenomena in Ceramics*. Edited by A. R. Cooper and A. H. Heuer. Plenum Publishing Co., New York, 1975.
- <sup>13</sup>S. C. Singhal, "Oxidation Kinetics of Hot-Pressed SiC," *J. Mater. Sci.*, **11** 1246-53 (1976).
- <sup>14</sup>E. Fitzer and R. Ebi, "Kinetic Studies on the Oxidation of Silicon Carbide," pp. 320-28 in *Silicon Carbide 1973*. Edited by R. C. Marshall, J. W. Faust, and C. E. Ryan. University of South Carolina Press, Columbia, SC, 1973.
- <sup>15</sup>J. Schlichting, "SiC as an Oxidation Reactant Refractory Material. Parts I and II," *Ber. Dtsch. Keram. Ges.*, **56** [8-9] 196-206 (1979).
- <sup>16</sup>J. Schlichting and K. Kriegsmann, "Oxidation Behaviour of Hot-Pressed SiC," *Ber. Dtsch. Keram. Ges.*, **56** [3-4] 72-75 (1979).
- <sup>17</sup>S. C. Singhal and F. F. Lange, "Effect of Alumina Content in the Oxidation of Hot-Pressed SiC," *J. Am. Ceram. Soc.*, **58** [9-10] 433-35 (1975).
- <sup>18</sup>J. A. Costello, R. E. Tressler, and I. S. T. Tsong, "Boron Redistribution in Sintered  $\alpha$ -SiC During Thermal Oxidation," *J. Am. Ceram. Soc.*, **64** [5-6] 332-35 (1981).
- <sup>19</sup>A. S. Grove, O. Leistiko, Jr., and C. T. Sah, "Redistribution of Acceptor and Donor Impurities During Thermal Oxidation of Silicon," *J. Appl. Phys.*, **35** [9] 2693-704 (1964).
- <sup>20</sup>E. A. Irene and R. Ghez, "Silicon Oxidation Studies: The Role of H<sub>2</sub>O," pp. 313-23 in *Semiconductor Silicon 1977*. Edited by H. R. Huff and E. Sirth. The Electrochemical Society, Inc., New York, 1977.
- <sup>21</sup>E. W. Sucov, "Diffusion of Oxygen in Vitreous Silica," *J. Am. Ceram. Soc.*, **46** [11] 14-20 (1963).
- <sup>22</sup>R. H. Doremus, "Oxidation of Silicon by Water and Oxygen and Diffusion in Fused Silica," *J. Phys. Chem.*, **80** [16] 1773-75 (1976).
- <sup>23</sup>J. Mikkelson: private communication, 1983.
- <sup>24</sup>See, for example, D. M. Mieskowski, T. E. Mitchell, and A. H. Heuer, "Bubble Formation in Oxide Scales on SiC," *J. Am. Ceram. Soc.*, **67** [1] C-17-C-18 (1984).
- <sup>25</sup>J. F. McDowell and G. H. Beall, "Immiscibility and Crystallization in Al<sub>2</sub>O<sub>3</sub>-SiO<sub>2</sub> Glasses," *J. Am. Ceram. Soc.*, **52** [1] 17-25 (1969). □

Reprinted from the *Journal of the American Ceramic Society*, Vol. 71, No. 6, June 1988  
Copyright 1988 by The American Ceramic Society, Inc.

*J. Am. Ceram. Soc.*, 71 [6] 472-77 (1988)

## Accumulation of Creep Damage in a Siliconized Silicon Carbide

DANIEL F. CARROLL\* and RICHARD E. TRESSLER\*

Department of Materials Science and Engineering, The Pennsylvania State University, University Park, Pennsylvania 16802

The accumulation of creep damage in a siliconized silicon carbide was investigated as a function of applied stress, creep strain, and microstructure. At 1100°C, creep damage was observed to accompany deformation in specimens tested to creep strains greater than 0.10%, under applied stresses greater than 137 MPa. At low creep strains, creep damage occurred in regions of the microstructure of high silicon carbide content. As deformation progressed, creep damage extended into regions of the microstructure of lower silicon carbide content. The area density and area fraction of cavities were found to increase linearly with creep strain. From these results, a threshold stress for the formation of creep damage was determined to be 132 MPa at 1100°C. It was suggested that the formation of creep damage was controlled by the heterogeneous nucleation of cavities at the silicon-silicon carbide interface, with the aid of high localized stresses and iron impurities in the silicon phase.

### I. Introduction

SILICON CARBIDE based ceramics are currently being considered for high-temperature structural applications due to their good mechanical strength and oxidation resistance at elevated temperatures.<sup>1,2</sup> One such material is siliconized silicon carbide. Siliconized silicon carbide is a two-phase material whose microstructure consists of interpenetrating phases of silicon and silicon carbide. The silicon phase is dispersed throughout the continuous silicon carbide phase in either a continuous or noncontinuous matrix, depending upon the amount of free silicon in the material.

Past investigations have shown that cavity formation or creep damage occurs in some types of siliconized carbides under load at elevated temperatures.<sup>2-3</sup> In these bend tests, the creep damage was confined to the tensile side of the bend beams and increased with deformation. Carroll and Tressler<sup>3</sup> have shown that this creep damage can result in strength degradation at room temperature. Wiederhorn *et al.*<sup>4</sup> have shown that creep damage can also lead to strength degradation and failure at elevated temperatures. Since strength degradation and delayed failure can occur in siliconized silicon carbide, the accumulation of creep damage must be understood as a function of deformation, before these materials can be used in high-temperature structural applications.

Typically, deformation studies are conducted in bending. However, stress redistribution may occur in a bend beam during deformation. Stress redistribution is possible when a material exhibits

Manuscript No. 199921. Received July 15, 1987; approved December 9, 1987.  
Presented at the 89th Annual Meeting of the American Ceramic Society, Pittsburgh,  
PA, April 28, 1987 (Basic Science Division, Paper No. 143-B-87).  
Supported in part by the U.S. Army Research Office, Metallurgy and Materials  
Science Division.

\*Member, the American Ceramic Society.

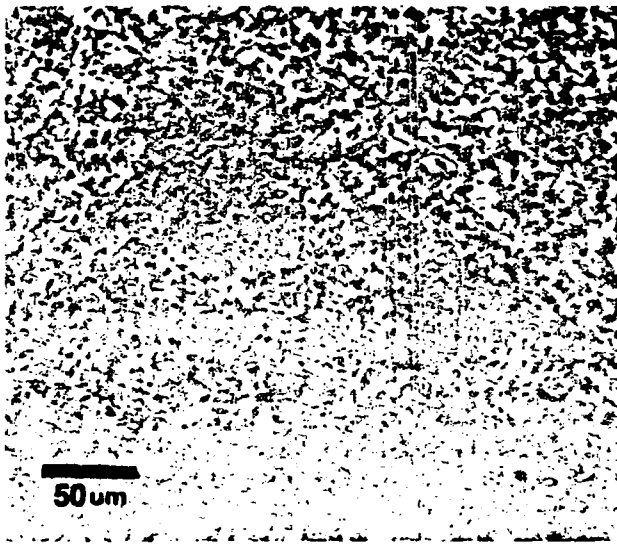


Fig. 1. Optical micrograph of the as-received siliconized silicon carbide.

nonlinear creep or a different creep rate in tension than in compression.<sup>6,7</sup> This process results in the reduction of the outer tensile fiber stress with time. A changing stress state in the bend beam can complicate an analysis of the creep behavior and the damage accumulation process.

Many investigations have shown that stress redistribution does occur in siliconized silicon carbides tested in bending at elevated temperatures.<sup>3,4,8,9</sup> Creep deformation studies in bending, conducted by Wiederhorn *et al.*<sup>4</sup> at 1300°C, have shown that siliconized silicon carbide exhibits only primary creep at stresses less than 200 MPa. At stresses greater than 250 MPa, they observed primary creep with a transition to tertiary creep. The extended primary creep behavior was a result of stress redistribution, which reduced the outer tensile fiber stress of the bend beam. Therefore, in order to avoid complications caused by stress redistribution, investigations of creep deformation and damage accumulation must be conducted in a uniform stress state.

The objective of this study was to investigate the creep behavior of a siliconized silicon carbide under uniaxial tension and to quantify the accumulation of creep damage as a function of deformation. The results will be discussed in two papers. This paper will deal with the accumulation of creep damage as a function of stress, creep strain, and microstructure. The subsequent paper will summarize the creep results and discuss the contribution of creep damage to the deformation process.<sup>10</sup>

## II. Experimental Procedure

### (1) Material

The material used in this investigation was a siliconized silicon carbide\* containing approximately 33.7 to 35.7 vol% free silicon metal and 4- to 6- $\mu\text{m}$  silicon carbide grains. An optical micrograph of the as-received material is shown in Fig. 1. The light gray regions of the microstructure correspond to the continuous silicon matrix while the dark gray regions are the silicon carbide grains. No porosity was observed in the as-received material. The silicon carbide grains are not evenly distributed throughout the microstructure. Some regions contain a higher density of silicon carbide grains than the surrounding microstructure. A backscattered electron micrograph of a high-density silicon carbide region (Fig. 2) revealed that a third phase is also confined to these areas. Energy-

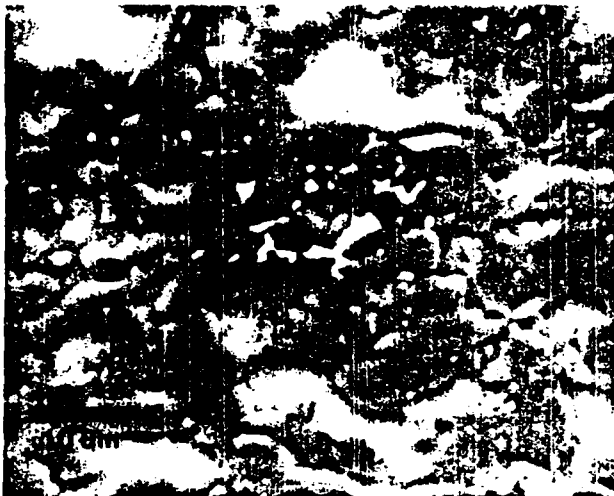


Fig. 2. SEM micrograph of the as-received siliconized silicon carbide, showing a third phase confined to regions of the microstructure of high silicon carbide content.

dispersive X-ray spectroscopy determined that the third phase contained a high concentration of iron. Occasionally, a high concentration of titanium and vanadium is also found.

### (2) Creep Tests

Creep tests were conducted in tension under stresses ranging from 103 to 172 MPa at temperatures of 1100° to 1200°C in air. The design of the tensile specimen was similar to the modified flat dog-bone-shaped specimen used by Wakai *et al.*<sup>11</sup> An electro-optical extensometer was used to measure creep deformation as a function of time. The specimen design and testing technique will be discussed in a companion paper.<sup>10</sup> Typically, tensile specimens were deformed under a constant applied stress and temperature, to a desired creep strain. The deformed specimens were then analyzed using scanning and transmission electron microscopy to quantify the amount of creep damage in the gauge sections.

### (3) Quantitative Microscopy

The accumulation of creep damage was quantified by measuring the area density and area fraction of cavities in each deformed gauge section. The area density and area fraction of cavities were determined on two to three sections of each gauge length. The gauge sections were cut parallel to the stress axis. Each section was polished to a 1- $\mu\text{m}$  finish and examined with the scanning electron microscope. Fifteen equally spaced areas along the center line of each longitudinal section were examined for creep damage. SEM micrographs of each area were taken at a magnification of 500 $\times$  for quantitative analysis. Each micrograph was enlarged to an effective magnification of 1000 $\times$  so that the area density and area fraction of cavities could be easily determined.

The microstructural dependence of the creep damage process was determined by examining the relationship between the interparticle distance of the silicon carbide grains and the location of creep damage in the microstructure, as a function of deformation. In this analysis, approximately five areas of a deformed gauge section were examined at a magnification of 1000 $\times$ . Each area contained approximately 1800 grains. In these selected areas of microstructure, the average radius ( $r$ ) of each silicon carbide grain with a cavity at its boundary was measured and normalized to its average interparticle distance ( $d$ ). The interparticle distance ( $d$ ) was defined as the distance between the centers of neighboring silicon carbide grains. The size of the cavity was not included in this measurement. The total number of grains which had a cavity at its boundary, with a particular  $r/d$  range, was then normalized by the total number of grains with cavities. This calculation resulted in the fraction of grains with cavities, as a function of  $r/d$ .

\*KX-01, Standard Oil Engineered Materials Co., Niagara Falls, NY.

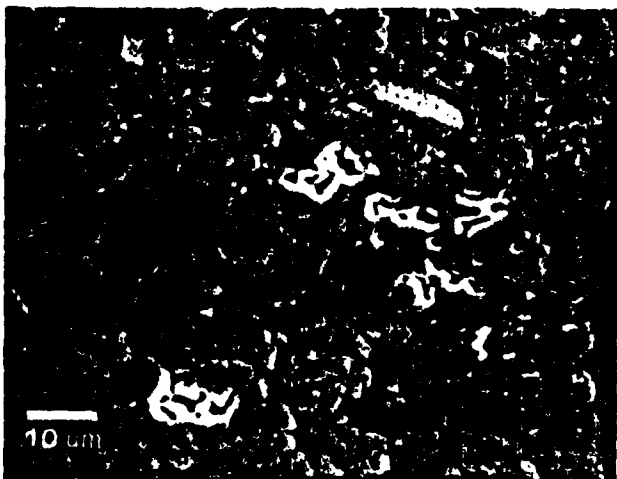


Fig. 3. SEM micrograph of creep damage in a specimen tested under a stress of 172 MPa to a creep strain of 0.30%, at 1100°C.

The relationship between the silicon carbide interparticle distance and the location of creep damage in the microstructure was determined by conducting this analysis as a function of creep strain.

### III. Results

#### (1) Creep Damage

The microstructures of deformed specimens tested at 1100°C under stresses ranging from 103 to 172 MPa were analyzed using scanning electron microscopy. The results show that at the lower stresses of 103 and 120 MPa, no observable microstructural changes occurred in any of the deformed specimens. However, for the specimens tested at the higher applied stresses of 137, 155, and 172 MPa, creep damage was observed to accompany deformation. Figure 3 is a secondary electron image of the creep damage in a specimen tested under an applied stress of 172 MPa to a creep strain of 0.30% at 1100°C. Although the cavities which formed during deformation were randomly distributed throughout the microstructure, they always formed at silicon–silicon carbide interfaces. No cavities were observed isolated in the silicon phase. Generally, there was an absence of cavity coalescence, except in locations near the fracture surfaces of specimens tested to failure.

#### (2) Area Density and Area Fraction of Cavities

The results of the area density and area fraction of cavities for the specimens deformed under the various stress levels at 1100°C are

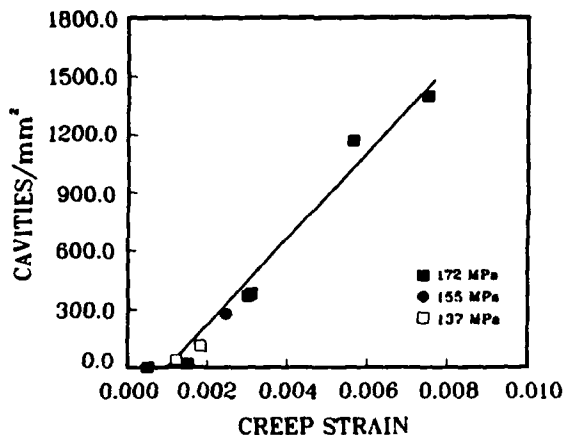


Fig. 4. Area density of cavities as a function of creep strain at 1100°C.

shown in Figs. 4 and 5, respectively. Both the area density and the area fraction of cavities increased linearly with creep strain with little or no stress dependence. The data points for the specimens tested at the lower stresses of 103 and 120 MPa were omitted, since no creep damage was observed under these stress levels. From these results, it appears that a threshold creep strain may exist for the formation of creep damage. A threshold strain of 0.10% is approximately the creep strain at the transition from primary to secondary creep behavior.<sup>10</sup> This result suggests that creep damage does not form until the latter stages of primary creep behavior or the initial stages of secondary creep behavior. To investigate this point, a specimen was deformed under a stress of 172 MPa at 1100°C, to a creep strain of 0.05%. This test lasted for approximately 8 h and was terminated in the early stages of the primary creep regime. Microstructural analysis of the specimen revealed no creep damage.

Specimens tested at lower stresses, where creep damage was not observed, were typically interrupted after reaching creep strains of 0.10% to 0.12%. To determine whether creep damage would eventually form at the lower stresses at larger creep strains, a specimen was deformed under a stress of 103 MPa to a creep strain of 0.18%. This test was conducted at a higher temperature of 1200°C so that an appreciable amount of deformation could be obtained in a reasonable amount of time (approximately 250 h). It was assumed that the same rate-controlling mechanism for creep at 1100°C controlled deformation at 1200°C. This assumption is reasonable since the activation energies for steady-state creep are approximately the same at 1100° and 1200°C for this stress level.<sup>10,12</sup> Microstructural analysis of this deformed specimen revealed no creep damage. Therefore, these results suggest that at 1100°C, a threshold stress for creep damage may exist between the applied stresses of 120 and 137 MPa.

#### (3) Threshold Stress for Creep Damage

A threshold stress for creep damage at 1100°C can be predicted by plotting the rate at which the area fraction of cavities develops with time versus the applied stress (Fig. 6). The rate at which the area fraction of cavities developed with time was determined by dividing the area fraction of cavities in the specimen by the total time of the creep test spent above the threshold strain of 0.10%. This analysis was only conducted for the specimens interrupted during the secondary creep regime. The threshold stress for creep damage can be estimated by extrapolating a line through the data and determining the *x* intercept. A threshold stress of approximately 132 MPa is determined from this analysis. This result suggests, at applied stresses below 132 MPa, that creep damage will not occur during deformation. However, under applied stresses greater than 132 MPa, creep damage will form and contribute to deformation.

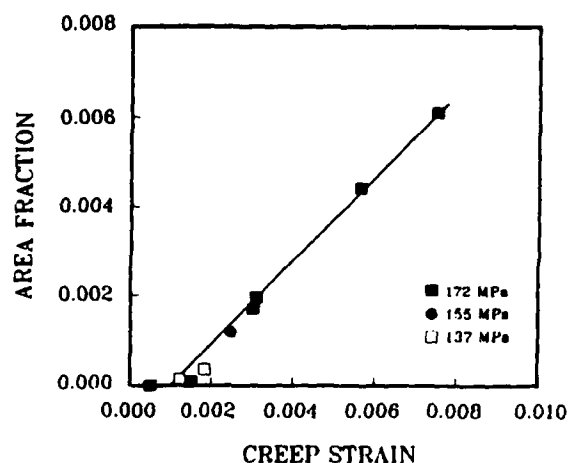


Fig. 5. Area fraction of cavities as a function of creep strain at 1100°C.

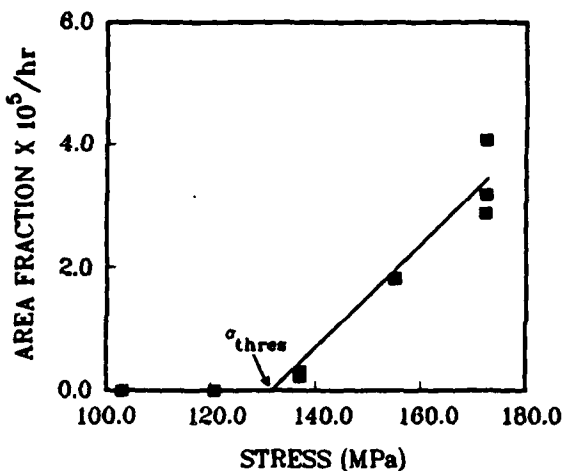


Fig. 6. Rate at which the area fraction of cavities developed with time versus applied stress, at 1100°C.

#### (4) Microstructural Dependence of Creep Damage

The accumulation of creep damage as a function of creep strain is shown in Figs. 7(A) and (B). These specimens were tested at 1100°C under an applied stress of 172 MPa to creep strains of 0.30% and 0.75%, respectively. These micrographs show that at low creep strains (Fig. 7(A)), cavities tend to form in clusters throughout the gauge length. At higher creep strains (Fig. 7(B)), the cluster regions are still evident but the density of individual cavities has increased. A closer look at a cluster region (Fig. 8) reveals that these cavities formed in the areas of the microstructure containing a higher silicon carbide content. The individual cavities, however, were generally confined to regions of the microstructure containing a lower silicon carbide content. These results suggest that at low creep strains, cavities tend to form in regions of the microstructure which contain a high volume fraction of silicon carbide grains. At higher creep strains, cavities then tend to form in regions of the microstructure of lower silicon carbide content. In order to support this observation, a quantitative analysis

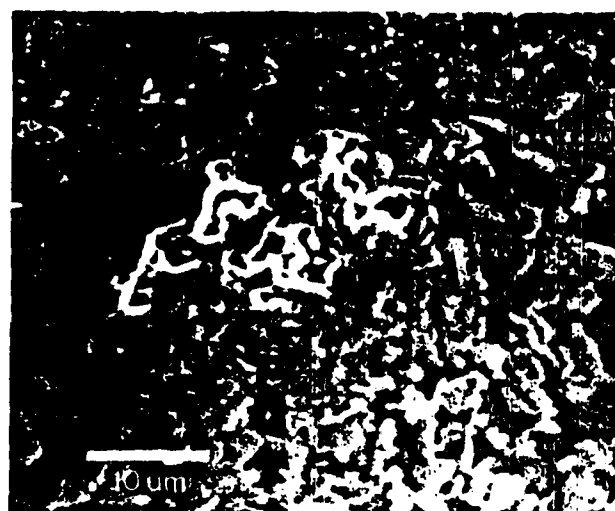


Fig. 8. High magnification of a cavity cluster in a specimen tested under 172 MPa to a creep strain of 0.30%, at 1100°C.

involving the relationship between the location of creep damage and silicon carbide interparticle distance was conducted, as described in the Experimental Procedure.

The relationship between  $r/d$  and the location of creep damage in the microstructure for two deformed specimens is shown in Fig. 9. These two specimens were deformed under an applied stress of 172 MPa at 1100°C to creep strains of 0.11% and 0.31%. In this analysis, large  $r/d$  values correspond to the area of the microstructure of high silicon carbide content whereas small  $r/d$  values correspond to regions of low silicon carbide content. At a creep strain of 0.11%, the majority of the cavities formed at grains with  $r/d$  values greater than 0.5.<sup>1</sup> At the higher creep strain of 0.31%, the majority of the cavities formed at grains with lower  $r/d$  values ranging from 0.3 to 0.5. These results confirm that during deformation, cavities first form in regions of high silicon carbide content and then extend into the regions of lower silicon carbide content.

## IV. Discussion

### (1) Accumulation of Creep Damage

The results of the quantitative microscopy have shown that the

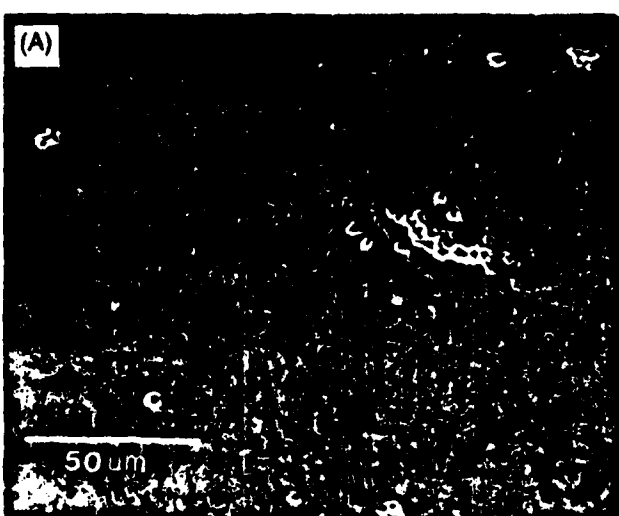
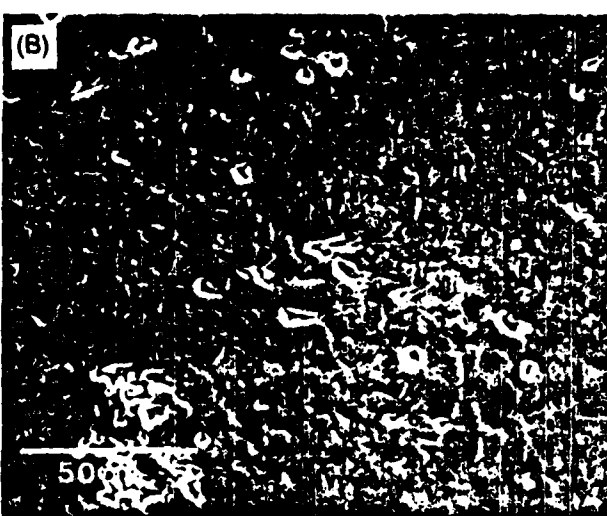


Fig. 7. Accumulation of creep damage for specimens tested under a stress of 172 MPa, at 1100°C, to creep strains of (A) 0.30%, and (B) 0.75%.



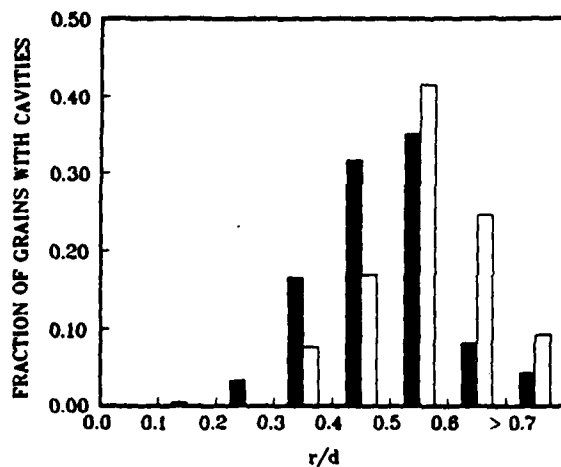


Fig. 9. Fraction of grains in the microstructure with a particular  $r/d$  range which formed a cavity at 1100°C. Specimens tested under a stress of 172 MPa to creep strains of 0.11% (□) and 0.31% (■).

area density of cavities increased linearly with creep strain with little stress dependence. This result indicates that under applied stresses where cavity formation occurs, creep damage accumulates linearly with deformation. The continuous formation of creep damage is most likely the result of load transfer in the material. During creep deformation, the stress state in the siliconized silicon carbide is nonuniform since the areas of high silicon carbide content cannot deform as fast as the surrounding matrix.<sup>13</sup> This nonuniform stress state makes cavity formation more energetically favorable in areas of the microstructure where the stress concentrations are the highest. When a cavity forms, the stress carried across that boundary is transferred to the surrounding matrix. This localized load transfer changes the stress state throughout the material, thus making cavity formation more energetically favorable in other areas of the microstructure. This load-transfer process enables creep damage to accumulate with deformation.

A linear relationship was also observed in the area fraction results as well as the area density results. This relationship suggests that once cavities form, they must grow very rapidly to an equilibrium size, whereupon further growth with creep strain is minimal. If significant cavity growth had occurred with deformation, an exponential relationship would have been observed in the area fraction results. Microstructural evidence supports this conclusion. There is no observable difference in cavity size for specimens deformed to creep strains of 0.11% and 0.75%. The size of all cavities was limited to the length of the silicon carbide grain facets. This maximum size suggests that the cavities are limited by the constraint imposed by the silicon carbide grains. Since no cavities smaller than the silicon carbide grain facets were observed in this analysis, cavity growth must occur very rapidly under these test conditions. This result suggests that cavity growth is not the limiting step in the formation of creep damage in this material.

## (2) Formation of Creep Damage

In order to provide more information about the formation of creep damage, transmission electron microscopy was used to investigate the cavity formation process in deformed specimens. Many attempts were made to view the creep damage process in its early stages of formation. However, this analysis proved to be fruitless, since all of the observed creep cavities had already grown to the size of the silicon carbide grain facet. The lack of evidence for the early stages of cavity formation, again, supports the conclusion that cavity growth occurs very rapidly in this material. The only evidence suggesting how creep damage forms is shown in Fig. 10. This figure shows the latter stages of cavity formation in the intergranular silicon phase between two silicon carbide grains. On this boundary, a large cavity has already grown the length of

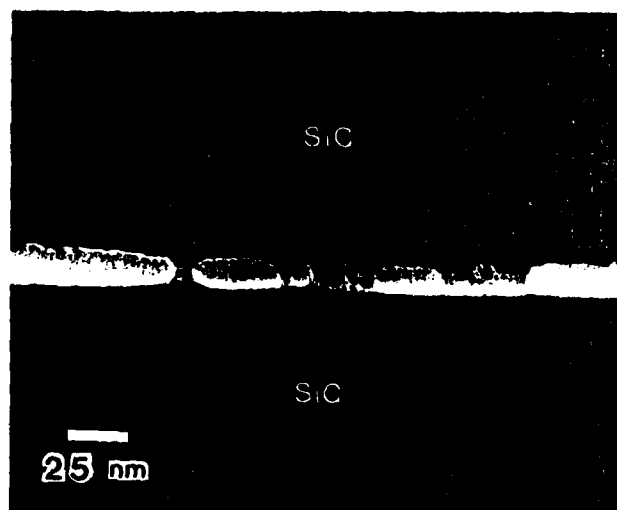


Fig. 10. TEM micrograph of cavity formation in the silicon phase between two silicon carbide grains.

the silicon carbide grain facet. This portion of the boundary is the only remaining ligament in the silicon phase. The formation of creep damage appears to be the result of multiple cavity nuclei in the silicon phase growing together to form a large cavity. In the as-received material, preexisting cavities or voids of this type are not observed along these boundaries.<sup>12</sup> Therefore, the formation of creep damage may be controlled by the nucleation of these cavities.

If the formation of creep damage is nucleation controlled, the threshold stress for creep damage predicted in Fig. 6 describes that stress level below which the rate of cavity nucleation becomes infinitesimally small. In order to determine whether cavity nucleation can occur in this material at 1100°C for applied stresses greater than the threshold, the rate of cavity nucleation was calculated using nucleation theory.

If the cavities are assumed to nucleate heterogeneously at the silicon–silicon carbide interface, the rate of nucleation ( $\dot{n}$ ) is proportional to<sup>14</sup>

$$\dot{n} \propto \exp \left\{ \left( \frac{-16\pi\gamma_{Si}}{3\sigma_i kT} \right) \left( \frac{(2 + \cos\Theta)(1 - \cos\Theta)^2}{4} \right) \right\} \quad (1)$$

where  $\gamma_{Si}$  is the surface energy of the silicon,  $\sigma_i$  is the local stress in the boundary phase,  $k$  is Boltzmann's constant,  $T$  is temperature, and  $\Theta$  is the contact angle of nucleation. The  $\cos\Theta$  term is determined by the surface energies of the silicon ( $\gamma_{Si}$ ), silicon carbide ( $\gamma_{SiC}$ ), and silicon on silicon carbide ( $\gamma_{Si-SiC}$ ) according to the equation<sup>14</sup>

$$\cos\Theta = \frac{\gamma_{Si-SiC} - \gamma_{SiC}}{\gamma_{Si}} \quad (2)$$

In the literature, there are no values for these surface energy terms at 1100°C. However, these surface energy terms have been measured above the melting point of silicon. Barsoum *et al.*<sup>15</sup> have determined  $\gamma_{Si}$ ,  $\gamma_{SiC}$ , and  $\gamma_{Si-SiC}$  to be approximately 0.8, 1.8, and 1.2 J/m<sup>2</sup>, respectively, at 1430°C. Using these values, and assuming that the local stresses in the boundary phase are twice the applied stress,<sup>13,16</sup> the rate of heterogeneous nucleation for the stress levels used in this study is predicted to be infinitesimally small, since the exponential term in Eq. (1) is  $\ll 1$ . However, the rate of cavity nucleation is very sensitive to the localized stress and surface energy of the silicon phase.

According to Argon *et al.*,<sup>17</sup> a material undergoing creep deformation can develop very large, localized transient stress concentrations from grain-boundary sliding events. During the early

stages of grain-boundary sliding, localized stresses as large as 10 to 20 times the applied stress can develop at the grain boundary. These stress concentrations can make cavity nucleation energetically favorable at the applied stresses observed in this study, particularly when the effects of iron impurities on the surface energy of silicon are considered.

Figure 2 revealed that regions of the microstructure which contain the highest volume fraction of silicon carbide also contain high concentrations of iron. Since creep damage tends to also form in these areas, the impurities may assist the cavity nucleation process by reducing the surface energy of the silicon boundary phase. Ness *et al.*<sup>10</sup> have shown that these regions of high iron content in reaction-bonded siliconized silicon carbides can take the form of low-melting iron silicides. If iron silicide is present along these boundaries, the combination of the high transient stresses from grain-boundary sliding and the reduction in the surface energy of the boundary phase may make cavity nucleation energetically favorable at the applied stresses observed in this study. Further transmission electron microscopy is needed to investigate the role of iron impurities in the cavity nucleation process.

In this study, the threshold stress for creep damage was determined to be 132 MPa at 1100°C. If the threshold stress for creep damage is nucleation controlled, the threshold stress should decrease with increasing temperature. Wiederhorn *et al.*<sup>11</sup> have shown that the threshold stress in this siliconized silicon carbide does decrease at higher temperature. They determined the threshold stress for creep damage to be approximately 100 MPa at 1300°C.

### (3) Microstructural Dependence of Creep Damage

The results of the interparticle distance analysis indicate that at low creep strains, creep damage tends to form in areas of the microstructure of high silicon carbide content. These areas of high silicon carbide content are the preferred sites for creep damage at low creep strains, due to the high localized stresses and high concentration of impurities. High localized stresses develop in these regions from two processes. First, since the areas of high silicon carbide content cannot deform as fast as the surrounding matrix which contains more silicon, an overall stress concentration develops in these heterogeneities. Dalgleish *et al.*<sup>12</sup> have shown that localized stress concentrations can occur in microstructural heterogeneities when the viscosity of the heterogeneities differs from that of the matrix. This process can increase the overall localized stress in the heterogeneities to approximately twice the applied stress. The second process which leads to stress concentrations is grain-boundary sliding. When two silicon carbide grains tend to slide over one another, large, localized stresses develop in the boundary phase. These transient stress concentrations develop because there is an insufficient supply of silicon to flow into the boundaries, to accommodate the volume increase associated with grain-boundary sliding. Argon *et al.*<sup>13</sup> have reported that grain-boundary sliding can result in stress concentrations of 10 to 20 times the applied stress. A combination of these high localized stresses and impurities enables the regions of high silicon carbide content to be the preferred sites for creep damage at low creep strains.

As cavity formation occurs during deformation, the load is transferred from the regions of higher silicon carbide content to the regions of lower silicon carbide content. This load-transfer process enables creep damage to be more prevalent in regions of lower silicon carbide content, at the higher creep strains.

### V. Summary

The accumulation of creep damage in a siliconized silicon carbide was investigated as a function of applied stress, creep strain, and microstructure. At 1100°C, creep damage was observed to accompany deformation in specimens deformed to creep strains greater than 0.10%, under applied stresses greater than 137 MPa. The location of creep damage in the material was found to be microstructurally dependent. At low creep strains, creep damage occurred in regions of the microstructure of high silicon carbide content. As deformation progressed, creep damage then formed in regions of the microstructure of lower silicon carbide content.

The area density and area fraction of cavities were found to increase linearly with creep strain. This linear dependence indicates that once a cavity forms, it must rapidly grow to an equilibrium size. The maximum size of the cavities was limited to the size of the silicon carbide grain facet. A threshold stress for creep damage at 1100°C was determined to be 132 MPa from the area fraction results. This threshold stress is an indication of that stress below which the rate of cavity nucleation is essentially zero. The nucleation of creep damage was suggested to occur heterogeneously at the silicon-silicon carbide interfaces with the aid of high localized transient stresses and iron impurities in the silicon phase.

### References

- <sup>1</sup>B. North and K. E. Kilchrist, "Effect of Impurity Doping on a Reaction-Bonded Silicon Carbide," *Am. Ceram. Soc. Bull.*, **66** [5] 549-52 (1981).
- <sup>2</sup>C. W. Forrest, P. Kennedy, and J. V. Shennan; pp. 99-123 in *Special Ceramics*, Vol. 5, Edited by P. Popper. British Ceramic Research Association, Stoke-on-Trent, England, 1972.
- <sup>3</sup>D. F. Carroll and R. E. Tressler, "Time-Dependent Strength of Siliconized Carbide under Stress at 1000° and 1100°C," *J. Am. Ceram. Soc.*, **68** [3] 143-46 (1985).
- <sup>4</sup>S. M. Wiederhorn, L. Chuck, E. R. Fuller, and N. J. Tighe; pp. 755-73 in *Materials Science Research*, Vol. 20, *Tailoring Multiphase and Composite Ceramics*, Edited by R. E. Tressler, G. L. Messing, C. G. Pantano, and R. E. Newnham. Plenum Press, New York, 1987.
- <sup>5</sup>D. F. Carroll, R. E. Tressler, Y. Tsui, and C. Near; pp. 775-88 in *Materials Science Research*, Vol. 20, *Tailoring Multiphase and Composite Ceramics*. Edited by R. E. Tressler, G. L. Messing, C. G. Pantano, and R. E. Newnham. Plenum Press, New York, 1987.
- <sup>6</sup>H. Cohr, G. Grathwohl, and F. Thummel, "Non-stationary Stress Distribution in Ceramic Bending Beam During Constant Load Creep," *Res. Mech.*, **10**, 55-71 (1984).
- <sup>7</sup>T.-J. Chuang, "Estimation of Power-Law Creep Parameters from Bend Test Data," *J. Mater. Sci.*, **21** [1] 165-75 (1986).
- <sup>8</sup>H. Cohr, G. Grathwohl, and F. Thummel; pp. 515-26 in *Creep and Fracture of Engineering Materials and Structures*, Part I. Edited by B. Wilshire and D. R. J. Owen. Pineridge Press, Swansea, U.K., 1984.
- <sup>9</sup>T.-J. Chuang and S. M. Wiederhorn, "Damage-Enhanced Creep in a Siliconized Silicon Carbide: Mechanics of Deformation"; unpublished work.
- <sup>10</sup>D. F. Carroll and R. E. Tressler, "Effect of Creep Damage on the Tensile Creep Deformation of a Siliconized Silicon Carbide"; unpublished work.
- <sup>11</sup>F. Wakai, S. Sakaguchi, Y. Matsuno, and H. Okunda, "Tensile Creep Test of Hot-Pressed Si<sub>3</sub>N<sub>4</sub>", presented at the International Symposium on Ceramic Components for Engines, Hakone, Japan, Oct. 17-21, 1983.
- <sup>12</sup>D. F. Carroll, "Tensile Creep Behavior and Cavity Damage in a Siliconized Silicon Carbide"; Ph.D. Thesis. Pennsylvania State University, University Park, PA, May 1987.
- <sup>13</sup>B. J. Dalgleish, S. M. Johnson, and A. G. Evans, "High-Temperature Failure of Polycrystalline Alumina: I. Crack Nucleation," *J. Am. Ceram. Soc.*, **67** [11] 741-50 (1984).
- <sup>14</sup>J. C. Fisher, "The Fracture of Liquids," *J. Appl. Phys.*, **19**, 1062 (1948).
- <sup>15</sup>M. W. Barsoum and P. D. Owens; pp. 457-66 in *Materials Science Research*, Vol. 14, *Surfaces and Interfaces in Ceramic and Ceramic Metal Systems*. Edited by J. Park and A. Evans. Plenum Press, New York, 1981.
- <sup>16</sup>D. C. Drucker; pp. 795-833 in *Proceedings of the Second Berkeley International Materials Conference*. Edited by V. F. Zackay. Wiley, New York, 1965.
- <sup>17</sup>A. S. Argon, I.-W. Chen, and C. W. Lau; pp. 23-49 in *Three Dimensional Constitutive Relations and Ductile Fracture*. Edited by S. Nemat-Nasser. North-Holland Publishing Co., New York, 1981.
- <sup>18</sup>J. N. Ness and T. F. Page, "Microstructural Evolution in Reaction-Bonded Silicon Carbide," *J. Mater. Sci.*, **21**, 1377-97 (1986).
- <sup>19</sup>S. M. Wiederhorn, L. C. Chuck, and T.-J. Chuang, "Damage-Enhanced Creep in a Siliconized Silicon Carbide: Phenomenology"; unpublished work.

# Threshold Stress Intensity for Crack Growth at Elevated Temperatures in a Silicon Nitride Ceramic

MICHAEL R. FOLEY\* and RICHARD E. TRESSLER\*

Department of Materials Science and Engineering, The Pennsylvania State University,  
University Park, PA 16802

The flaw behavior in an as-machined and oxidized hot isostatically pressed silicon nitride (HIPSN) under static load was investigated at various stress intensities, times, and temperatures. Flaw origins were of the pore/cavity type and iron-based inclusion type. There was no strength increase or degradation in as-machined and oxidized specimens static loaded for 10 h at 1100°C in air below the threshold stress intensity. The threshold stress intensities for crack growth at 1100°C were determined to be 1.75 and 2.00 MPa · m<sup>1/2</sup> for the as-machined and oxidized HIPSN, respectively. A strength decrease with increased applied stress was observed in as-machined specimens static loaded at 1200° and 1300°C in air. This effect is due to the creation of a new flaw population with more severe flaws. Threshold stresses of 160 and 90 MPa were observed at 1200° and 1300°C, respectively. Oxidized HIPSN does not experience any strength degradation when static loaded at 1200°C below a threshold stress intensity of 1.50 MPa · m<sup>1/2</sup>. The oxidation treatment causes microstructural changes in the ceramic, resulting in a material with improved creep and crack growth resistance.

Silicon nitride-based ceramics are being studied for high-temperature structural applications such as gas turbine engine components. By using these ceramics, the new high-efficiency heat engines can be operated at temperatures higher than allowed by current superalloys. Silicon nitride is an excellent candidate for this application because of its high strength-to-weight ratio, retained strength at elevated temperatures, and good oxidation, corrosion, and thermal-shock resistance.

Polycrystalline ceramics such as silicon nitride-based ceramics are susceptible to subcritical or slow crack growth in severe atmospheres and/or at elevated temperatures.<sup>1-4</sup> As in most ceramics, silicon nitride components will contain flaws either intrinsic from processing or extrinsic from machining, etc. The growth of these flaws to a critical size when subjected to mechanical or thermal stresses leads to catastrophic failure.

Knowledge of the short-term strength and fracture toughness of the material is essential for design purposes, but these properties do not explain how a material will behave over extended periods of time under loads well below the fracture stress or critical stress-intensity load levels. Determining the existence and estimating the value of a threshold stress intensity (static fatigue limit) below which no crack growth will occur is of great engineering importance.

One could design structural ceramics to be used at service stresses or stress intensities below this limit so that theoretically the component would never fail. Most of the early work on threshold values was done on amorphous materials. Only recently have investigators studied polycrystalline non-oxide ceramics such as SiC and Si<sub>3</sub>N<sub>4</sub>.<sup>5-10</sup> This investigation was undertaken to estimate the value of the static fatigue limit and study the behavior of flaws in a hot isostatically pressed silicon nitride (HIPSN) material at elevated temperatures in air.

## EXPERIMENTAL PROCEDURE

### SAMPLE PREPARATION

The modified static load technique used in this study has been fully described by Minford and co-workers.<sup>5-6</sup> It involves heating the sample to test temperature, rapidly loading to a predetermined static load level, and maintaining that load level for a specified time. If the sample does not fail during the soak time, it is rapidly loaded to failure at the test temperature. This technique directly measures the effect of an applied stress intensity during static loading on the fracture stress which reflects any changes in flaw severity.

The material used for this investigation was a commercial silicon nitride\* which contains alumina and yttria as densification aids and is one of the leading candidate materials for use in turbocharger rotors. The HIPSN material was received in rectangular billets measuring ≈20 by 30 by 5 mm. Test specimens were cut from the billets using an 8-in. continuous resin bonded diamond cutoff wheel. The major faces of the samples were surface-ground to a 600-grit finish. Tensile surface edges were hand-beveled using a 15-μm diamond disk to eliminate any edge checking flaws that may have formed during grinding. The final test bar dimensions were ≈4 by 2 by 30 mm.

To determine the effects of oxidation on the threshold stress intensity, several samples were oxidized in air for 15 h at 1200°C. To characterize the initial condition of the samples, 33 samples were fractured at room temperature in air using four-point loading with upper and lower spans of 5.2 and 19.7 mm, respectively. The stressing rate used during testing was ≈30 to 35 MPa/s. To better define the critical flaw size in this material, the remaining samples were proof-tested in liquid nitrogen. The proof testing was done to truncate the flaw-size distribution, thereby allowing one to obtain well-defined threshold stress-intensity values. Strength distributions were also obtained on as-machined and oxidized samples at 1100°, 1200°, and 1300°C in air. Fracture surfaces examined by electron microscopy revealed two types of flaw origins: iron-based inclusions and pore/cavity type flaws. Typical flaw origins are shown in Fig. 1.

The elevated temperature load train assembly consisted of alumina rams entering the furnace from the top and bottom and hot-pressed magnesia-doped silicon nitride knife edges with the aforementioned dimensions.

### TESTING

Fracture toughnesses were determined by a controlled-flaw technique. A Knoop indentation was introduced into the surface of

\*Member, the American Ceramic Society.  
†AY6 silicon nitride. GTE, Towanda, PA.

Manuscript No. 199792. Received August 17, 1987; approved December 31, 1987.

Supported by the U.S. Army Research Office, Metallurgy and Materials Science Division.

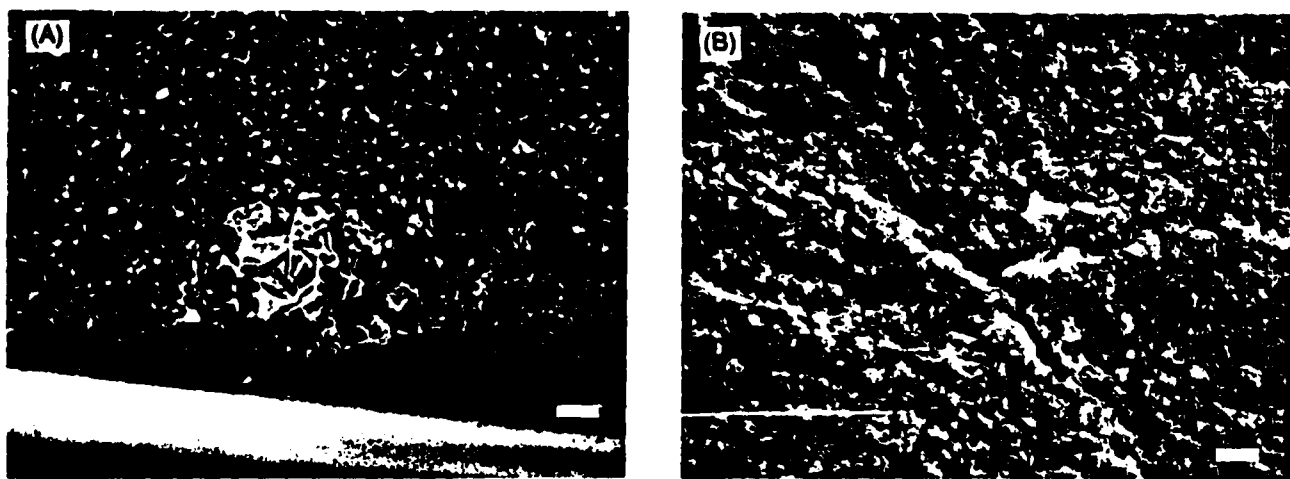


Fig. 1. Scanning electron micrographs of the fracture surface of the AY6 material fractured at room temperature in air: (A) secondary electron image at  $\times 600$ ,  $\sigma_f = 650$  MPa and fracture origin = iron-based inclusion and (B) secondary electron image at  $\times 600$ ,  $\sigma_f = 993$  MPa and fracture origin = pore/cavity (bars = 10  $\mu\text{m}$ ).

a four-point bend specimen. The indent was polished off to remove residual stresses, leaving behind only a subsurface crack. The specimens were heated to temperature and fast-fractured in the four-point bend configuration stated earlier. Flaw sizes were measured using both electron and optical microscopy. The  $K_{IC}$  values for the oxidized specimens were measured using samples oxidized after indentation.

The average fracture stress and fracture toughness at each test condition were used to calculate the average critical flaw size. This flaw size was used to calculate the load required to apply the desired initial stress intensity. The test bars were loaded into the furnace and the knife edges aligned prior to heat up. All testing was done in air. Furnace heat up to test temperature took ~20 to 30 min. Because of thermal expansion during heat up, the test specimens were kept under a small load (1 to 2 lbs) to keep the knife edges aligned. The assembly was held at temperature for 10 to 15 min before starting the test to allow the sample and loading assembly to reach thermal equilibrium. The sample was then loaded to the precalculated level, which fixed the initial applied stress intensity. The load was maintained for the desired length of time, after which the load was increased at the fast fracture stress-rate until failure occurred.

Since the sample is loaded to failure directly from the static load level, the changes in flaw severity are examined without the complicating factors of changes in temperature or unloading the specimen prior to fracture. One can observe the fracture stress as a function of initial applied stress intensity, which directly yields the threshold value. Also one can select the time scale of the test such that all samples loaded above the threshold stress intensity fail during static loading.

## RESULTS

The modified static load technique was applied to estimate the threshold stress intensity for crack growth at 1100°, 1200°, and 1300°C in air for the HIPSN.

### RESULTS OF 1100°C EXPERIMENTS

**As-Machined Samples.** Samples were tested at various initial stress intensities ( $K_I$ ) at 1100°C in air for static load times of 2 and 10 h. Figure 2 shows the results of as-machined samples static loaded for 10 h. Plotted at an initial stress intensity of zero are samples fractured at 1100°C in air with no prior static loading. The symbols and error bars represent the mean fracture stress and 95% confidence interval, respectively. There is no significant change in the mean fracture stress over the range of  $K_I$  from 0.5 to 1.50  $\text{MPa} \cdot \text{m}^{1/2}$ . The first evidence of mixed behavior is seen

at a  $K_I$  of 1.75  $\text{MPa} \cdot \text{m}^{1/2}$  in that one of five samples failed during static loading. At slightly higher  $K_I$  values, there is still some mixed behavior, but at  $K_I = 2.5 \text{ MPa} \cdot \text{m}^{1/2}$  all samples failed during static loading, most within minutes of reaching the static load level. The threshold stress intensity (static fatigue limit) is indicated by the first evidence of mixed behavior, i.e.,  $K_{Ic} = 1.75 \text{ MPa} \cdot \text{m}^{1/2}$ . The range for  $K_{Ic}$  shown is due to the range of flaw sizes for HIPSN calculated from the strength distribution at 1100°C in air. The  $K_{Ic}$  arrow shown on the figure indicates the fracture toughness at the test temperature and specimen conditions (i.e., 1100°C and as-machined in this case).

The plot for the 2-h test is not shown here, since behavior similar to the 10-h test was observed. The only difference was the stress level at which the first evidence of mixed behavior occurred. The threshold stress intensity value was at 2.0  $\text{MPa} \cdot \text{m}^{1/2}$ . Because of the static load time exposure increase from 2 to 10 h, the  $K_{Ic}$  value at 10 h (1.75  $\text{MPa} \cdot \text{m}^{1/2}$ ) is considered to be a more accurate and conservative estimate than the 2-h value. Note also that, because there is no significant change in the mean fracture stress with increased  $K_I$  up to  $K_{Ic}$ , it is assumed that the strength-limiting flaw population is unchanged.

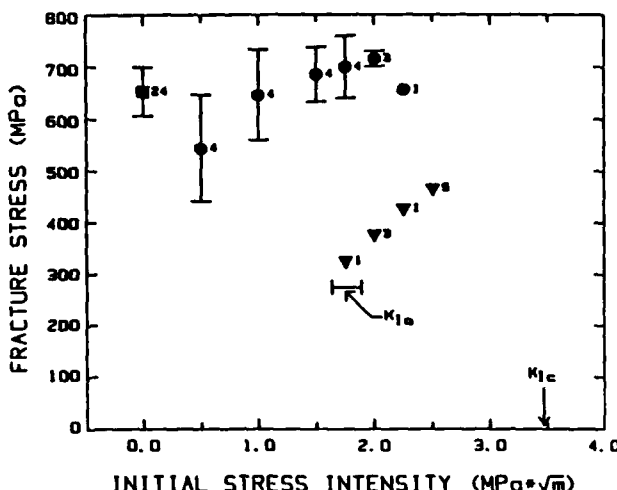


Fig. 2. Effect of initial applied stress intensity on fracture stress of as-machined HIPSN at 1100°C in air; static load time: 10 h. (■ Tested after proof testing, no prior static loading; ● tested after static loading; ▽ failed during static loading; and 24 indicates the number of samples tested.)

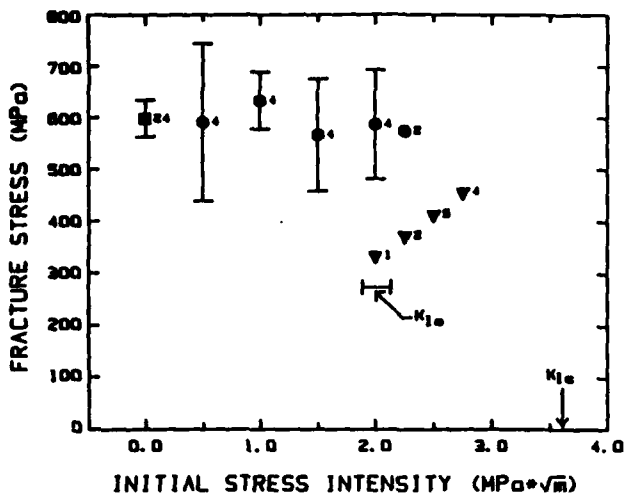


Fig. 3. Effect of initial applied stress intensity on fracture stress of oxidized HIPSN at 1100°C in air; static load time: 10 h. (■ Tested after proof testing, no prior static loading; ● tested after static loading; ▼ failed during static loading; and 24 indicates the number of samples tested.)

**Oxidized Samples.** Again samples were tested for static load times of 2 and 10 h. Figure 3 shows the results of the 10-h test. There was basically no difference between the 2- and 10-h tests. Both showed no significant change in mean fracture stress with increasing  $K_I$  up to  $2.0 \text{ MPa} \cdot \text{m}^{1/2}$ , where the first evidence of mixed behavior was observed, i.e.,  $K_I = 2.0 \text{ MPa} \cdot \text{m}^{1/2}$ . Note that, even though the initial strength (i.e.,  $K_I = 0$ ) of the as-machined samples is greater than that of the oxidized samples, statistical analysis using the Students' *t*-test (comparison of means) showed no significant difference in the mean fracture stress between the as-machined and oxidized specimens at 1100°C.

#### RESULTS OF 1200°C EXPERIMENTS

**As-Machined Samples.** Static load tests were performed on the as-machined HIPSN material at 1200°C in air; again exposures were 2 and 10 h. Similar behavior was observed for both test times. Figure 4 shows the results for tests done with a static load time of 10 h. There is a sharp decrease in mean fracture stress with increasing initial applied stress intensity. Estimates of  $K_I$  for the 2- and 10-h tests are 1.45 and  $1.00 \text{ MPa} \cdot \text{m}^{1/2}$ , respectively.

**Oxidized Samples.** The same tests were performed on oxidized HIPSN at 1200°C. The 2- and 10-h tests showed identical behavior, i.e., no significant change in mean fracture stress with increasing  $K_I$  up to the  $K_{Ic}$  value of  $1.50 \text{ MPa} \cdot \text{m}^{1/2}$ . This behavior is shown in Fig. 5. Again note that statistical analysis showed no significant difference in the mean fracture stress at  $K_I = 0$  between the as-machined and oxidized samples at 1200°C.

The differences in  $K_I$  values between the as-machined and oxidized materials during static load testing must be due to a microstructural change. The decreasing mean fracture stress with increasing  $K_I$  for the as-machined samples is thought to be due to the creation of a new flaw population which produced flaws that were more severe. This new flaw population could easily have been created at this temperature because of creep cavitation. The work of Tighe and co-workers,<sup>8-10</sup> Grathwohl,<sup>11</sup> and Quinn<sup>12,13</sup> has identified this process. The 10-h test of the as-machined specimens amplifies the effect of the new flaw population over the 2-h test, as indicated by the large drop in  $K_I$  for the 10-h test. Note that, because of the creation of new flaws, the sizes of which are not well-characterized, the actual  $K_I$  values used during testing were different from those calculated from the original flaw population. Therefore, it would be more informative to record the effect of initial applied stress on the fracture stress for the as-machined specimens.

The fact that the oxidized samples do not experience the same

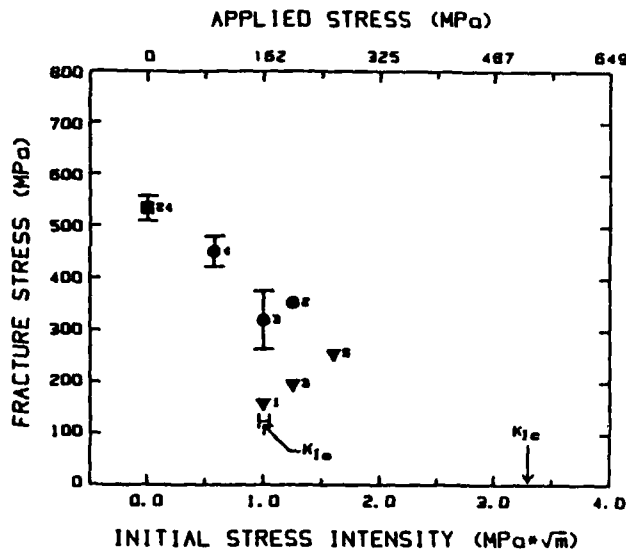


Fig. 4. Effect of initial applied stress intensity on fracture stress of as-machined HIPSN at 1200°C in air; static load time: 10 h. (■ Tested after proof testing, no prior static loading; ● tested after static loading; ▼ failed during static loading; and 24 indicates the number of samples tested.)

detrimental effects during static loading at 1200°C as did the as-machined samples probably results from an oxidation-induced microstructural change. This change may have been accomplished by (1) annealing or healing of the critical flaws originally present and/or (2) producing a more creep-resistant material. If the original flaws were blunted, it would take higher apparent stress intensities to cause crack growth, i.e., an apparent shift of  $K_{Ic}$  to higher values. Also at this temperature it is well known<sup>14-18</sup> that additives and impurities such as Fe, Al, and Y present in the grain-boundary phase diffuse toward the surface. This rejection of impurities from the grain boundaries creates a more refractory grain-boundary phase, and thus, produces a more creep-resistant material.

#### RESULTS OF 1300°C EXPERIMENTS

Figure 6 shows the results of as-machined specimens statically loaded for 2 h at 1300°C in air. Decreases in mean fracture stress with increasing  $K_I$  are again observed. The apparent  $K_{Ic}$  is  $1.00 \text{ MPa} \cdot \text{m}^{1/2}$  with a 95% confidence interval of 0.9 to  $1.13 \text{ MPa} \cdot \text{m}^{1/2}$ . The drop in mean fracture stress also suggests the creation of a new population analogous to the behavior of the as-machined specimens at 1200°C. Again, it is more informative to look at the effect of applied stress on the fracture stress for the as-machined samples at 1300°C. The plotted apparent  $K_I$  values are not correct because of the creation of new flaws during static load testing. Note that some of the HIPSN samples plastically deformed enough to contact the lower knife edge support beam before failure. Because of the very low fracture stresses (<250 MPa) and plastic deformation under load, no further static load testing at 1300°C was performed.

#### DISCUSSION

It is well-known<sup>24</sup> that using certain densification aids for sintering of ceramics can produce a fully dense material with a glassy grain-boundary phase. It is this grain-boundary phase that when subjected to loads at elevated temperatures can have deleterious effects on the mechanical properties of the bulk material.

Powder XRD revealed  $\beta\text{-Si}_3\text{N}_4$  as the only crystalline phase in this material. Therefore, it is reasonable to assume that the yttria and alumina used to promote densification of the  $\text{Si}_3\text{N}_4$  material is present as a glassy grain-boundary phase either as a thin film at two grain junctions or pockets at three and four grain junctions. When a material such as HIPSN is subjected to stresses at high tempera-

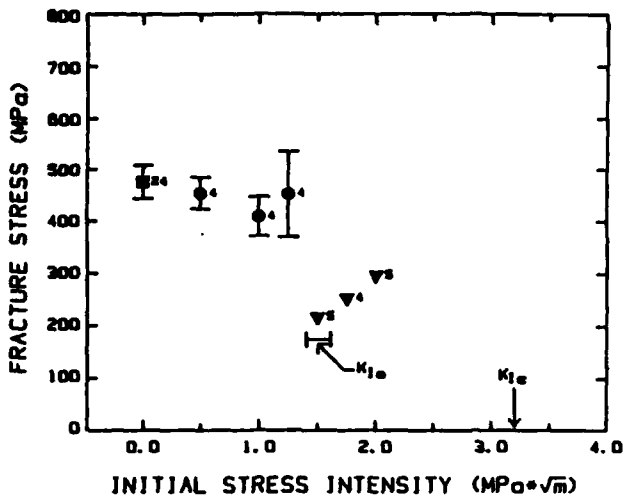


Fig. 5. Effect of initial applied stress intensity on fracture stress of oxidized HIPSN at 1200°C in air; static load time: 10 h. (■ Tested after proof testing, no prior static loading; ● tested after static loading; ▼ failed during static loading; and 24 indicates the number of samples tested.)

tures, cavities can nucleate and grow in this second phase. The cavities will eventually grow and coalesce to form cracks and finally lead to catastrophic failure.

In this study well-defined estimates of the threshold stress intensity were observed at 1100°C for as-machined and oxidized HIPSN as well as at 1200°C for the oxidized HIPSN. In attempting to rationalize these  $K_{Ic}$  values and keeping in mind that failure is predominantly intergranular at these temperatures, various models for crack growth can be examined for applicability to the HIPSN material as Chuang *et al.*<sup>19</sup> have done for silicon carbide ceramics. The threshold stress intensity as shown in Fig. 2 lies between 1.63 and 1.89 MPa·m<sup>1/2</sup>. A model by Hull and Rimmer<sup>20</sup> described a critical stress for cavity growth by a vacancy flux at the grain boundary in the absence of a grain-boundary phase which is clearly not applicable to the present material.

A diffusive creep model of creep crack growth through the formation of cavities on the grain boundaries was developed by Chuang.<sup>21</sup> Again, the presence of a grain-boundary phase which controls the initiation of crack growth is not explicitly treated in this model.

Lange<sup>22</sup> presented a simplistic model for slow crack resulting from grain-boundary separation in a system with a viscous boundary phase. Assuming the existence of voids in the boundary, the critical stress necessary for void growth is

$$\sigma_c = \frac{4\gamma_s}{d_v} \quad (1)$$

where  $\gamma_s$  is the solid-vapor surface energy of the boundary phase and  $d_v$  is the grain-boundary width. This expression in terms of the threshold stress intensity is

$$K_{Ic} = \left( \frac{8M}{d_v} \right) \left( \frac{c}{\pi} \right)^{1/2} \gamma_s \quad (2)$$

where  $M$  is 1.03 (a geometrical constant for flaw shape<sup>23</sup>) and  $c$  is the flaw size.

The threshold stress intensity predicted by this model using either available data from the literature or data obtained from this investigation is presented in Table I along with the experimentally determined value of  $K_{Ic}$  at 1100°C. Lange's model overestimates the observed threshold value for HIPSN at 1100°C in air. However, the data used in this calculation are approximate values in some cases and the model is very approximate. Clearly, a refined model and accurate values for the physical and chemical parameters are required to better reconcile the experimentally observed threshold stress-intensity values.

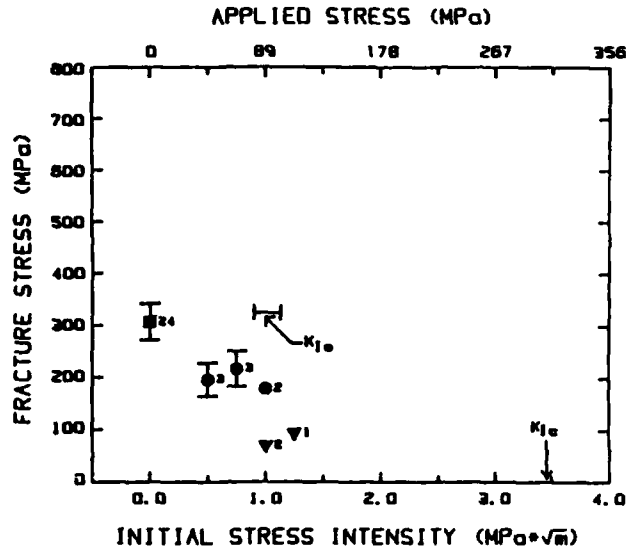


Fig. 6. Effect of initial applied stress intensity on fracture stress of as-machined HIPSN at 1300°C in air; static load time: 2 h. (■ Tested after proof testing, no prior static loading; ● tested after static loading; ▼ failed during static loading; and 24 indicates the number of samples tested.)

## SUMMARY

The modified static loading technique for estimating threshold stress intensities was applied to as-machined and oxidized HIPSN at 1100°, 1200°, and 1300°C in air. The values were estimated to be 1.75 and 2.00 MPa·m<sup>1/2</sup> at 1100°C in air for the as-machined and oxidized HIPSN, respectively. There was no significant change in mean fracture stress with increasing  $K_I$  up to  $K_{Ic}$  at this temperature, indicating that neither flaw-blunting nor flaw-growth processes were occurring.

A significant decrease in mean fracture stress with increasing applied stress was observed for as-machined HIPSN static loaded at 1200° and 1300°C in air. It is believed that creep cavitation is occurring in this material at these temperatures in air resulting in changes in the flaw population, which renders this experimental technique invalid. The oxidized HIPSN does not experience any strength degradation when static loaded at 1200°C in air. The oxidation treatment prior to testing is thought to produce microstructural changes in the HIPSN resulting in a material with improved creep and crack growth resistance.

## REFERENCES

- S. M. Wiederhorn, "Subcritical Crack Growth in Ceramics"; pp. 613-46 in *Fracture Mechanics of Ceramics*, Vol. 2. Edited by R. C. Brandt, L.D.P. Hasselman, and F.F. Lange. Plenum Press, New York, 1974.
- G. D. Quinn and J. B. Quinn, "Slow Crack Growth in Hot-Pressed Silicon Nitride"; pp. 6033-636 in *Fracture Mechanics of Ceramics*, Vol. 6. Edited by R. C. Brandt, A. G. Evans, D. P. H. Hasselman, and F. F. Lange. Plenum Press, New York, 1983.
- T. M. Yonushonis, "Crack Propagation in Silicon Nitride Ceramics"; M.S. Thesis. The Pennsylvania State University, University Park, PA, May 1976.
- T. E. Easter, "Environmental Effects on the Strength Distributions of Silicon Carbide and Silicon Nitride"; M.S. Thesis. The Pennsylvania State University, University Park, PA, August 1980.
- E. J. Minford and R. E. Tressler, "Determination of Threshold Stress Intensity

Table I. Comparison of the Threshold Stress Intensity for Crack Growth Predicted by the Lange Model and the Experimentally Observed Value at 1100°C

Model	Calculated $K_{Ic}$ (MPa·m <sup>1/2</sup> )	Estimated (from graph) $K_{Ic}$ (MPa·m <sup>1/2</sup> )
Lange	3.70	1.75

NOTE:  $M = 1.03$  (23),  $c = 20.7 \times 10^{-6}$  m,  $P_H = 1$  atm = 0.10 MPa,  $\gamma_s = 0.35$  N/m for silicate boundary phase (Ref. 22),  $\rho_s = 10 \times 10^{-6}$  m (Ref. 24),  $E = 270.3$  GPa @ 1100°C,  $\nu = 0.2771$ , and  $d_v = 2 \times 10^{-6}$  m (Ref. 25).

- for Crack Growth at High Temperature in Silicon Carbide Ceramics," *J. Am. Ceram. Soc.*, **66** [5] 338-40 (1983).
- <sup>18</sup>E. J. Minford, D. M. Kupp, and R. E. Tressler, "Static Fatigue Limit for Sintered Silicon Carbide at Elevated Temperatures," *ibid.*, [11] 769-73.
- <sup>19</sup>R. E. Tressler, E. J. Minford, and D. F. Carroll, "Static Fatigue Limit for Silicon Carbide Based Ceramics—Flaw Blunting vs Flaw Growth"; pp. 551-63 in *Creep and Fracture of Engineering Materials and Structures Part I*. Edited by B. Wilshire and D. R. J. Owen. Pineridge Press, Swansea, UK, 1984.
- <sup>20</sup>N. J. Tighe, S. M. Wiederhorn, T.-J. Chuang, and C. L. McDaniel, "Creep Cavitation and Crack Growth in Silicon Nitride"; pp. 587-604 in *Deformation of Ceramic Materials II*. Edited by R. E. Tressler and R. C. Bradt. Plenum Press, New York, 1984.
- <sup>21</sup>S. M. Wiederhorn, N. J. Tighe, T.-J. Chuang, C. L. McDaniel, and E. R. Fuller, Jr., "Structural Reliability of Brittle Material at High Temperatures," National Bureau of Standards Technical Report for Project No. 5610464 (1983).
- <sup>22</sup>S. M. Wiederhorn and N. J. Tighe, "Structural Reliability of Yttria-Doped Hot-Pressed Silicon Nitride at Elevated Temperatures," *J. Am. Ceram. Soc.*, **66** [12] 584-89 (1983).
- <sup>23</sup>G. Grathwohl, "Regimens of Creep and Slow Crack Growth in High Temperature Rupture of Hot-Pressed Silicon Nitride"; pp. 573-86 in Ref. 8.
- <sup>24</sup>G. D. Quinn, "Static Fatigue in High Performance Ceramics"; presented at ASTM Conference, San Francisco, CA (1982).
- <sup>25</sup>G. D. Quinn, "Fracture Mechanism Map for Hot Pressed Silicon Nitride"; presented at Eighth Annual Conference of the Ceramic-Metal Systems Division, Cocoa Beach, FL (1984).
- <sup>26</sup>H. Du; private communication.
- <sup>27</sup>J. E. Siebelis, "Oxidation and Strength of Silicon Nitride and Silicon Carbide"; pp. 793-804 in *Ceramics for High Performance Applications III Reliability*. Edited by E. M. Lenoe, R. N. Katz and J. J. Burke. Plenum Press, New York, 1983.
- <sup>28</sup>S. C. Singhal, "Oxidation and Corrosion-Erosion Behavior of  $\text{Si}_3\text{N}_4$  and  $\text{SiC}$ "; pp. 553-48 in *Ceramics for High Performance Applications*. Edited by J. J. Burke, A. E. Gorum, and R. N. Katz. Brook Hill, Chestnut Hill, MA, 1974.
- <sup>29</sup>S. C. Singhal, "Oxidation of Silicon Nitride and Related Materials"; pp. 607-26 in *Nitrogen Ceramics*. Edited by F. L. Riley. Noordhoff International, 1977.
- <sup>30</sup>D. R. Clarke and F. F. Lange, "Oxidation of  $\text{Si}_3\text{N}_4$  Alloys: Relation to Phase Equilibria in the System  $\text{Si}_3\text{N}_4\text{-SiO}_2\text{-MgO}$ ," *J. Am. Ceram. Soc.*, **63** [9-10] 586-93 (1980).
- <sup>31</sup>T.-J. Chuang, R. E. Tressler, and E. J. Minford, "On the Static Fatigue Limit at Elevated Temperatures," *Mater. Sci. Eng.*, **82**, 187-95 (1986).
- <sup>32</sup>D. Hull and D. E. Rimmer, "The Growth of Grain Boundary Voids Under Stress," *Philos. Mag.*, **4**, 673-87 (1959).
- <sup>33</sup>T. J. Chuang, "A Diffusive Crack Growth Model for Creep Fracture," *J. Am. Ceram. Soc.*, **65** [2] 93-103 (1982).
- <sup>34</sup>F. F. Lange, "Non-Elastic Deformation of Polycrystals with a Liquid Boundary Phase"; pp. 361-368 in *Deformation of Ceramic Materials*. Edited by R. C. Bradt and R. E. Tressler. Plenum Press, New York, 1975.
- <sup>35</sup>I. J. Petovic, L. A. Jacobson, P. K. Tally, and A. K. Vasudevan, "Controlled Surface Flaws in Hot-Pressed  $\text{Si}_3\text{N}_4$ ," *J. Am. Ceram. Soc.*, **58** [3-4] 113-16 (1975).
- <sup>36</sup>K. D. McLean, "Elevated Temperature Slow Crack Growth in Hot Pressed and Sintered Silicon Carbide," Ph.D. Thesis, The Pennsylvania State University, University Park, PA, May 1979.
- <sup>37</sup>R. L. Tsai and R. Raj, "Creep Fracture in Ceramics Containing Small Amounts of a Liquid Phase," *Acta Metall.*, **30**, 1043-58 (1982). □

EFFECT OF CREEP DAMAGE ON THE TENSILE CREEP BEHAVIOR  
OF A SILICONIZED SILICON CARBIDE \*

D. F. Carroll and R. E. Tressler

The Pennsylvania State University  
Department of Materials Science and Engineering  
University Park, PA 16802

---

\*This work was partially supported by The U. S. Army Research Office,  
Metallurgy and Materials Science Division.

## ABSTRACT

The tensile creep behavior of a siliconized silicon carbide was investigated in air, under applied stresses of 103 to 172 MPa for the temperature range of 1100 to 1200°C. At 1100°C, the steady-state stress exponent for creep was approximately four under applied stresses less than the threshold for creep damage (132 MPa). At applied stresses greater than the threshold stress for creep damage, the stress exponent increased to approximately ten. The activation energy for steady-state creep at 103 MPa, was approximately 175 kJ/mole for the temperature range of 1100 to 1200°C. Under applied stresses of 137 and 172 MPa, the activation energy for creep increased to 210 and 350 kJ/mole, respectively, for the same temperature range. Creep deformation in the siliconized silicon carbide below the threshold stress for creep damage, was determined to be controlled by dislocation processes in the silicon phase. At applied stresses above the threshold stress for creep damage, creep damage enhanced the rate of deformation, resulting in an increased stress exponent and activation energy for creep. The contribution of creep damage to the deformation process was shown to increase the stress exponent from four to ten.

## INTRODUCTION

The formation of creep damage or cavities during deformation at elevated temperatures has been observed in a wide variety of materials such as silicon nitrides,<sup>1,2</sup> aluminas,<sup>3</sup> glass ceramics<sup>4</sup> and siliconized silicon carbides.<sup>5-7</sup> In these studies, the stress exponents<sup>1-7</sup> and activation energies<sup>3,5,6</sup> for steady-state creep have been observed to

increase when creep damage accompanied deformation. The increase in the stress exponents and activation energies for creep is the result of an enhanced creep rate produced by the formation of creep damage. Since creep damage influences the creep rate, it is important to understand how creep damage contributes to the deformation process in order to develop models that predict the creep rupture behavior of these materials.

In a previous paper, creep damage was shown to accompany deformation in a siliconized silicon carbide at 1100°C, when the material was deformed under applied stresses greater than 132 MPa, to creep strains greater than 0.10%.<sup>6</sup> This paper will describe the tensile creep behavior of this siliconized silicon carbide under applied stresses above and below the threshold stress for creep damage. The contribution of creep damage to the deformation process is discussed with particular emphasis on the stress exponent for steady-state creep.

#### EXPERIMENTAL PROCEDURE

##### (1) Material and Specimen Design

The siliconized silicon carbide<sup>a</sup> examined in this study contained approximately 33.7 to 35.7 volume percent free silicon metal with the remainder of the material composed of silicon carbide grains, four to six microns in size. The microstructure of this material was characterized in a previous paper.<sup>6</sup>

Tensile creep specimens were cut from rectangular blanks, approximately 76.2 x 12.7 x 2.5 mm in size with a 320 grit finish, using a wire EDM (electro-discharge machining) technique. The design of the

<sup>a</sup>KX-01, Standard Oil Engineered Materials Company, Niagara Falls, NY.

tensile specimen is shown in figure 1. This design was similar to the modified flat dogbone-shaped specimen developed by Wakai et al.<sup>9</sup> The specimen has two target arms and a gauge length of approximately 17.5 mm. The two holes in the specimen were used to pin the specimen to the loading system. It was very important that the holes were machined directly on the centerline of the specimen and machined to a uniform smoothness. A bending moment could be produced during loading if the pins did not sit properly in the holes or if the holes were offset from the center line.

## (2) Loading System

Figure 2 is a schematic of the tensile loading system. The tensile specimen was attached to the two siliconized silicon carbide<sup>b</sup> grips using sintered alpha silicon carbide<sup>c</sup> pins. The pin and grip arrangement was located inside the furnace and resided at the test temperature. The two grips extended outside the furnace and were connected to two universal joints and the other parts of the loading system. The load was applied to the specimen by hanging the appropriate weights from the loading platform. This loading system was designed to load the creep specimens under tensile conditions with a minimal bending moment. In order to determine the amount of bending introduced into the specimen, strain gauges were mounted to all four sides of the gauge section and a stress of 69 MPa was applied. The elastic strains on the four sides of the specimen were measured to be within 2% of each other. This value corresponds to a maximum stress

<sup>b</sup>Crystar, Norton Company, Worcester, MA.

<sup>c</sup>Hexolloy SA, Standard Oil Engineered Materials Company, Niagara Falls, NY.

variation in the gauge section of approximately 1.4 MPa, at this load level.

### (3) Measurement Technique

The creep elongation of the specimen was measured using an optical extensometer.<sup>d</sup> The optical extensometer focused on the two target arms of the tensile specimen through a fused silica window in the furnace. The target arms of the specimen were back-lighted using a halogen light source that was transmitted through another fused silica window located directly behind the specimen. The optical extensometer could detect the shadows of the two target arms using photo-cathode screens. As the target arms moved apart during the creep test, the optical extensometer followed their movement, producing an output proportional to the displacement. The resolution of this device was approximately one micron at 1100°C, in air.

### (4) Test Procedure

Creep tests were conducted at 1100 to 1200°C, under stresses ranging from 103 to 172 MPa for times up to 250 hours. In order to ensure that bending was kept to a minimum in the loading system, the majority of the creep tests were interrupted before failure so that the amount of bending in the gauge section could be measured. A calibrated eyepiece was used to optically measure differences in the displacements between the two target arms on both sides of the gauge section. For the specimens used in this study, the differences in the displacements between the target arms were less than 8% of each other. The deformed specimens were then

<sup>d</sup>Model 200-X-2, Zimmer OHG, West Germany

sectioned, polished and examined using scanning and transmission electron microscopy.

A few of the specimens were also analyzed for bending by a technique developed by Jakus et al.<sup>10</sup> This technique determined the amount of bending in a specimen by measuring the surface curvature of the gauge section. The apparatus\* consisted of a linear voltage displacement transducer (LVDT) which systematically moved across the surface of the gauge section. Any curvature in the section was recorded as a positive or negative displacement of the LVDT. A computer program analyzed the measured displacements and calculated the curvature of the gauge sections. With this technique, the amount of strain variation in deformed gauge sections was determined to be approximately 6 to 8%.

## RESULTS AND DISCUSSION

### (1) Creep Results

Figure 3 summarizes some of the tensile creep curves at 1100°C for applied stresses of 103, 137 and 172 MPa. All of these tests were interrupted after a certain period to ensure that bending in the gauge section was minimal. The strain versus time results exhibited an initial primary regime where the creep rate decreased rapidly with time. After this transient period, a secondary or steady-state creep regime was observed, where the creep rate was constant with time. All tests shown in figure 3 were terminated prior to specimen failure. If these tests were conducted until failure, a regime of tertiary creep behavior would have also been observed. The shape of these creep curves are similar to

---

\*National Bureau of Standards, Gaithersburg, MD.

those found in tensile creep studies involving other ceramic materials.<sup>1,4</sup>

The transition point between primary and secondary creep behavior was determined using a computer program. In this analysis, the primary creep regime was fit to a logarithmic relationship and the secondary creep regime was fit to a linear relationship. The procedure used in this analysis has been described elsewhere.<sup>5</sup> Generally, the transition from primary to secondary creep behavior occurred between 10 and 20 hours.

Wiederhorn et al.<sup>7</sup> and Carroll et al.<sup>11</sup> have also observed secondary creep to be established very quickly in this siliconized silicon carbide. Their tensile creep<sup>7</sup> and creep rupture studies<sup>11</sup> have shown that after a short primary stage (<20 hours), an extended period of secondary creep is observed prior to the onset of tertiary creep and failure. In almost all cases, the secondary creep regime was found to extend for more than 80% of the specimen's creep life.<sup>7,11</sup> The few exceptions involved specimens which exhibited a longer than normal tertiary creep regime.

The creep results for two specimens tested to failure, at 1100°C under an applied stress of 172 MPa, are shown in figure 4. Specimens K5 and K7 both exhibited tertiary creep behavior with failure strains of 0.75% and 0.56%, respectively. These results show a variation in the creep behavior in both the secondary and the tertiary creep regimes. Specimen K7 exhibited a relatively long secondary creep regime, with a short period of tertiary creep behavior prior to failure. The secondary creep regime of this specimen lasted for approximately 80% of its creep life. The creep curve of specimen K5 is much different than specimen K7. This specimen exhibited a shorter secondary creep regime with a longer

period of tertiary creep behavior. In specimen K5, the secondary creep regime lasted approximately 40% of its creep life.

This variation in the creep behavior is most likely due to microstructural differences, such as the amount and distribution of the silicon phase in the material. Microstructural analysis of this siliconized silicon carbide has revealed that this material is very inhomogeneous.<sup>8</sup> Some areas of the microstructure contained a high density of silicon carbide while other areas contained large pockets of silicon. This uneven distribution of silicon throughout the material will result in a variation in the creep behavior between specimens. In a related study, Carter et al.<sup>12</sup> have shown that the creep behavior of a reaction-bonded silicon carbide was sensitive to these microstructural differences. In this study, they found a direct correlation between the amount of silicon in the specimen and the observed steady-state creep rate. For the specimens which contained the most silicon (approximately 12.2 volume %), they found the steady-state creep rate was six times greater than the specimen which contained the least amount of silicon (approximately 10.9 volume %).

## (2) Stress and Temperature Dependence of Steady-state Creep

The steady-state stress exponent at 1100°C was determined by plotting the  $\log \dot{\epsilon}_s$  versus  $\log \sigma$ , where  $\dot{\epsilon}_s$  is the secondary creep rate and  $\sigma$  is the applied stress. The slope of the best-fit line through the data is equal to the steady-state stress exponent for creep. The results revealed an increasing stress exponent with stress (figure 5). At stresses below 137 MPa, the steady-state stress exponent was approximately

four. At stresses greater than this value, the slope of the line is considerably greater, approaching a value of ten. The increase in the stress exponent in the high stress regime indicates that the mechanism(s) responsible for creep may be changing. SEM analyses have shown that creep damage accompanies deformation in the specimens tested under the higher applied stresses. In a previous paper, a threshold stress for creep damage at 1100°C was determined to be approximately 132 MPa.<sup>8</sup> This threshold stress value lies on the stress exponent curve where the exponent changes from four to ten. This result suggests that the increase in the stress exponent above the threshold stress is due to the formation of creep damage. A similar type of behavior has also been observed by Wiederhorn et al.<sup>7</sup> for this particular siliconized silicon carbide. Their tensile tests were conducted at a higher temperature of 1300°C for applied stresses of 60 to 135 MPa. They observed a stress exponent of approximately four at applied stresses less than 100 MPa and a stress exponent of thirteen at stresses greater than 100 MPa. They suggested that the increase in the stress exponent was also due to the formation of creep damage.

The activation energy for steady-state creep was determined for the temperature range of 1100 to 1200°C under applied stresses of 103, 137 and 172 MPa (figure 6). A plot of  $\ln \dot{\epsilon}$ , versus  $1/T$ , where T is temperature, yields the activation energy for steady-state creep from the slope of the best-fit line through the data. At a stress level of 103 MPa, the activation energy was approximately 175 kJ/mole for the temperature range of 1100 to 1200°C. This stress level corresponds to the region where the steady-state stress exponent was approximately four at 1100°C. At the

higher applied stresses of 137 and 172 MPa, the activation energy for creep increased to 210 and 350 kJ/mole, respectively, for the same temperature range. The change in the activation energies also indicates that the mechanism for creep is changing as the applied stress increases. These stress levels correspond to the regime where the stress exponent for steady-state creep was approximately ten, at 1100°C.

### (3) Transmission Electron Microscopy

Deformed specimens were examined using transmission electron microscopy. The results revealed dislocation activity in the silicon phase for all stress levels in this investigation. There was no observable movement or increase in the number of dislocations in the silicon carbide grains. Figure 7 is a bright field transmission electron micrograph of a silicon pocket in a specimen tested at 1100°C under 172 MPa to a creep strain of 0.56%. The Burger's vector of these dislocations was  $a/2[1\bar{1}0]$ . Typically, dislocation densities were relatively low and confined in groups randomly distributed throughout the silicon pockets. There were no signs of large dislocation networks in the silicon phase. These results indicate that creep deformation occurs by deformation of the silicon phase and that the silicon carbide grains essentially behave as rigid elastic particles.

### (4) Creep Mechanism Below the Threshold for Creep Damage

The stress exponent of four, which is below the threshold stress for creep damage, is a representative value for the stress exponents normally obtained for dislocation controlled creep. According to the deformation

map of silicon, the applied stresses and temperatures used in this study correspond to the regime where dislocation creep is the rate-controlling mechanism.<sup>13</sup> Therefore, the creep deformation of this siliconized silicon carbide below the threshold stress for creep damage, is controlled by dislocation processes in the silicon phase. The activation energy for steady state creep at 103 MPa was approximately 175 kJ/mole for the temperature range of 1100 to 1200°C. If dislocation climb were the rate controlling process for steady-state creep, the observed activation energy should be equal to the activation energy for the lattice diffusion of silicon.<sup>14</sup> The activation energy of 175 kJ/mole is approximately one-third of the activation energy for lattice diffusion of silicon.<sup>15</sup> Since the observed activation energy is less than that for lattice diffusion, dislocation climb probably does not control secondary creep, unless short-circuit diffusion processes are operative.

However, the activation energy of 175 kJ/mole is close to the activation energy obtained during dislocation velocity measurements in silicon.<sup>16,17</sup> Suzuki et al.<sup>16</sup> and Kannan et al.<sup>17</sup> have determined the activation energy for dislocation motion to be approximately 221 and 176 kJ/mole, respectively. They concluded that these activation energies corresponded to the energy for thermally-activated dislocation glide in silicon, where the rate-controlling process was overcoming the Peierls barrier by the formation of double kinks. Therefore, based upon these results, steady-state creep in this siliconized silicon carbide below the threshold stress for creep damage, may be controlled by this mechanism. However, further TEM analysis is necessary to confirm this conclusion.

### (5) Creep Mechanism Above the Threshold Stress for Creep Damage

The increase in the stress exponent and the activation energy above the threshold stress for creep damage can be attributed to the formation of creep damage. Similar changes in the stress exponents<sup>1-7</sup> and activation energies<sup>3,5,6</sup> for steady-state creep have been observed in other studies when creep damage or grain boundary cracking occurred during deformation. This type of behavior is due to the enhancement in the creep rate by the formation of creep damage.

Both Hasselman et al.<sup>18,19</sup> and Raj<sup>20</sup> have discussed the effects of creep damage on the creep rate of a material. The model of Hasselman et al.<sup>18,19</sup> is based upon two mechanisms through which creep damage or cavity formation can contribute to the creep rate of a material. The first mechanism is called crack-enhanced creep ( $\dot{\epsilon}$ ) and describes the local transfer of stress from grain boundaries where cavities formed, to the surrounding matrix. This local stress transfer increases the effective stress on the matrix, resulting in an accelerated creep rate. The contribution of crack-enhanced creep is given by:<sup>18,19</sup>

$$\dot{\epsilon}_c = \dot{\epsilon}_{mat} (1 + 2\pi Na^2 n^{1/2}) \quad (1)$$

where  $\dot{\epsilon}_{mat}$  is the rate of creep for the material in the absence of cavities, N is the areal density of cavities at a given time, a is the cavity half length and n is the steady-state stress exponent of the cavity-free material.

The second mechanism through which cavities can enhance the measured creep rate is referred to as elastic creep ( $\dot{\epsilon}_{elast}$ ). This process describes the time dependent decrease in the elastic modulus of the

material, through the formation of creep damage. The elastic creep rate of a material is:<sup>18,19</sup>

$$\dot{\epsilon}_{elast} = 2\pi a \sigma (2\dot{a}N + aN) / E_{mat} \quad (2)$$

where  $\dot{a}$  is the rate of cavity growth,  $N$  is the rate of cavity nucleation per unit area, and  $E_{mat}$  is the elastic modulus of the cavity-free material.

According to Hasselman et al.,<sup>18,19</sup> the total creep rate of a material including the contribution of creep damage, is sum of equations (1) and (2). However, a third contribution to the creep rate should also be considered. Raj<sup>20</sup> has shown that the formation of creep damage or cavities results in a volume increase in the gauge section. The volume increase will appear as a time-dependent strain which is measured along with the creep strain. This contribution of creep damage ( $\dot{\epsilon}_{cav}$ ) to the measured creep rate of a material is given by:<sup>20</sup>

$$\dot{\epsilon}_{cav} = (1/3)\Delta\dot{V}/V = (1/3)\dot{V}_f \quad (3)$$

where  $\Delta\dot{V}/V$  is the rate of change in the volume of the gauge section with time and  $\dot{V}_f$  is the rate of change in the volume fraction of cavities with time.

In order to determine if the increase in the stress exponent (figure 5) is due to the formation of creep damage, equations (1), (2) and (3) were used to subtract the contribution of creep damage from the measured creep rates. The parameters used in these calculations were obtained from the results of the quantitative microscopy presented in the previous paper.<sup>8</sup> In this analysis, creep damage was assumed to occur

during the secondary creep regime. This assumption was based upon the results of the areal density and area fraction of cavities analyses, which indicate that creep damage does not form until the later stages of primary creep or the initial stages of secondary creep behavior.<sup>8</sup> This analysis was only conducted for those specimens which were interrupted during the secondary creep regime, before the onset of tertiary creep behavior.

The total measured creep strain during the secondary creep regime can be calculated by:

$$\epsilon_t = \dot{\epsilon}_s \cdot t \quad (4)$$

where  $\dot{\epsilon}_s$  is the measured secondary creep rate and  $t$  is time of the test in the secondary creep regime. The amount of the measured strain due to the formation of creep damage can be determined by integrating equations (1), (2) and (3) with respect to time. By integrating equation (1), the amount of creep strain in the secondary creep regime due to crack-enhanced creep ( $\epsilon_c$ ) is:<sup>2</sup>

$$\epsilon_c = \epsilon_{mat} (1 + \pi N a^2 n^{1/2}) \quad (5)$$

where  $\epsilon_{mat}$  is the creep strain of the cavity-free material. The amount of elastic creep strain ( $\epsilon_{elast}$ ) is found from integrating equation (2). Assuming that the contribution of cavity growth to deformation is minimal

---

<sup>2</sup>In this integration, it was assumed that the areal density of cavities increases linearly with time.

( $\dot{a} = 0$ ),  $\epsilon_{elast}$  is:<sup>6</sup>

$$\epsilon_{elast} = 2\pi a^2 \sigma N / E_{mat} \quad (6)$$

where  $N$  is the number of cavities per unit area. The integration of equation (3) yields the amount of strain due to the increase in the volume of the gauge section from the formation of creep damage ( $\epsilon_{cav}$ ) as:

$$\epsilon_{cav} = (1/3) V_f \quad (7)$$

where  $V_f$  is the volume fraction of cavities in the specimen.

By using the results of the areal density and area fraction analyses presented in the previous paper<sup>6</sup> and the assumption that the volume fraction of cavities is equal to the area fraction of cavities,  $\epsilon_c$ , can be calculated using:

$$\epsilon_c = \epsilon_t - \epsilon_{elast} - \epsilon_{cav} \quad (8)$$

The creep strain of the siliconized silicon carbide specimens without the contribution of creep damage ( $\epsilon_{mat}$ ) is obtained from this result by rearranging equation (5) to:

$$\epsilon_{mat} = \epsilon_c / (1 + \pi N a^2 n^{1/2}) \quad (9)$$

The creep rate of the siliconized silicon carbide in the absence of creep damage, can then be calculated by dividing  $\epsilon_{mat}$  by the total time of the secondary creep regime.

---

<sup>6</sup>This conclusion was based upon SEM and quantitative microstructural analyses. These techniques have shown that once a cavity nucleates, it grows very rapidly to a maximum size, whereupon further growth with deformation is minimal. The maximum size of the cavity is dictated by the size of the silicon carbide grain facet. In this analysis, it was assumed the cavities nucleate with a final size of  $a = 3 \times 10^{-6}$  m.<sup>6</sup>

After calculating the creep rate of the siliconized silicon carbide without the contributions of creep damage, the results were plotted on the stress exponent curve (figure 8). The creep data below the threshold stress for creep damage was also included. The lines with the slope of four and ten correspond to the original data. After subtracting the effects of creep damage from the measured creep rates, the creep data above the threshold, tends to fall on the line corresponding to a stress exponent of four. This result indicates that the increase in the stress exponent was due to the formation of creep damage. By comparing the contribution of each mechanism to the enhanced creep rate, the volume increase as described by Raj,<sup>20</sup> is responsible for most of the increased stress exponent.

The models of Hasselman et al.<sup>18,19</sup> and Raj<sup>20</sup> have accounted for the majority of the enhanced creep rates at 137 and 155 MPa. At 172 MPa, however, the calculated creep rates were somewhat higher than the values predicted by the line having a slope equal to four. It is possible that at this stress level, the cavity densities were large enough for cavity interactions to contribute to the deformation process. Cavity interactions could increase the creep rate by raising the effective stress in the material.

#### SUMMARY

The tensile creep behavior of a siliconized silicon carbide was measured using an optical extensometer and a modified flat dogbone-shaped specimen. Creep tests were conducted in air under applied stresses of 103 to 172 MPa for the temperature range of 1100 to 1200°C. The steady-state

stress exponent for creep at 1100°C was determined to be approximately four under applied stresses less than the threshold for creep damage (132 MPa). Under applied stresses greater than the threshold for creep damage, the steady-state stress exponent increased to approximately ten. The activation energy for steady-state creep at 103 MPa was approximately 175 kJ/mole for the temperature range of 1100 to 1200°C. Under applied stresses of 137 and 172 MPa, the activation energy increased to 210 and 350 kJ/mole, respectively, for the same temperature range.

At applied stresses less than the threshold for creep damage, creep deformation in the siliconized silicon carbide was controlled by dislocation processes in the silicon phase. The activation energy of 175 kJ/mole and a stress exponent of four suggests that the rate-controlling mechanism may involve dislocation glide in the silicon phase. Creep deformation above the threshold stress for creep damage, was enhanced due to the formation of creep damage. The increase in the stress exponent and activation for creep was due to the contribution of creep damage to the deformation process. The models of Hasselman et al.<sup>18,19</sup> and Raj<sup>20</sup> were used to describe the enhancement in the creep rate and to account for the increase in the stress exponent caused by the formation of creep damage.

## REFERENCES

1. R. Kossowsky, D. G. Miller and E. S. Diaz, "Tensile and Creep Strengths of Hot-Pressed  $\text{Si}_3\text{N}_4$ ," *J. Mater. Sci.*, 10, 983-997 (1975).
2. R. M. Arons and J. K. Tien, "Creep Strain Recovery in Hot-Pressed Silicon Nitride," *J. Mater. Sci.*, 15, 2046-2058 (1980).
3. A. Crosby and P. E. Evans, "Creep in Pure and Two Phase Nickel-Doped Alumina," *J. Mater. Sci.*, 8, 1573-1580 (1973).
4. R. Morrell, K. H. G. Ashbee, "High Temperature Creep of Lithium Zinc Silicate Glass-Ceramics," *J. Mater. Sci.*, 8, 1253-1270 (1973).
5. D. F. Carroll, "Tensile Creep Behavior and Cavity Damage in a Siliconized Silicon Carbide"; Ph. D. Thesis, The Pennsylvania State University, May 1987.
6. S. M. Wiederhorn, L. Chuck, E. R. Fuller, and N. J. Tighe; pp. 755-773 in Tailoring Multiphase and Composite Ceramics, *Mat Sci. Res.* Vol. 20. Edited by R. E. Tressler, G. L. Messing, C. G. Pantano and R. E. Newnham. Plenum Press, New York, 1987.
7. S. M. Wiederhorn, L. C. Chuck, T. -J. Chuang, "Damage-Enhanced Creep in a Siliconized Silicon Carbide: Phenomenology," To be Published in the *J. Am. Ceram. Soc.*
8. D. F. Carroll and R. E. Tressler, "Accumulation of Creep Damage in a Siliconized Silicon Carbide," To be published in the *J. Am. Ceram. Soc.*
9. F. Wakai, S. Sakaguchi, Y. Matsuno, and H. Okunda, "Tensile Creep Test of Hot-Pressed  $\text{Si}_3\text{N}_4$ "; presented at the International Symposium on Ceramic Components for Engines. Hakone, Japan, October 17-21, 1983.
10. K. Jakus and S. M. Wiederhorn, "Creep Deformation of Ceramics in Four Point Bending," To be Published.
11. D. F. Carroll and S. M. Wiederhorn, to be published.
12. C. H. Carter, R. F. Davis and J. Bentley, "Kinetics and Mechanisms of High-Temperature Creep in Silicon Carbide: I, Reaction-Bonded," *J. Am. Ceram. Soc.*, 67, 409-417 (1984).
13. H. J. Frost and M. F. Ashby, pp. 71-74 in Deformation-Mechanism Maps. Pergamon Press, New York, 1982.
14. J. Weertman, "Dislocation Climb Theory of Steady-State Creep", *ASM*, 61, 681-694 (1968).
15. B. J. Masters and J. M. Fairfield, "Silicon Self-Diffusion," *Appl. Physics Letters*, 8, 280-281 (1966).

16. T. Suzuki and H. Kojima, "Dislocation Motion in Silicon Crystals as Measured by the Lang X-ray Technique," *Acta Metall.*, 14, 913-924 (1966)
17. V. C. Kannan and J. W. Washburn, "Direct Dislocation Velocity Measurements in Silicon by X-ray Topography," *J. Appl. Phys.*, 41, 3589-3597 (1970).
18. D. P. H. Hasselman and A. Venkateswaran, "Role of Cracks in the Creep Deformation of Brittle Polycrystalline Ceramics," *J. Mater. Sci.*, 18, 161-172 (1983).
19. D. P. H. Hasselman and A. Venkateswaran, pp. 525-546 in *Deformation of Ceramic Materials, II*. Edited by R. E. Tressler and R. C. Bradt. Plenum Press, New York, 1984.
20. R. Raj, "Separation of Cavitation-Strain and Creep-Strain During Deformation," *J. Am. Ceram. Soc.*, 65, C-46 (1982).

**FIGURE CAPTIONS**

Figure 1. Tensile specimen design.

Figure 2. Loading system of creep apparatus.

Figure 3. Creep strain versus time at 1100°C for specimens tested under stresses of 103, 137 and 172 MPa.

Figure 4. Creep strain versus time at 1100°C for specimens tested under a stress of 172 MPa.

Figure 5. Log steady-state creep rate ( $\dot{\epsilon}_s$ ) versus log applied stress ( $\sigma$ ) at 1100°C.

Figure 6. Ln steady-state creep rate ( $\dot{\epsilon}_s$ ) versus temperature for applied stresses of 103, 137 and 172 MPa.

Figure 7. TEM bright field micrograph of dislocations in a silicon pocket of a specimen tested under a stress of 172 MPa to a creep strain of 0.56% at 1100°C.

Figure 8. Log steady-state creep rate ( $\dot{\epsilon}_s$ ) versus log applied stress ( $\sigma$ ) at 1100°C. Cavity contribution has been subtracted from the measured creep rate.

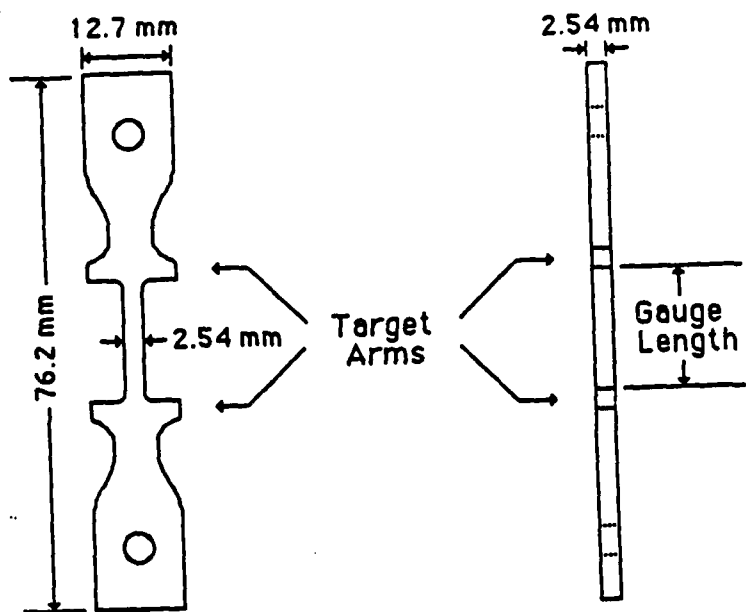


Fig 1

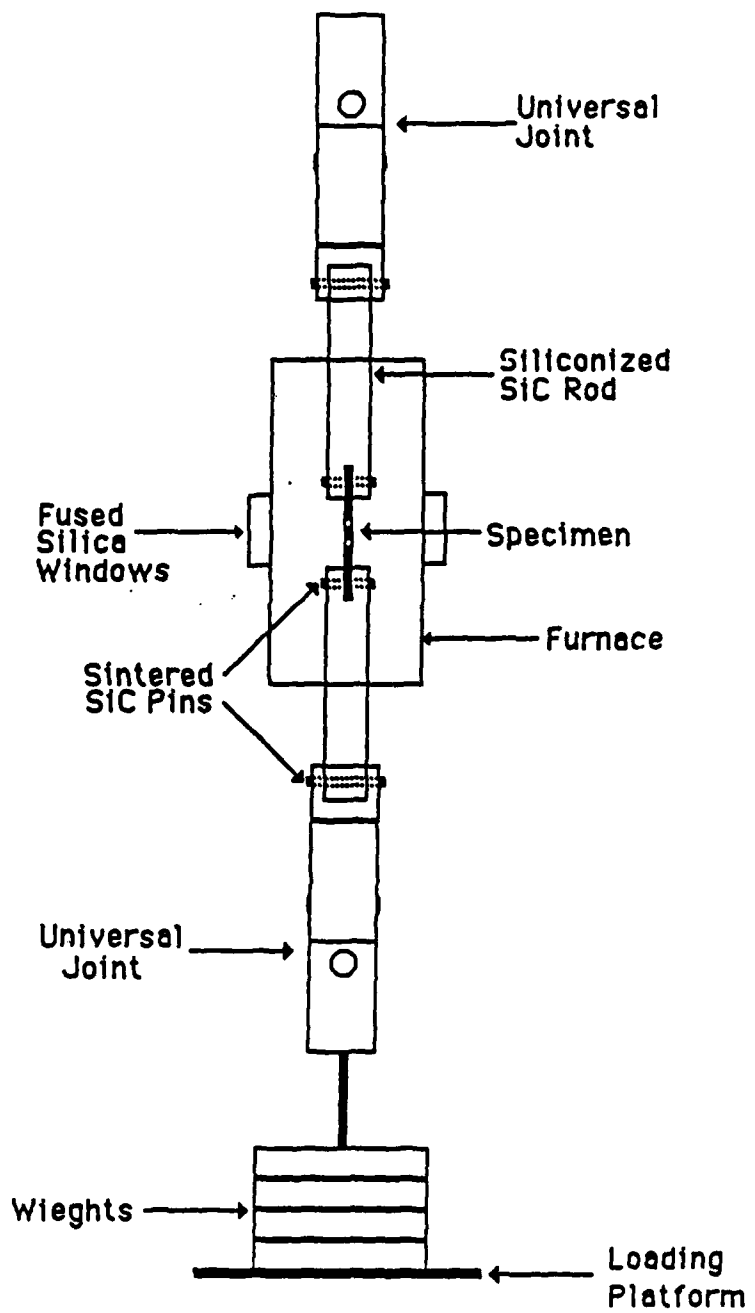
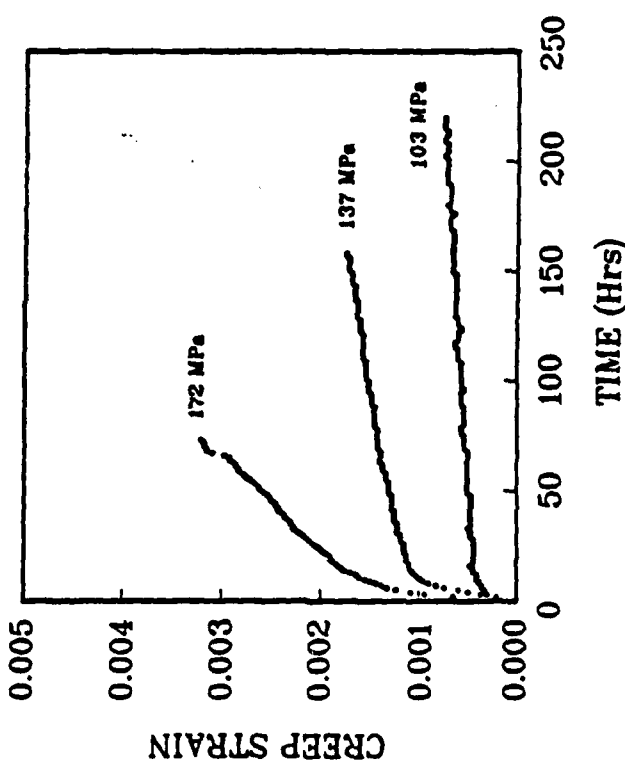


Fig 2

Fig. 3



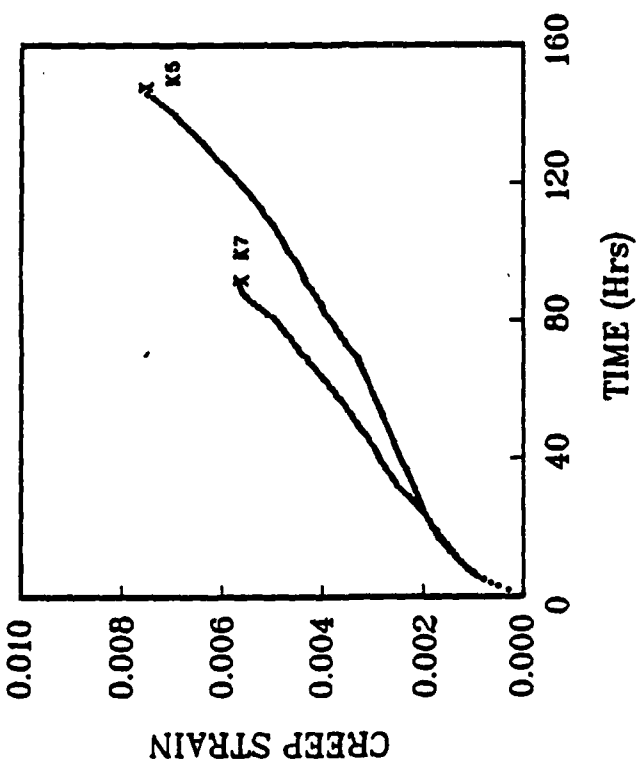
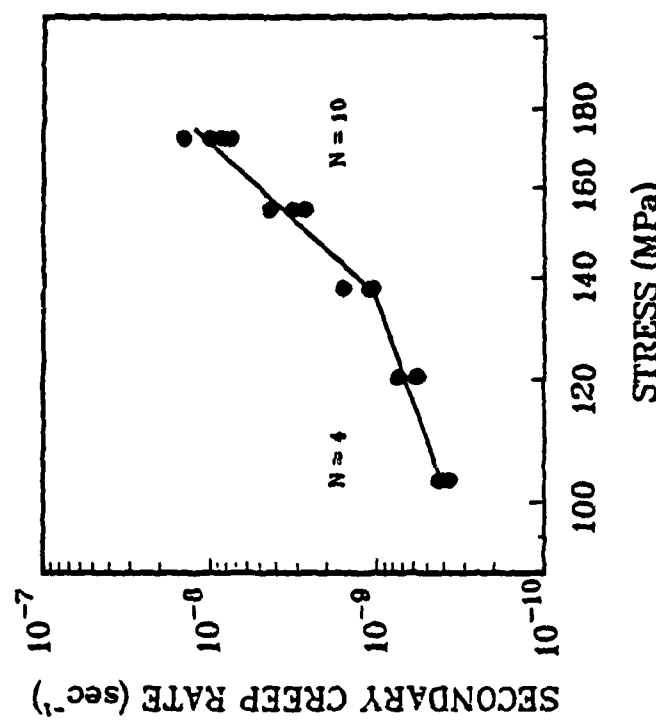


Fig 4

Fig. 5



T<sub>18</sub> 6

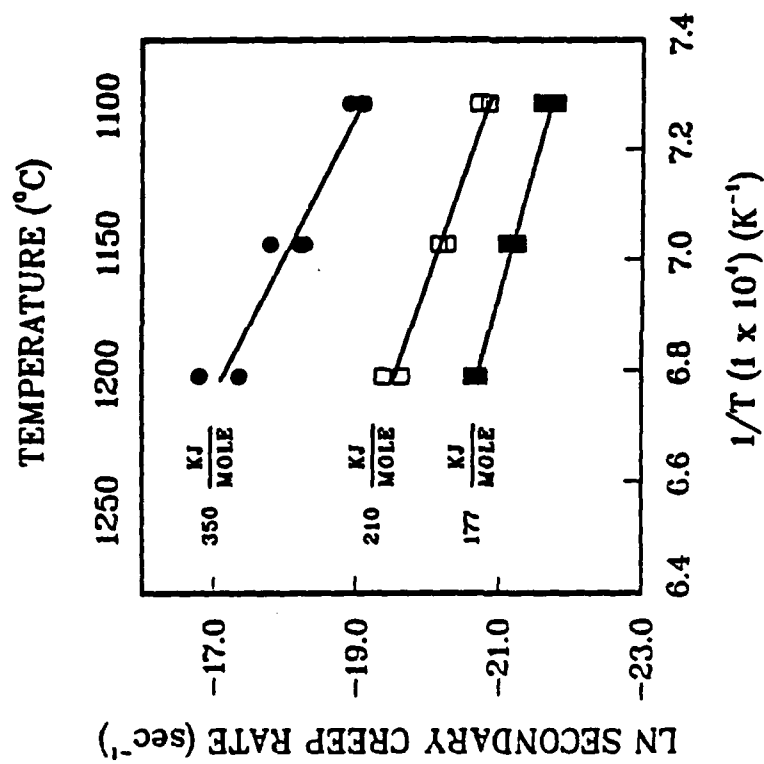
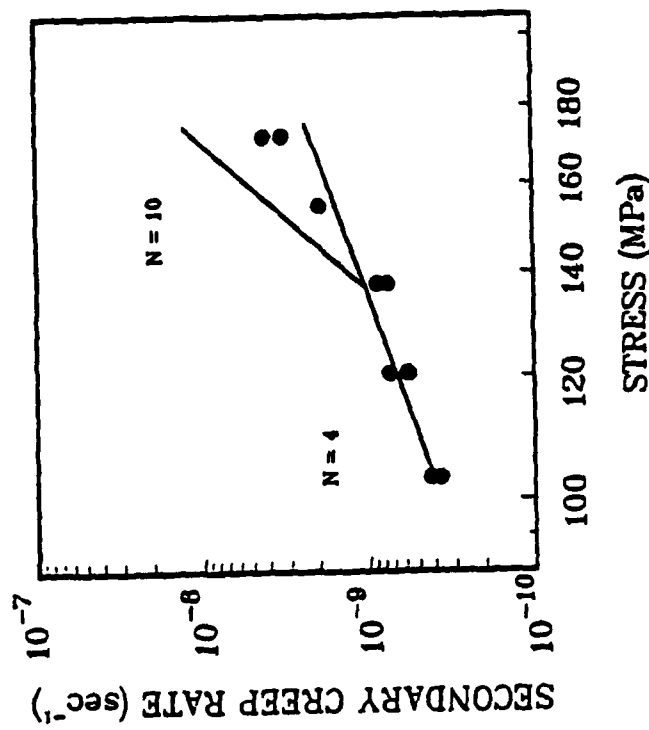


Fig 7



F18



## TIME DEPENDENT MECHANICAL BEHAVIOR OF SILICON NITRIDE CERAMICS ABOVE 1100°C

M. R. Foley and R. E. Tressler  
The Pennsylvania State University  
Department of Materials Science and Engineering  
Ceramic Science Program  
University Park, PA 16802

### ABSTRACT

Slow crack growth and creep damage accumulation in silicon nitride ceramics are important processes which limit their usefulness in highly stressed components at elevated temperatures in heat engines. The threshold stress intensities for crack growth at elevated temperatures in air for a commercially available silicon nitride ceramic have been estimated from interrupted static fatigue tests. Tensile creep measurements for this material are being used to delineate the regimes of temperature and stress in which creep cavitation causes flaw nucleation and eventual failure.

### INTRODUCTION

Silicon nitride-based ceramics are being studied for high temperature structural applications such as gas turbine engine components. By using these ceramics, the new high efficiency heat engines can be operated at temperatures higher than allowed by current super alloys. Although an excellent candidate for this application, silicon nitride-based ceramics are limited at elevated temperature due to their susceptibility to slow crack growth and creep damage.

Measurements of short-term strength, fracture toughness, slow crack growth and creep at high temperature have been reported for various silicon nitride ceramics<sup>1-7</sup>. In general, these properties are time, temperature and stress dependent and therefore, a detailed knowledge of these interrelationships are required to make long term reliability predictions. It has been shown<sup>8-10</sup> that there are two distinct regions of delayed failure for a typical silicon nitride ceramic at high temperatures. At low stress levels, rupture behavior is strain limited and failure occurs by creep rupture. At high stress levels the failure strains are very small and failure is governed by slow crack growth of preexisting flaws. For an MgO-doped HPSN a specific stress level has been reported by Grathwohl<sup>8</sup> dividing these two regions of behavior suggesting a threshold stress or stress intensity for crack growth. Below this threshold preexisting flaws apparently blunt, and either accommodated creep or cavitation creep control the time dependent strength.

In this paper our measurements of the threshold stress intensity for crack growth in an alumina yttria-doped silicon nitride using static loading tests are presented. In addition tensile creep experiments have been performed to characterize the behavior of this material below the threshold stress intensity for crack growth. Tensile tests were chosen to study the material

behavior in the creep regime since the stresses are poorly defined in a creeping bend specimen<sup>11</sup>.

## EXPERIMENTAL PROCEDURE

### 1) Material and Specimen Design

The silicon nitride\* examined in this investigation contained 2 wt% alumina and 6 wt% yttria as densification aids. The bulk density of this material was 3.24 - 3.26 g/cc<sup>12</sup>. The microstructure as shown in Figure 1 consisted of equiaxed grains of  $\beta$ -Si<sub>3</sub>N<sub>4</sub> ranging in size from less than 0.25 up to 4 microns, elongated grains with aspect ratios ranging from 3:1 to 9:1, and an amorphous grain boundary phase. Bend specimens were cut from rectangular blanks, approximately 20 x 30 x 5 mm in size using a diamond cut-off wheel. The major faces of the samples were surface-ground to a 600-grit finish. Tensile surfaces were hand-beveled using a 15 micron diamond disc to eliminate any edge-checking flaws that may have formed during grinding. The final test bar dimensions were approximately 4 x 2 x 30 mm.

Tensile creep specimens were cut from rectangular blanks, approximately 15 x 15 x 76.2 mm in size. The specimen design (Figure 2) was similar to the modified flat dogbone-shaped specimens developed by Wakai<sup>13</sup> and co-workers and also used by Carroll and Tressler<sup>14</sup>. The specimen design used in this study, however, eliminated the use of machined-in target arms for strain measurements using an optical extensometer. Target arms of the same composition as the specimen were attached to the specimen using platinum wire giving a gauge length of approximately 19 mm. The two holes in the specimen were used to pin the specimen to the loading system. It should be noted that the holes were double tapered and the holes were machined directly on the centerline of the specimen in order to avoid bending moments. The edges of the gauge length were polished using diamond paste down to 3 microns to minimize grinding flaws.

### 2) Loading Systems

#### a) Flexure

The four point bend test system consisted of alumina rams entering a furnace from the top and bottom and hot pressed magnesia-doped silicon nitride knife edges with upper and lower spans of 5.2 and 19.7 mm, respectively. A double plate and bearing assembly was used to allow alignment of the rams. The furnace was positioned between the lead screws of a computer controlled testing machine.

#### b) Tension

A schematic of the tensile loading system designed by Carroll and Tressler<sup>14</sup> is shown in Figure 3. The tensile specimen was attached to the two siliconized silicon carbide grips\*\* using sintered alpha silicon carbide\*\*\* pins. The pin and grip arrangement was located inside the furnace and resided at the test temperature. The two grips extended outside the furnace and were connected to the remainder of the load trains. The load was applied to the specimen by hanging weights from the loading platform.

\* AY6 silicon nitride, GTE, Towanda, PA

\*\* Crystar, Norton Company Worcester, MA

\*\*\* Hexalloy SA, Standard Oil Engineered Materials Co., Niagara Falls, NY

The creep elongation of the specimen was measured using an optical extensometer\*. The optical extensometer focussed on the two target arms on the tensile specimen through a fused silica window. The target arms were back-lighted using a halogen light source transmitted through a second fused silica window located in the back of the furnace. The optical extensometer detects the shadows of the two target arms using photo-cathode screens. As the target arms move apart during the creep test, the optical extensometer follows their movement, producing an output proportional to the displacement. The resolution of this measuring technique is approximately one micron at 1100-1200°C in air.

## TEST PROCEDURE

### a) Interrupted Static Fatigue Test

The interrupted static fatigue test used on the bend specimens in this study has been fully described by Minford<sup>15,16</sup> and co-workers. The test involves heating the sample to test temperature, rapidly loading to a predetermined static load level for a specified time. If the sample does not fail during the soak time, it is rapidly loaded to failure at the test temperature. This test directly measures the effect of an applied stress during static loading on the fracture stress of the material. The strength reflects any changes in flaw severity and gives one an estimate of the threshold stress intensity for crack growth in the material. Tests were performed on as-machined and oxidized samples at 1100 and 1200°C in air for ten hours. The stressing rate was 30-35 MPa/sec.

### b) Creep Tests

Creep tests were performed at 1100 to 1200°C in air at stresses of 100, 150 and 200 MPa for up to 100 hours. Specimens were placed into the loading train under a prestress of 12 MPa before furnace heat up in order to seat the pins in the holes and minimize bending moments. The furnace was then heated to 1200°C in air for a minimum of 16 hours to oxidize the sample. The temperature of the furnace was then set to the test temperature (1100-1200°C) and held for another 8 hours to bring the entire loading system to thermal equilibrium before starting the creep test. Due to the sensitivity of the measuring technique to changes in ambient temperature, the entire loading train system was thermally isolated from the room. After oxidation and thermal equilibration of the sample and system, the sample was loaded to the desired stress level for the creep test.

## RESULTS AND DISCUSSION

### 1) Threshold Stress Intensity for Crack Growth

Figures 4 and 5 summarize the interrupted static fatigue test results at 1100°C in air for the as-machined and oxidized (15 hrs @ 1200°C in air) silicon nitride samples, respectively. Plotted at an initial stress intensity of zero are samples fractured at 1100°C in air with no prior static loading. The symbols and error bars represent the mean fracture stress and 95% confidence interval, respectively. The threshold stress intensity,  $K_{I_0}$ , is estimated as the lowest initial applied stress intensity at which at least one of the samples failed during static loading. The threshold stress intensity for crack growth for the as-machined and oxidized samples are 1.75 MPa·m<sup>1/2</sup> and 2.00 MPa·m<sup>1/2</sup>, respectively. The range of  $K_{I_0}$  values is due to the range of flaw sizes calculated from the initial strength distributions. Note also that, because there is no

\* Model 200 x-2, Zimmer OHG, West Germany

significant change in mean fracture stress (indicated by the solid circle) with increased initial stress intensity up to  $K_{I_0}$ , it is assumed that the original strength-limiting flaw population is unchanged.

The interrupted static fatigue test results for as-machined and oxidized samples at 1200°C in air are summarized in Figures 6 and 7. For the as-machined samples, a sharp decrease in mean fracture stress is observed with increasing initial applied stress intensity along with an apparent threshold stress intensity of 1.00 MPa·m<sup>1/2</sup>. The oxidized samples during static loading do not show any significant decrease in mean fracture stress with increasing initial applied stress intensity up to the  $K_{I_0}$  of 1.50 MPa·m<sup>1/2</sup>.

The differences in  $K_{I_0}$  values between the as-machined and oxidized materials during static load testing are apparently due to a microstructural change, and this effect is most apparent at 1200°C for this material. The decreasing mean fracture stress for the as-machined samples is probably due to the creation of a new flaw population which produced flaws that were more severe. This new flaw population could possibly have been created by creep cavitation at this temperature as identified by Tighe<sup>7,17,18</sup> and co-workers, Grathwohl<sup>8</sup> and Quinn<sup>9,10</sup>. Note that, because of the creation of new flaws, the sizes of which are not well-characterized, the actual initial applied stress intensity values used during testing were different from those calculated from the original flaw population. Therefore, it is more informative to record the effect of initial applied stress on the mean fracture stress for the as-machined specimens (Fig. 6).

The fact that the oxidized samples do not experience the same detrimental effects during static loading at 1200°C as did the as-machined samples presumably results from an oxidation-induced microstructural change. At this temperature it is well known<sup>19-23</sup> that additives and impurities such as Fe, Al and Y present in the grain boundary phase diffuse toward the surface. This rejection of impurities from the grain boundaries creates a more refractory grain boundary phase, and thus, produces a more creep resistant material.

## 2) Correlation between Flexural and Tensile Behavior

In order to delineate the regimes of temperatures and stress in which slow crack growth and creep cavitation are the dominant processes responsible for failure at high temperatures, tensile creep measurements were used. From the strengths of the bend specimens at these elevated temperatures, the strengths of tensile specimens can be predicted using Weibull statistics. In order to predict strengths on specimens with different volumes under stress, the effective volume must be calculated from the geometry of the specimen, the loading configuration and Weibull statistics. In the case of the rectangular cross section used in the bend tests (4 x 2 mm) and four-point bending test geometry (upper and lower spans of 5.2 and 19.7 mm, respectively), the effective volume ( $V_E$ ) is given by the relationship for four-point bending<sup>24</sup>:

$$V_E = K V_B$$

where  $K$ , the load factor, is given by

$$K = \frac{\left(\frac{a}{b}\right)m + 1}{2(m+1)^2}$$

where  $a$  is the upper span,  $b$  is the lower span,  $m$  is the Weibull modulus and  $V_B$  is the total volume under stress. Assuming that volume-distributed flaws dominate, the bend and tensile strengths are related by

$$\left(\frac{\sigma_T}{\sigma_B}\right)^m = \left(\frac{V_E}{V_T}\right)$$

where  $\sigma_T$  is the predicted tensile strength from four-point bend data,  $\sigma_B$  is the four-point bend strength and  $V_T$  is the total volume within the gauge length in a tensile specimen. The strengths of the tensile specimens can be estimated from the strength of the four-point bend specimens using the above relationship and the experimental Weibull parameters for the bend strengths. Because of the more stable behavior of the oxidized samples in bending, only oxidized specimens were used in tensile creep tests. The calculated applied stresses for fast fracture and for cracks to grow at the threshold stress intensity at 1100°C and 1200°C in air for oxidized tensile specimens are shown in Table 1. The Weibull moduli for the oxidized samples at 1100 and 1200°C were 7.0 and 5.0, respectively<sup>25</sup>.

Table 1. Tensile strength and threshold stress predictions from flexural data on oxidized specimens

TEMP (°C)	FLEXURAL		TENSILE	
	$\bar{\sigma}_f$ (MPa)	$\sigma_{th}$ (MPa)	$\bar{\sigma}_f$ (MPa)	$\sigma_{th}$ (MPa)
1100	599	333	346	192
1200	476	224	238	112

### 3) Creep Results

Preliminary tensile creep tests were performed on oxidized specimens at temperatures from 1100 and 1200°C under stresses of 100, 150 and 200 MPa. Figure 8 summarizes some of the tensile creep curves at 1100°C in air for applied stresses of 100, 150 and 200 MPa. An initial primary creep regime (up to 10-15 hrs), followed by a secondary or steady-state creep regime was observed. The tests shown in Figure 8 were terminated prior to specimen failure except for the 200 MPa test which was part of a temperature-change test. Similar tensile creep curves have been observed for other silicon nitride-based ceramics<sup>5,13,26, 27</sup> as well as for other ceramic materials<sup>14,28</sup>. No samples were tested to failure at 1100°C at these three stress levels and, hence, the presence or absence of tertiary creep cannot be ascertained.

The stress dependence of the steady state creep rate ( $\dot{\epsilon}_s$ ) at 1100°C was estimated by fitting to the Dorn equation:

$$\dot{\epsilon}_s = A \sigma^n \exp(-Q_c/kT)$$

where A is a constant, n is the stress exponent for steady state creep, Q<sub>c</sub> is the apparent activation energy for creep and k is the Boltzman constant. Plotting the  $\log \dot{\epsilon}_s$  versus  $\log \sigma$  for different samples at constant temperature (Figure 9), no concrete dependence is obvious from this preliminary data. Other values of the steady state stress exponent for silicon nitride ceramics have been reported<sup>5,8,29-31</sup> and range from 1.5 to 2.4 at temperatures of 1200 to 1400°C in air. They all indicate that creep deformation is controlled by viscous flow of the grain boundary phase leading to creep cavitation, flaw nucleation and eventual failure. Grathwohl<sup>8</sup> has shown that above a distinct stress level it is slow crack growth that governs rupture behavior and below which rupture behavior is controlled by creep cavitation. It is obvious that more stress change tests and temperature change tests are needed along with microscopic analysis to characterize the creep behavior of this material.

Results of the bend data predict a value of applied stress of 192 MPa in tension at 1100°C to equal the threshold stress intensity for crack growth (Table 1). Thus, at stresses above 200 MPa one expects slow crack growth to dominate and very small strains to failure to be observed.

Two creep tests were conducted at 1150°C at 200 MPa. Figure 10 shows the creep curve for one of the tests. Failure had not occurred after 75 hours, but the test was terminated due to equipment malfunction. The second test led to specimen failure in approximately 4 to 5 minutes and no creep strain data was measured. These specimens seem to have bracketed the threshold stress intensity for crack growth at this temperature.

The predicted threshold stress for crack growth in tension is 112 MPa at 1200°C (Table 1). Tensile creep experiments at 1200°C resulted in failure after 3 minutes and 1 minute at stresses of 100 and 200 MPa, respectively. Further experiments at stresses near and below the predicted threshold stress are needed to confirm these approximate predictions.

To estimate the activation energy for steady-state creep a temperature change test at constant stress (200 MPa) was performed from 1100 to 1175°C. The results are presented in Figure 11. Specimen failure occurred after a total test time of 92.05 hours and at a total strain of 0.444%.

From a plot of  $\ln \dot{\epsilon}_s$  versus  $1/T$ , one can estimate the apparent activation energy for the Dorn equation. The data are presented in Figure 12. The data are too scattered and too few to estimate the activation energy with confidence. However, it is in the range of 300 to 500 kJ/mole.

Activation energies reported<sup>5,8,29-31</sup> for other silicon nitride ceramics for the temperature regime from 1100 to 1400°C range from 535 to 709 kJ/mole again suggesting that viscous flow of the grain boundary phase governs creep deformation.

## SUMMARY

Interrupted static fatigue tests and tensile creep tests were performed in order to delineate the regimes of temperature and stress in which slow crack growth and creep cavitation are the dominate processes responsible for failure at high temperature. The threshold stress intensity for crack growth was estimated to be 1.75 and 2.00 MPa·m<sup>1/2</sup> at 1100°C in air for as-machined and oxidized samples, respectively. However, at 1200°C a strength degradation is observed for as-machined sample and is probably due to the creation of a new flaw population which produced flaws that were more severe by creep cavitation. The fact that the oxidized samples do not experience the same detrimental effect at 1200°C presumably results from an oxidation-induced microstructural change thus producing a more creep resistant material.

The tensile creep behavior of the more stable oxidized silicon nitride was measured using a optical extensometer and a flat dogbone-shaped specimen. Tensile creep tests conducted at applied stresses near or below the predicted threshold stress at 1100°C exhibited typical primary and secondary creep behavior. No concrete dependence of stress on the steady-state creep rate was obvious from this preliminary data. Creep tests at 1150°C at 200 MPa show both creep behavior and slow crack growth rupture behavior suggesting that these specimens have bracketed the threshold stress for crack growth at this temperature. All creep tests performed at 1200°C led to very short term failure at applied stresses of 100-200 MPa. Thus, the threshold stress for crack growth is near or below 100 MPa as predicted by flexural data.

#### ACKNOWLEDGEMENT

This work was supported by the U.S. Army Research Office, Metallurgy and Materials Science Division.

#### REFERENCES

1. S. M. Wiederhorn, "Subcritical Crack Growth in Ceramics," pp. 613-46 in Fracture Mechanics of Ceramics, Vol. 2, Edited by R. D. Bradt, D. P. H. Hasselman and F. F. Lange, Plenum Press, NY, 1974.
2. G. D. Quinn and J. B. Quinn, "Slow Crack Growth in Hot-Pressed Silicon Nitride," pp. 603-636 in Fracture Mechanics of Ceramics, Vol. 6., Edited by R. C. Bradt, A. G. Evans, D. P. H. Hasselman and F. F. Lange, Plenum Press, New York, 1983.
3. T. M. Konushonis, "Crack Propagation in Silicon Nitride Ceramics," M. S. Thesis, The Pennsylvania State University, University Park, PA, May 1976.
4. T. E. Easler, "Environmental Effects in the Strength Distribution of Silicon Carbide and Silicon Nitride," M. S. Thesis, The Pennsylvania State University, University Park, PA, August 1980.
5. R. Kossowsky, D. G. Miller and D. S. Diaz, "Tensile and Creep Strengths of Hot-Pressed  $\text{Si}_3\text{N}_4$ ," J. Mater. Sci., 10 983-997 (1975).
6. R. M. Arons and J. K. Tien, "Creep Strain Recovery in Hot-Pressed Silicon Nitride," J. Mater. Sci., 15 2046-2058 (1980).
7. N. J. Tighe, S. M. Wiederhorn, T. J. Chuang and C. L. McDaniel, "Creep Cavitation and Crack Growth in Silicon Nitride," pp. 587-604 in Deformation of Ceramic Materials II, edited by R. E. Tressler and R. C. Bradt, Plenum Press, New York, 1984.
8. G. Grathwohl, "Regimes of Creep and Slow Crack Growth in High Temperature Rupture of Hot-Pressed Silicon Nitride," pp. 573-86 in Ref. 7.
9. G. D. Quinn, "Static Fatigue in High Performance Ceramics," presented at ASTM Conference, San Francisco, CA (1982).
10. G. D. Quinn, "Fracture Mechanism Map for Hot Pressed Silicon Nitride," presented at Eighth Annual Conference of the Ceramic-Metal Systems Division.

11. D. F. Carroll, R. E. Tressler, Y. Tsai and C. Near, "High Temperature mechanical Properties of Siliconized Silicon Carbide Composites," in Tailoring Multiphase and Composite Ceramics, held at The Pennsylvania State University, University Park, PA, July 17-19, 1985.
12. M. R. Foley and R. E. Tressler, "Threshold Stress Intensity for Crack Growth at Elevated Temperatures in a Silicon Nitride Ceramic," to be published in *Adv. Ceram. Mater.*, 2 [1] 1988.
13. F. Wakai, S. Sakaguchi, Y. Matsuno and H. Okunda, "Tensile Creep Test of Hot-Pressed  $\text{Si}_3\text{N}_4$ ," presented at the International Symposium on Ceramic Components for Engines, Hakone, Japan, October 17-21, 1983.
14. D. F. Carroll and R. E. Tressler, "Effect of Creep Damage in the Tensile Creep Behavior of a Siliconized Silicon Carbide," to be published.
15. E. J. Minford and R. E. Tressler, "Determination of Threshold Stress Intensity for Crack Growth at High Temperature in Silicon Carbide Ceramics," *J. Am. Ceram. Soc.* 66 [5] 338-40 (1983).
16. E. J. Minford, D. M. Kupp and R. E. Tressler, "Static Fatigue Limit for Sintered Silicon Carbide at Elevated Temperatures," *ibid.*, 11 769-73.
17. S. M. Wiederhorn, N. J. Tighe, T.-J. Chuang, C. L. McDaniel and E. R. Fuller, Jr., "Structural Reliability of Brittle Material at High Temperatures," NBS Technical Report for Project No. 5610464 (1983).
18. S. M. Wiederhorn and N. J. Tighe, "Structural Reliability of Yttria-Doped Hot-Presses Silicon Nitride at Elevated Temperatures," *J. Am. Ceram. Soc.* 66 [12] 884-89 (1983).
19. H. Du; private communication.
20. J. E. Siebel, "Oxidation and Strength of Silicon Nitride and Silicon Carbide," pp. 793-804 in *Ceramics for High Performance Applications III Reliability*, edited by E. M. Lenoe, R. N. Katz and J. J. Burke, Plenum Press, New York, 1983.
21. S. C. Singhal, "Oxidation of Silicon Nitride and Related Materials," pp. 607-26 in *Nitrogen Ceramics*, edited by F. L. Riley, Noordhoff International, 1977.
22. S. C. Singhal, "Oxidation and Corrosion-Erosion Behavior of  $\text{Si}_3\text{N}_4$  and  $\text{SiC}$ ," pp. 535-48 in *Ceramics for High Performance Applications*, edited by J. J. Burke, A. E. Gorum and R. N. Katz, Brook Hill, Chesnut Hill, MA, 1974.
23. D. R. Clarke and F. F. Lange, "Oxidation of  $\text{Si}_3\text{N}_4$  Alloys: Relation to Phase Equilibria in the System  $\text{Si}_3\text{N}_4\text{-SiO}_2\text{-MgO}$ ," *J. Am. Ceram. Soc.*, 63 [9-10] 586-93 (1980).
24. C. A. Johnson, "Fracture Statistics in Design and Application," General Electric Technical Information Series Report No. 79CRO212 (1979).

25. M. R. Foley, "Flaw Behavior Near the Threshold Stress Intensity in a Hot Isostatically Pressed Silicon Nitride at Elevated Temperatures," M. S. Thesis, The Pennsylvania State University, University Park, PA May 1987.
26. F. F. Lange, E. S. Diaz and C. A. Andersson, "Tensile Creep Testing of Improved Si<sub>3</sub>N<sub>4</sub>, Am. Ceram. Soc. Bulletin 58 [9] 845-848 (1979).
27. H. Tanaka and Y. Inomata, "Primary Creep of Sintered Silicon Nitride," presented at the International Symposium on Ceramic Components for Engines, Hakone, Japan, 1983.
28. R. Morrell and K. H. G. Ashbee, "High Temperature Creep of Lithium Zinc Silicate Glass-Ceramics," J. Mater. Sci., 8 1253-1270 (1973).
29. G. Grathwohl and F. Thümmler, "Interaction Between Creep, Oxidation and Microporosity in Reaction-Bonded Silicon Nitride," Ceramurgia International 6 [2] 43-50 (1980).
30. S. V. Din and P. S. Nicholson, "Creep of Hot-Pressed Silicon Nitride," J. Mater. Sci., 10 1375-1380 (1975).
31. J. M. Birch and B. Wilshire, "The Compression Creep Behavior of Silicon Nitride Ceramics," J. Mater. Sci. 13 2627-2636 (1978).

## FIGURE CAPTIONS

Figure 1. Transmission electron micrographs showing general microstructural features by bright field imaging (a) and dark field imaging of amorphous grain boundary phase (b)

Figure 2. Tensile specimen design.

Figure 3. Loading system of creep apparatus

Figure 4. Effect of initial applied stress intensity on fracture stress of as-machined HIPSN at 1100°C in air, static load time: ten hours.

- - Tested after proof testing, no prior static loading
- - Tested after static loading
- ▼ - Failed during static loading
- 24 - Indicates the number of samples tested.

Figure 5. Effect of initial applied stress intensity on fracture stress of oxidized HIPSN at 1100°C in air, static load time: ten hours.

- - Tested after proof testing, no prior static loading
- - Tested after static loading
- ▼ - Failed during static loading
- 24 - Indicates the number of samples tested.

Figure 6. Effect of initial applied stress intensity on fracture stress of as-machined HIPSN at 1200°C in air, static load time: ten hours.

- - Tested after proof testing, no prior static loading
- - Tested after static loading
- ▼ - Failed during static loading
- 24 - Indicates the number of samples tested.

Figure 7. Effect of initial applied stress intensity on fracture stress of oxidized HIPSN at 1200°C in air, static load time: ten hours.

- - Tested after proof testing, no prior static loading
- - Tested after static loading
- ▼ - Failed during static loading
- 24 - Indicates the number of samples tested.

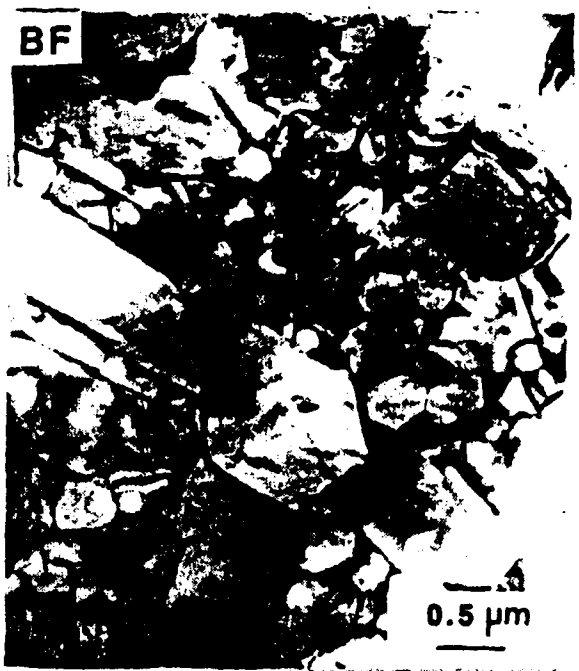
Figure 8. Creep strain versus time at 1100°C in air for specimens under stresses of 100, 150 and 200 MPa.

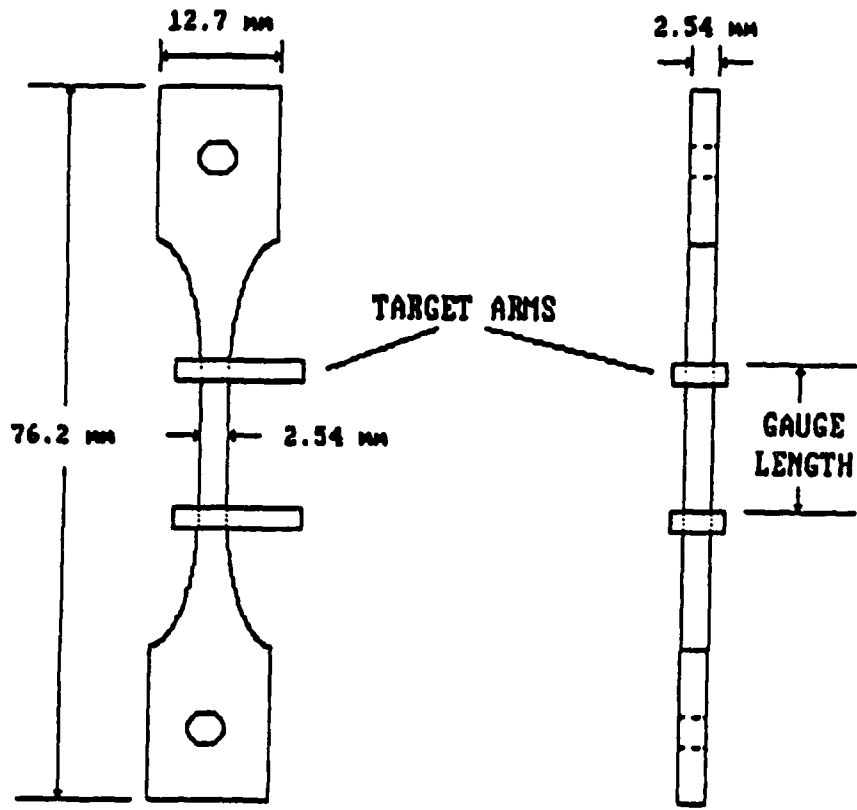
Figure 9. Log steady state creep rate versus log applied stress at 1100°C in air.

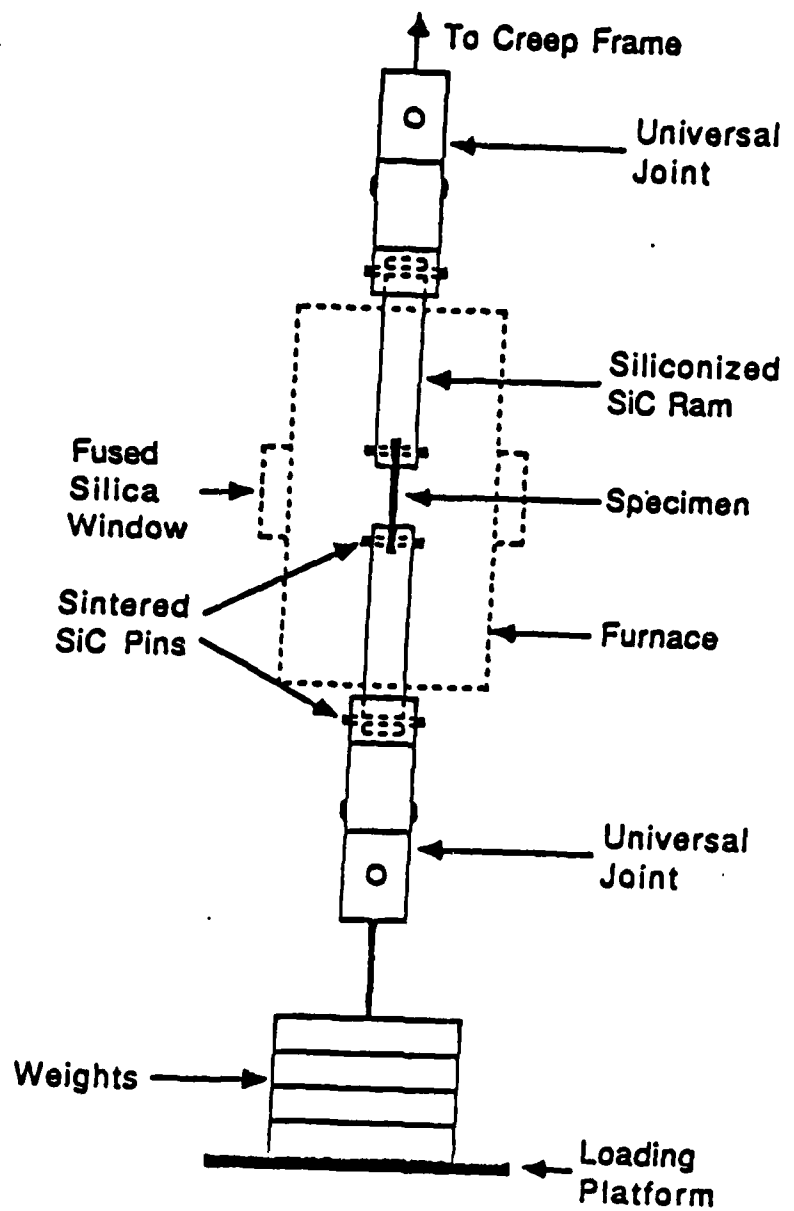
Figure 10. Creep strain versus time at 1150°C for a specimen under a stress of 200 MPa.

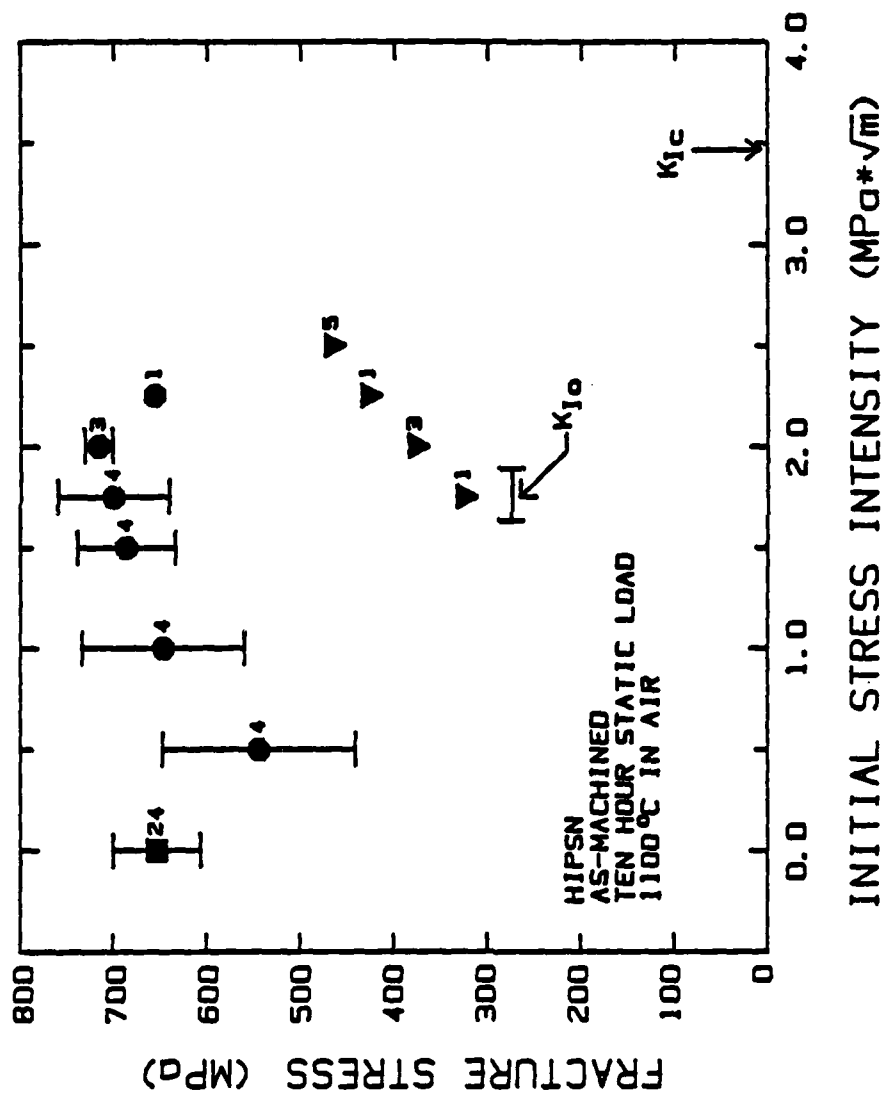
Figure 11. Creep strain versus time at 1100-1175°C for a specimen under an applied stress of 200 MPa.

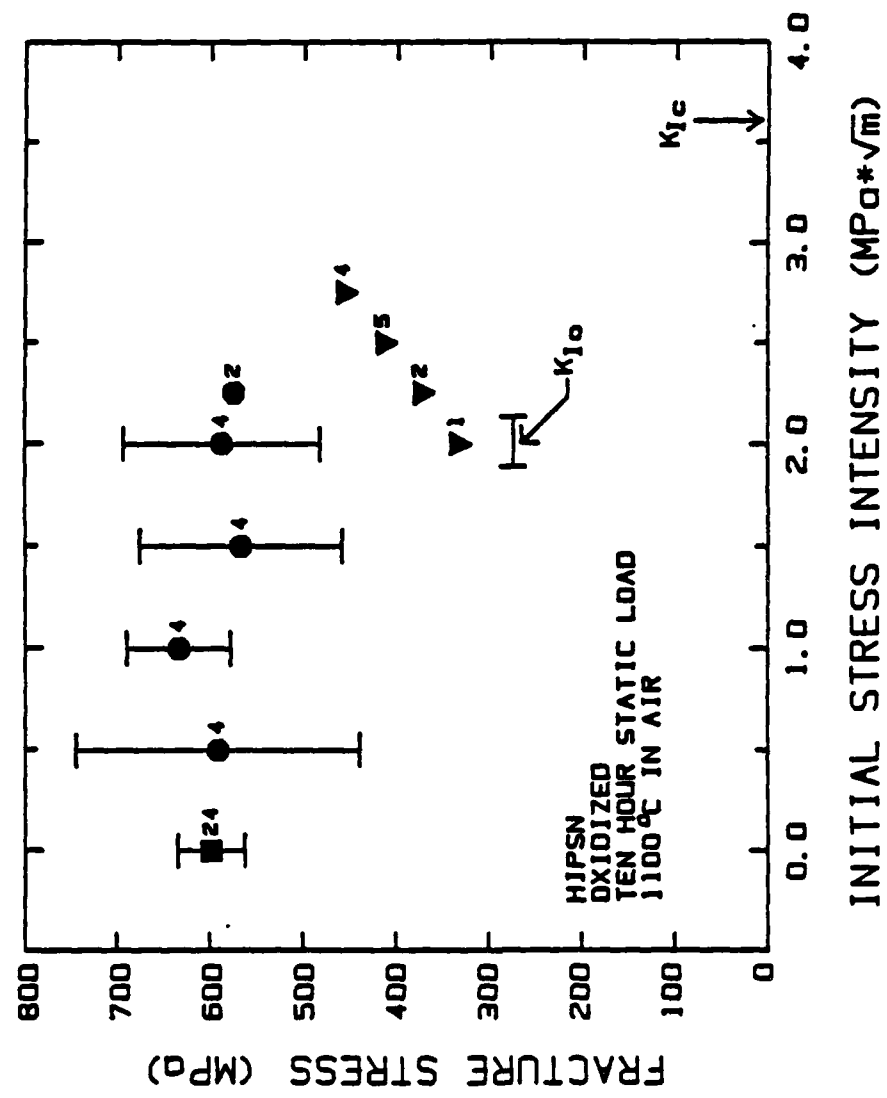
Figure 12. Ln steady-state creep rates versus temperature for an applied stress of 200 MPa.

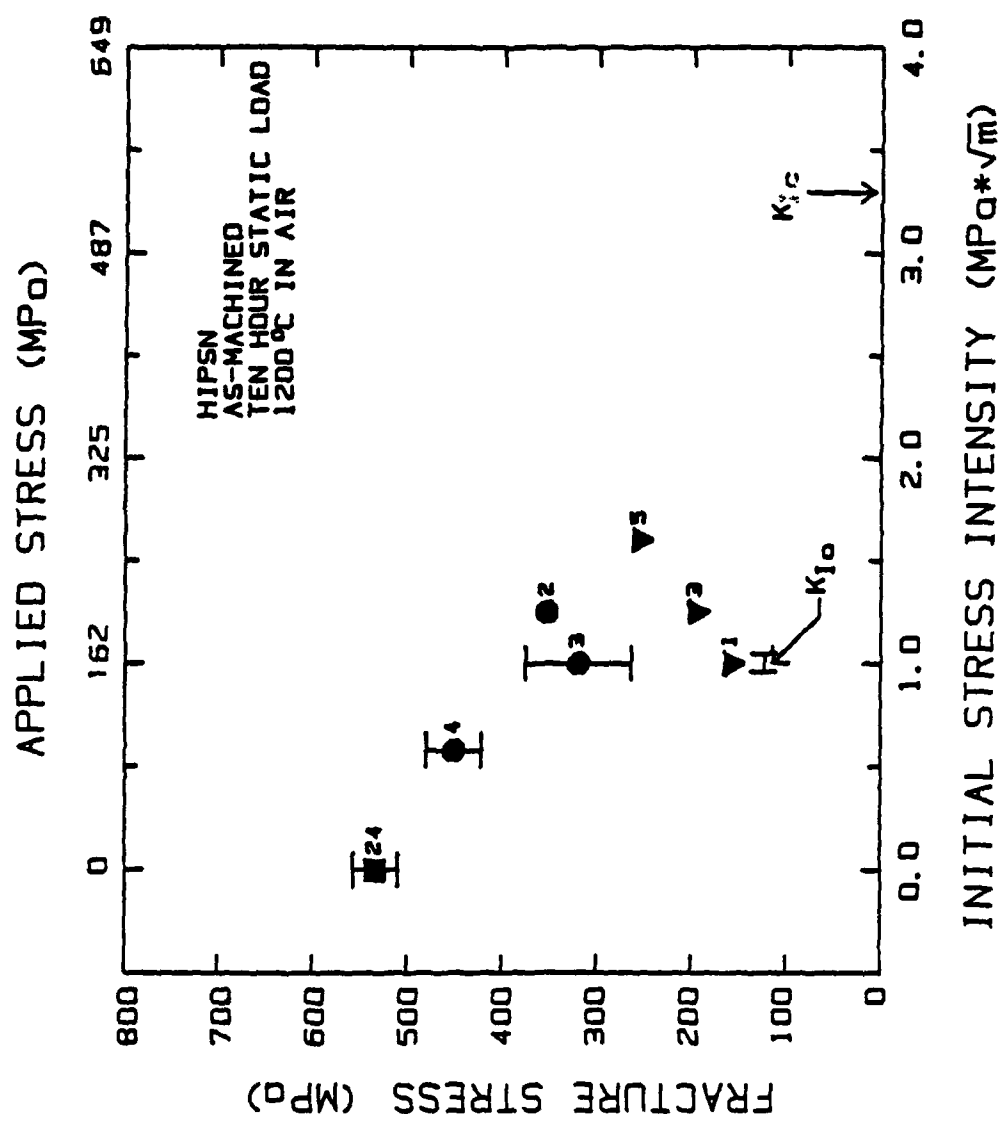


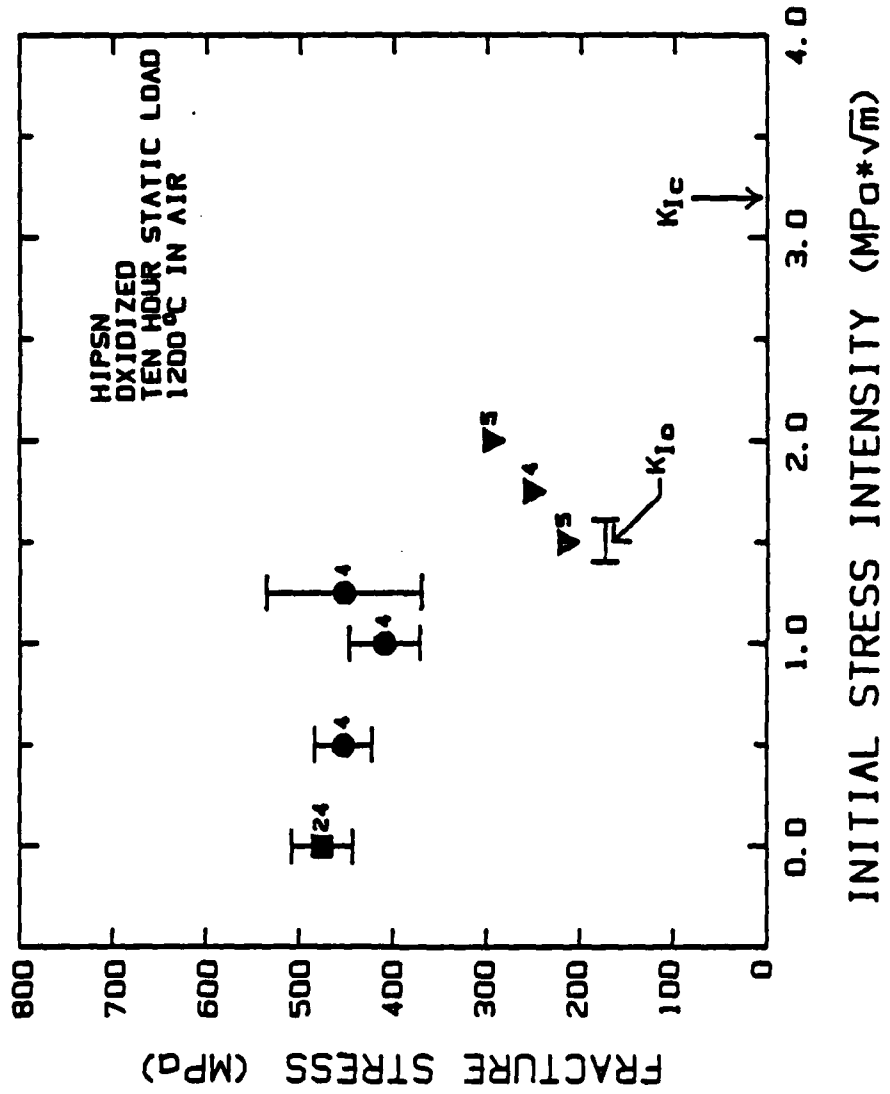




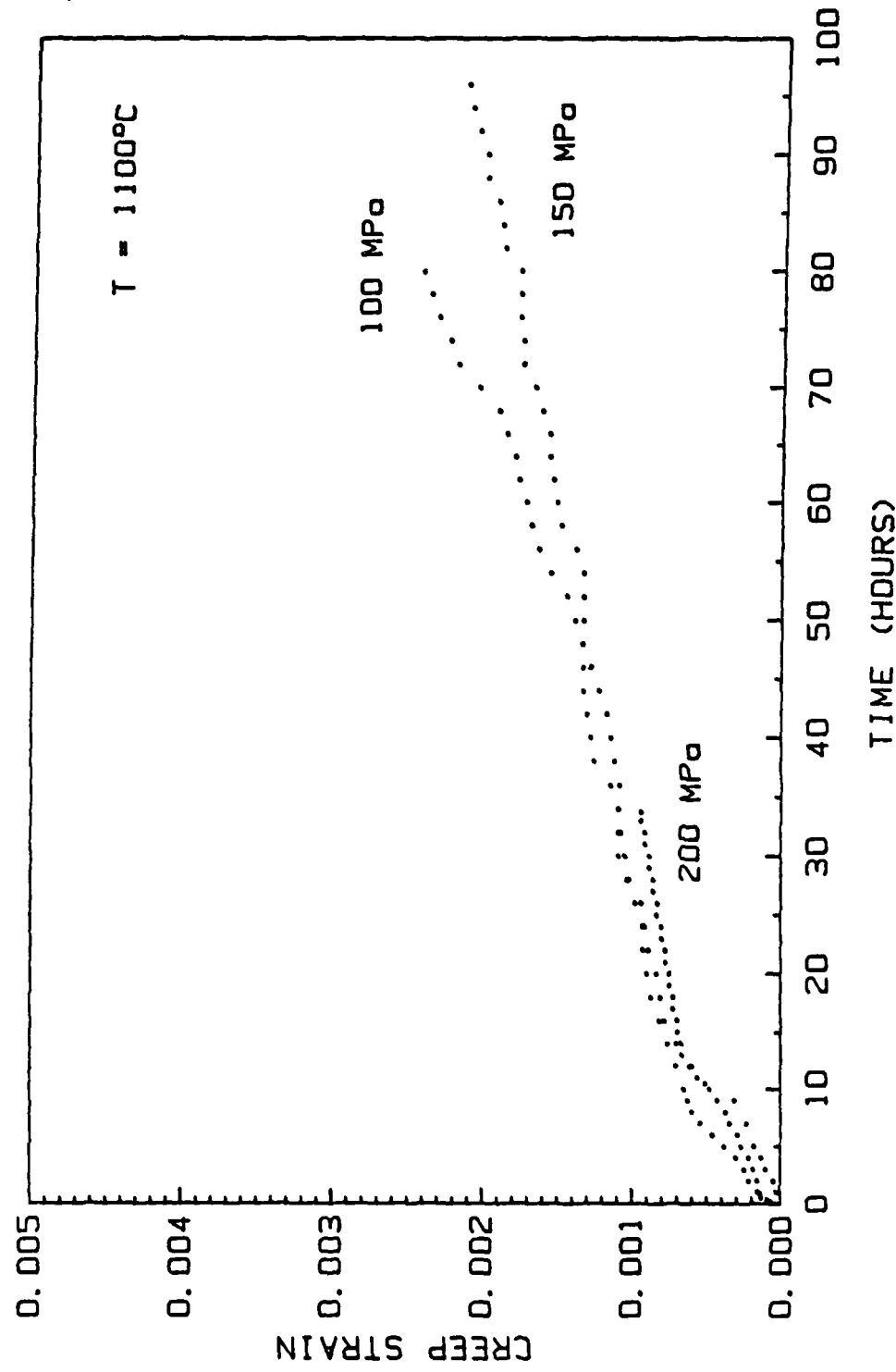


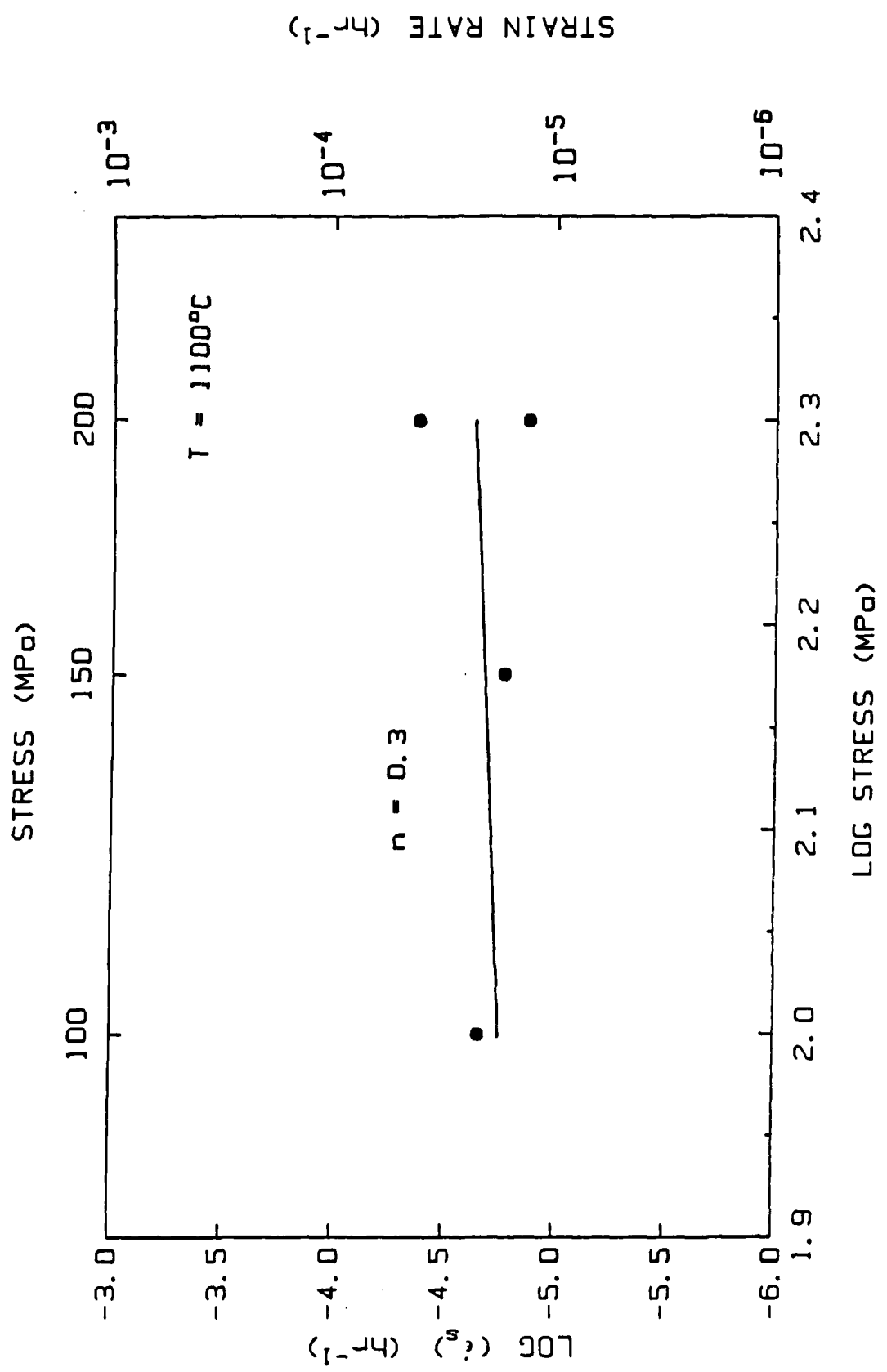




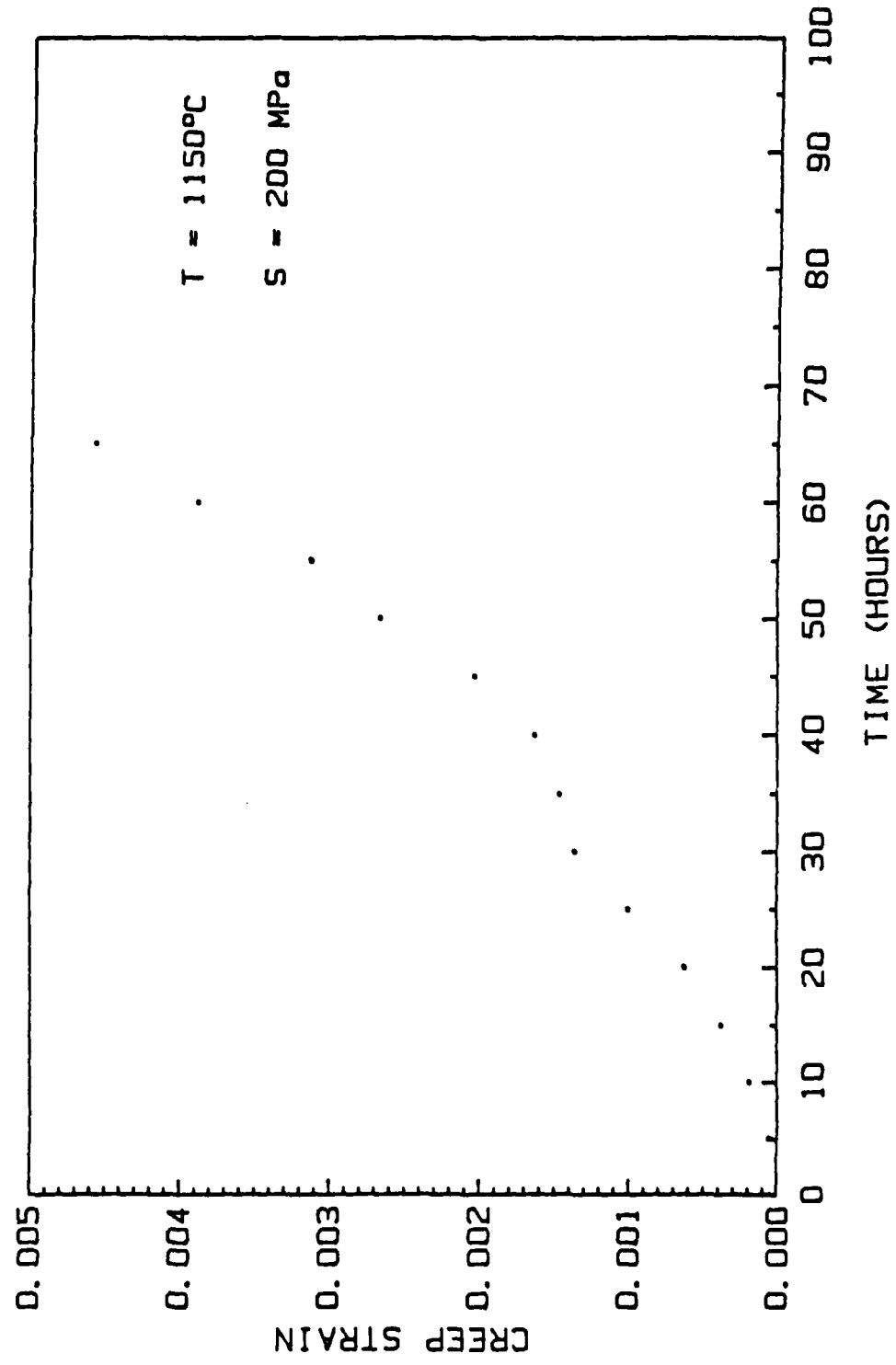


Creep Strain vs. Time for AYG

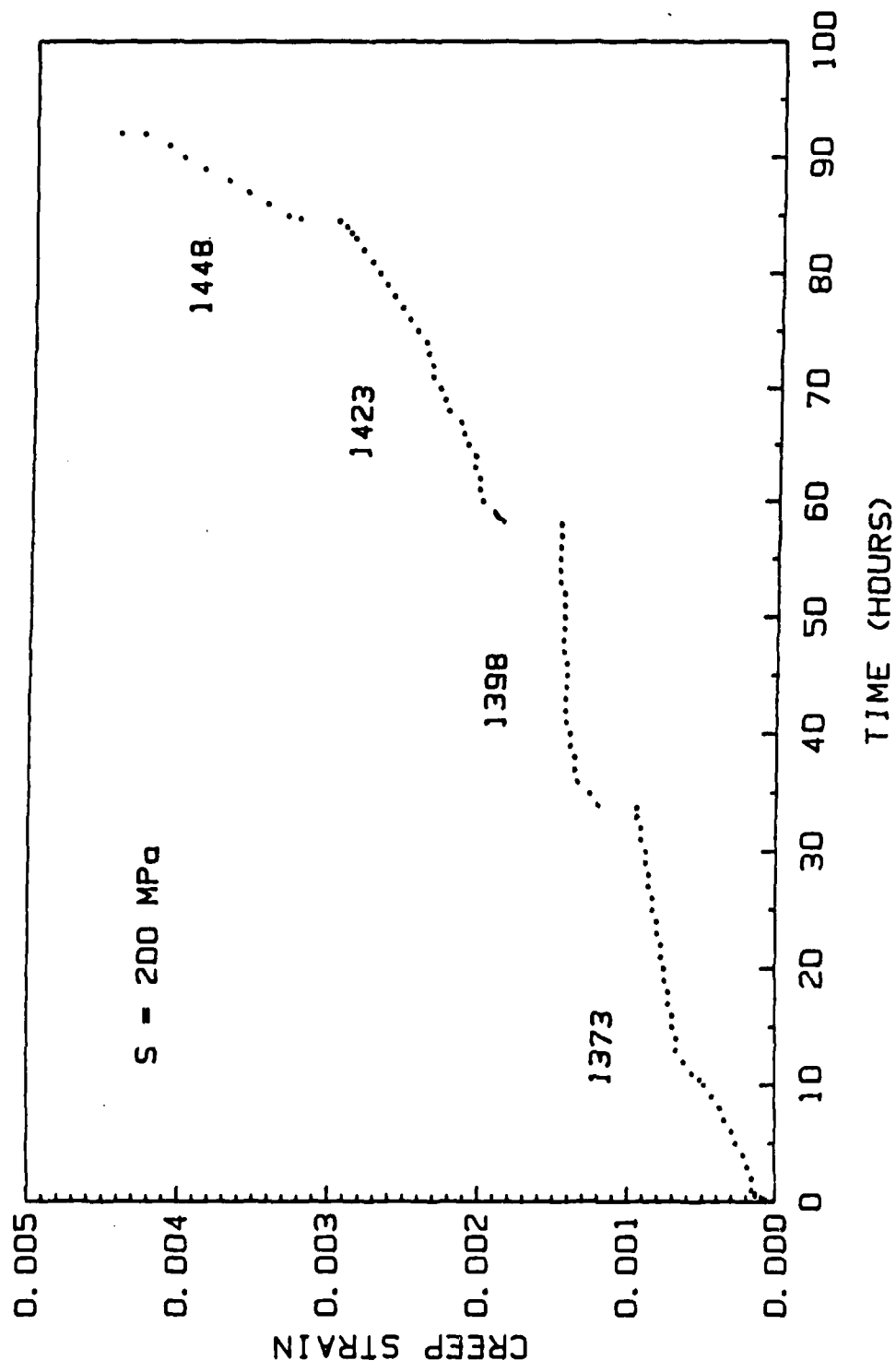


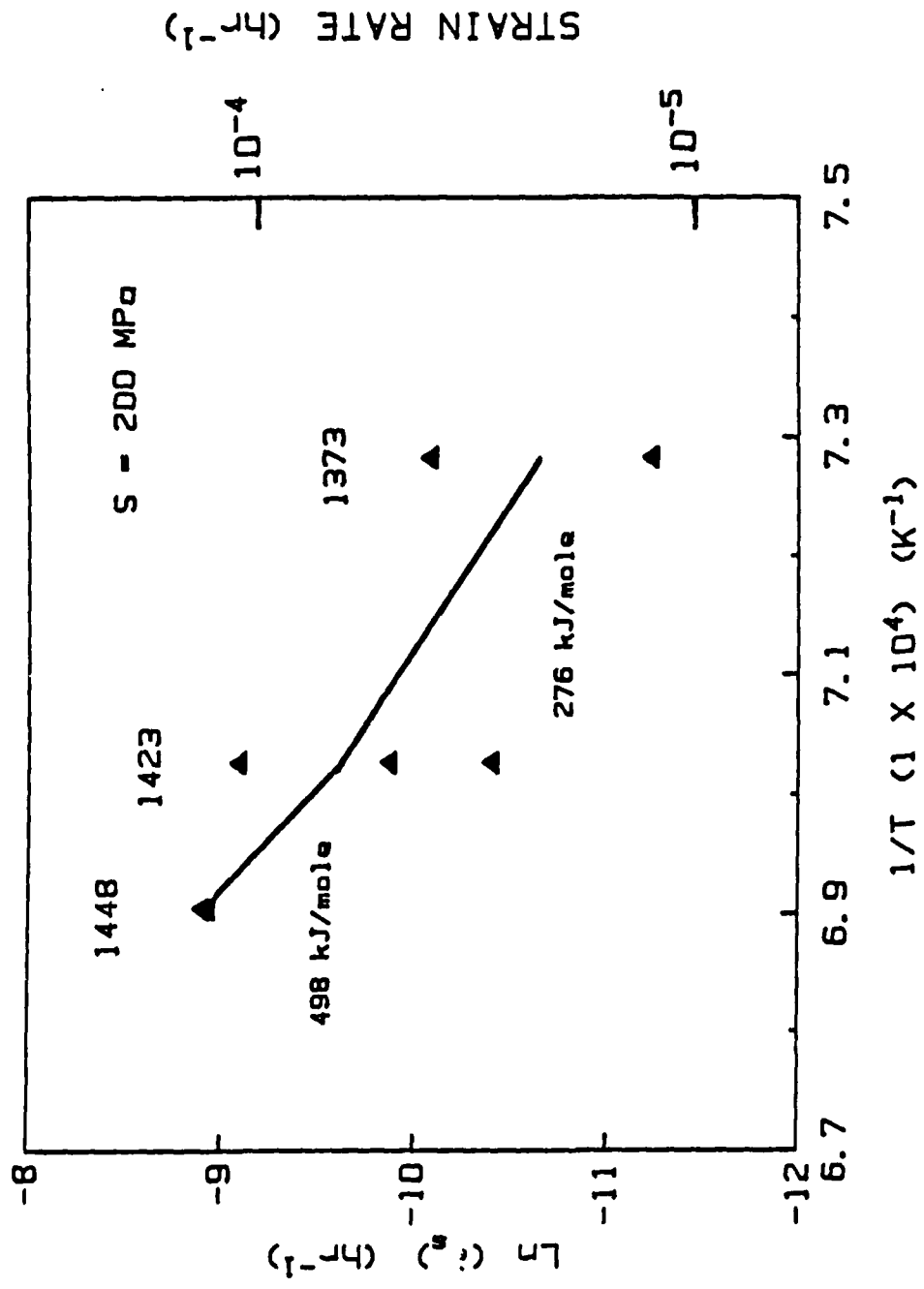


Creep Strain vs. Time for AY6



Creep Strain vs. Time for AY6





COMPARISION OF THE TIME DEPENDENT  
STRENGTH OF THREE COMMERCIALLY  
AVAILABLE SILICON NITRIDE MATERIALS

by M. R. Foley, C. A. Randall, R. E. Tressler

## INTRODUCTION

In recent years, advanced engineering ceramics have been developed and studied for elevated temperature structural applications. Heat recovery systems, heat engines, turbine blades and rotors in gas turbine engines are prime examples of the use of these ceramics. Because of the combination of high strength to weight ratio, retained strength at elevated temperature and favorable oxidation, corrosion and thermal shock resistance silicon nitride - based ceramics are excellent candidates for these application.

Polycrystalline ceramics such as silicon nitride are susceptible to slow crack growth in severe atmospheres and elevated temperatures. A knowledge of the short term strength and fracture toughness of these ceramics are essential for design purposes, but these properties do not determine how a material will behave over time at stresses well below the fracture stress or stress intensities above the threshold stress intensity for slow crack growth.

Early studies on threshold values were concerned with amorphous materials. More recently investigators have studied polycrystalline non-oxide ceramics such as SiC and Si<sub>3</sub>N<sub>4</sub> at elevated temperatures.

The high temperature properties of Si<sub>3</sub>N<sub>4</sub> - based ceramics are strongly influenced by the grain boundary phases. Magnesia-doped and alumina-yttria-doped silicon nitride materials show some promise for use at elevated temperatures (>1000 C), but softening of the amorphous grain boundary phase(s) has limited there application temperatures. New Si<sub>3</sub>N<sub>4</sub> ceramics using yttria or yttria-silica as sintering aids have been introduced with improved high temperature strengths over the older generation Si<sub>3</sub>N<sub>4</sub> ceramics.

The objectives of this study is to compare the behavior of flaws near the threshold stress intensity for crack growth in three commercially available silicon nitride ceramics, and to explain the differences in terms of the grain boundary composition and structure.

## EXPERIMENTAL PROCEDURE

The three silicon nitride - based ceramics used in this study are all commercially available. The manufacturers, grade designations, sintering aids, processing and bulk densities are summarized in Table 1. The AY6 material was received in rectangular billets measuring -20 by 30 by 5 mm. Test specimens were cut from the billets using an 8-in. continuous resin bonded diamond cut-off wheel. The PY6 and SN250M materials were received as bend bars measuring -6.4 by 3.2 by 51 mm. These were cut in half to increase the number of samples available for testing. The major faces of all the samples were surface ground to a 600 grit finish using a diamond wheel. Tensile surfaces were hand beveled using a 15 micron diamond disk to eliminate any edge checking flaws that may have formed during grinding.

The interrupted static fatigue test used in this study has been fully described by Minford and co-workers. The test involves heating the sample to test temperature, rapidly loading to a predetermined static load level and maintaining that load level for a specified time. If the sample does not fail during the soak time, it is rapidly loaded to failure at the test temperature. This test directly measures the effect of an applied stress intensity during static loading on the fracture stress. This in turn reflects any changes in flaw severity and gives one an estimate of the threshold stress intensity for crack growth in the material.

The specific experiment consisted of a four point bend test using a lower span of 20 mm and an upper span of 5 mm. All samples were static loaded in the as-machined condition at 1200 C in air for 10 hours, if they survived. After the 10 hour soak the samples were loaded to failure at a stressing rate of 30-35 MPa/sec.

Due to the limited number of samples available the flaw distribution and fracture toughness of the PY6 and SN250M materials could not be accurately determined. Therefore a specific threshold stress intensity could not be measured directly. However an estimate of the threshold stress intensity can be measured by observing the effect of an applied stress on the fracture stress of these Si<sub>3</sub>N<sub>4</sub> materials.

Test bars were loaded into the furnace and the knife edges aligned prior to heat up. Furnace heat up to 1200 C in air took -30 minutes. Because of thermal expansion during heat up, the test specimens were kept under a small load (<5 lbs.) to keep the knife edges aligned. The assembly was held at test temperature for -20 minutes before starting the test to allow the sample and load train to reach thermal equilibrium. The sample was then loaded to a specific stress and held for ten hours, assuming the sample survived, after which the load was increased at the fast fracture stressing rate until failure occurred.

Since the sample is loaded to failure directly from the static load level, the changes in flaw severity are examined without the complicating factors of changes in

temperature or unloading the specimen prior to fracture. One can observe the fracture stress as a function of initial applied stress (or stress intensity), which directly yields the threshold value. Also one can select the time scale of the test such that all samples loaded above the threshold fail during static loading.

## RESULTS AND DISCUSSION

The interrupted static fatigue test was applied to estimate the threshold stress for crack growth at 1200 C in air for the three materials.

AY6 SAMPLES. Figure 1 shows the results of the Al2O3-Y2O3-doped material static loaded at various initial applied stresses at 1200 C in air. Plotted at an initial applied stress of zero are samples fractured at 1200 C with no prior static loading. The symbols and error bars represent the mean fracture stress and 95% confidence interval, respectively. There is a sharp decrease in mean fracture stress with increasing initial applied stress. The first evidence of slow crack growth is observed at an initial applied stress of 162 MPa in that one of four samples failed during static loading. At a slightly higher applied stress value there is still some mixed behavior (3 of 5 failed), but at applied stresses > 225 MPa all samples failed during static loading, most within minutes of reaching the static load level. The threshold stress is indicated by the first evidence (lowest stress) of mixed behavior, i.e. 162 MPa. The decreasing mean fracture stress with increasing initial applied was attributed to the creation of a new flaw population which produced flaws that were more severe. This has been discussed in earlier work by Foley and Tressler.

PY6 SAMPLES. The static load data for the Y2O3-doped material is shown in Figure 2. Potted at an initial applied stress of zero are the mean fast fracture stresses at 1150 C (diamond) and 1250 C (square) in air (Allison). The remaining data is at 1200 C in air. The first evidence for crack growth occurs at an initial applied stress of 375 MPa in that only one of six samples failed during static loading. Mixed behavior is also observed at applied stresses up to 450 MPa but no samples survived the ten hour static load above that. Therefore the threshold stress for crack growth in the PY6 material is estimated to be 375 MPa.

SN250M SAMPLES. Shown in Figure 3 are the interrupted static fatigue test results for the Y2O3-SiO<sub>2</sub>-doped material. The mean fast fracture stress is -700 MPa (Kyocera) and is plotted at an initial applied stress of zero. The first evidence of slow crack growth occurs at an initial applied stress of 388 MPa which is very close to that observed for the PY6 material. It should be noted that at an initial applied stress of 350 MPa four of the samples (circle) were loaded to failure after ten hours of static loading and one sample was held for 27.5 hours before loading to failure (diamond). Table 2 summarizes the threshold stress results for all three materials.

It is well known that using certain densification aids for sintering of ceramics can produce a fully dense material with a grain boundary phase. It is this grain boundary phase that when subjected to loads at elevated temperatures can have deleterious effects on the mechanical properties of the bulk material. Tables 1 and 2 outline the differences in bulk composition and threshold behavior between the three silicon nitride materials. In order to more fully characterize and explain the large differences in threshold behavior between these ceramics, XRD was performed on as-machined surfaces.

Qualitative macro analysis by XRD revealed that B-Si<sub>3</sub>N<sub>4</sub> was the only crystalline phase in the AY6 material. In contrast, the PY6 and SN250M material contain both B-Si<sub>3</sub>N<sub>4</sub> and a second crystalline phase Y<sub>2</sub>Si<sub>2</sub>O<sub>7</sub>.

Transmission electron microscopy was performed to further analyze general microstructural features and grain boundary compositional differences.

In Figure 4a, a bright field image of the AY6 material shows the general microstructure. There is a range of grain sizes from <0.25 - 4 microns and elongated grains with aspect ratios of approximately 5. Also observed is an inhomogeneous distribution of grain boundary phase from very thin regions to large pockets. Localized analysis of the grain boundary phase using convergent beam microdiffraction revealed an amorphous ring and dark field imaging of the amorphous ring shows the distribution of the grain boundary phase as shown in Figure 4b. Energy dispersive spectroscopy (EDS) of the grain boundary phase detected Al, Si, and Y as shown in 4c. The Ar is from the ion thinning process and the Cu is from the grid used to hold the sample. There were small regions of iron-rich particle also observed in the AY6 material and is shown in 4d.

Figure 5 contains the TEM data for the PY6 material. 5a is bright field image of the general microstructure with similar features to the AY6 material in grain size range and grain boundary distribution. However, localized analysis of the grain boundary phase using convergent beam microdiffraction revealed a diffraction pattern indicative of the crystalline grain boundary phase and is shown in 5b. The EDS of this phase detected only Si and Y (5c). Also, in isolated cases small pockets of Y<sub>2</sub>Si<sub>2</sub>O<sub>7</sub> are trapped in a low angle grain boundary between two silicon nitride grains (5d).

The TEM observations for the SN250M material is shown in Figure 6. Again the general microstructural features are similar in grain size range and grain boundary phase distribution to both the AY6 and PY6 (5a). Convergent beam microdiffraction revealed that the grain boundary phase is crystalline, similar to the PY6 material (6b and c). EDS detected Si, Y, and Sr.

In this study, estimates of the threshold stress for crack growth in three different silicon nitride ceramics were observed at 1200 C in air on as-machined samples. In attempting to rationalize the large variation in threshold behavior and keeping in mind that failure is predominately intergranular at this temperature, qualitative

analysis of the grain boundary phase(s) was utilized. The PY6 and SN250M both with a crystalline grain boundary phase showed an increase in threshold stress by more than a factor of two over the AY6 material with an amorphous grain boundary phase. The effect of the more refractory crystalline grain boundary is not only seen in increases in the threshold stress but there is no significant decrease in the mean fracture stress with increasing applied stress. In the AY6 material, a new more severe flaw population was produced by creep cavitation processes as identified by Grathwohl (ref), Quinn (ref) and Tighe and co-workers (ref). The PY6 and SN250M showed no evidence of this phenomenon at 1200 C in air.

#### SUMMARY

An interrupted static fatigue test for estimating threshold stress intensities was applied to three commercially available silicon nitride-based materials in the as-machined conditioned at 1200 C in air. The effect of initial applied stress on the fracture stress as an indication of the threshold stress intensity indicated threshold stresses of 162 MPa, 375 MPa and 388 MPa for the AY6, PY6 and SN250M materials, respectively. The threshold stress (or threshold stress intensity) was found to depend on the nature of the grain boundary phase in beta-Si<sub>3</sub>N<sub>4</sub> ceramics with similar grain size and morphology. Differences in grain boundary structure from amorphous to crystalline would account for an increase in the threshold stress by more than a factor of two.

MATERIALS

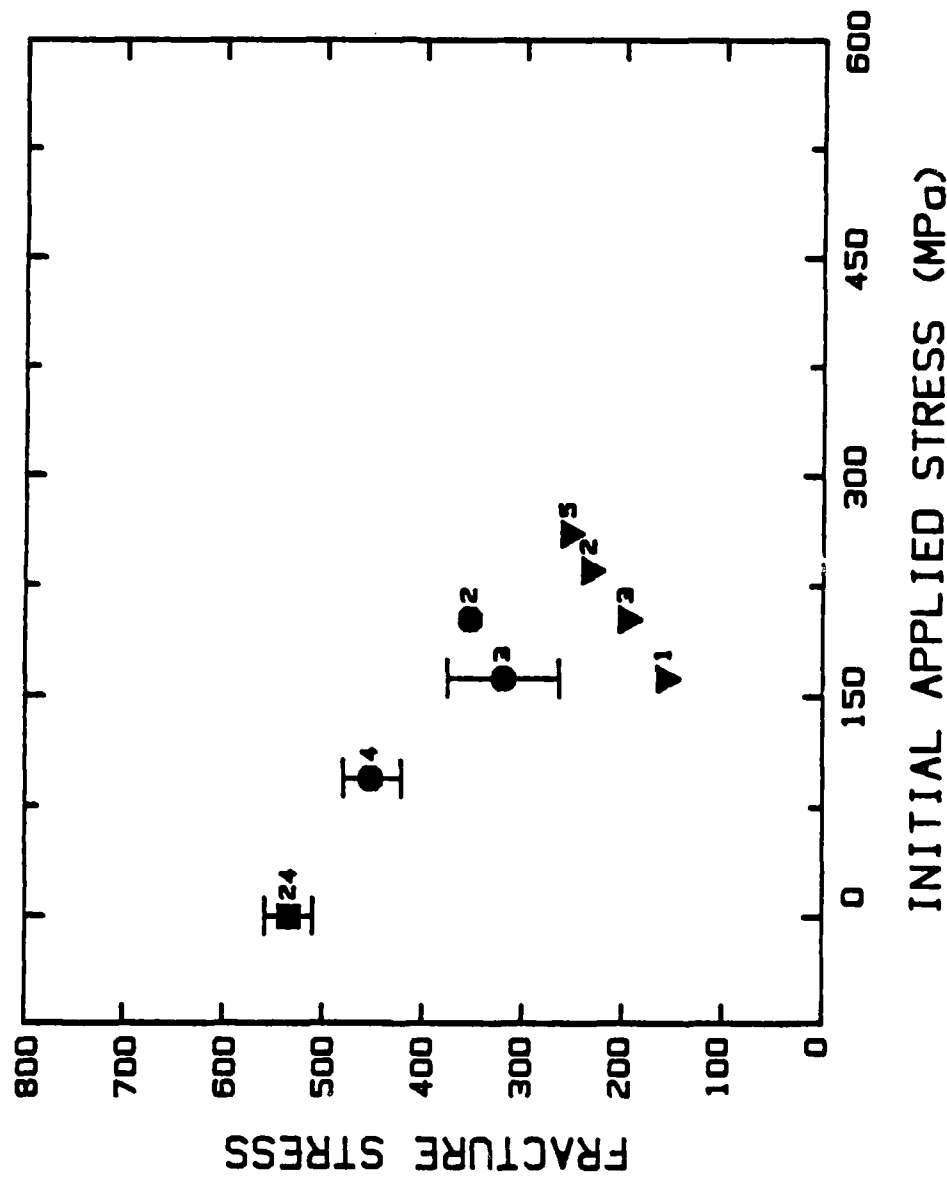
	A	B	C
MANUFACTURER	GTE	GTE	KYOCERA
CODE	AY6	PY6	SN250M
ADDITIVES	Al <sub>2</sub> O <sub>3</sub> , Y <sub>2</sub> O <sub>3</sub>	Y <sub>2</sub> O <sub>3</sub>	SiO <sub>2</sub> , Y <sub>2</sub> O <sub>3</sub>
PROCESSING	HIP'ED	HIP'ED	SINTERED
DENSITIES (G/CC)	3.2-3.26	3.2-3.26	3.2-3.26

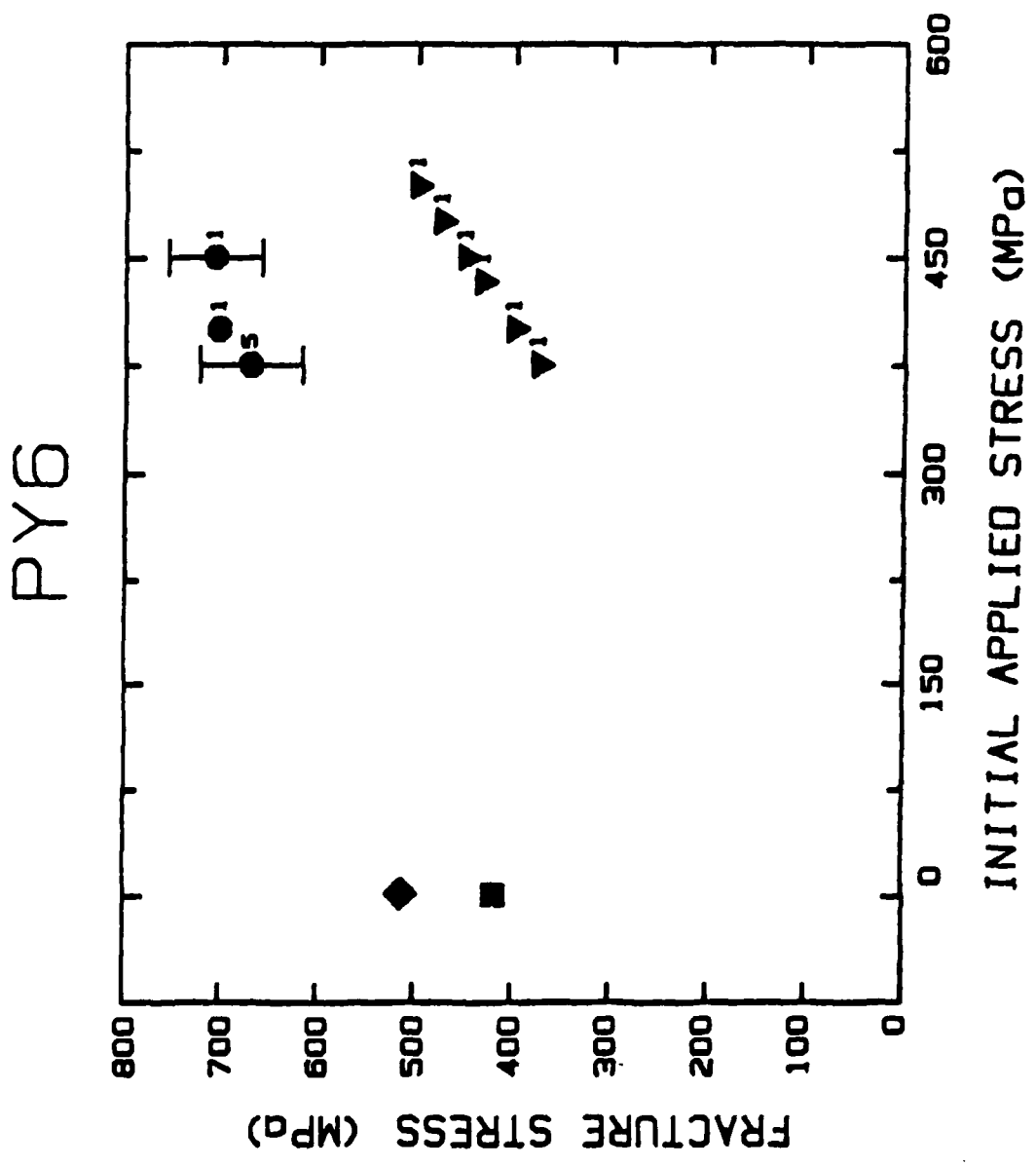
TABLE 1-

STATIC LOAD RESULTS

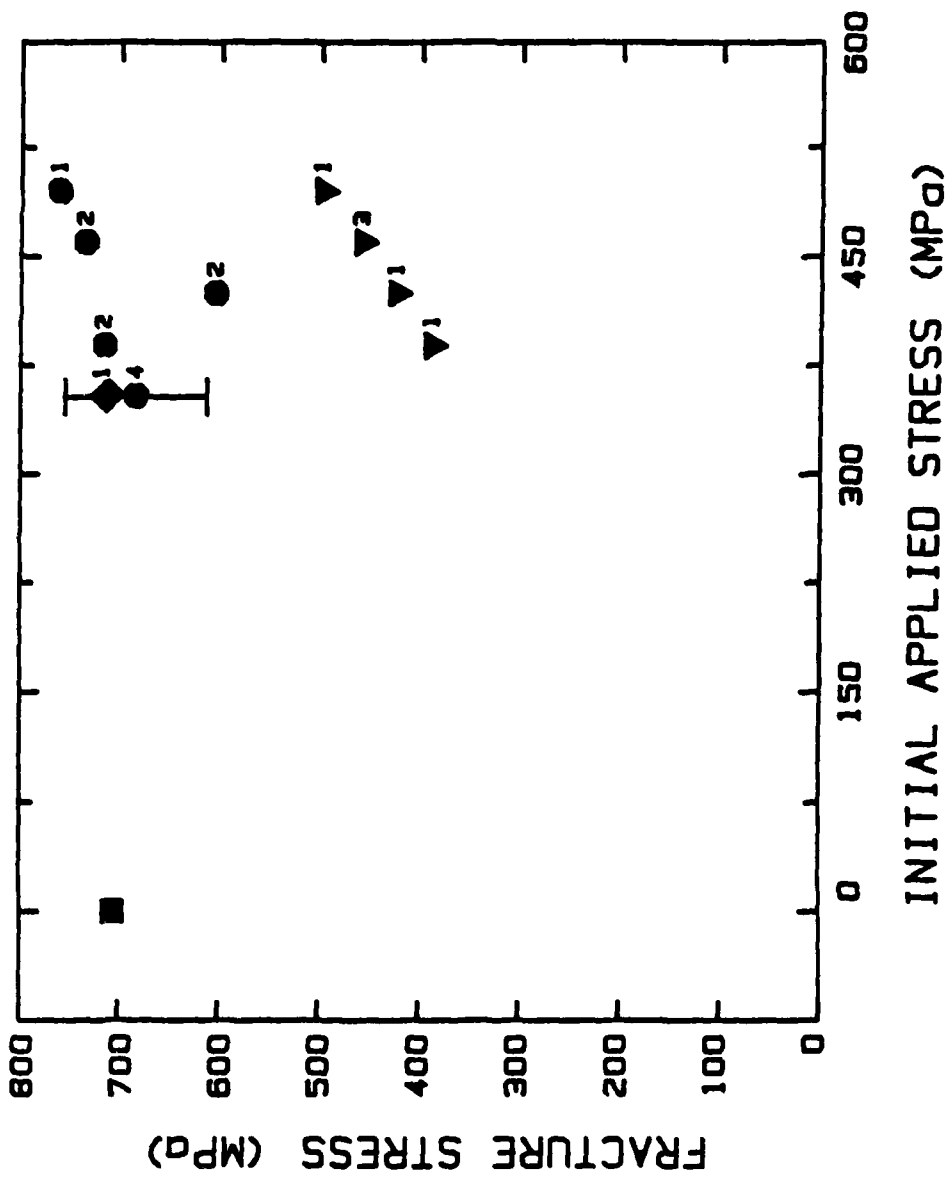
	AY6	PY6	SN250M
THRESHOLD STRESS	-160 MPa	-375 MPa	-390 MPa

A Y 6





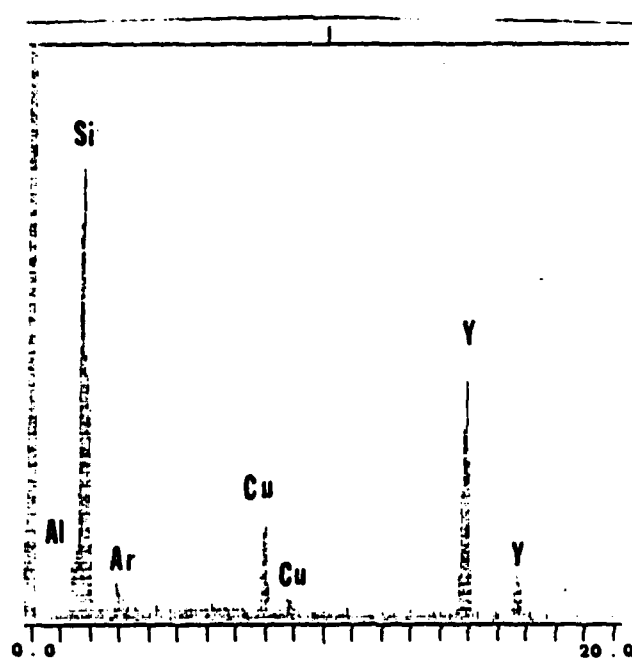
# SN250M



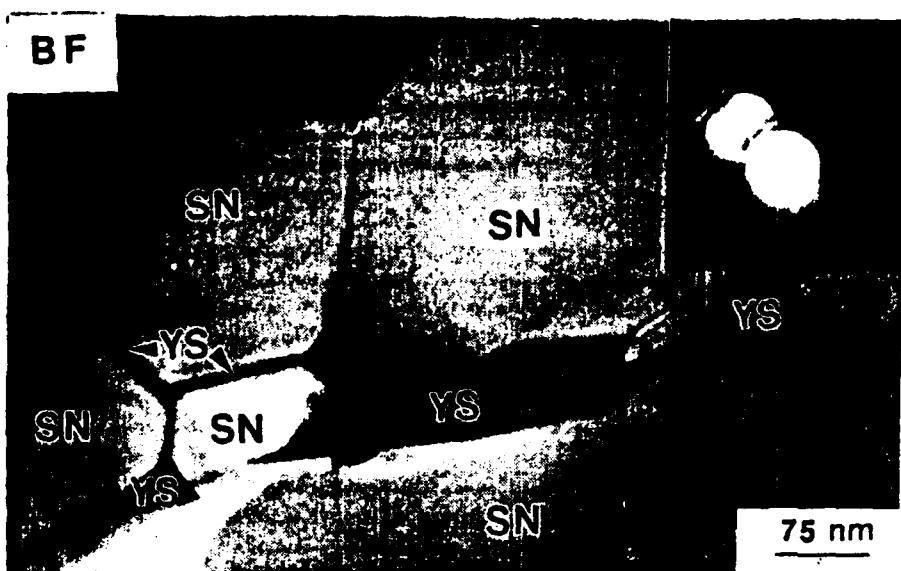
A Y6



b

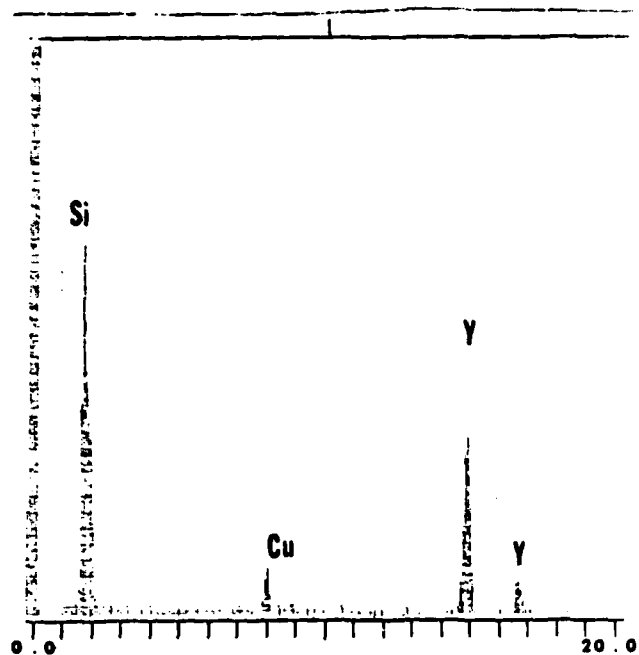
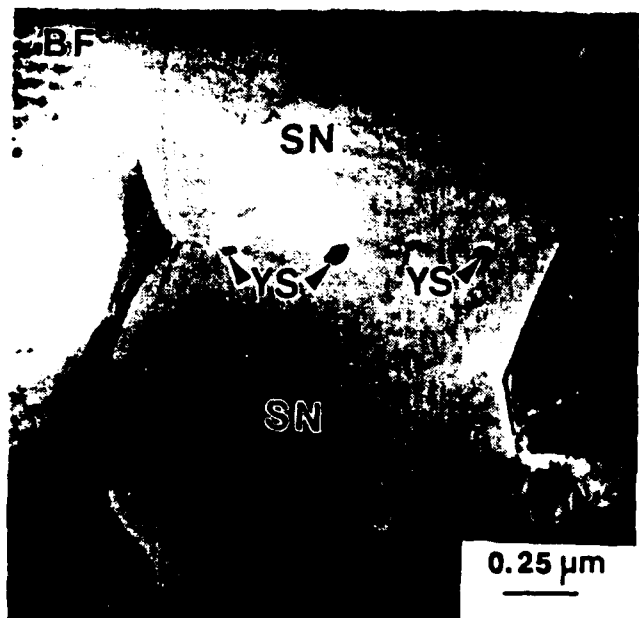


PY6



a

b



SN<sub>2</sub>SiO<sub>4</sub>

